Strength of Welded Thin-walled Square Hollow Section T-joint Connections by FE Simulations and Experiments

A Thesis Submitted to

The College of Graduate Studies and Research

In Partial Fulfillment of the Requirements

For the Degree of Doctor of Philosophy

In the Department of Mechanical Engineering

University of Saskatchewan

Saskatoon, Canada

By

Reza Moazed

PERMISSION TO USE

In presenting this thesis in partial fulfilment of the requirements for a postgraduate degree from the University of Saskatchewan, I agree that the Libraries of this University may make it freely available for inspection. I further agree that permission for copying of this thesis in any manner, in whole or in part, for scholarly purposes may be granted by the professor or professors who supervised my thesis work or, in their absence, by the Head of the Department or the Dean of the College in which my thesis work was done. It is understood that any copying or publication or use of this thesis or parts thereof for financial gain shall not be allowed without my written permission. It is also understood that due recognition shall be given to me and to the University of Saskatchewan in any scholarly use which may be made of any material in my thesis.

Requests for permission to copy or to make other use of the material in this thesis in whole or part should be addressed to:

Head of the Department of Mechanical Engineering
College of Engineering, University of Saskatchewan
Saskatoon, Saskatchewan, Canada S7N 1L5

Abstract

Hollow section members are widely used in industrial applications for the design of many machine and structural components. These components are often fabricated at lower cost by welding rather than by casting or forging. For instance, in agricultural machinery, the hollow tubes are typically connected together through welding to form T-joints. Such T-joint connections are also employed in other engineering applications such as construction machinery, offshore structures, bridges, and vehicle frames. In this dissertation, the behaviour of tubular T-joint connections, in particular square hollow section (SHS)-to-SHS T-joints, subjected to static and cyclic loads is studied both experimentally and numerically.

The techniques used for the fabrication of the T-joint connections can affect their strengths to different degrees. With modern advances in manufacturing technologies, there are many alternatives for the fabrication of the T-joint connections. For instance, in recent years, the use of the laser beam has become increasingly common in industrial applications. From a manufacturing point of view, the T-joint connections can be fabricated by using traditional mechanical cutting or laser cutting techniques. Currently, for the fabrication of the T-joint connections, the straight edge of one tube is cut using mechanical tools (e.g., flame cutting) and then welded to the body of the other tube. A major contribution of this research work is investigating the feasibility of using laser cutting to produce welded square hollow-section T-joints with similar or higher fatigue strengths than their conventional mechanical cut counterparts. For this purpose, a total of 21 full-scale T-joint samples, typical of those found in the agricultural machinery, are included for the study. Finite Element (FE) models of the T-joints manufactured with the

different cutting techniques are also developed and the FE results are verified with the experiments. The results of the numerical and experimental study on the full-scale T-joint samples show that the fatigue strength of the samples that are manufactured with laser cutting is higher than those fabricated with conventional mechanical cutting.

From a structural analysis view point, despite of the wide use of tubular T-joint connections as efficient load carrying members, a practical but yet simple and accurate approach for their design and analysis is not available. For this purpose, engineers must often prepare relatively complicated and time consuming FE models made up of shell or solid elements. This is because unlike solid-section members, when hollow section members are subjected to general loadings, they may experience severe deformations of their cross-sections that results in stress concentrations in the connection's vicinity. One of the objectives/contributions of this research work is the better understanding of the behaviour of SHS-to-SHS T-joint connections under in-plane bending (IPB) and out-of-plane bending (OPB) loading conditions. Through a detailed Finite Element Analysis (FEA) using shell and solid elements, the stiffness and stress distribution at the connection of the tubular T-joints are obtained for different loading conditions. It is observed that at a short distance away from the connection of the T-joints, the structure behaves similar to beams when subjected to loadings. The beam like stresses cease to be valid only in the vicinity of the connection. Therefore, several parameters are defined to recognize the joint's stress concentrations and the bending stiffness reduction. These parameters permit the accurate modelling of the tubes and the T-connection by simple beam elements with certain modifications. The models consisting of beam elements are significantly easier to prepare and analyze. Through several numerical examples, it is

shown that the modified beam models provide accurately all important information of the structural analysis (i.e. the stresses, displacements, reaction forces, and the natural frequencies) at substantially reduced computational effort in comparison with the complicated Finite Element (FE) models built of shell or solid elements.

Another contribution of this research work is the FE modelling of the weld geometry and its effect on the stresses at the vicinity of the connection. The results of the FE modelling are verified through a detailed experimental study. For the experimental study, two test fixtures with hydraulic actuators capable of applying both static and cyclic loadings are designed and used. Strain gauges are installed at several locations on full-scale T-joint samples to validate the developed FE models. It is shown that the membrane stresses which occur at the mid-surface of the tubes remain similar regardless of the weld geometry. The weld geometry only affects the bending stresses. It is also shown that this effect on bending stresses is highly localized and disappears at a distance of about half of the weld thickness away from the weld-toe. To reduce the stress concentrations at the T-joint, plate reinforcements are used in a number of different arrangements and dimensions to increase the load carrying capacity of the connection.

Acknowledgments

I would like to take this opportunity to express my sincere and heartfelt thanks to my supervisor, Professor Reza Fotouhi, for his invaluable guidance and continuous encouragement throughout the years. Without his support and direction through my PhD program, this work would not have been possible.

I would like to express my earnest gratitude and appreciation to Professor Walerian Szyszkowski for the many technical discussions and insightful suggestions which greatly enhanced my knowledge of the subject matter. I would also like to extend my special thanks to the other members of my advisory committee: Professor Ikechukwuka Oguocha and Professor Mohamed Boulfiza for their valuable support and constructive consultations throughout the course of this project.

I also acknowledge Mr. Jim Henry for his valuable help during the course of this project. His assistance was of great importance for the manufacturing of the experimental test beds and specimens in a timely fashion. Mr. Doug Bitner was also of great help for the preparation of the experimental setups used in this study. Financial support of this work provided by Case New Holland (CNH), the University of Saskatchewan Graduate Scholarship, and NSERC CRD grant is gratefully acknowledged.

Dedicated to my mom and dad

Dr. Hadi Moazed and Mrs. Malikeh Jafar Nejadi

Copyright Permission of the Papers

At the time of the publication of this thesis, two of the papers included in the dissertation:

1) "Welded T-joint connections of square thin-walled tubes under a multi-axial state of stress. *IMECE: Journal of Strain Analysis for Engineering Design" (in press)*

2) "The in-plane behaviour and FE modeling of a T-joint connection of thin-walled square tubes. *Journal of Thin-Walled Structures* (2009)" *(published)*

are accepted/published, and permissions to reprint these papers are included in the following.

Permission to include: "The in-plane behaviour and FE modeling of a T-joint connection of thin-walled square tubes. *Journal of Thin-Walled Structures* (2009)". The following statement has been copied from the website of Elsevier Ltd.[1], the official, sole publisher of the Journal of Thin-walled Structures, on April 7, 2010.

As a journal author, you retain rights for large number of author uses, including use by your employing institute or company. These rights are retained and permitted without the need to obtain specific permission from Elsevier. These include:

- the right to make copies (print or electric) of the journal article for their own personal use, including for their own classroom teaching use;
- the right to make copies and distribute copies (including via e-mail) of the journal article to research colleagues, for personal use by such colleagues (but not for Commercial Purposes**, as listed below);
- the right to post a pre-print version of the journal article on Internet web sites including electronic pre-print servers, and to retain indefinitely such version on such servers or sites (see also our information on **electronic preprints** for a more detailed discussion on these points);
- the right to post a revised personal version of the text of the final journal article (to reflect changes made in the peer review process) on the author's personal or institutional web site or server, incorporating the complete citation and with a link to the Digital Object Identifier (DOI) of the article;
- the right to present the journal article at a meeting or conference and to distribute copies of such paper or article to the delegates attending the meeting;
- for the author's employer, if the journal article is a 'work for hire', made within the scope of the author's employment, the right to use all or part of the information in (any version of) the journal article for other intra-company use (e.g. training), including by posting the article on secure, internal corporate intranets;
- patent and trademark rights and rights to any process or procedure described in the journal article;
- **the right to include the journal article, in full or in part, in a thesis or dissertation;**
- the right to use the journal article or any part thereof in a printed compilation of works of the author, such as collected writings or lecture notes (subsequent to publication of the article in the journal); and
- the right to prepare other derivative works, to extend the journal article into book-length form, or to otherwise re-use portions or excerpts in other works, with full acknowledgement of its original publication in the journal.

[1] http://www.elsevier.com/wps/find/authorsview.authors/copyright#whatrights (accessed April 7, 2010)

Permission to include the paper: “Welded T-joint connections of square thin-walled tubes under a multi-axial state of stress. *IMECE: Journal of Strain Analysis for Engineering Design”*

Journal of Strain Analysis for Engineering Design

LICENCE TO PUBLISH FORM

OUR REF NUMBER: JSA609R1
TITLE: Welded T-joint connections of square thin-walled tubes under a multi-axial state of stress
AUTHORS: Reza Moazed, Ph.D. Candidate; Reza Fotouhi, Ph.D.; Walerian Szyszkowski, Ph.D.; Doug Bitner, M.Sc.

In order to publish your article we need your agreement in writing. Please read the terms of this licence, sign the form and return it to us as quickly as possible.

Name of Journal: Journal of Strain Analysis for Engineering Design

Title of Article: Welded T-joint connections of square thin-walled tubes under a multi-axial state of stress

Name(s) of Author(s): Reza Moazed, Ph.D. Candidate; Reza Fotouhi, Ph.D.; Walerian Szyszkowski, Ph.D.; Doug Bitner, M.Sc.

* By signing this form, you (the author(s)) agree to grant to us (Professional Engineering Publishing Ltd) the exclusive right both to reproduce and/or distribute your article ourselves throughout the world in printed, electronic or any other medium, and in turn to authorise others to do the same. You agree that we may publish your article in the journal named above, and that we may sell or distribute it within the journal, on its own, or with other related material.

* You affirm that the article is your original work, has not previously been published, and is not currently under consideration by another journal. If it contains material which is someone else's copyright, you promise that you have obtained the unrestricted permission of the copyright owner (please attach evidence of this) and that the material is clearly identified and acknowledged within the text. You also promise that the article does not, to the best of your knowledge, contain anything which is libellous, illegal, or infringes anyone's copyright or other rights.

* We promise that we will respect your rights as the author(s). That is, we will make sure that your name(s) is/are always clearly associated with the article and, we will not make any substantial change to your article without consulting you. We will have your article fairly reviewed by impartial referees, and will let you know the outcome as quickly as possible. If the article is accepted, we undertake to publish it as soon as we reasonably can. If it is rejected, this agreement is automatically cancelled and all the rights come back to you. On publication, we will send you a free copy. We will take all reasonable steps to maximise the visibility of the journal, and of your article within it.

* Copyright remains yours, and we will acknowledge this in the copyright line which appears on your article. However, you authorise us to act on your behalf to defend your copyright if anyone should infringe it, and to retain half of any damages awarded, after deducting our costs. You also retain the right to use your own article
(provided you give full acknowledgement of the published original) as follows, as long as this does not conflict with our business: for the internal educational or other purposes of your own institution or company; mounted on your personal web page; in whole or in part, as the basis for your own further publications or spoken presentations. In addition, you may post a copy of the final published version of your article to a free public institutional or subject repository, no sooner than 2 months after publication in the journal; such copy must include the following notice:

C [name of author, year]. The definitive, peer reviewed and edited version of this article is published in [name of journal, volume, issue, pages, year, DOI]

Table of Contents

List of Figures

Chapter 1:

Chapter 2:

Chapter 3:

Chapter 4:

Chapter 5:

Appendix A:

Chapter 1. Introduction

The first chapter of this thesis provides a brief background on tubular T-joint connections (in particular square hollow section (SHS)-to-SHS T-joints) and their use in industrial applications and structural components. The chapter also discusses the research objectives and a summary of the papers included in the thesis. The results of this study have been summarized in six research papers and have been submitted/published in technical journals and the proceedings of international conferences [1-6]. Six technical reports were also submitted to the industrial partner, Case New Holland (CNH) [7-12]. However, due to the need for brevity, only four of the research papers have been included in this thesis. These papers are presented in chapters 2-5.

1.1. Background

Hollow tubes have been widely used in the industry for the design of many structural components and load carrying members. The tubes are often connected together through welding, with one tube (i.e., cross-member) positioned perpendicular to the other tube (i.e., longitudinal member), thereby forming a T-joint connection (as shown in Figure 1). The applications of these T-joint connections range from bridge components and agricultural machinery in the construction industry to vehicle frames and pillars in the automotive sector [13,14].

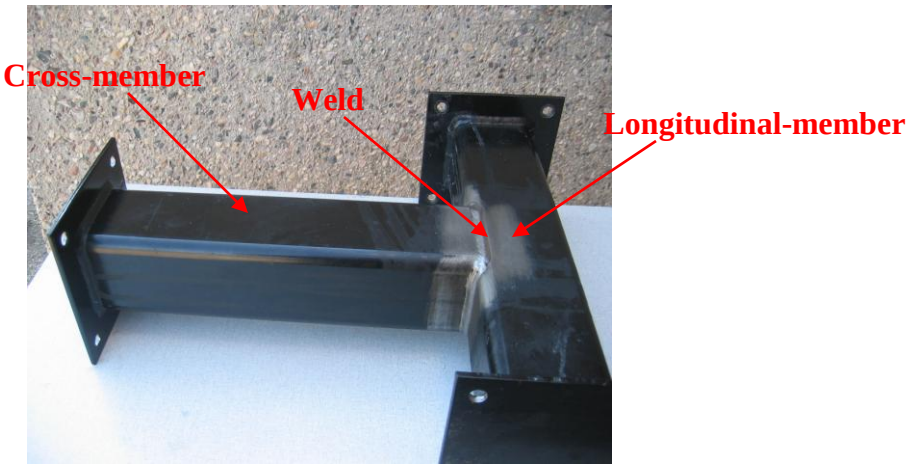

Figure 1: Full-scale T-joint connection used in agricultural machinery

From a manufacturing point of view, modern developments in cutting and welding techniques have provided engineers with a range of alternatives for fabricating structural components such as the aforementioned T-joints [15-18]. Consider a welded T-joint connection such as the one presented in Figure 1. Traditionally, for the construction of the T-joint, the straight edge of one SHS tube is cut by conventional mechanical cutting tools (i.e., torch or flame cutting) and then welded to the body of the other SHS tube to form the connection. In order to fill in all the gaps and to obtain an acceptable level of strength for the welded connection, two or three passes of weld are usually required. Alternatively, the cross member can be cut using a laser beam to fit the profile of body of the longitudinal member before welding (as shown in Figure 2). Then one pass of weld may be enough to obtain the same strength as conventional cut and several pass of welds.

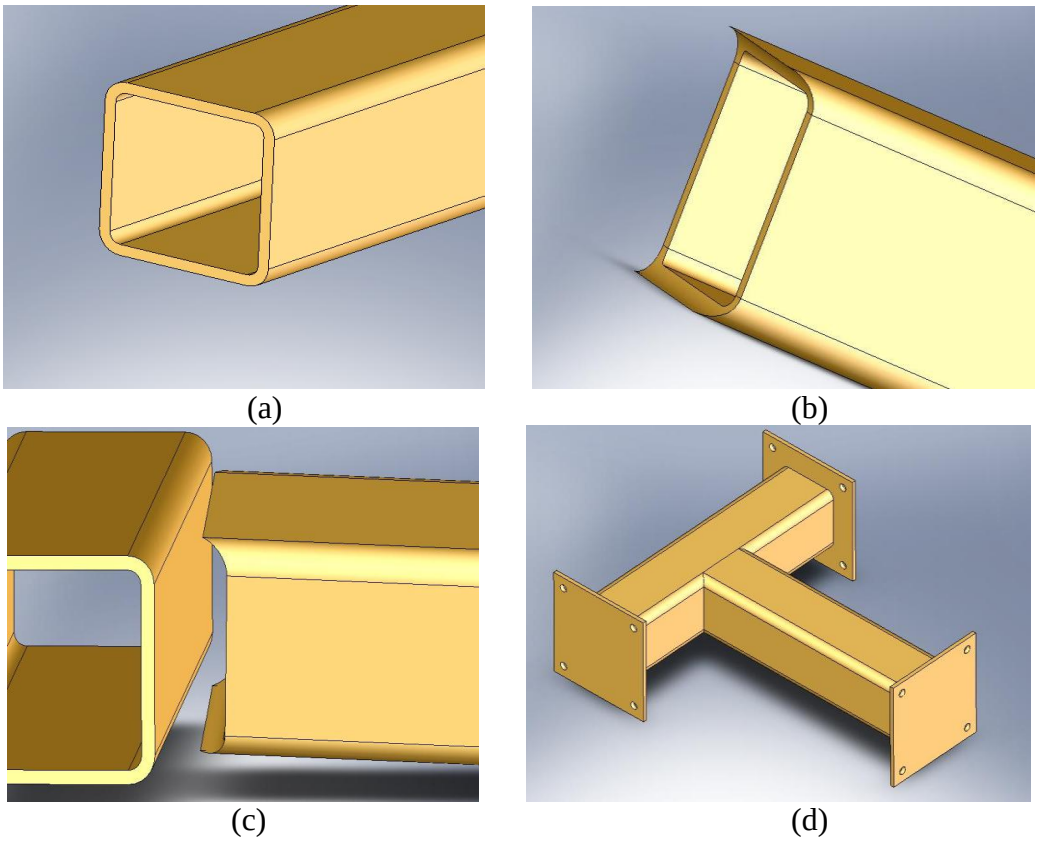

Figure 2: Test specimen: (a) Schematics of traditional mechanical cut edge (b-c) Schematics of laser cut edge and (d) T-joint connection fabricated using laser cutting.

The use of laser beam allows the possibility to cut components with complicated geometries with high precision. Even though laser cutting may increase the cost of manufacturing initially; however, it will reduce the overall cost and time of welding in the long run. Aside from the possibility to cut very complex geometries, cutting with laser has other advantages over conventional mechanical cutting. For instance, the high flexibility in changing from one geometry to another due to numerical control and the absence of mechanical tools. This is beneficial as it translates to shorter production series and quicker prototype developments [19-20].

The cut edges of steel components by laser cutting differ from mechanically cut edges in properties, which influence the fatigue life of components to different degrees. Even though the use of laser beam in the industry is becoming more and more common, only a few researchers have studied the influence of mechanical cutting versus laser cutting. It is well known that the surface finish resulting from different machining operations can significantly affect the fatigue life of structural components [21]. The effect of different cutting techniques on the fatigue properties and hence the fatigue life of sheet steels have also been investigated in previous studies [19, 22-24]. The investigators have concluded that both under constant and variable amplitude cyclic loads, laser cutting produces higher fatigue strengths than its mechanical cut counterpart.

Albeit the above mentioned studies on sheet steels that have suggested the improvement in fatigue properties of the specimens as a result of laser cutting, there are no such studies performed on full-scale and more complicated steel structures such as the aforementioned T-joints. To increase the use of laser cutting for such structures, there is a need for more testing and analysis.

From a structural analysis view point, the design of tubular T-joints constructed from thin-walled members poses a challenge. This is because unlike solid-section members, when thin-walled members are subjected to certain types of loadings, they may experience severe deformations of their cross-sections in the connection's vicinity. Such deformations are local and their effects typically disappear within a short distance from the connection. However, these local deformations distort the stress flow between the cross and the longitudinal members. Under general loadings, some portions of the connection become "un-loaded" or carry very little load, causing the remaining portions to carry additional stresses. This results in an uneven stress distribution at the connection with high stress/strain concentrations occurring at some points. In addition to the distortion of the cross-sections in the vicinity of the connection, stress concentrations can also occur due to the requirement to match the deformation patterns along the walls at the connection of the longitudinal and cross members.

The stresses which occur locally at the connection, can be many times larger than the nominal stresses in the connecting members. The ratios of the local stresses at the connection to the nominal stresses occurring away from the joint on the connecting members are referred to as the stress concentration factors (SCFs) [25,26]. The hotspot stresses are those which are obtained by the extrapolation of the local stresses to the perceived failure-critical points (such as weld toes) [27]. The significant stress/strain concentrations that occur in the vicinity of the connection of the tubular T-joints, substantially reduce the load carrying capacity of the structure as a whole. Therefore, the T-joint connections must be designed and reinforced in such a way to allow for the

smooth transfer of the forces and bending moments from one member to another; minimizing the stress/strain concentrations at the connection [28-29].

Currently, despite the wide use of hollow section T-joints as efficient load-carrying members, a practical but yet simple and accurate approach for their analysis and design is not available. As a result, for the accurate design of a T-joint structure made up of hollow tubes, engineers must perform a detailed and relatively complex finite element (FE) analysis. Even though a detailed FE model constructed from solid or plate/shell elements with an accurate meshing can satisfactorily provide the stress distribution and the stiffness of the connection, it is computationally expensive [30-32]. The preparation of such models and their meshing can also be time consuming. However, without such models, the exact nature of the stress flow from one member to the other is not easy to predict and consequently the values of maximum stress and the connection's stiffness are difficult to estimate from standard engineering calculations. This has some practical implications on the design process. Such uncertainty of the joint behaviour is often the main cause of typical but unnecessary over-design of the members connected. Therefore, the development of a practical but yet simple and accurate approach for the prediction of the stresses and the stiffness of the connection of such T-joints is desirable to engineers. Also, for the development of such an approach, a better understanding of the underlying mechanics for the transfer of the loads (i.e., forces and moments) from one member of the T-joint to the other is required.

1.2. Research Objectives

The research work that is presented in the following chapters of this thesis was undertaken to further understand the behaviour of SHS-to-SHS T-joint connections

subjected to static and cyclic loads. This will pave the ground for their increased and more reliable industrial implementation. Due to the wide use of SHS-to-SHS T-joints in many industrial applications, as explained in section 1.1, the development of a practical and accurate approach for their design and analysis is essential. For this purpose, the thorough understanding of the deformation patterns and the mechanism for the transfer of the loads (i.e., forces and moments) from one tube to the other is of significant importance. In addition, the behaviour of the T-joint connections under cyclic loads can significantly be affected by the techniques used for their fabrication. As stated in section 1.1, with modern advances in the field of manufacturing, there are many alternatives for the cutting and welding of the T-joints. The use of laser technology has become increasingly common in the industry due to its potential of offering both technical and economical advantages. With this in mind, this research work also focuses on the practicability of using laser cutting technology to produce welded connections of higher strength than the "conventional" (i.e., fabricated using mechanical cutting tools) T-joints. Therefore, the objectives of this research can be summarized as follows:

1- The use of laser cutting technology to produce SHS-to-SHS T-joint connections of higher fatigue strength in comparison with those produced using traditional mechanical cutting tools (chapter 5).

2- Accurate FE modelling of the welded SHS-to-SHS T-joint, and the effect of the weld geometry on the stresses at the connection (chapter 4).

3- The thorough understanding of the behaviour of SHS-to-SHS T-joint connections subjected to in-plane and out-of-plane bending loads (chapters 2 and 3).

4- The development of a simplified and accurate approach (based on objective 1) for the prediction of the maximum stresses and stiffness of the connection of SHS-to-SHS T-joints (chapters 2 and 3).

5- The proper reinforcement of the T-joint connection in order to improved its load carrying capacity (chapter 4).

In order to achieve the objectives listed above, both a numerical (using finite elements) and an experimental study were carried out. For the verification of the developed FE models, two experimental test fixtures were designed and constructed. A summary of the methodologies used to accomplish these objectives is explained in section 1.3. The details of these approaches can be found in chapters 2-5.

Remark: Because of the manuscript style of this thesis, equations, figures and references may be repeated in the thesis.

1.3. Summary of manuscripts

Chapters 2 through 5 of this thesis have been included to cover the objectives explained in section 1.2. That is, a thorough understanding of the behaviour of the T-joint connection subjected to IPB and OPB loads is first developed. For this purpose, FE models using shell and solid elements of relatively high density are employed. In chapters 2 and 3, the FE models constructed for this purpose are presented. With the help of these models, the local stresses and the stress concentrations at the connection, as well as the joint's stiffness are determined. Based on this knowledge, a simplified approach using beam elements (with certain properties modified) is proposed for the analysis of SHS-to-

SHS T-joint connections. The effectiveness of the approach is then presented through numerical examples and the consideration of a T-joint connection typical to that found in the agricultural industry. It is shown that the developed FE models constructed from the modified beam elements can accurately and efficiently predict the maximum stresses, reaction forces, deflections and the natural frequencies of the T-joint connection at considerably reduced computational effort.

The experimental test fixtures developed for the verification of the finite element analysis (FEA) results are presented in chapters 4 and 5. In chapter 4, the detailed FE modelling of the weld at the connection of the tubular members is first discussed. Once an accurate model of the weld and the tubular members is developed, the results of the FEA are verified experimentally. Upon the verification of the constructed FE models, the effects of the weld geometry on the stresses at the connection are considered. Also, in order to improve the load carrying capacity of the T-joint with respect to plastic deformations and fatigue cracking, the reinforcement of the connection is considered. In chapter 5, the second experimental test fixture which has been designed for the study of the T-joint connections is presented. The focus of this chapter is on investigating the practicability of using laser technology to produce welded SHS-to-SHS T-joint connections with higher fatigue strengths than traditional mechanical cut T-joints. FE models of the two types of T-joints fabricated with the different cutting techniques are developed and the results of the FEA are further validated through their comparison with experimental results. The following sections provide a summary of each chapter.

1.3.1. Chapter 2: The In-plane Behaviour and FE modelling of a T-joint Connection of Thin-walled Square tubes (objectives 3 and 4)

The contents of chapter 2 have been published in the Journal of *Thin-Walled structures* under the title of "The in-plane behaviour and FE modeling of a T-joint connection of thin-walled square tubes" [6]. In this chapter, detailed FE models of the SHS-to-SHS T-joint connection using shell and solid elements are constructed. The T-joint's meshing patterns for the shell and solid elements are shown in Figure 3.

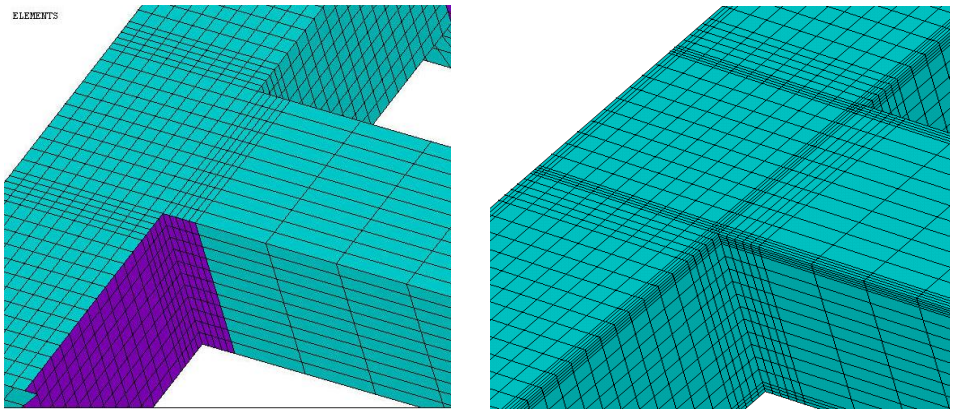

(a) (b)

Figure 3: The T-joint's meshing patterns for the a) shell and b) solid elements

From the FEA results obtained using these models, the stresses and the stiffness of the connection are determined when the T-joint is subjected to IPB loading conditions (as shown in Figures 4a and b). It is observed that for such loading conditions, the stresses and the stiffness of the connection are only a function of the 'thin-wallness' ratio, *a/t*, of the tubes. This thin-wallness ratio is defined as the ratio of the side length, *a*, of the tubes' square cross-section to its thickness, *t*. Therefore, the parameters identifying the joint's stress concentrations (ξ_m, ξ_b), and the bending stiffness reduction (α_K) are defined in

terms of the *a/t* ratio. The parameters ξ_m and ξ_b correspond to the values of the membrane stress and the bending stress amplifications, respectively. Also in this chapter, the reason for the stress concentrations at the connection of the thin-walled T-joint subjected to IPB loads is discussed in detail. It is shown that under IPB loading conditions, some portions of the connection carry very little or no load at all, consequently causing the remaining portions to carry additional stresses. This results in large stress concentrations in the vicinity of the connection (as shown in Figure 4c). In this figure, σ_{nom} refers to the nominal beam bending stresses and σ_{max} refers to the maximum local stresses that occur at the connection of the thin-walled tubes.

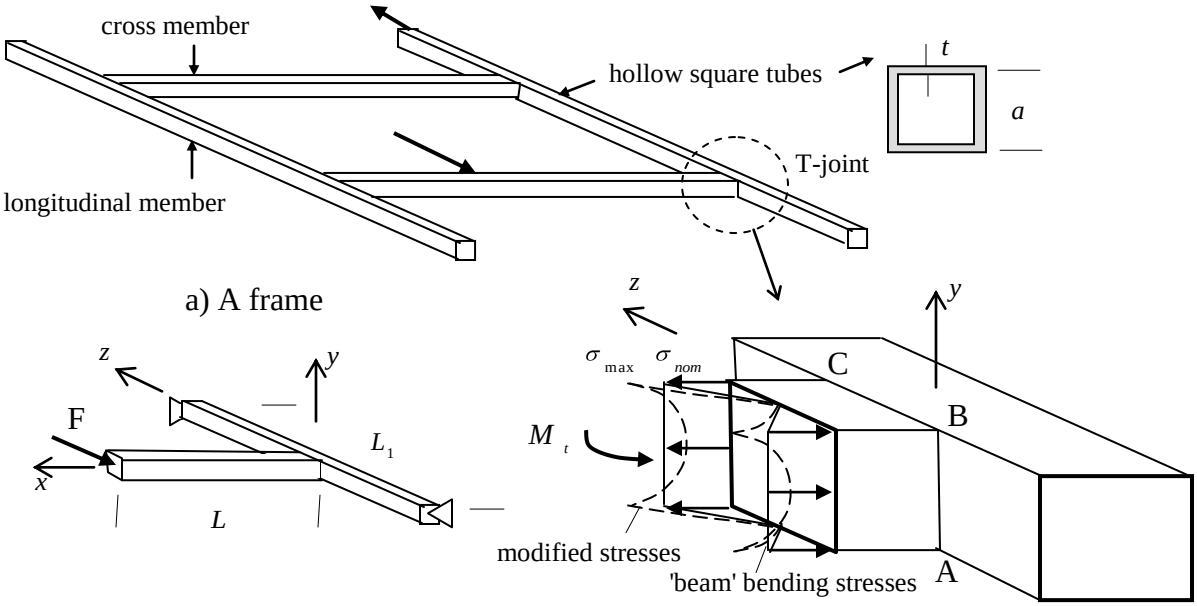

Figure 4: A thin-walled frame with T-joints

It should be noted that if the stress distribution through the thickness of the tubes is non-linear, solid elements should be employed for the FE modeling. This is because in the models constructed from solid elements, the displacement and stresses are calculated at every node and therefore the stress distribution across the tubes' thickness can be

determined. On the other hand, for the model constructed from shell elements, only the mid-surface of the structure is represented and a linear distribution of the through the thickness stresses is assumed. From the FEA results of the solid element model, a generally linear stress distribution across the thickness of the tubes is observed. Therefore, the use of shell elements for the analysis of the T-joint connection is appropriate.

As mentioned in section 1.1, at a relatively short distance from the connection, the effects of the local stresses and deformations disappear. In chapter 2, it is shown that this distance is approximately equal to one side length of the tube's cross-section. It is observed that at this distance from the connection, the thin-walled T-joint behaves like a beam. This is used to identify the joint's rotational (bending) stiffness. For this purpose, the displacements of the tubular T-joint connection are divided into two components; the portion due to bending the tubes as beams, and the portion due to local deformations as a result of the thin-wallness. It is shown that the stiffness of the connection, K_T, and the stiffness reduction parameter, α_κ , are only dependent on the thin-wallness ratio, *a/t*.

Based on the stress amplification and the stiffness reduction parameters presented in chapter 2, the T-joint connection can be modelled by simple beam elements when subjected to IPB conditions. The FE models constructed from beam elements are substantially easier to prepare and analyze. The effectiveness of the parameters and the proposed approach is demonstrated by applying it to a structure with a T-connection and dimensions typical for the agricultural industry. The stresses, displacements, reaction forces and also natural frequencies are first obtained from a model constructed from shell elements with over 36,000 degrees of freedom (DOF). Then the T-joint connection is

modelled by the modified beam elements with 90 (DOF). It is shown that the modified beam model provides accurately all the important aforementioned information of the structural analysis. This is done at a substantially reduced computational effort in comparison with the complicated FE models built of shell or solid elements.

1.3.2. Chapter 3: Out-of-plane behaviour and FE modelling of a T-joint connection of thin-walled square tubes (objectives 3 and 4)

The contents of this chapter have been submitted for publication in the Journal of *Thin-Walled structures* under the title of "Out-of-plane behaviour and FE modelling of a T-joint connection of thin-walled square tubes" [5]. One of the objectives of this chapter is the better understanding of the behaviour of SHS-to-SHS T-joint connections when subjected to OPB loading conditions (as shown in Figure 5). This chapter is an extension of chapter 2, in which the behaviour of T-joint connections under IPB loading conditions is examined. Similar to chapter 2, the FE models constructed from shell and solid elements are employed for this purpose. In this chapter, the transfer of the out-of-plane bending moment, M_t , through the connection of the T-joint is examined numerically.

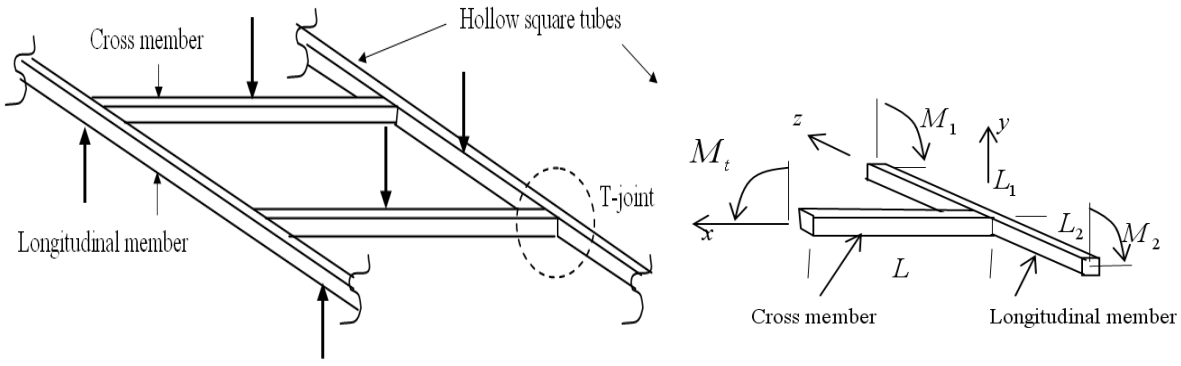

Figure 5: A thin-walled frame with T-joints subjected to OPB loads

Just as in the case of the T-joint connections subjected to IPB loading conditions, it is observed that for OPB loads, the T-joint connections behave as beams at a short distance from the connection. It is shown that this distance is equal to approximately *a/2* as opposed to *a* for the case of IPB loads (as shown in Figure 6). In figure 6, σ_m^x depicts the membrane stresses (i.e., those stresses which occur at the mid-thickness of the tubes) in the x-direction. It is observed that only in the very vicinity of the connection the beam-like stresses cease to be valid. This is because the transfer of the bending moment through the connection of the T-joint is accompanied by severe local deformations and stress concentrations.

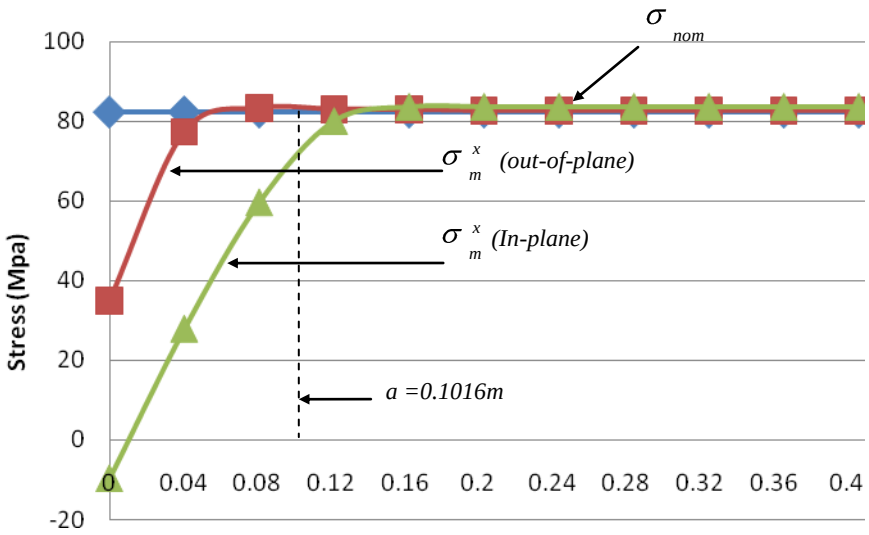

(c)

Figure 6: Nominal beam stresses and membrane stresses obtained from FE models constructed from shell elements.

For T-joint connections subjected to OPB loads, the reason for the stress concentrations at the connection appears to be mainly due to the requirement to match the deformation patterns between the longitudinal and the cross members. In such loading conditions, the parameters describing the joint's stress concentrations and the bending stiffness are not

only a function of the 'thin-wallness' ratio, but also depend on the length of the longitudinal member. Such a phenomenon will be examined and explained in detail by the FE analysis presented in chapter 3. Based on the analysis, several parameters will be identified to relate the increases of the stress and compliance in the connection in terms of the member's a/t ratio (thin-wallness) and the length of the longitudinal member. For the calculation of the connection's stiffness and the corresponding bending stiffness reduction parameter, an approach similar to that discussed in section 1.3.1 is employed. That is, the displacements of the tubular T-joint connection are divided into two portions; one portion is due to the bending of the tubes as beams and another due to the local deformations at the joint.

In order to demonstrate the effectiveness of the stress amplification and stiffness reduction parameters for OPB loading conditions, two numerical examples are considered. The first example demonstrates the effectiveness of the parameters for a static stress analysis, and the second for dynamics where the out-of-plane free vibrations of the frame are considered. A thin-walled frame with one T-joint is considered for both cases. The T-joint connection is modelled by both shell elements and the modified beam elements. Similar to the IPB loading conditions, it is observed that the reaction forces/moments, deflections, and the natural frequencies of vibrations can be calculated accurately with the use of the proposed parameters. As demonstrated, such an approach is capable of rendering the results that are similar to the results of the FE models consisting of much more complicated shell or solid elements. These models however, include several thousands more degrees of freedom and are much more difficult to construct and operate.

1.3.3. Chapter 4: Welded T-joint connections of square thin-walled tubes under a multi-axial state of stress (objectives 2 and 5)

The contents of chapter 4 have been accepted (in press) for publication in the IMECE Journal of *Strain Analysis for Engineering Design* under the title: "Welded T-joint connections of square thin-walled tubes under a multi-axial state of stress" [3]. As mentioned in section 1.1., T-joint connections are often fabricated through the welding of their tubular members. When the T-joint is subjected to loadings, there exists significant stress and strain concentrations at the toe of the weld. As a result of these local notch stress concentrations, the weld toe is predominantly the location where fatigue cracks and plastic deformations first occur. In this chapter, a welded SHS-to-SHS T-joint connection is examined both experimentally and numerically under a multi-axial state of stress. The experimental test fixture and the FE model developed for this study are shown in Figure 7 on the following page.

In the experimental study, a test fixture with a hydraulic actuator capable of applying both static and cyclic loads is designed and used (shown in Figure 7a). In order to verify the FEA results of the numerical study, strain gauges are installed at several locations around the connection of two full-scale T-joints as shown in Figures 7c and 7d. The T-joint specimens are identical to those found in many agricultural machinery. On these specimens, the strain gauges installed at each location are a two-channel 90º tee rosette strain gauge. These strain gauges can measure the strains perpendicular and parallel to the weld toe.

The FE modelling of the welded T-joint connection is a challenging and delicate task due to the 3D profile of the weld. In chapter 4, the weld geometry is modelled using FE. For

this purpose, several full-scale T-joints are cut at different locations around the welded connection in order to obtain the size and depth of penetration of the weld. For the FE modelling of both the weld and the tubes, solid elements are employed. The reason for choosing solid elements is due to the inability of shell elements to accurately model the interaction between the weld and the tubular members. To assess the effectiveness and accuracy of the modelling, the numerical and experimental results are compared at several locations and different load levels to verify the reliability of the FE model. The results of this comparison are discussed in chapter 4, where it is shown that the developed model is reliable for the accurate prediction of the hotspot stresses of the T-joint.

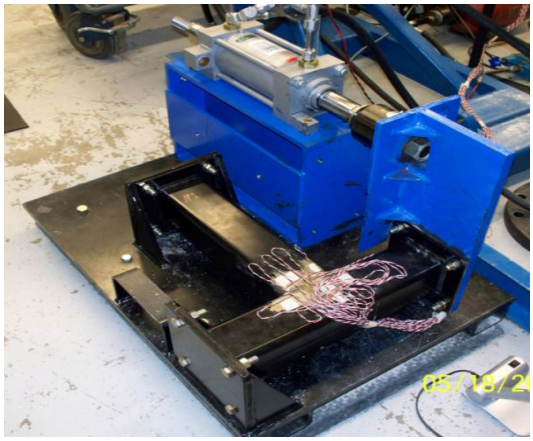

(a)

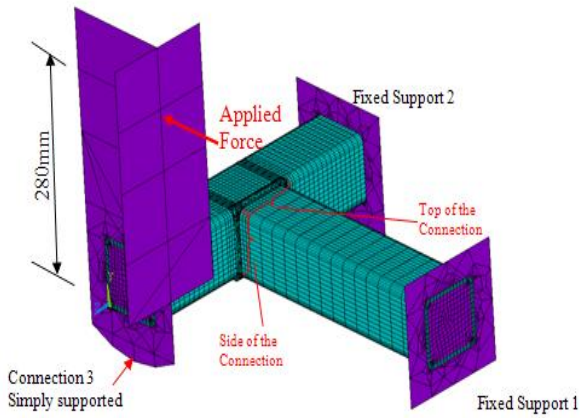

(b)

(c)

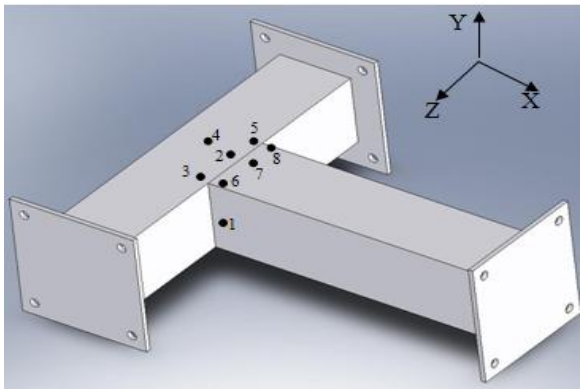

(d)

Figure 7: a) Overall view of the test fixture, b) Corresponding FE model with loading mechanism and applied boundary conditions, c) Close up view of the strain gauges installed, and d) locations of the strain gauges

The verified FE model is then used to study the through-the-thickness stress distributions of the tubes. In structural analysis, the stress distribution over the tubes' thickness can be divided into 3 components: 1) the membrane stresses (σ_m) , 2) the bending stresses (σ_b), and 3) the stresses from the local notch effect which in this thesis are referred to as $\sigma_{nonlinear}$. This decomposition of the local stresses in the vicinity of the notch is given as follow:

$$\sigma_{Notch} = \sigma_m + \sigma_b + \sigma_{nonlinear} \quad (1)$$

The membrane stresses are constant through the thickness of the tubes, while the bending stresses assume a linear distribution through the thickness, with the mid-thickness of the tubes serving as the neutral point. The remaining stresses, $\sigma_{nonlinear}$, are from the local notch effect and are nonlinear. It is shown that the membrane stresses remain similar regardless of the weld geometry. The weld geometry only affects the bending stresses. It is also shown that this effect on the bending stresses is highly localized at the vicinity of the weld toe. At a distance of about ½ of the weld thickness from the weld-toe, the effects of the weld geometry on the bending stresses becomes insignificant as well.

As mentioned in section 1.1, the T-joint connection must be designed and reinforced in such a way that the hotspot stresses and strains at the connection are minimized. However, the reinforcement of tubular joints poses a challenge in engineering applications. The ideal reinforcement should not only reduce the maximum stresses at the connection, but also must be practical for employment in new and existing structures. In chapter 4, to reduce the stress concentrations at the T-joint, plate reinforcements are used in a number of different arrangements and dimensions. The effects of internal and external reinforcements for the T-joint are considered. The purpose of such reinforcement

plates is to limit the local deformations that occur in the vicinity of the connection of the tubular T-joints. It is shown that the external reinforcement plates can significantly increase the load carrying capacity of the connection.

1.3.4. Chapter 5: The influence of mechanical and laser cutting on the fatigue strengths of square hollow-section welded T-joints (objective 1)

The contents of chapter 5 have been submitted for publication in the *ASME: Journal of Offshore Mechanics and Arctic Engineering*, under the title: "The influence of mechanical and laser cutting on the fatigue strengths of square hollow-section welded T-joints" [4]. A brief version of this paper will also appear in the CSME Forum 2010 [2]. As mentioned in section 1.1., modern developments in manufacturing (i.e., cutting and welding techniques) have provided engineers and designers with a wide range of alternatives for fabricating the tubular T-joint connections. With the use of laser technology becoming more common in the industry, it is important to investigate the possibility of using this technology as part of the fabrication process for the T-joint connections. Albeit previous investigations on sheet steels that have suggested superior fatigue properties as a result of laser cutting, there are no such studies in the literature on more complicated steel structures such as the T-joints considered in this study. To increase the use of laser cutting for such structures, there is a need for more testing and analysis. In chapter 5, the feasibility of using laser technology to produce SHS-to-SHS T-joint connections of higher fatigue strengths than their traditional mechanical cut counterparts is investigated. For this purpose, both an experimental and a numerical study are carried out.

For the experimental study, the fatigue properties of the weld (i.e., electrode) and the parent material (i.e., steel used for the manufacturing of the tubes) were determined using laboratory krouse samples. The krouse samples were subjected to rotating bending fatigue tests and the S-N curves for both materials were obtained. It is observed that the fatigue strength of the weld material is higher than that of the parent material. For the fatigue tests of the full-scale T-joint samples, a total of 21 specimens typical of those found in the agricultural industry, were included. The samples that were fabricated using mechanical cutting (i.e., torch) are referred to as "conventional" samples, while those constructed using laser cutting technology are referred to as "couped". The T-joint samples were examined with the intention to form a fatigue crack of approximately 3.8 cm (1.5 inches) in length. A typical failed T-joint sample is shown in Figure 8.

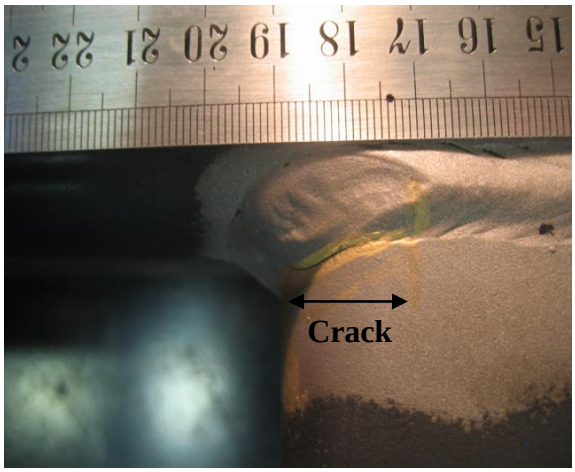

Figure 8: T-joint sample with fatigue crack initiated at the weld toe

On two T-joints (one couped and one regular), several strain gauges were attached around the connection of each joint. The measured strains served for two purposes: 1) comparison of the strains that occur in the vicinity of the connection of the T-joints fabricated with the different cutting techniques, and 2) verification of the FEA results. The strain measurements from the couped and conventional T-joints show that the strains

in the connection's vicinity for both samples are very similar. The details of the results are included in chapter 5.

Finite Element models of the conventional and couped samples are also developed in chapter 5. To examine the welding, and to accurately model the welds for the FE study, several couped and conventional samples were cut at different locations of the connection. The FEA results of the numerical study were verified with the strain readings from the strain gauges for both types of T-joints. Similar to the experimental results, the FEA results also show that the stresses and the strains at the connection of the couped and regular samples are very similar to one another. The details of the FE modelling and FEA results are provided in chapter 5.

The experimental results of the full-scale T-joints subjected to cyclic loads show that the couped samples have higher fatigue strengths than the conventional samples. This can be observed in Figure 9 which presents the load-life diagram of the couped and conventional samples.

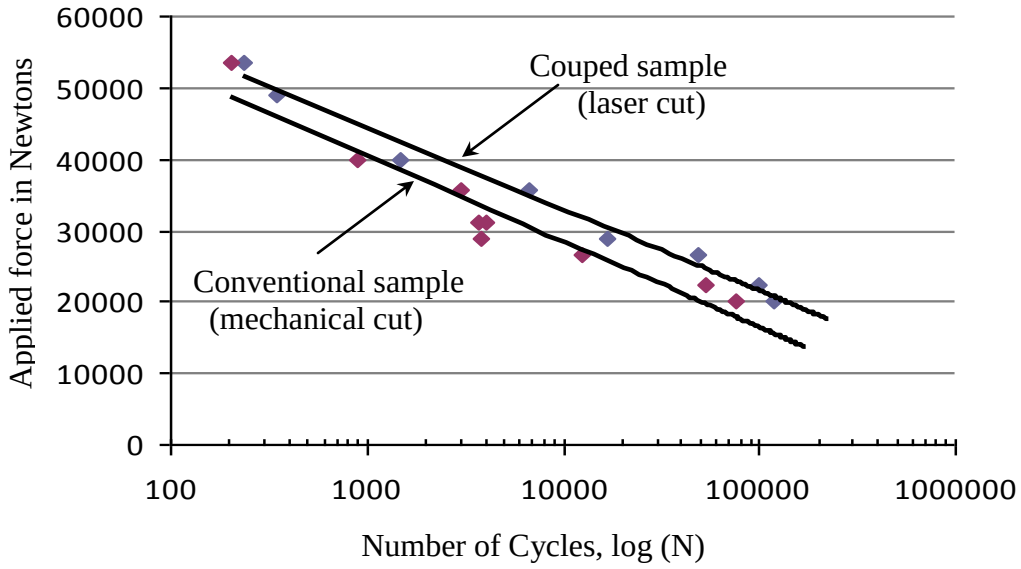

Figure 9: Load-life diagram to failure for 3.8 cm (1.5 inch) fatigue crack for loads ranging from 4,500-12,000 lbs (20,017 to 53,379 N).

It should be noted that the crack length of 1.5 inches was chosen to ensure that the fatigue crack on all of the T-joint samples has reached a size which is visible without difficulty by the naked eye. The results of the experimental investigations presented in chapter 5 suggest that the tubes can be effectively cut using a laser beam to fit the profile of body of the other tube before welding. Then the connection of the tubes only requires one pass of weld to obtain a higher fatigue strength than conventional cut and several pass of welds. This will be more economical and result in shorter production series and quicker prototype developments. The results of this research work can be used as a tool for engineers and researchers working in the manufacturing and construction industries.

1.3.5. Chapter 6: Conclusions, Contributions and Future works

The summary and conclusions of this research work are presented in this chapter. The contributions of the research are discussed. The directions for the future work on this research topic are also included in this chapter.

1.4. References

Candidate's papers and technical reports

[1] Moazed R, Fotouhi R, Henry J. Behaviour of a T-Joint Connection of Thin-Walled Tubes under a Multi-Axial State of Stress, 12th International Conference on Fracture (ICF12). July 12-17, 2009, Ottawa, Ontario, Canada.

[2] Moazed R, Fotouhi R, Henry J. Fatigue strengths of square hollow-section welded T-joints: mechanical vs. laser cutting. Proceedings of The Canadian Society for Mechanical Engineering Forum 2010. June 7-9, 2010, Victoria, British Columbia, Canada.

[3] Moazed R, Fotouhi R, Szyszkowski W, and Bitner D. Welded T-joint connections of square thin-walled tubes under a multi-axial state of stress. *IMECE: Journal of Strain Analysis for Engineering Design* (In Press).

[4] Moazed R, Fotouhi R. The influence of mechanical and laser cutting on the fatigue strengths of square hollow-section welded T-joints. Submitted to the *transactions of the ASME: Journal of Offshore Mechanics and Arctic Engineering* (2010).

[5] Moazed R, Fotouhi R, Szyszkowski W. Out-of-plane behaviour and FE modeling of a T-joint connection of thin-walled square tubes. *Submitted to the Journal of Thin-Walled Structures* (2010).

[6] Moazed R, Szyszkowski W, Fotouhi R. The in-plane behaviour and FE modeling of a T-joint connection of thin-walled square tubes. *Journal of Thin-Walled Structures* (2009); 47(7): 816-825.

[7] Fotouhi R, Moazed R. Fatigue Strength in laser cut welding, progress report 4, a CRD-NSERC-CNH Project. Technical report to CNH (January 2009); 117 pages.

[8] Fotouhi R, Moazed R. Fatigue Strength in laser cut welding, Report update 3, a CRD-NSERC-CNH Project. Technical report to CNH (March 2008); 10 pages.

[9] Fotouhi R, and Moazed R. Fatigue Strength in laser cut welding Report 3, a CRD-NSERC-CNH Project. Technical report to CNH (August 2007); 35 pages.

[10]Fotouhi R, and Moazed R. Fatigue Strength in laser cut welding Report 2, a CRD-NSERC-CNH Project. Technical report to CNH (July 2007); 32 pages.

[11]Fotouhi R, Moazed R. Fatigue Strength in laser cut welding update 1, a CRD-NSERC-CNH Project. Technical report to CNH (January 2007); 7 pages.

[12]Fotouhi R, and Moazed R. Fatigue Strength in laser cut welding Report 1, a CRD-NSERC-CNH Project. Technical report to CNH (November 2006); 24 pages.

Other References

[13] Lee M-M-K, Pine T, Jones T-B. An Experimental and Finite Element Study of the Torsional Behaviour of T-joints in Automotive Structures. Proceedings of the Institution of Mechanical Engineers, Part D: *Journal of Automobile Engineering* (2001); 215(2): 231-240.

[14] Lee M-M-K. Strength, Stress and Fracture Analyses of offshore tubular joints using finite elements. *Journal of Constructional Steel Research* (1999); 51(3): 265-286.

[15] Stournara A, Stavropoulos P, Salonitis K, Chryssolouris G. An investigation of quality in CO2 laser cutting of aluminum. *Journal of Manufacturing Science and Technology* (2009); 2(1): 61-69.

[16] Nichici A, Cicala E.F. A new approach in the gas jet assisted CO2 laser cutting off line optimization. *Proceedings of the international conference on lasers* (1997); 446-453.

[17] Chen J, Zuo T. Effect of laser beam incident angle on laser cutting quality. *Chinese Journal of lasers* (2001); 28(11): 1037-1040.

[18] Miyamoto I, Maruo H. Mechanism of laser cutting. *Journal of Welding in the world* (1991); 29(10): 283-294.

[19] Meurling F, Melander A, Linder J, Larsson M, Trogen H. The influence of laser cutting on the fatigue properties of thin sheet steels. *Swedish Institute for Metals Research Report* (1998); IM-3691.

[20] Meurling F, Melander A, Linder J, Larsson M. The influence of mechanical and laser cutting on the fatigue strengths of carbon and stainless sheet steels. *Scandinavian Journal of Metallurgy* (2001); 30(5): 309-319.

[21] Sperle J.O. Influence of parent metal strength on the fatigue strength of parent material with machines and thermally cut edges. *Welding in the World Journal* (2008); 52(7-8): 79-92.

[22] Maronne E, Galtier A, Robert J.L, Ishikawa T. Cutting process influence on fatigue properties of steel sheets. *Advances in Damage Mechanics* (2003); 13-22.

[23] Rashed F, and Nassef A. Effect of low cycle fatigue on surface finish. *American Society of Mechanical Engineers (ASME)*: Contact Problems and Surface Interactions in Manufacturing and Tribological Systems (1993); v(67): 327-332.

[24] Meurling F, Melander A, and Linder J. Comparison of the fatigue characteristics of punched and laser cut stainless steel sheets. *Scandinavian Journal of Metallurgy* (1998); v(30): 351-372.

[25] Mashiri F-R, Zhao X-L. Stress concentration factors and fatigue failure under in-plane bending. *Journal of Thin-Walled Structures* (2006); 44(2): 159-69.

[26] Fung T-C, Soh C-K, Chan T-K. Stress concentration factors of doubler reinforced tubular T joints. *Journal of Structural Engineering* (2002); 128(11): 1399-1412.

[27] Lotsberg I, Sigurdsson G. Hot spot stress S-N curve for fatigue analysis of plated structures. *Transactions of the ASME. Journal of Offshore Mechanics and Arctic Engineering* (2006); 128(4): 330-336.

[28] Fung T-C, Soh C-K, Chan T-K. Stress concentration factors of doubler reinforced tubular T joints. *Journal of Structural Engineering* (2002); 128(11): 1399-1412.

[29] Lee M-K, Llewelyn-Parry A. Offshore tubular T-joints reinforced with internal plain annular ring stiffeners. *Journal of Structural Engineering* (2004); 130(6): 942-951.

[30] Pang H-J, Lee C-W. Three-dimensional finite element analysis of a tubular T-joint under combined loading. *International Journal of Fatigue* (1995); 17(5): 313-320.

[31] Shao Y-B, Lie S-T, Chiew S-P, Huang Z-W. Evaluation of geometrical effect on stress distribution for tubular T-joints under axial load. *International Journal of Space Structures* (2006); 21(2): 77-91.

[32] Shao Y-B. Geometrical effect on the stress distribution along weld toe for tubular T- and K-joints under axial loading. *Journal of Constructional Steel Research* (2007); 63(10): 1351-60.

Chapter 2. The In-plane Behaviour and FE modelling of a T-joint Connection of Thin-walled Square Tubes

ABSTRACT

The behaviour of square hollow tubes with T-joints subjected to in-plane loading conditions is examined numerically. The stresses in the joint and its stiffness are determined from the finite element (FE) models using 2-D shell and 3-D solid elements. The parameters identifying the joint's stress concentration (ξ_m, ξ_b), and the bending stiffness reduction (α_K) are defined in terms of the 'thin-wallness' ratio (the side length to thickness) of the tube. These parameters permit modelling accurately the tubes and the T-connection by simple 1-D beam elements with certain properties modified. The FE models consisting of beam elements are significantly easier to prepare and analyze. The effectiveness of the approach is demonstrated by applying it to a structure with a T-connection and dimensions typical for the agricultural industry. It is shown that such beam models provide accurately all important information of the structural analysis (i.e. the stresses, displacements, reactions forces, and also the natural frequencies) at substantially reduced computational effort in comparison with the complicated FE models built of shell or solid elements.

Keywords: hollow tubes, T-joint, finite elements, stress concentration, stiffness reduction.

1.0 Introduction

Hollow tubes are used extensively in the industry as load carrying members for many automotive parts, agricultural equipment and machinery. Such members are often welded together to form T-joints. Typically, a T-joint connection is formed by cutting the straight edge of one tube and welding it to the body of the other tube.

The design and analysis of the T-joints of thin-walled members pose a challenge because, unlike solid-section members, thin-walled members may experience severe local

deformation of their cross-sections in the connection's vicinity when subjected to certain types of loadings. Such deformation distorts the stress flow between the members and may reduce substantially the load-carrying capacity of the connection. Some portion of the section becomes unloaded and carry very little or no load at all causing the remaining portion (usually closer to the corners of the connections) to carry a greater share of the load. This results in stress concentrations and may lead to the joint's premature failure. Unless a relatively complex and time consuming finite element (FE) analysis using either 3-D solid or 2-D shell elements is performed, the exact nature of the stress flow is not easy to predict and consequently the value of maximum stress and the connection's stiffness are difficult to estimate from standard engineering calculations. Also, such uncertainty of the joint behaviour is often the main cause of typical but unnecessary over-design of the members connected.

There are several numerical and experimental studies on the behaviour of T-joints under different types of loading. Lee et al. [1-2] examined the torsional behaviour of T-joints used in the automotive industry by using finite elements and comparing the results with experiments.

The stresses in the connection of a double fillet-welded T-joint were investigated numerically in [3] under the plane-stress loading conditions, the accuracy was then verified by a photo-elastic stress analysis. The geometrical effect on the stress distribution at the weld toe for tubular T- and K-joints under axial loading was considered in [4-6]. The behaviour of reinforced T-joints with a doubler plate using the finite element method subjected to four basic loading conditions was considered in [7]. A

numerical/experimental study of composite T-joints was performed in [8]. The study investigated the T-joints behaviour subjected to tension force up to the ultimate failure. Simplified load-moment interaction curves for square steel tubes filled with high-strength concrete were proposed in [9-10]. Parametric equations relating the stress concentration factors to basic geometrical parameters of reinforced T-joints of circular tubes were presented in [11-12].

This paper focuses on understanding the in-plane behaviour of the T-joint connection of two hollow tubes of square cross-sections. Relatively high density shell/solid models are used to analyze the transfer of bending moment through such a connection. The membrane and bending effects in the walls of the connecting tubes and their effects on the joint's strength are examined in detail. Several parameters characterizing the connection's stiffness and the stress concentrations are introduced and defined in terms of the tube's width-to-thickness ratio. These parameters permit modelling the connection accurately by beam elements. This renders a drastic reduction of the computational effort in comparison to the shell/solid elements models. The approach is illustrated by the example of a general thin-walled frame with the T-joint loaded in-plane which is first solved by a shell model and then by a beam elements model. The stresses, deflections, reaction forces, and frequency spectra obtained for both models are compared to verify the approach's correctness.

2.0 Thin-walled frames with T-joint connections.

The problem of efficient modelling of thin-walled frames with T-joints loaded in -plane is considered (see Figure 1a). In engineering practice the T-joints are weak points of such

frames, with the first signs of fatigue cracking or plastic deformations typically appearing there. On the other hand, at some distance from the joints, the hollow tubes behave similarly to beams in bending. From the viewpoint of stress/deformation analysis, the joint requires a complex 3-D stress analysis with a large number of elements to achieve sufficient accuracy, while the beams can be handled by either simple beam elements or even by hand calculations.

The main reason for the difficulties with the joint's analysis may be attributed to the fact that for thin-walled tubes the stress flow due to the total (resultant) bending moment M_t in the cross member cannot be transferred smoothly to the longitudinal member because of the lack of sufficient support along side AB of the connection. As a result the constant 'beam' type stresses at the central portion of this side are reduced as sketched in Figure 1c. Therefore, the part of stress flow from side AB must be redirected to the supported side BC, which of course brings about the stress concentration and additional deformations (sides AB and BC will be referred to as 'side' and 'top' respectively from hereon). The nominal 'beam' stress σ_{nom} due to bending M_t becomes amplified to the value $\sigma_{\max}$.

The relative amplification $\sigma_{\max} / \sigma_{nom}$ as well as the extra deformation experienced by the joint will be dependent only on the a/t ratio of the tube. These effects are highly localized at the T-joint and can be analysed separately from the rest of the frame. That's why only a fragment of the frame shown in Figure 1b, with a cross member of length L and a longitudinal member of length L_1, is modeled for the FE analysis. As long as $L, L_1 >> a$ the values of L, L_1, and the boundary conditions at the ends of the tubes are somewhat arbitrary.

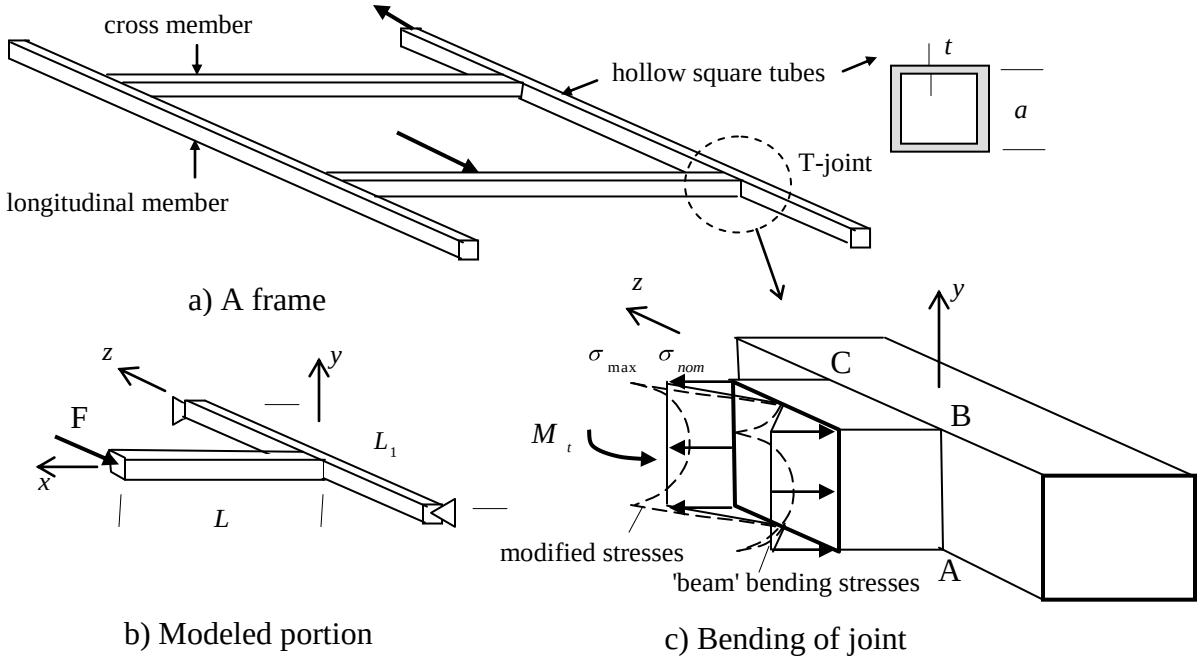

Figure 1. A thin-walled frame with T-joints

The bending moment to be transferred from the cross member to the longitudinal member is $M_t = F(L - a/2)$. The cross member axis is denoted by x. The components of stress in the wall of this member in the plane $x=a/2$ are the main interest of the analysis.

For the numerical analysis the following dimensions were adopted: L= 406.4mm. L_1 = 444.5mm, a= 101.6mm, while the thickness t varied from 0.794mm (a 'thin-walled' case of a/t=128) to 49.53mm (a 'thick-walled' case of a/t=2.1). The force F=17,793N (4,000lbs) was applied throughout the calculations reported in the next section. For the above geometry, the FE stress results at the T-connection (sections AB and BC) presented in the following sections were found to be numerically identical independent of whether F was equally distributed or applied at four corners of the tube's end.

3.0 Finite Element Analysis

The tube's wall of the frame members can be modeled either by several 3-D solid elements across the thickness *t* (we used 4 elements as shown in Figure 2a) or, for a sufficiently large *a*/*t* ratio, by one shell element with the in-plane and bending stiffness capabilities built-in (Figure 2b). Elements *solid45* (8 nodes, linear shape functions) or *solid95* (20 nodes, quadratic shape functions), and *shell63* (4 nodes) from the ANSYS program library are selected.

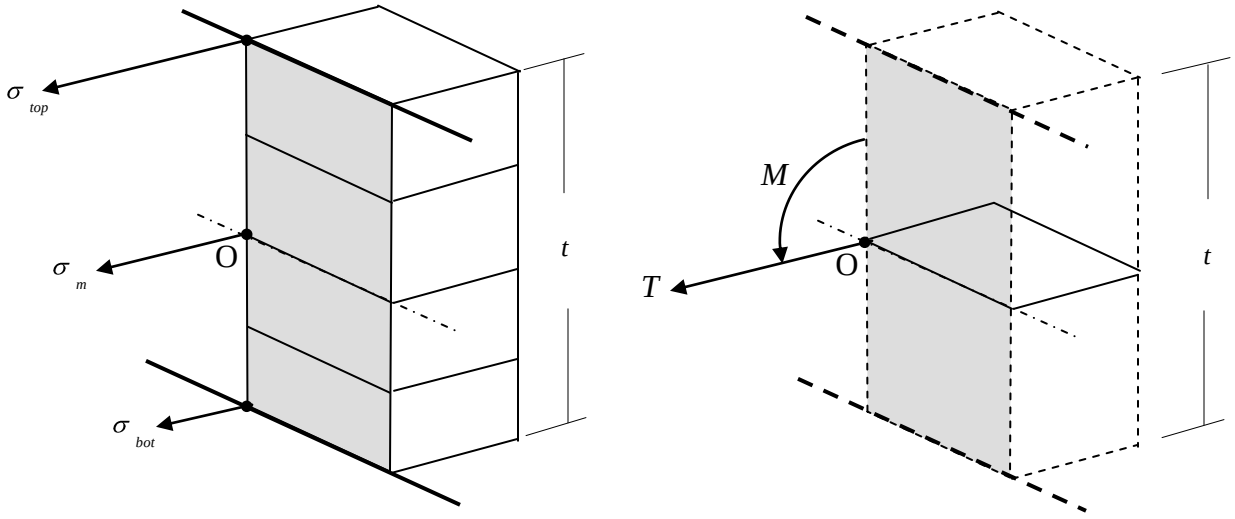

a) Solid elements b) Shell element

Figure 2. Modeling the tube's wall

These two different types of the FE models (to be referred to as *solid* and *shell* models respectively) are used for comparison and to verify convergence. In the *solid* model the displacements and stresses are calculated at every node so that the stress distribution across the thickness can be determined. In turn, the *shell* element assumes the linear variation of the displacements and stresses across the thickness. The *shell* model allows

calculating the displacements and rotations, and then the forces and moments at the nodes which are always positioned at the middle surface of the tube.

3.1 The stress results

In the *solid* model a generally linear stress distribution across the thickness was observed with $\sigma_m \cong (\sigma_{top} + \sigma_{bot})/2$, where σ_m, σ_{top}, and σ_{bot} can be read from the results files for the middle, top, and bottom nodes respectively. The stress at the middle node, σ_m, can be considered average for the wall and it will be referred to as the membrane stress. At a distance of about *a* from the connection on the X1 axis (see Figure 3c, which was obtained for *a*/*t*=16) this stress becomes the 'beam' bending stress defined as:

$$\sigma_m = -\frac{M_t}{I_y} z \quad \text{where} \quad I_y = \frac{2}{3} a^3 t \left(1 + \frac{t^2}{a^2}\right) \tag{1}$$

I_y denotes the area moment of inertia for the tube. Note that the nominal stress (see Figure 1c) representing the tension/compression in the side walls of the cross member in the case of members with undistorted cross-sectional areas is:

$$\sigma_{nom} = \pm \frac{M_t}{I_y} \frac{a}{2} \tag{2}$$

The plot in Figure 3c also helps in understanding why a particular pattern of applying *F* at X1=0.41m is not affecting the stresses at the T-connection (i.e. at X1=0).

In turn the stress $\sigma_b = (\sigma_{top} - \sigma_{bot})/2$ is interpreted as locally bending the wall. At the sufficient distance from the connection $\sigma_b = 0$ for the top wall CB, while for the side wall AB:

$$\sigma_b = \pm \frac{M_t}{I_y} \frac{t}{2}. \tag{3}$$

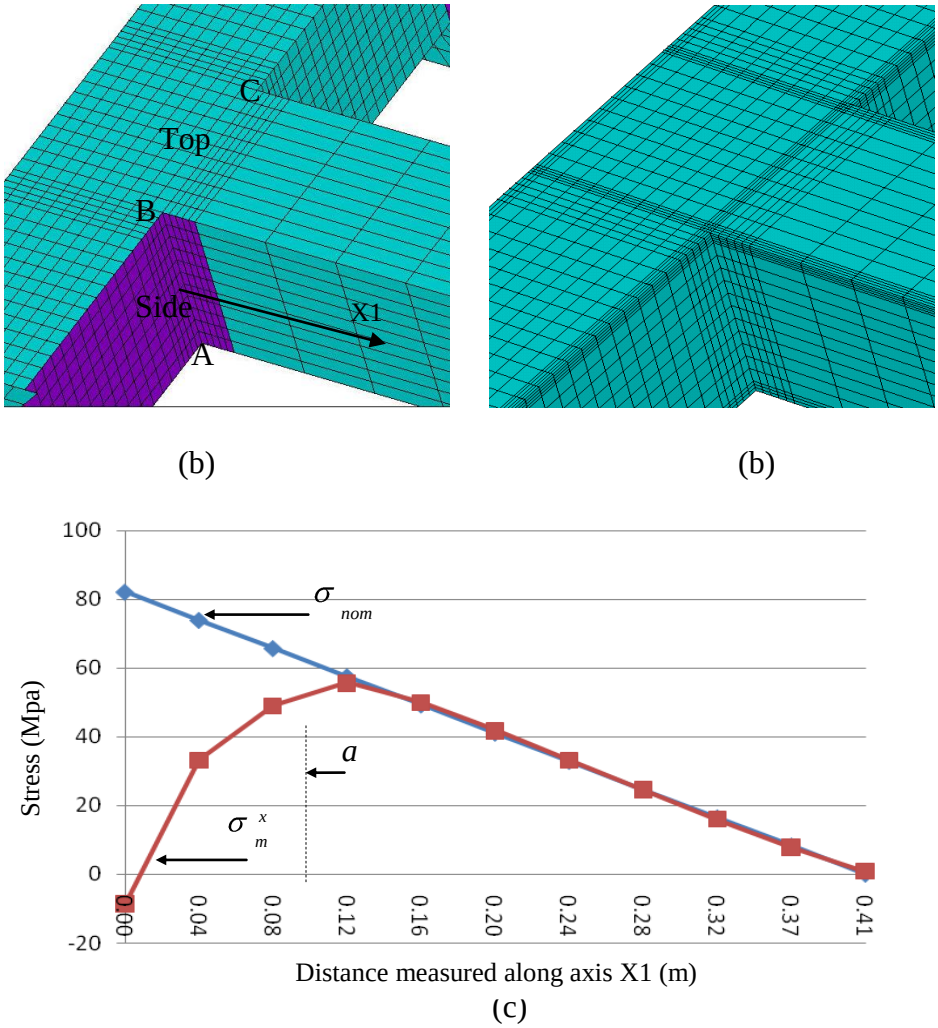

Figure 3. The T-joint's meshing patterns for the shell (a) and solid (b) elements, and (c) nominal beam stresses and membrane stresses obtained from shell model

In the *shell* model the corresponding membrane and bending stresses are calculated from:

$$\sigma_m = \frac{T}{t} \text{ and } \sigma_b = \pm \frac{6M}{t^2} \qquad (4)$$

where T and M are the nodal force and bending moment (see Figure 2b) available from the results files.

The meshing patterns for these two models are similar, as indicated in Figure 3a and b.

It should be noted that the shaded area in Figure 2 is modelled by 30 DOF (10 nodes × 3 DOF/node) when using linear solids, or by 12 DOF (2 nodes × 6 DOF/node) when using

shells. Consequently the *solid* model requires about 2.5 as many DOF as the *shell* model (this ratio increases to about 5.5 if the quadratic solids are used).

Typical stress distribution for the connections along AB and CD are shown in Figure 4. These results were obtained using the shell model for t=6.35mm (a/t=16) for which σ_{nom} =82.2MPa . The membrane forces T_x on side BC and AB as obtained from ANSYS are plotted in Figure 4a, similar plots can be obtained for T_y, T_z, M_x, and so on. The stresses are thereafter calculated from these in-plane forces and moments.

The stresses shown in Figure 4 are denoted as follows: σ_m^x and σ_b^x represent the membrane and bending stresses in the *x*-direction respectively for sides AB and CD, σ_m^y and σ_b^y represent the membrane and bending stresses in the y-direction acting on top BC, σ_m^z and σ_b^z represent the membrane and bending stresses in the z-direction acting on side AB, and τ_m^{xz} and τ_b^{xz} are the in-plane membrane and bending shear stresses. Note the dominating role of the stresses in the *x*-direction. Also note that $(\sigma_m^x)_{\max}/\sigma_{nom} \cong 3.41$. The stresses in the walls of the connection for other *a/t* ratios were analyzed in a similar manner.

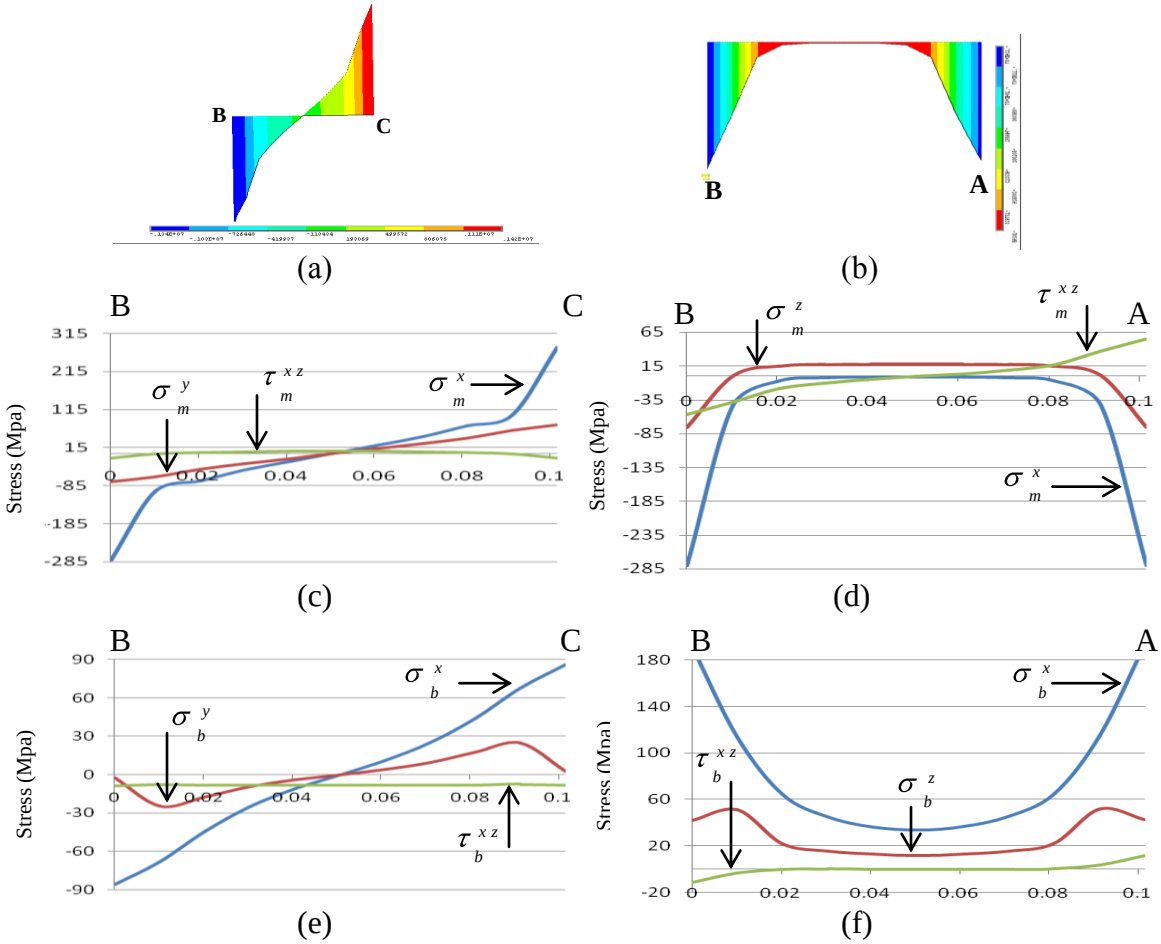

Figure 4. The forces and stress variations for t=6.35mm: (a, b) Force T_x on BC and AB, (c, d) Membrane stresses on BC and AB, (e, f) Bending stresses on BC and AB.

For comparison, the plots of σ_m^x obtained from the solid and shell models are presented in Figure 5 for the case of t=6.35mm (a/t=16) and the meshing shown in figure 3 with the sides AB and CB each divided into 11 elements. It is observed that the quadratic (20-noded) and linear (8-noded) solid elements provide nearly identical stress values. In addition, these stress values are in close agreement with the stresses obtained from the shell model. Similar results can be plotted for the other a/t ratios.

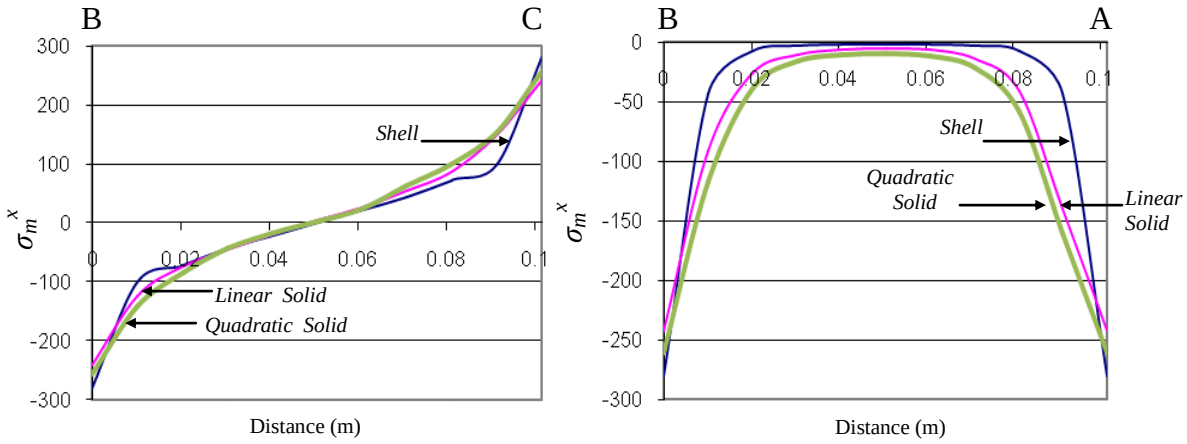

Figure 5: Comparison of σ_m^x by using different elements.

The effects of the *a*/*t* ratio on the σ_m^x distribution are shown in Figure 6. The stress values are normalized by dividing them by the corresponding nominal stresses. Note that for the ratio *a*/*t*=16 and higher the central part of side AB does not carry almost any load. On the other hand, the stresses become more uniformly distributed (with $\sigma_m^x \approx \sigma_{nom}$) for thick-walled tubes.

The values of the maximum membrane and bending stresses, as well as the nominal beam bending stress for different *a/t* ratios are listed in Table 1.

Table 1: Beam membrane, bending, and nominal stresses in the T-connection

(a/t)	Maximum σ_m^x (MPa)	Maximum σ_b^x (MPa)	σ_{nom} (MPa)
2.1	11.2	17.3	7.34
2.7	17.4	24.9	11.0
4.0	34.6	43.6	18.6
8.0	107	102.1	40.3
16.0	280	192.6	82.2
32.0	629	287.1	165
64.0	1300	347.5	331
128.0	2600	367.8	662

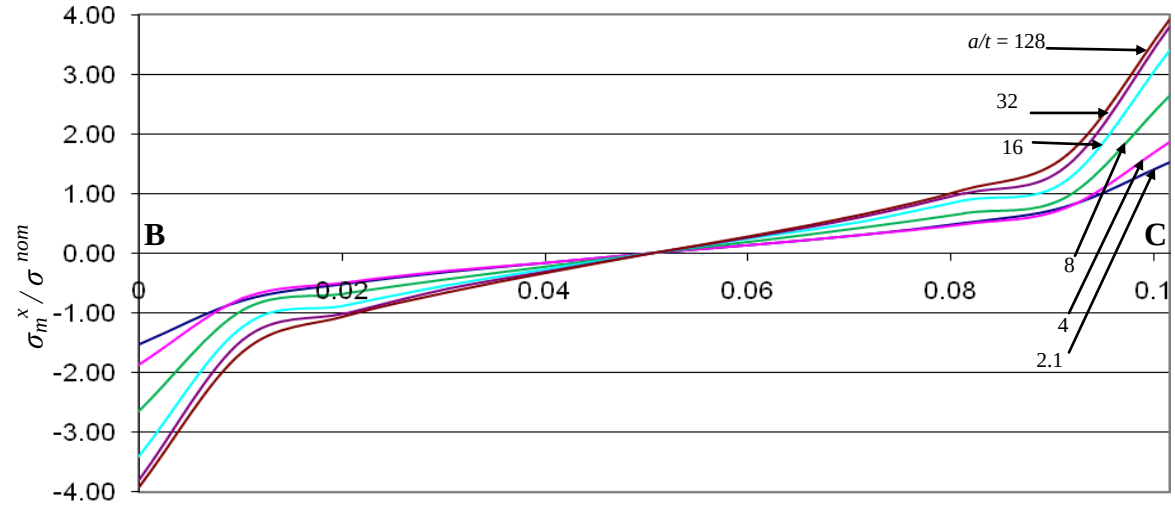

Top (BC) – distance from B to C in meters

(a)

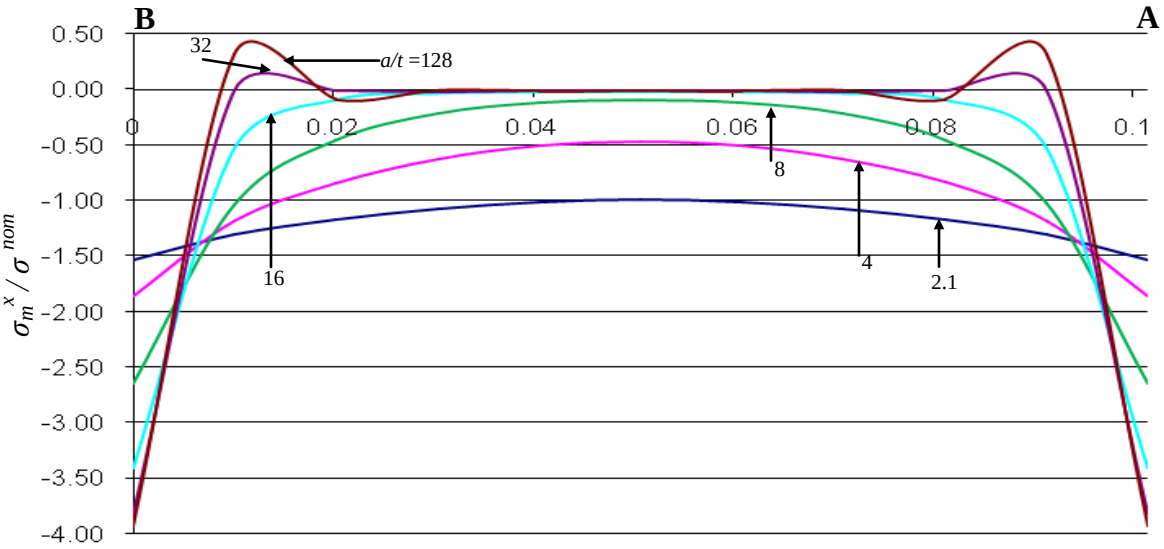

Side (AB) – distance from A to B in meters

(b)

Figure 6: The normalized membrane stresses, $\sigma_m^x / \sigma_{nom}$ for BC (a) and AB (b)

The amplification of the maximum membrane stress (at corner B) due to the thin-wallness of the tube is characterized by the stress amplification coefficient ξ_m defined as:

$$\xi_m = \left| \frac{(\sigma_m^x)_{\max}}{\sigma_{nom}} \right| \qquad (5a)$$

A similar amplification for the maximum bending stress (at corner B) can be defined as follows:

$$\xi_b = \left| \frac{(\sigma_b^x)_{\max}}{\sigma_{nom}} \right| \qquad (5b)$$

These two coefficients are plotted in Figure 7 for different *a*/*t* ratios (the meaning of *b* is explained later). Note that the value of ξ_m approaches four as the connection becomes very thin-walled. With the amplification ξ_m known, it is possible to calculate the maximum membrane stresses in the T-joint based on σ_{nom} calculated from the simple beam model. Similarly, the amplification ξ_b can be used to find the maximum bending stresses in the T-joint.

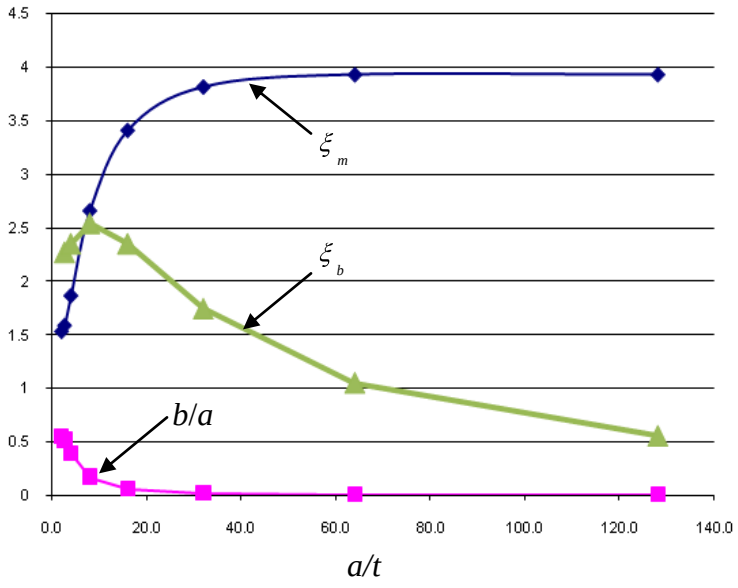

Figure 7: Effect of *a*/*t* ratio on the stress amplification and the equivalent width *b*.

It should be emphasized that considering the membrane (σ_m) and bending (σ_b) stresses separately has some practical advantages. Our numerical experiments indicate that the effects of a particular geometry of welds (which can be included in the 3D solid model)

on the membrane stresses are negligible (only σ_b is affected). Also, the real shape of the weld, especially inside the tube, is usually somewhat random and difficult to determine precisely. On the other hand, for thin-walled tubes the membrane stresses carry almost the entire moment M_t applied to the connection (for straight beams the stress σ_b bending the walls contributes only to a fraction, equal to about $(t/2a)^2$, of M_t). That's why the membrane stresses are crucial for understanding how M_t is being transferred through the connection. Similar conclusions were drawn in [13-14].

The results in Table 1 indicate that with the *a*/*t* ratio increasing, the membrane stresses increase faster than both the bending stresses and the nominal stresses. Interestingly, the membrane stress amplification parameter ξ_m, which grows steeply for small *a*/*t*, levels off for larger values of *a*/*t* ratio. Despite the bending stresses continuously increasing with *a*/*t* values, the bending stress amplification parameter ξ_b peaks at *a*/*t*=8, which seems to be a consequence of the bending stresses increasing less than the nominal stresses for higher *a*/*t* ratios.

The *shell* model of the connection was also checked for local buckling of the tube's wall indicating high values of safety factors for stability. This can be explained by the fact that the compressive membrane stresses from the middle portion of section AB are shifted to the corners reducing the possibility of buckling the wall.

The results in Figure 7, in particular the limiting value of ξ_m for large values of the *a*/*t* ratios can be physically interpreted as follows. As the connection becomes more and more thin-walled, from the plots in Figure 6 it is observed that the stresses become less and less uniformly distributed and the majority of the load is being carried by the top BC

and the corners of the connection. Thus, one can assume that for $a/t>>1$ only the top side BC and the corresponding bottom side of the tube (shadowed in Figure 8b) carry the total moment M_t. The area moment of inertia for such a section is reduced to $I_y^{\infty} \cong \frac{1}{6}a^3 t$ from $I_y \cong \frac{2}{3}a^3 t$ for the full section in Figure 8a. Therefore, the ratio of the nominal stresses for sections (b) and section (a) is:

$$\frac{\sigma_{nom}^{\infty}}{\sigma_{nom}} = \frac{I_y}{I_y^{\infty}} = 4 \qquad (6)$$

which is the same as the value of parameter ξ_m at the limit (for $a/t>>1$). Accordingly, it may be assumed that for any intermediate value of a/t, only a fraction of the side AB of width b is carrying the stress $\sigma_{\max}^{B}$ (calculated for corner B from FE models) as indicated in Figure 8d.

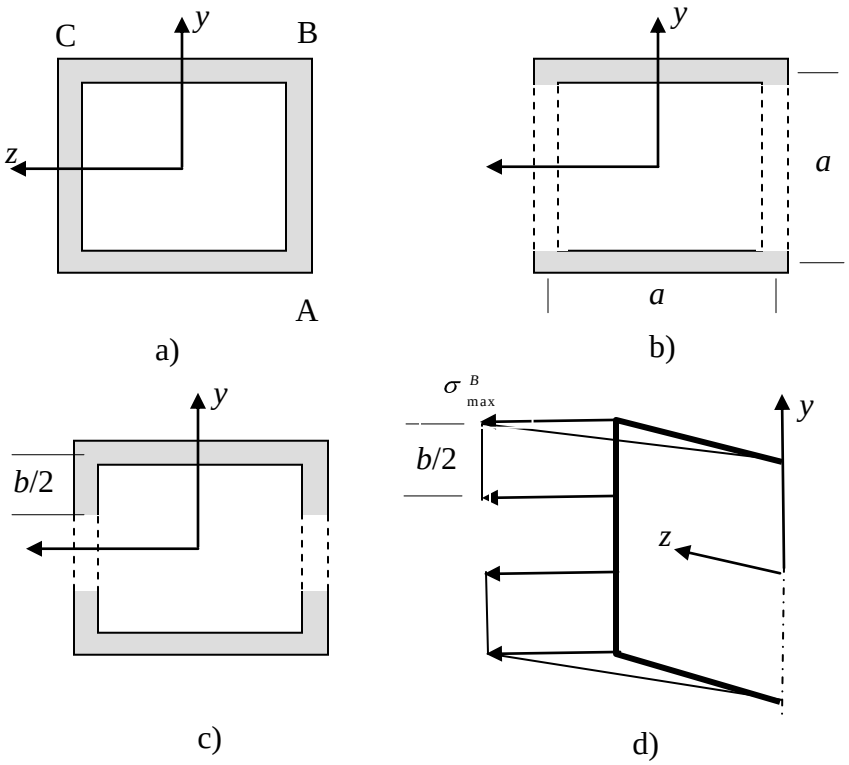

Figure 8. Equivalent width of side AB of the tube.

This way $\sigma^{B}_{\max}$ plays the role of the nominal stress for the section in Figure 8c for which $I^{b}_{y} \cong \frac{1}{6} a^{3} t(1+3b/a)$. Therefore:

$$\xi_m = \frac{\sigma^{B}_{\max}}{\sigma_{nom}} = \frac{I_y}{I^{b}_{y}} = \frac{4}{1+3b/a} \quad \text{or} \quad \frac{b}{a} = \frac{1}{3}\left(\frac{4}{\xi_m} - 1\right) \tag{7}$$

The dependence of the *b*/*a* ratio on the thin-wallness *a*/*t* is shown in Figure 7. For example, if *a*/*t*=16 then *b*/*a*=0.058 (the stress distributions for this case were presented in Figure 4), which indicates that only 5.8% of the side wall carries the load due to the bending moment M_t.

In conclusion, the plots in Figure 7 permit treating the thin-wall tubes in the stress calculation of the T-joints as standard beams with either using only width *b* of the side AB (as in Figure 8c with the moment of inertia I^{b}_{y}) of the cross-section , or using the full cross-section (as in Figure 8a with the moment of inertia I_b) and multiplying the stress by the parameter ξ_m.

3.2 The bending stiffness of the T-joint

As shown previously, at a sufficient distance (approximately equal to *a*) from the T-joint connection the tubes behave like beams. This can be used to identify the joint's rotational (bending) stiffness using the following approach. The total displacement under the force F can be decomposed into the portion due to bending the tubes as beams, and the portion due to local deformations at the joint (see Figure 9), that is:

$$u_F = u_{beam} + \phi L \tag{8}$$

The total displacement u_F for an assumed *a*/*t* ratio can be calculated from the FEM model (using either solid or shell elements). Displacement u_{beam} can in turn be obtained if

the tubes are modeled as beams (we used the ANSYS' *beam3* elements) with the bending stiffness EI_y rigidly connected at *T*.

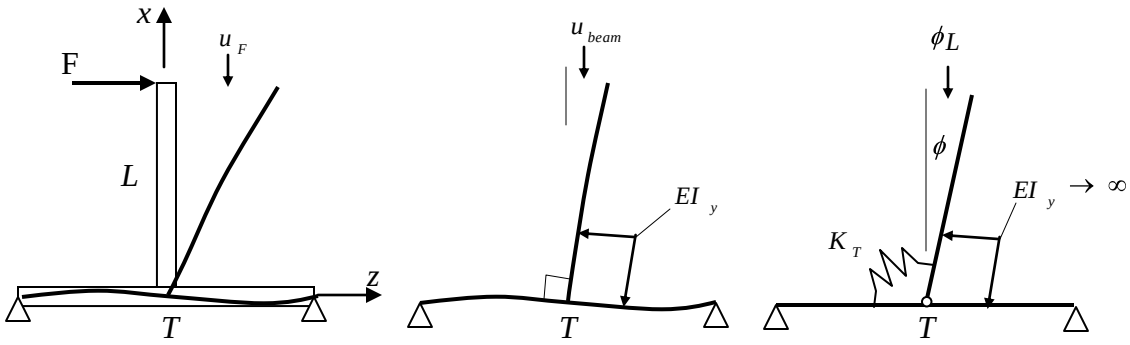

Figure 9: Rotational stiffness of the T-joint

Therefore, the rotational stiffness of the joint can be defined as:

$$K_T = \frac{M_T}{\phi} = \frac{FL^2}{u_F - u_{beam}} \tag{9}$$

Note that both u_F and u_{beam} vary with the *a*/*t* ratio as depicted in Figure 10.

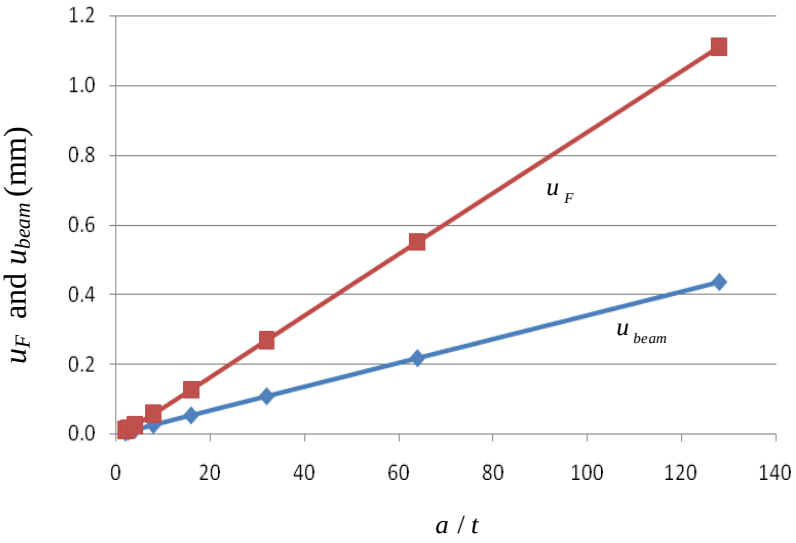

Figure 10: Effects of *a*/*t* ratio on the displacements u_F and u_{beam}

The calculated values of the stiffness K_T for the range of the *a*/*t* ratio are plotted in Figure 11. It is convenient to interpret the stiffness K_T in relations to the beam stiffness EI_y using the following reasoning.

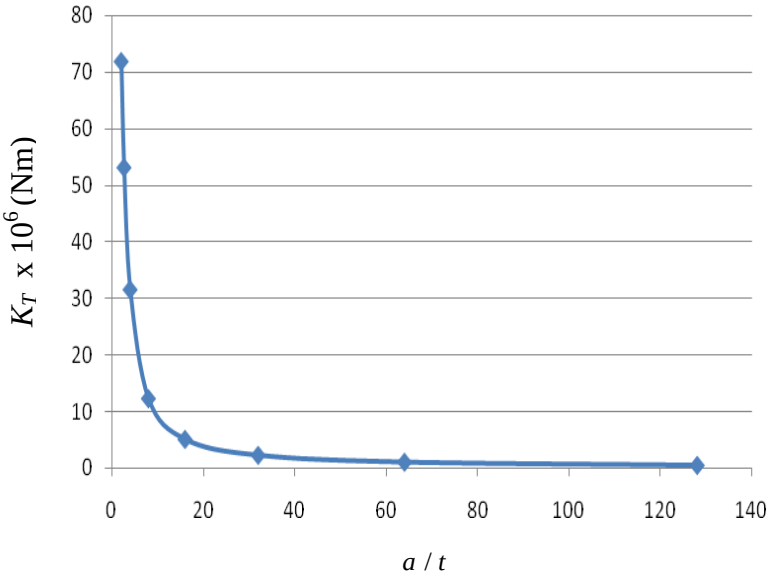

Figure 11. Effects of *a*/*t* ratio on the rotational stiffness of the T-joint.

Assume that the tubes in the vicinity of the T-joint are modeled by the beam elements as depicted in Figure 12. The rotational stiffness of the connection can be embedded in the element TT_1 of length $a/2$ in the form of the bending stiffness reduction parameter α_K (i.e., the bending stiffness of this element is EI_y / α_K).

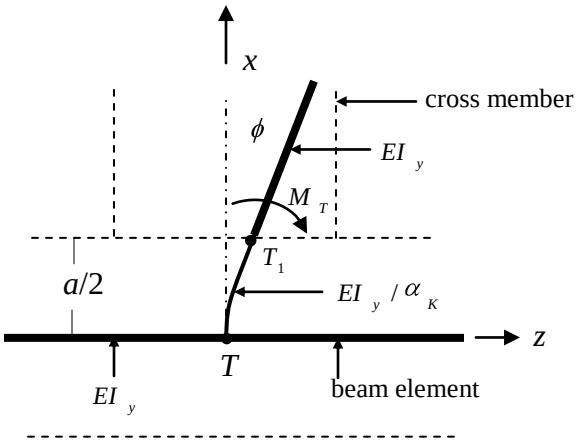

Figure 12. The bending stiffness reduction coefficient

Note that for this element $\phi = \frac{M_T a/2}{EI_y}\alpha_K$. Substituting into (9) renders:

$$K_T = \frac{EI_y}{a/2}\frac{1}{\alpha_K} \qquad \text{or} \qquad \alpha_K = \frac{EI_y}{a/2}\frac{1}{K_T} \tag{10}$$

The values of α_K calculated for different *a*/*t* ratios are plotted in Figure 13.

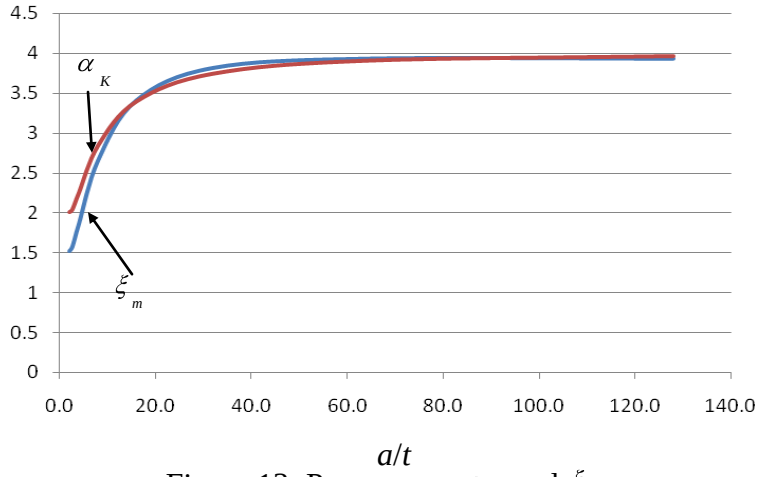

Figure 13: Parameters, α_K and ξ_m

Interestingly, in terms of the a/t ratios, the plot of α_K is almost identical to the plot of ξ_m. In particular $\alpha_K \rightarrow 4$ for $a/t >> 1$ which again indicates that for very thin-walled tubes only the section in Figure 8b contributes to the stiffness of element TT_1. Clearly, parameter α_K permits inclusion of the local deformation at the T-joint without actually using complex models such as those shown in Figure 3. Instead, the joint's stiffness characteristics can be recreated by using one modified beam element TT_1 as shown in Figure 12. This should substantially simplify any static (and dynamic) FE analysis of the frame structures similar to that shown in Figure 1a, which is numerically verified in the next section.

4.0 Application of the stress amplification and stiffness reduction parameters

In this section, the thin-walled frame with one T-joint and the dimensions as shown in Figure 14, loaded by two forces F_1 and F_2 is considered. For this frame the ratio *a*/*t*=16 and the corresponding stiffness reduction and stress amplification parameters (plotted in Figure 13) are α_K =3.40 and ξ_m = 3.41 , respectively. The displacements of the center of

the frame at the ends A and B are fixed, while the end C is free. The calculated reaction forces at A and B, the displacement of C, and the maximum stresses at the joint were recorded for two loadings: case 1 for which F_1=44,482N (10,000lb), F_2=0, and case 2 with F_1=44,482N, F_2=25,000N (5620lb). The frame was first modeled by 30 beam elements (90 DOF) as shown in Figure 14a.

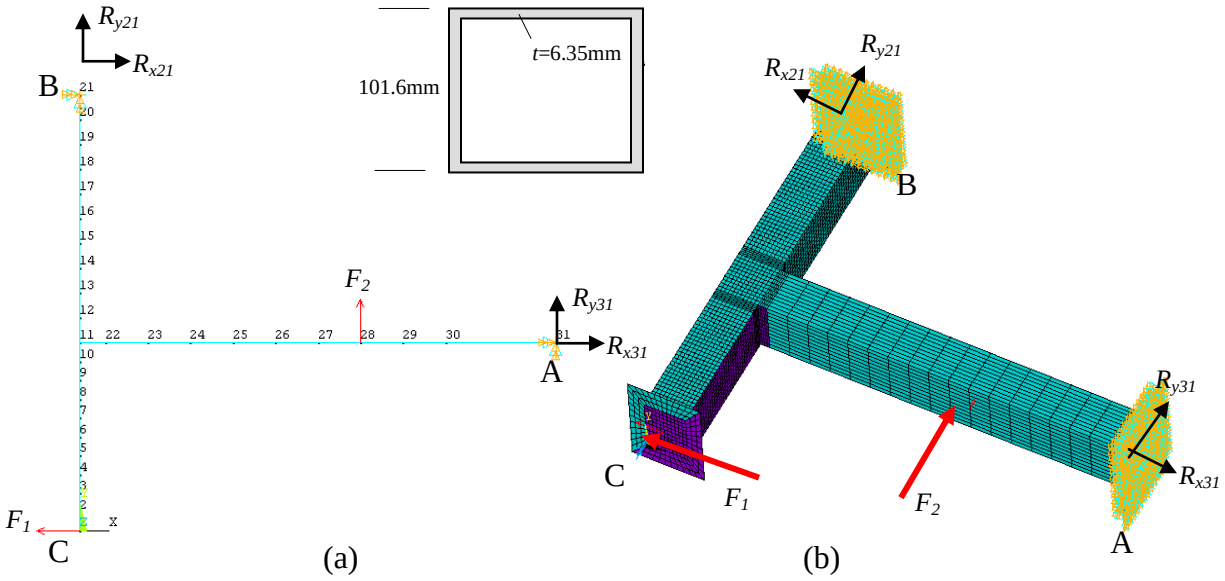

Figure 14: The thin-walled frame modelled by: a) beam elements, b) shell elements

The stiffness of the element between nodes 11 and 22 was reduced by 3.40. Then the frame was modeled by shell elements (this model had over 36000 DOF). The reaction forces, the displacement of C, and the maximum stress from both models are listed in Table 2. The bending moment in node 22 of the beam model is used to determine the nominal bending stress for this T-joint.

As can be seen the percent errors of the modified beam model for the case 1 loading are all less than 2%, and for the case 2 loading are all within 5%. As a point of interest, if the element between nodes 11 and 22 is not modified then the reaction error increases to

about 24% (R_{y31} =10,901N) for case 1 and 26% (R_{y31} =-6,334N) for case 2. If no stress amplification parameter is used then the error in the maximum stress increases to 58% (σ_{max} =107MPa) for case 1, and 62% (σ_{max} =106MPa) for case 2. The error in displacement of C increases to over 4% for both cases.

Table 2: Comparison of modified beam and shell models						
Case 1	R_{x2}(N)	R_{x31}	R_{y21}	R_{y31}	Defl. of C (mm)	Max Stress (Mpa)
Beam Model (modified)	-27897	72379	-8722	8722	-0.2159	250
Percent error	-1.12%	-0.43%	0.78%	0.78%	-1.47%	1.96%
Shell Model	-27587	72069	-8791	8791	-0.2128	255
Case 2						
Beam Model (modified)	-24828	69311	-16094	-8906	-0.2065	294
Percent error	-3.13%	-1.10%	2.00%	-3.82%	-1.75%	-5.00%
Shell Model	-24074	68556	-16422	-8578	-0.2029	280

In addition to the static stress/displacement analysis, the in-plane free vibrations of the frame were considered. The frequencies of the first two in-plane vibration modes for the shell model were 95.47Hz and 398.8Hz respectively. For the beam model with modified element 11-22 the same frequencies were 93.79Hz (-1.8% error) and 388.7 (-2.5% error) respectively. If the element 11-22 was not modified then the first frequency would become 107.7Hz (+12.8% error), while the second frequency would be 388.5Hz (-2.6% error). The second frequency was almost unaffected by the modification because the deformation of element 11-22 in this particular mode was insignificant.

It should be noted that the FE model of the frame made of beam elements is drastically easier to build and operate than any model made of shell or solid elements. The number of DOFs in the model in Figure 14a is about 4000 times smaller than the corresponding model in Figure 14b (for the static analysis the beam model can further be reduced by using only five elements between the nodes 1-11, 11-21, 11-22, 22-28, and 28-31).

5. Conclusions

This study proposed an accurate and numerically efficient approach to modeling in-plane loaded frames made of hollow square tubes connected by T-joints. The local effects at the joints are characterised by the stress concentration (ξ_m, ξ_b) and the stiffness reduction parameters α_K, which are determined in terms of the *a*/*t* ratio. The stiffness reduction parameter allows modelling the T-joint by one beam element with modified bending stiffness. Since away from the joint the tubes behave like beams, the entire frame can be effectively modeled by simple beam elements with the reaction forces/moments, deflections, and the natural frequencies of in-plane vibrations calculated accurately. Then, using the forces from the beam model, the maximum stress in the frame can be calculated by applying the parameters ξ_m, ξ_b. As demonstrated, such an approach is capable of rendering the results that are similar to the results of the FE model consisting of much more complicated shell or solid elements. These models however, include several thousands more degrees of freedom and are much more difficult to construct and operate.

References

[1] Lee M-M-K, Pine T, Jones T-B. An Experimental and Finite Element Study of the Torsional Behaviour of T-joints in Automotive Structures. Proceedings of the Institution of Mechanical Engineers, Part D: *Journal of Automobile Engineering* (2001); 215(2): 231-240.

[2] Lee M-M-K. Strength, Stress and Fracture Analyses of offshore tubular joints using finite elements. *Journal of Constructional Steel Research* (1999); 51(3): 265-286.

[3] Tsai C-L, Tsai M-J, McCauley R-B. Stress analysis and design of double fillet-welded T-joints. *Welding Journal* (1998); 77(2): 94-102.

[4] Saho Y-B. Geometrical effect on the stress distribution along weld toe for tubular T- and K-joints under axial loading. *Journal of Constructional Steel Research* (2007); 63(10): 1351-60.

[5] Shao Y-B, Tihen L-S. Parametric equation of stress intensity factor for tubular K-joint under balanced axial loads. *International Journal of Fatigue* (2005); 27(6): 666-679.

[6] Zhang B-F, Qu S-Y, Shao Y-B, Yang C-Q. Fatigue crack propagation analysis of tubular K-joints. I: Experimental test. *Chinese Journal of Computational Mechanics* (2007); 24(5): 643-647.

[7] Chan T-K, Fung T-C, Tan C-Y, Soh C-K. Behaviour of reinforced tubular T-joints. Proceedings of the Institution of Civil Engineers: *Structures and Buildings* (2001); 146(3): 263-274.

[8] Theotokogolou E, Moan T. Experimental and numerical study of composite T-joints. *Journal of Composite Materials* (1996); 30(2): 190-209.

[9] Choi Y-H, Foutch DA, LaFave JM. New approach to AISC P-M interaction curve for concrete filled tube beam-columns. *Journal of Engineering Structures* (2006); 28(11): 1586-98.

[10] Choi Y-H, Kim KS, Choi S-M. Simplified P-M interaction curve for square steel tube filled with high strength-concrete. *Journal of Thin-Walled Structures* (2008); 46(5): 506-515.

[11] Nazari A, Daniel W-J-T, Guan Z, Gurgenci, H. Parametric Equations Using Generic Representation of Joint Stiffness. Transactions of the ASME. *Journal of Offshore Mechanics and Arctic engineering* (2007); 129(2): 131-137.

[12] Nazari A, Daniel W-J-T, Guan Z, Gurgenci, H. Parametric Study of Hot Spot Stresses Around Tubular Joints With doubler Plates. *Practice Periodical on Structural Design and Construction* (2007); 12(1): 38-47.

[13] Lee M-M-K, Liewelyn A-P. Offshore Tubular T-Joints Reinforced with Internal Plain Annular Ring Stiffeners. *Journal of Structural Engineering* (2004); 130(6): 942-951.

[14] Dexter E-M, Kirkwood M-G, Lee M-M-K. Strength of Moment Loaded Tubular T/Y-Joints in Offshore Platforms. *Journal of Structural Engineering* (1995); 73(15): 239-246.

Chapter 3. Out-of-plane behaviour and FE modelling of a T-joint connection of thin-walled square tubes

ABSTRACT

The behaviour of square hollow tubes with T-joint connections subjected to out-of-plane loading conditions is examined numerically. Finite element (FE) models using 2D shell and 3D solid elements of relatively high density are used to determine the stresses in the joint and the joint's stiffness. The parameters describing the joint's stress concentration and the bending stiffness reduction are defined in terms of the 'thin-wallness' ratio (the ratio of side length to thickness of the tubes' cross-section) and the length of the longitudinal member and the geometric asymmetry of the T-joint connection. These parameters permit modelling accurately the tubes and the T-connection by simple one dimensional beam elements with certain modifications. The FE models consisting of beam elements are significantly easier to prepare and analyze. To illustrate the correctness of the approach, a structure with a T-connection and dimensions typical for the agricultural industry is considered. It is shown that the modified beam models provide accurately all important information of the structural analysis (i.e. the stresses, displacements, reaction forces, and the natural frequencies) at substantially reduced computational effort in comparison with the complicated FE models built of shell or solid elements. This can be considered the main contribution of this research paper. Using a simplified FE analysis for design has always been attractive to practicing engineers.

Keywords: hollow tubes, T-joint connection, finite elements, stress concentration, stiffness reduction.

2.0 Introduction

Hollow tubes have been widely used in the industry for the design of many structural components. The applications of these members range from bridge components in the construction industry to vehicle frames and pillars in the automotive sector. The hollow tubes are often connected together through welding to form T-joints. Despite of the wide use of these hollow tubes as efficient load-carrying members, a practical but yet simple and accurate approach for their analysis and design is not available. Consequently, for the accurate design of a T-joint structure made up of hollow tubes, engineers must perform a detailed and relatively complex finite element (FE) analysis. For this purpose, 3D solid or 2D plate/shell elements with fine mesh sizes at the connection must be employed. Such a meshing is required because of inherently local deformations present in this thin-walled connection under general loadings.

Unlike solid section beams, in the connection's vicinity, thin-wall members may experience severe distortion of their cross-sections. This disturbs the stress flow between the members bringing about significant stress concentrations at the corners of the connection [1]. The magnitude of these stress concentrations depends on the type of loading and certain geometrical parameters of the T-joint. Although a detailed 2D or 3D FE analysis of the thin-walled structure can satisfactorily provide the state of stress and stiffness of the connection, it is computationally expensive. This has some practical implications on the design process. For instance, in the automotive industry the initial design and analysis of the vehicles' frame is typically based on simple beam models [2-4]. The uncertainty and lack of a thorough understanding of the behaviour of the thin-walled structure is often causing unnecessary over-design of the T-joint.

Several researchers have examined the behaviour of T-joint connections both experimentally and numerically under different types of loadings. For example, circular hollow section (CHS) tubular T and K joints were studied by Shao et al [5-6]. The joints were subjected to axial loading and were studied both numerically and experimentally. To obtain the maximum stresses at the connection, parametric equations were proposed based on the geometric parameters of the circular hollow tubes. These parameters included the diameter and the thickness of the tubes. Pang et al. [7] performed a series of three dimensional finite element (FE) studies on CHS-to-CHS T-joints in order to determine the maximum stresses at the connection. The joints were subjected to the combined action of in-plane bending (IPB) and out-of-plane bending (OPB). The hot spot stress approach which requires the determination of the maximum stresses at the connection was used to study the cyclic fatigue behaviour of tubular T-joint connections in [8-9]. The joints were subjected to IPB and OPB loading conditions. In those studies, detailed 2D and 3D FE models were used to accurately determine the maximum stresses at the connection. Mashiri et al. [10-12] studied the strain and stress concentration factors (SCFs) of CHS-to-plate, CHS-to-CHS and square hollow section (SHS)-to-plate T-joints under IPB conditions.

Eight rectangular hollow section (RHS)-to-CHS T-joints were experimentally studied in [13]. In that study, both static and cyclic loadings were applied in IPB conditions and the SCFs were determined. Van der Vegte et al. [14] examined the effects of boundary conditions and chord length on the ultimate tensile strength of axially loaded CHS planar T-joints. Jun Li et al. [15] studied the behaviour of solid and thin-walled composite joints

subjected to coupled flexure-torsion. In that study, the dynamic behaviour of such joints was examined through a detailed numerical analysis using finite elements.

The present paper is an extension of the authors' previous work [1] on the behaviour of SHS-to-SHS T-joints under the IPB conditions, in which an approach was proposed to accurately and efficiently analyze such connections subjected to in-plane loads. This motivated the authors to extend the approach to situations where the T-joint connection is subjected to out-of-plane loading (OPB conditions).

One of the objectives of this paper is the better understanding of the out-of-plane behaviour of the T-joint connection of two hollow tubes of square cross-sections. The FE models using 2D shell and 3D solid elements are employed to examine the transfer of an out-of-plane bending moment through such a connection. Several parameters characterizing the connection's stiffness and the stress concentrations are introduced and defined in terms of the tube's thin-wallness ratio and the length of the longitudinal member. Using these parameters, a simple and accurate approach is proposed to allow modelling the thin-walled tubes' with the help of beam elements with certain properties modified. This one dimensional approach results in a significant reduction of computational effort in comparison to the high density shell/solid element models. In addition, the equivalent FE models made of beam elements are significantly easier to prepare and analyze. The approach's correctness is verified by two examples of general thin-walled frames with a T-joint connection and out-of-plane loading. The stresses, reaction forces, deflections, and the natural frequencies are obtained first by a shell model and then by an equivalent beam model to illustrate the effectiveness of the approach.

Using this simplified FE approach for the analysis of thin-walled T-joint connections subjected to OPB loads can be considered as the main contribution of this work.

2.0 Thin-walled frames with T-joint connections

The FE modelling of thin-walled frames with T-joints subjected to out-of-plane loading conditions is considered (see Figure 1a). The mesh generation is an important step to achieve a satisfactory accuracy of the results at a reasonable computational effort. To study the behaviour of thin-walled frames, researchers often use a so called "sub-zone" mesh generation technique for the FE modelling [16-18]. In this approach, based on the anticipated stress/strain gradients, the structure is divided into three regions: 1) the far field zones, 2) the transition zones, and 3) the refined zones.

In a thin-walled frame with T-joints, the far field zone regions should be sufficiently distant from the connection. Element sizes in these regions may be quite large and have no or insignificant effect on the stresses at the connection. The refined zone consists of regions very close to the connection of the tubes, and small elements are required to capture the state of stress and to determine the stress concentration factors at the connection. The transition region connects the refined and far field zones.

The T-joint connections of the thin-walled frame are usually weak points of the structure, experiencing local failures due to severe stress/strain concentrations. Therefore, the FE analysis of this portion of the structure should be done carefully, so that the meshing of the refined zones provides sufficient accuracy. Using the sub-zone mesh generation technique is very beneficial; it significantly reduces the number of degrees-of-freedom in the 2D or 3D FE models. This type of meshing of the tubes also results in lower

computational times. These models however, are still much more difficult to prepare and analyze than one-dimensional beam models proposed and analyzed in this paper, which can even be solved by hand calculations.

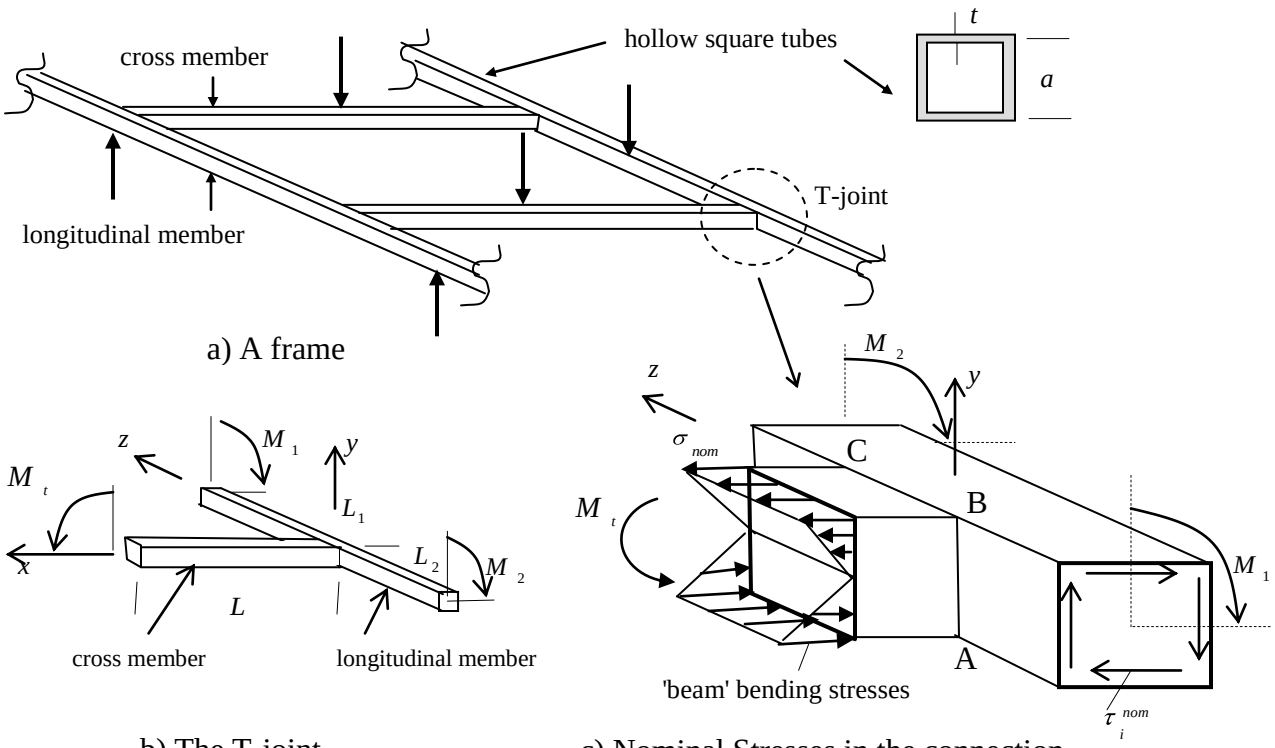

Figure 1: A thin-walled frame with T-joints

A thin-walled frame loaded transversally (see Figure 1a) is considered (OPB conditions). We assume that the cross members are butt-welded to the longitudinal members creating

T-joints. Away from such joints, the frame's members behave like beams with the main stresses due to the bending and torque moments. Only in a close vicinity of the T-joint connection the beam-like stress patterns cease to be valid. This is mostly because any bending moment M_t from the cross member transferred to the longitudinal member as torque moments ($M_t = M_1 + M_2$, see Figure 1b) may be accompanied by severe local deformations and stress concentrations. It should be noted that the transfer of bending and torque moments in the longitudinal member from one side of the T-joint to the other is almost negligibly disrupted. Therefore, only the effects of M_t are analyzed in detail.

The beam-like stresses in the cross member, referred to as the nominal, can be defined as $\sigma_{nom} = \frac{M_t}{I_z}\frac{a}{2}$ (bending, see Figure 1c), and in the longitudinal member as $\tau_i^{nom} = \frac{M_i}{2a^2 t}$ (i=1,2 for shear at both sides of the connection). The ratio M_1 / M_2 depends on the lengths (L_1 and L_2 in Figure 1b) and restraints imposed on the longitudinal member. This paper will focus mainly on the effects of the local deformation on the bending stresses in the cross member.

Experience and numerical analyses indicate high stress concentrations at one of the corner points C or B, with the maximum value denoted as σ_{max}. A typical 'modified' plot of the bending stress distribution is sketched in Figure 1d. The modification of the stress distribution along section AB (side wall) is mostly due to the lack of sufficient support to be provided by the longitudinal member away from the corners. It is worthwhile to mention that this was the main cause for the stress concentration for the in-plane loading (IPB conditions) reported in [1]. However, this phenomenon (i.e. lack of support) seems

to have a rather secondary effect in the case of out-of-plane loading. For this case the stress concentration is triggered mostly by the requirement to match the deformation patterns in the cross and longitudinal members along section BC (top wall). This problem and the reasoning for increasing the stress magnitude is sketched in Figure 2.

Assume that the longitudinal member is fixed at both sides and that $L_1 = L_2$. Because of some stress reduction in the side wall, (due to insufficient support, as mentioned above) the top wall of the cross section has to carry the tensile force that is in the range $0.75\frac{M_t}{a} < F^M < \frac{M_t}{a}$ (see Figure 2a). However, this force is transversal to the top of the longitudinal member, and therefore will bring about some bending and consequently 'curving' of section BC of this member (see Figure 2b). Clearly, section BC of the cross member must be adjusted accordingly, raising the stresses in the corners.

If $L_1 \neq L_2$ then the edges BC and AD will additionally deform anti-symmetrically (in the *x*-*z* plane). In general, it may be claimed that the stress concentration is due to the cross-sectional area ABCD being distorted (for $L_1 \neq L_2$ the distortion and the deformed shape of BC will be more complicated than shown in Figure 2b).

Such a phenomenon will be examined in detail by the FE analysis presented in the next section. Then, several parameters will be identified to relate the increases of the stress and compliance in the connection in terms of the member's *a*/*t* ratio (thin-wallness) and the length of the longitudinal member and L_1 / L_2 ratio (asymmetry of the longitudinal member).

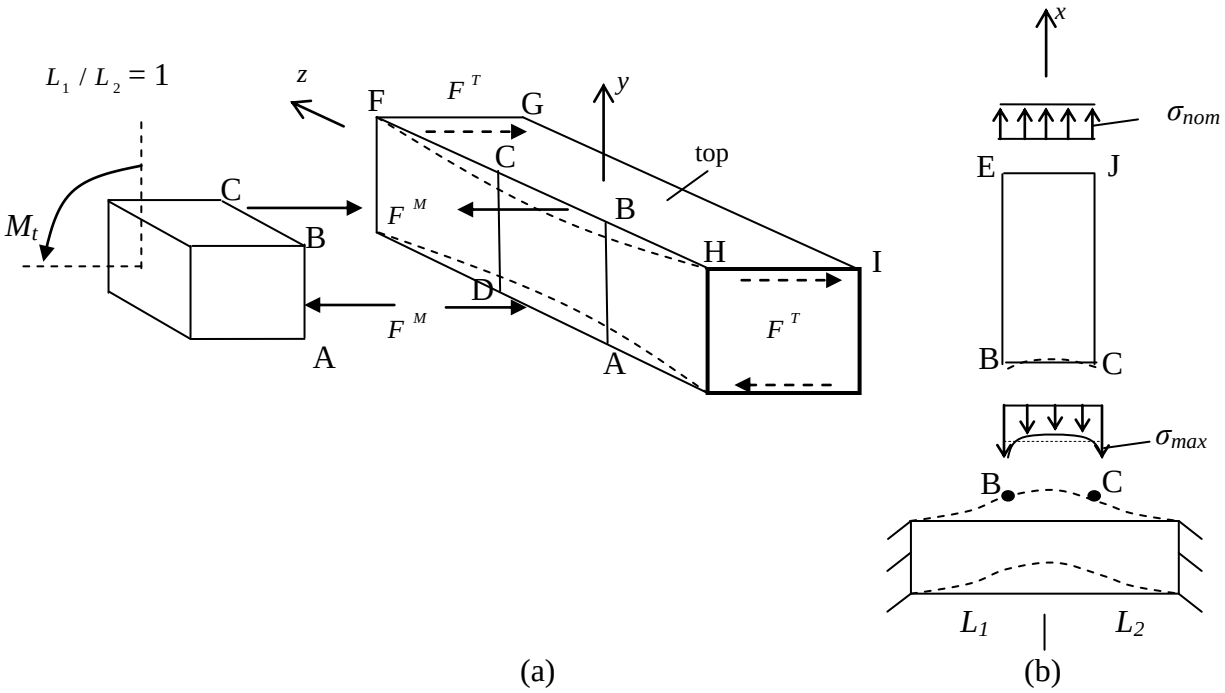

Figure 2. Equivalent force couple systems of the loaded frame (dashed lines represent the deformed shape)

For the numerical analysis, the bending moment M_t = 7,231Nm was applied throughout the calculations as reported in the next section. The following dimensions were adopted (the same as in [1]): L= 406.4mm, a = 101.6mm, while the thickness t varied from 0.794mm (a 'thin-walled' case of a/t=128) to 49.53mm (a 'thick-walled' case of a/t=2.1). The effects of geometrical asymmetry (i.e. the ratio L_2 / L_1) on the behaviour of the T-joint were also considered for $1 \leq L_2/L_1 \leq 4$. For symmetric T-joints (i.e., $L_1 = L_2$) the effect of the length of the longitudinal member with respect to the length of the cross member (L) was considered within the range $0.56L \leq L_1 = L_2 \leq 3L$.

3.0 Finite Element Analysis

The tube's wall of the frame members can be modeled either by several 3D solid elements across the thickness t (4 elements were used in this study as shown in Figure 3a)

or, for a sufficiently large *a*/*t* ratio, by one shell element with the in-plane membrane and bending stiffness capabilities built-in (Figure 3b). Elements *solid45* (8 nodes, linear shape functions) or *solid95* (20 nodes, quadratic shape functions), and *shell63* (4 nodes) from the ANSYS element library are selected.

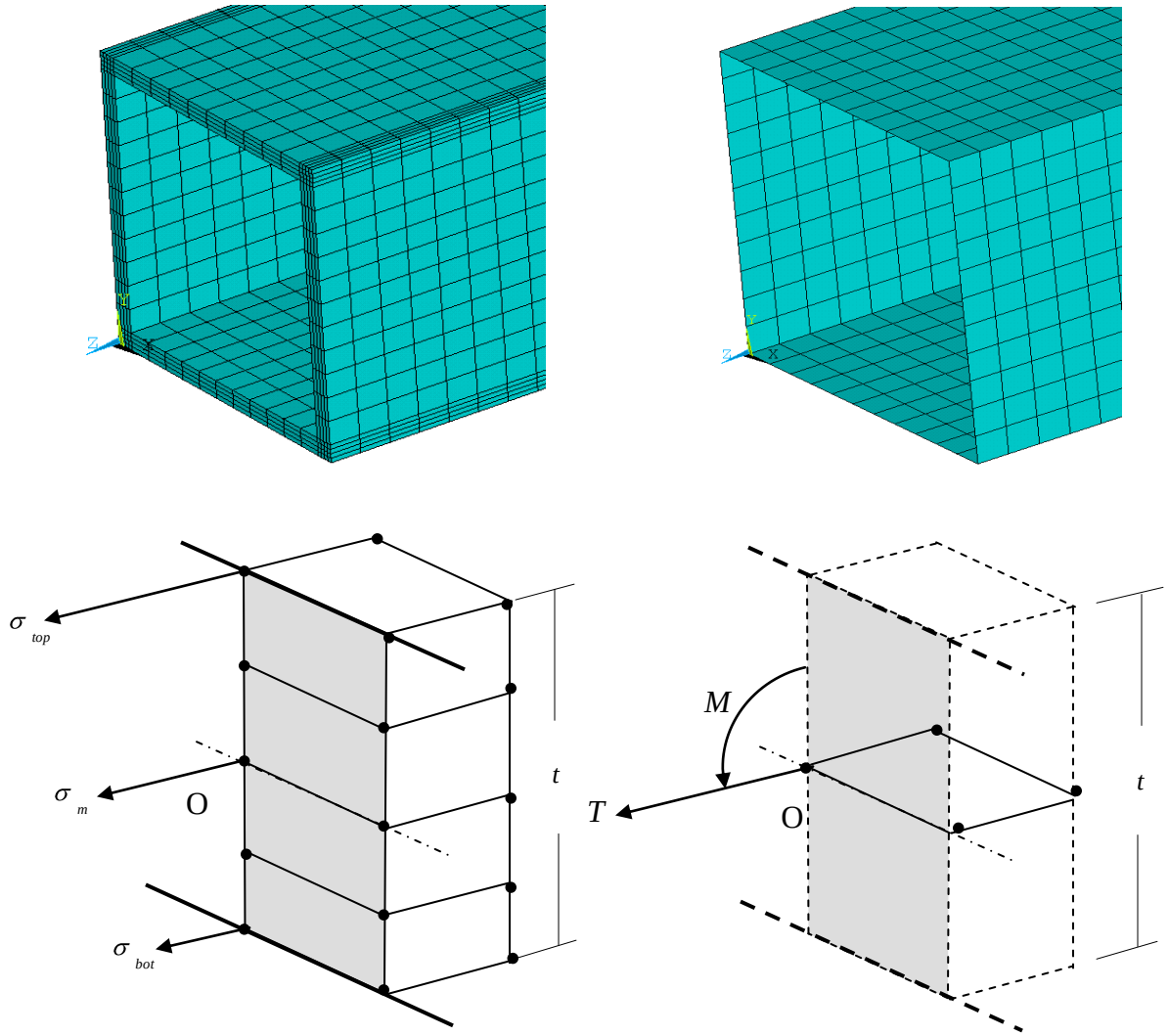

a) Solid element (Solid45) b) Shell element (Shell63)

Figure 3. Modeling the tube's wall

The FE models constructed from solid and shell elements (to be referred to as *solid* and *shell* models respectively from hereon) are employed for comparison and the convergence test. If the stress distribution through the tubes' thickness is non-linear, the solid model should be used for the analysis. This is because in the solid model, both

stresses and displacements are computed at every node allowing the determination of the stress distribution through the thickness. On the other hand, the FE model constructed from shell elements assumes a linear variation of the displacements and stresses across the thickness. In the shell model, the forces and moments which are always positioned at the middle surface of the tube are calculated from the displacements and rotations.

It should be noted that the solid elements have 3 DOF/node. The linear solid elements are constructed from 8-nodes, while the quadratic solid elements are constructed from 20-nodes. The shaded area in Figure 3 has 30 DOF (10 nodes $\times$ 3 DOF/node) when using linear solids, or has 12 DOF (2 nodes $\times$ 6 DOF/node) when using shell elements. Consequently, the *solid* model requires about 2.5 times as many DOF as the *shell* model (this ratio increases to about 5.5 if the quadratic solid elements are used).

3.1 The stress results

The meshing pattern for the solid model is shown in Figure 4b. The stress distribution through the thickness of the tubes that was obtained from the *solid* model was found to be generally linear. The stresses σ_m, σ_{top}, and σ_{bot} correspond to the stresses at the middle, top, and the bottom nodes respectively (see Figure 3a). In the *solid* model, it was observed that the stress at the middle is $\sigma_m \cong (\sigma_{top} + \sigma_{bot})/2$. This stress can be considered as the average stress for the wall and it will be referred to as the membrane stress. The stress $\sigma_b \cong (\sigma_{top} - \sigma_{bot})/2$ is interpreted as locally bending the walls. For a/t=16 and $L_1 = L_2 = 0.56L$ the stresses σ_m on the axis X1 are shown in Figure 4c. As can be observed, these stresses deviate from σ_{nom} only up to a distance of approximately equal to $a/2$. For comparison, for the in-plane problem (IPB loading) analyzed in [1],

the membrane stresses along the axis X2 deviated from σ_{nom} up to a distance of approximately equal to *a*.

For OPB loading conditions, at the sufficient distance from the connection (i.e., approximately equal to *a/2*) the membrane stress becomes the beam bending stress defined as:

$$\sigma_m = -\frac{M_t}{I_z} y \quad \text{where} \quad I_z = \frac{2}{3} a^3 t (1 + \frac{t^2}{4a^2}) \tag{1}$$

I_z denotes the area moment of inertia for the cross-member tube around the z-axis (as shown in Figure 1b). Note that the nominal beam stress (see Figure 1c) representing the tension/compression in the top and bottom walls of the cross member in the case of rigid longitudinal members is:

$$\sigma_{nom} = \pm \frac{M_t}{I_z} \frac{a}{2}. \tag{2}$$

The meshing pattern for the shell model is shown in Figure 4a, and is similar to the meshing of the solid model. In the *shell* model the membrane and bending stresses are calculated from:

$$\sigma_m = \frac{T}{t} \text{ and} \tag{3}$$

$$\sigma_b = \pm \frac{6M}{t^2} \tag{4}$$

where *T* and *M* are the nodal force and bending moment and *t* is the element thickness (see Figure 3b).

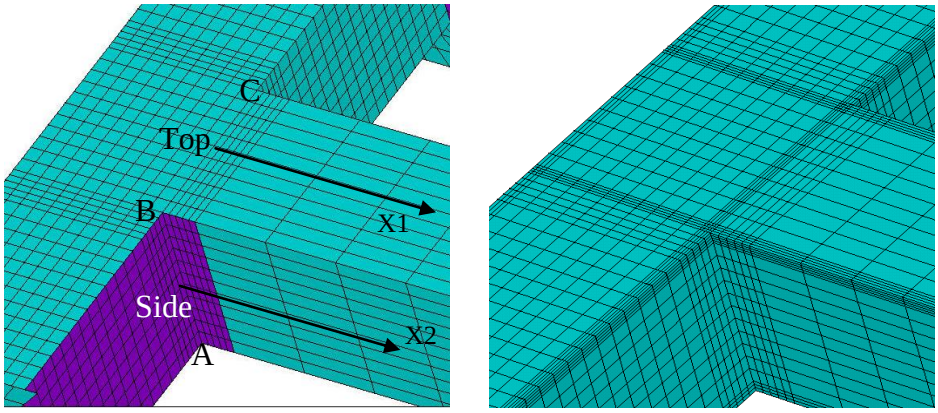

(c) (b)

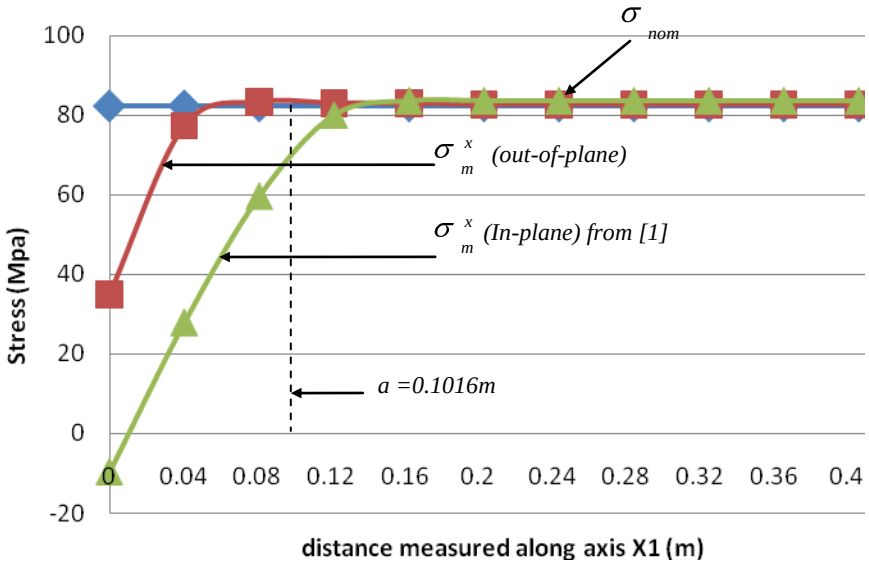

(c)

Figure 4. The T-joint's meshing patterns for the (a) shell and (b) solid elements, and (c) nominal beam stresses and membrane stresses obtained from shell model

For the connections along AB and CD typical stress distribution are shown in Figure 5. These results were obtained using the shell model for t=6.35mm (a/t=16) and $L_1 = L_2 = 0.56L$ for which σ_{nom} =82.2MPa. In Figures 5a and 5b, the membrane forces T_x on side AB and BC as obtained from the FE analysis are plotted. In a similar manner the plots for M_x can be obtained. The membrane and bending stresses are thereafter calculated from these in-plane forces and moments, respectively.

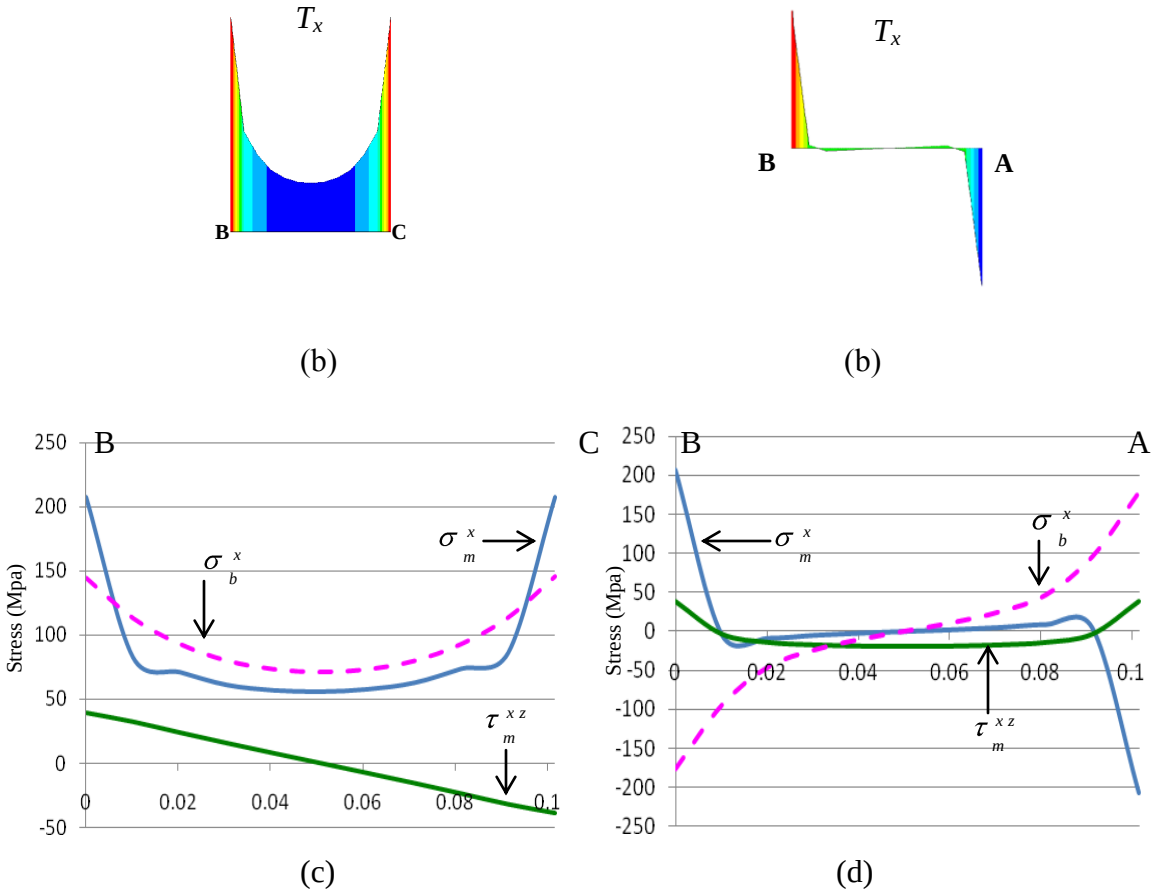

Figure 5. The forces and stress variations for t=6.35mm: (a,b) Force T_x on BC and AB, (c, d) Membrane and bending stresses on BC and AB

The stresses shown in Figure 5 are denoted as follows: σ_m^x and σ_b^x represent the membrane and bending stresses in the x-direction respectively for sides AB and CD. The character of membrane stresses is similar to that indicated in Figure 1d. Note that for the case considered $(\sigma_m^x)_{\max} / \sigma_{nom} = \frac{210}{80} \cong 2.52$. The stresses in the walls of the connection for other a/t ratios and lengths of longitudinal member were analyzed in a similar manner.

3.2 The Convergence Considerations

As mentioned previously, the mesh density and convergence of the results are important features in any FE analysis. In order to examine the effects of the element types and sizes, the stresses calculated from several solid models (both linear and quadratic) were compared to that of their shell model counterpart. For this purpose, the case of t=6.35mm (a/t=16) and $L_1 = L_2 = 0.56L$ with the meshing shown in Figures 4a and 4b was considered. The sides AB and CB were each divided into 11 elements with the same mesh pattern. The plots of σ_m^x that were obtained from the shell and two solid models are presented in Figure 6.

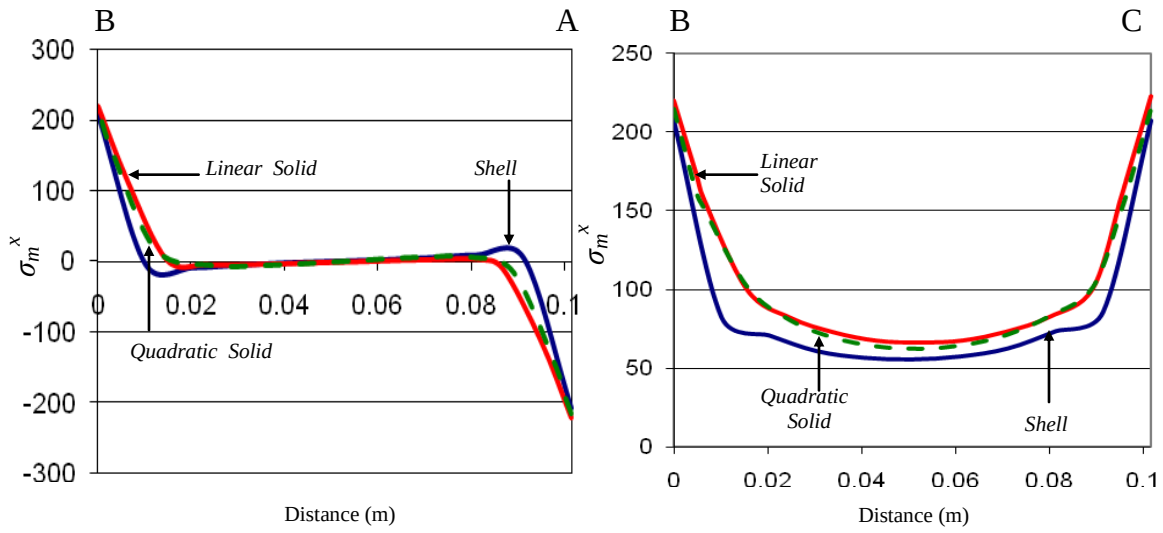

Figure 6: Comparison of membrane stress, σ_m^x, for different elements.

It is observed that the quadratic (20-noded) and linear (8-noded) solid elements provide nearly identical stress values. In addition, these stress values are in close agreement with the stresses obtained from the shell model. Similar results can be obtained for the other a/t ratios.

For the **convergence test**, the finer and coarser mesh sizes were varied. Three different cases were considered, where the sides AB and CB were modelled with 11, 21, and 41 elements each. Table 1 summarizes the three different FE models using shell elements. The mesh for the different element sizes are shown in Figures 7a, b and c. The membrane stress distribution on top CB in the X-direction, σ_m^x, obtained from these FE models for the case of t=6.35mm (a/t=16) and $L_1 = L_2 = 0.56L$ are shown in Figure 7d (similar stress plots were obtained using the solid model). Note that the stresses obtained with these meshing patterns are fairly close, therefore 11 elements were used in the further analyses of the connection as it is the most numerically efficient.

Table 1: Summary of the three different FE models using shell elements

Mesh	41 elements	21 elements	11 elements
Element size (mm)	2.48	4.84	9.24
Number of elements	21771	8211	3531
Number of nodes	21692	8172	3512

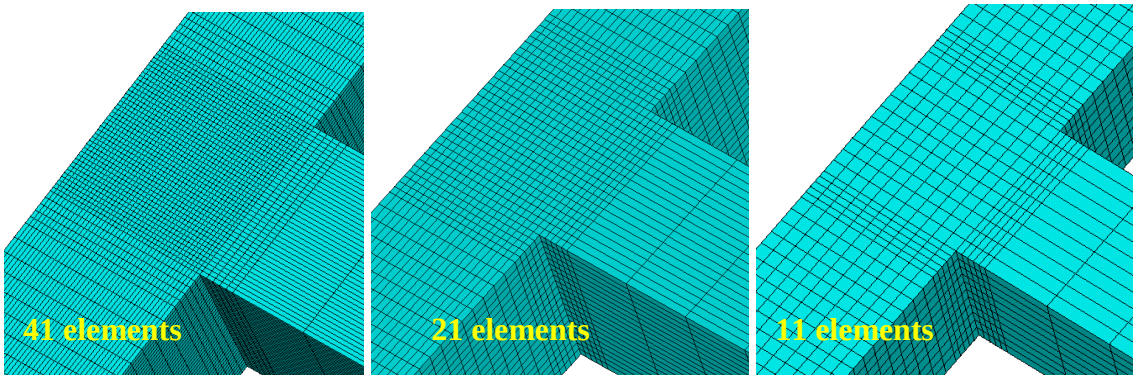

(a) (b) (c)

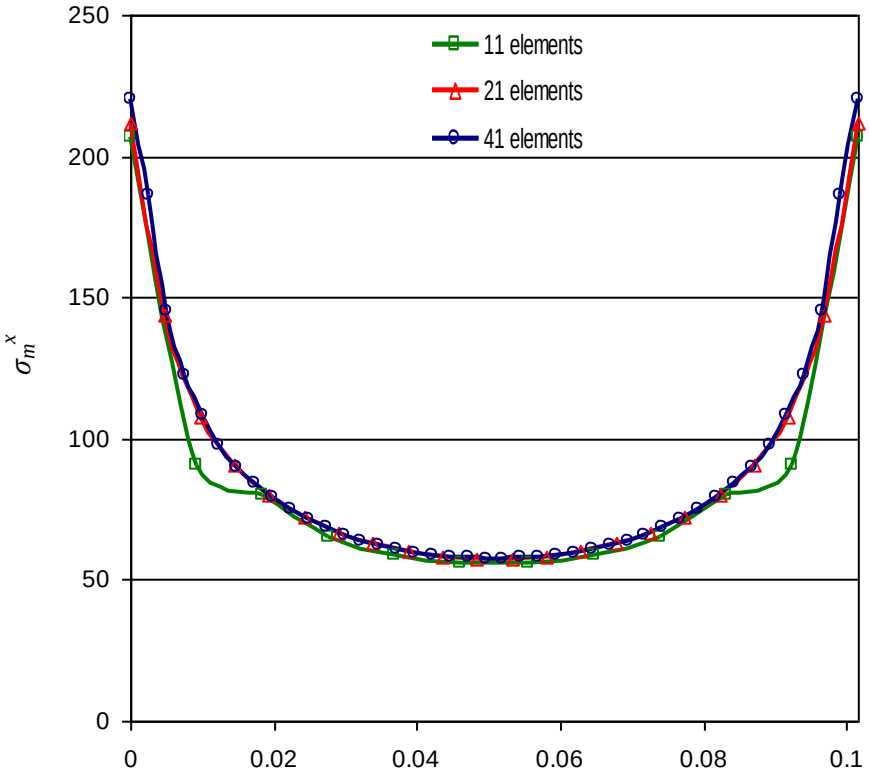

(d)

Figure 7: Results of the mesh sensitivity analysis using shell elements: a) 41 elements, b) 21 elements, c)11 elements, and d) Membrane Stresses in the X-dir at the connection

3.3 Effects of thin-wallness ratio

For $L_1 = L_2 = 0.56L$ the effects of the *a*/*t* ratio on the σ_m^x distribution for sides AB and CD are shown in Figures 8 and 9. The stress values are normalized with respect to the corresponding nominal stresses. Note that as the connection becomes more and more thin-walled the central part of side AB does not carry almost any load. The central part of BC also carries less load with the stresses concentrated at the corners. On the other hand, for thick-walled tubes, the stress distribution becomes closer to the nominal one, i.e., $\sigma_m^x \rightarrow \sigma_{nom}$, that is thick-walled tubes behave in a manner similar to beams. The values of the maximum membrane and bending stresses, as well as the nominal beam bending stress for different *a/t* ratios are listed in Table 2.

Table 2: Beam model nominal stresses and maximum shell stresses

(a/t)	Maximum σ_m^x (Mpa)	Maximum σ_b^x (Mpa)	σ_{nom} (Mpa)
2.1	13	16	7.34
2.7	18.6	23	11.0
4.0	32.7	40	18.6
8.0	87.5	94	40.3
16.0	207	177	82.2
32.0	428	251	165
64.0	846	289	331
128.0	1670	299	662

The amplification of the maximum membrane stress (at corner B) due to the thin-wallness of the tubes is characterized by the membrane *stress amplification parameter* ξ_m defined as:

$$\xi_m = \left| \frac{(\sigma_m^x)_{\max}}{\sigma_{nom}} \right| \qquad (5)$$

This parameter compares the beam model with the shell model. A similar bending amplification parameter for the maximum bending stress (at corner B) can be defined as

follows:

$$\xi_b = \left| \frac{(\sigma_b^x)_{\max}}{\sigma_{nom}} \right| \tag{6}$$

These two coefficients are plotted in Figure 10 for different *a*/*t* ratios.

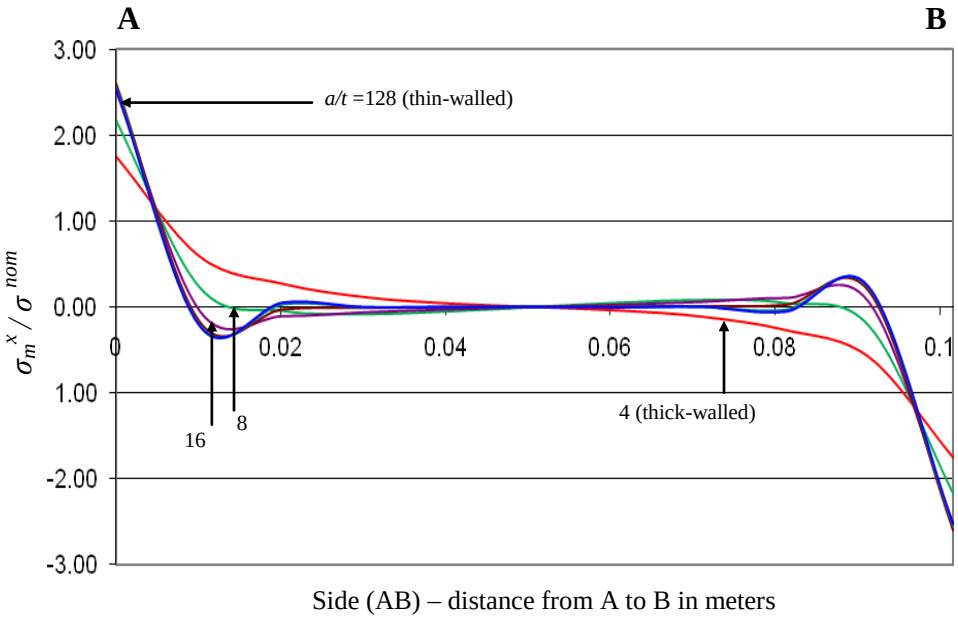

Figure 8: The normalized membrane stresses, $\sigma_m^x / \sigma_{nom}$ for AB obtained from shell model

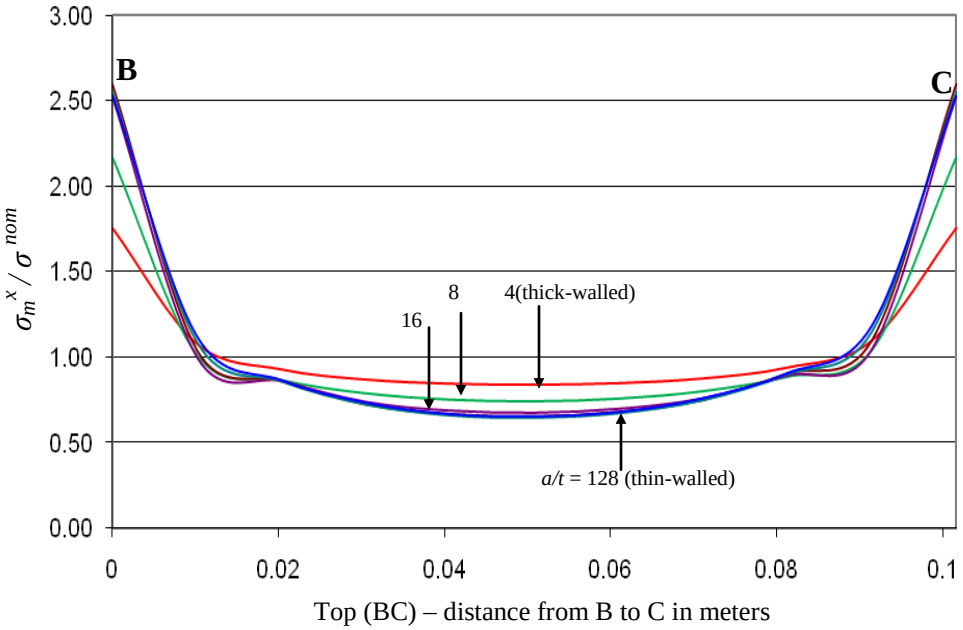

Figure 9: The normalized membrane stresses, $\sigma_m^x / \sigma_{nom}$ for BC obtained from shell model

It should be noted that the amplification for the membrane and bending stresses at the corners of the connection (i.e. A, B, C, etc) is the same for symmetric T-joints (i.e., $L_1 = L_2$). Also note that the value of ξ_m becomes close to 2.6 for *a/t* > 20 as the connection becomes very thin-walled. It is also worth to mention that for the IPB presented in [1], this stress amplification parameter approached a value of 4. With the known amplification, ξ_m, one may calculate the maximum membrane stresses in the T-joint based on σ_{nom} determined from the simple beam model. In turn, the amplification parameter, ξ_b, can be used to find the maximum bending stresses in the T-joint. Similar to the IPB conditions, this parameter is getting smaller with the thin-wallness ratio, *a/t*, increasing.

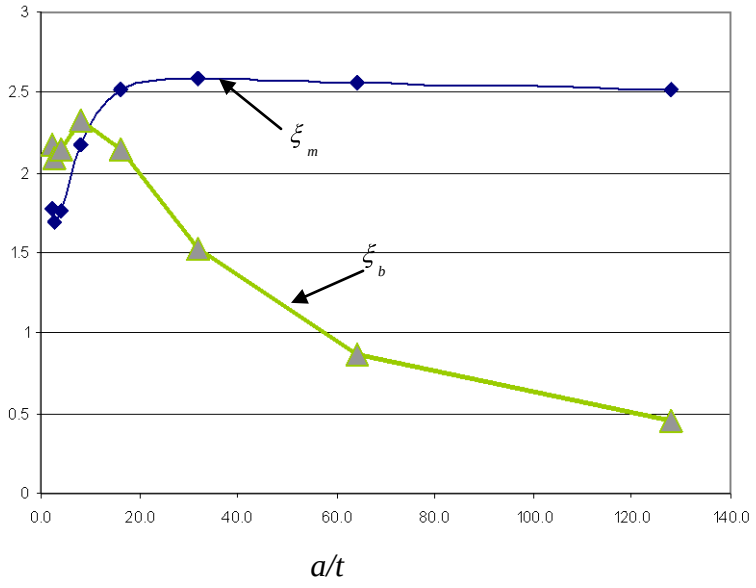

Figure 10: Effect of *a/t* ratio on the stress amplification parameters for $L_1 = L_2 = 0.56L$

3.4 Effects of the longitudinal member's length

As mentioned in section 2.0, the stress concentrations at the connection, besides being dependent on the thin-wallness ratio (i.e. *a/t*), should also be affected by the length of the

longitudinal member. To demonstrate these effects, the length of the longitudinal member, $L_1 = L_2$ was varied between 0.56*L* to 3*L* (see Figure 1b). Longitudinal member lengths longer than 3*L* were not considered since such frame dimensions are rare in practice. The analysis indicated that the stress plots in Figure 5, representing the distribution of the different components of stress along top AB and side CB remain generally the same with only the magnitude of the stresses changing for different lengths of the longitudinal member. However, the shape of the stress amplification parameter ξ_m, which in Figure 10 remained almost constant for $a/t > 20$, is generally increasing with no limiting value if $L_1/L > 1.5$. This can be observed in Figure 11.

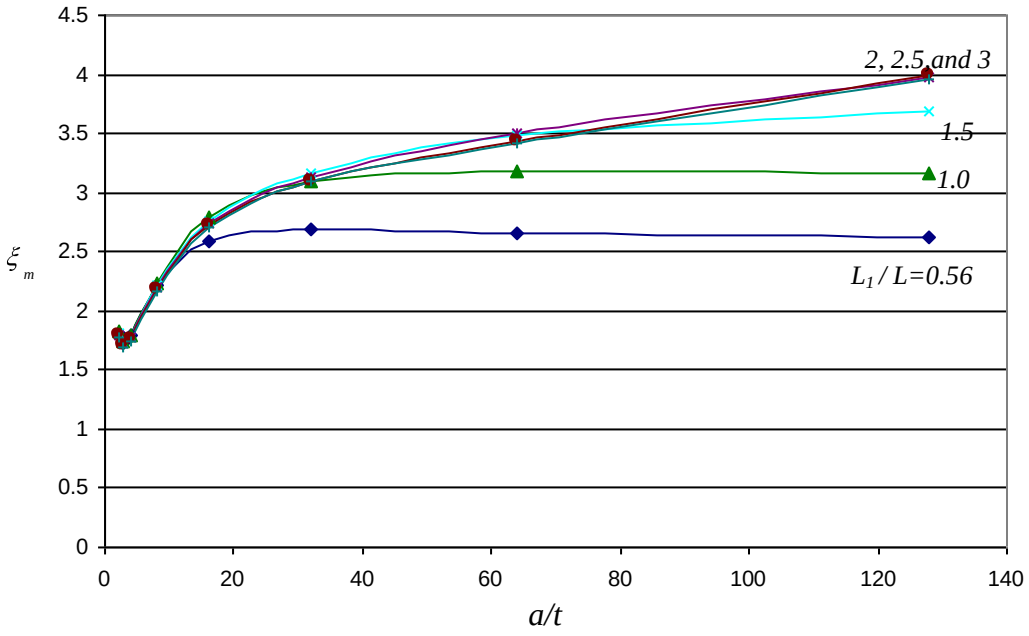

Figure 11: Effect of the length ratio L_1 / L (longitudinal member, $L_1 = L_2$ and cross member L) in terms of the thin-wallness ratio (*a/t*) on ξ_m

From the analysis, it was observed that if L_1 and L_2 are roughly equal to *L*, the length of the longitudinal member does not affect the stress amplification parameter, ξ_m, up to thin-wallness ratios of approximately $a/t = 30$. For T-joints with L_1 and L_2 approximately

higher than $2L$, the plots of ξ_m remain nearly unchanged, indicating that longer longitudinal members have a very little affect on the stress concentrations at the connection.

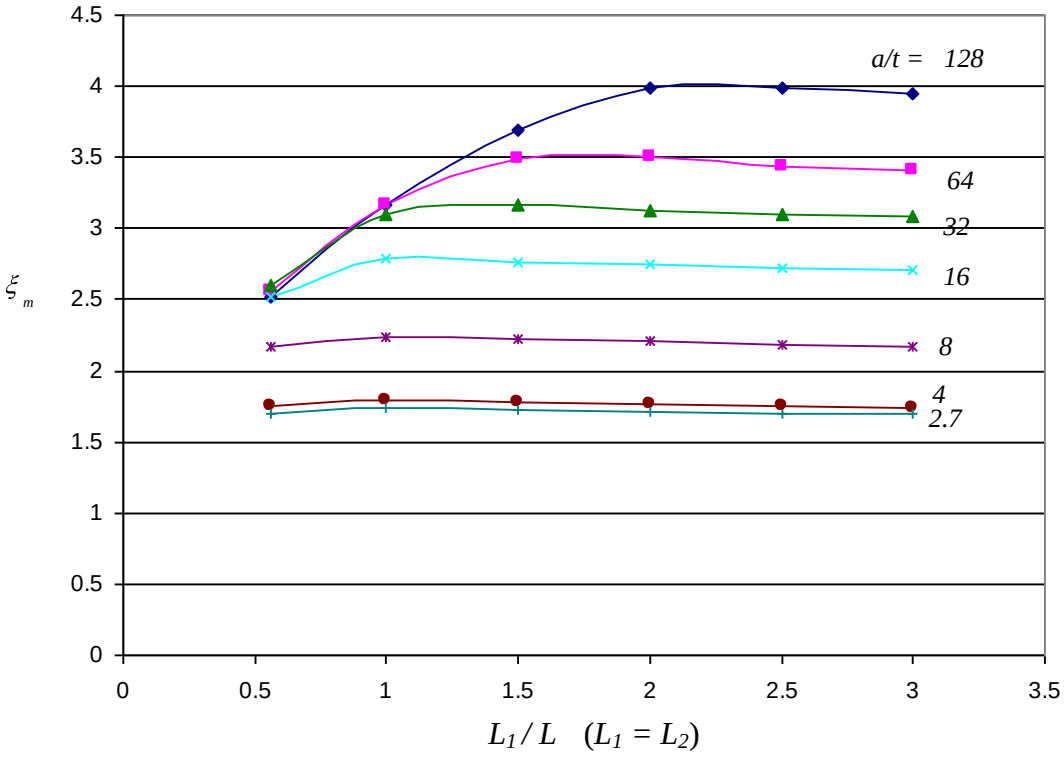

Figure 12: Membrane stress amplification parameter ξ_m versus length ratio L_1 / L for different thin-wallness ratios (a/t)

More conclusions can be drawn if the same results are presented as in Figure 12. It can be observed that for a certain value of the thin-wallness ratio, the shape of the ξ_m plots do not depend any more on the length of the longitudinal member. Clearly as the connection becomes more and more thin-walled, the effects of the length of the longitudinal member become more significant. It should be noted that for solid sections (i.e., beam elements) the length of the longitudinal member does not affect the stress distribution at the connection.

Similar to the membrane stress amplification parameter ξ_m, the bending stress amplification parameter ξ_b depends on both the thin-wallness ratio and the length of the longitudinal member of the T-joint. Analogous to ξ_m shown in Figure 11, Figure 13 depicts the effect of the longitudinal member's length on ξ_b. It should be noted that for higher L_1/L ratios, the values of ξ_b increase with the thin-wallness.

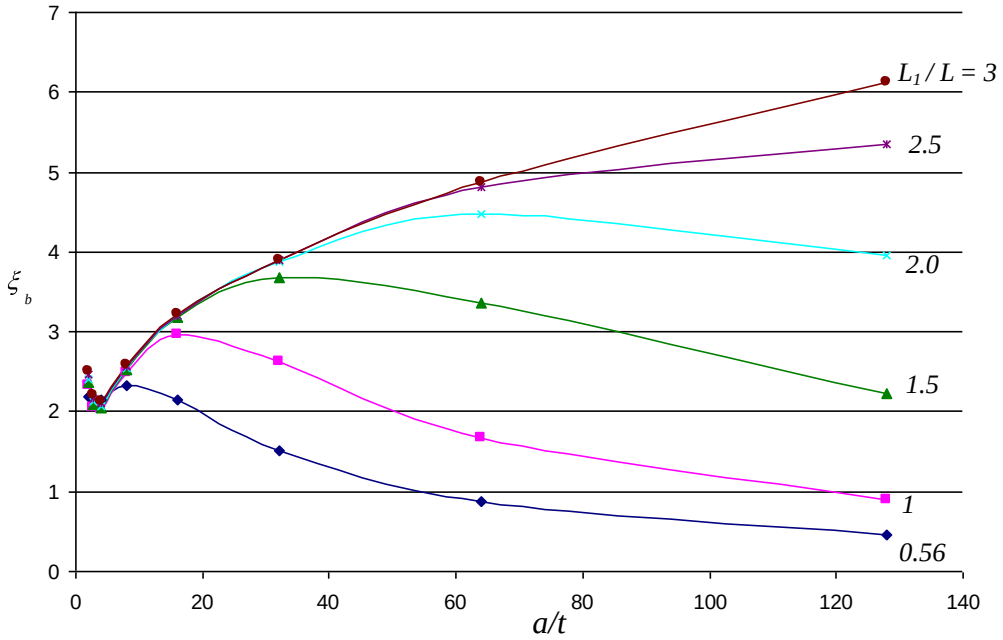

Figure 13: Bending stress amplification parameter, ξ_b, versus thin-wallness ratio (a/t) for different values of length ratio L_1 / L ($L_1 = L_2$)

3.5 Comparison of the OPB and IPB loading conditions

The previous sections of this paper analyzed the stress amplification parameters for T-joints subjected to OPB loading conditions. The local deformation and the stress concentrations in a T-joint due to the in-plane bending (IPB) conditions were discussed in [1]. If $L_1 = L_2 = 0.56L$ the parameters ξ_m for these two cases are presented in Figure 14. It is observed that the effect of IPB loads is much greater than those of the OPB loads for

this case. It was shown in section 3.4 that for OPB conditions, the parameter ξ_m is not only dependent on the thin-wallness ratio (*a/t*) but also on the length of the longitudinal member. As the length of the longitudinal member increases, the parameter ξ_m also increases. For T-joints with L_1 and L_2 approximately higher than 2*L*, the plots of ξ_m remained nearly unchanged. The highest magnitude of the stress amplification parameter ξ_m was for cases where $L_1 = L_2 > 2L$. As a point of interest, for the case of $L_1 = L_2 = 3L$, the parameter ξ_m for the out-of-plane bending load is also presented in Figure 14. It can be seen that the stress amplification parameter ξ_m (*In-plane*) is generally about 60% lager than that of ξ_m (*out-of-plane*) for longer cross members ($L \geq 1.8L_1$). For shorter cross members the value of ξ_m (*out-of-plane*) increases. In the case of $L_1 = L_2 = 3L$ or $L \approx 0.3L_1$, ξ_m (*out-of-plane*) and ξ_m (*In-plane*) are close to one another for very thin-walled T-joints (i.e., a/t ≈ 130).

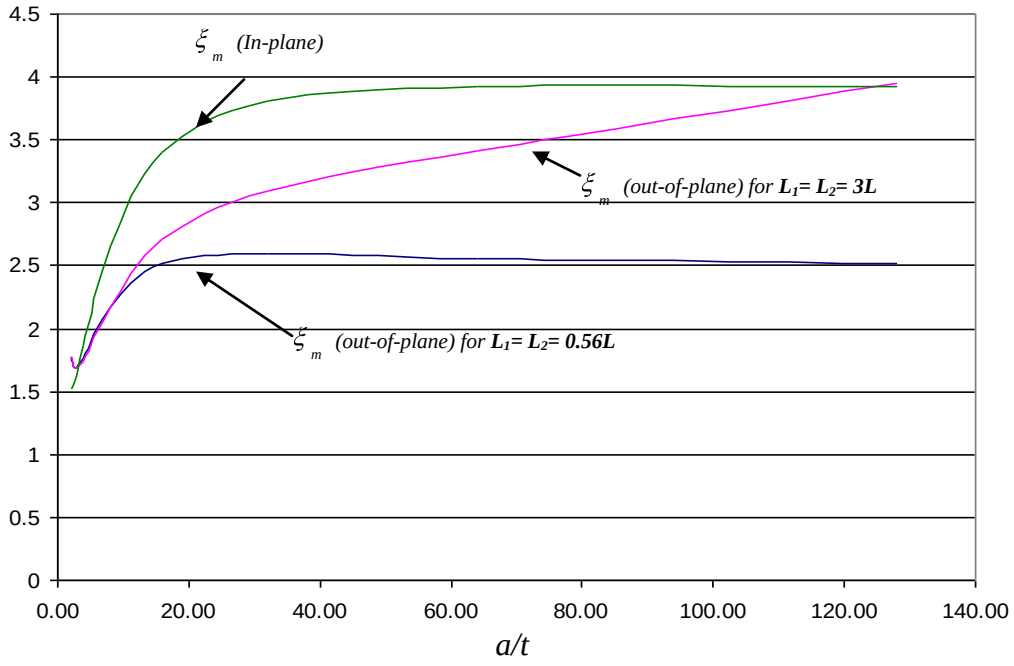

Figure 14: Membrane stress amplification parameters for IPB and OPB loads

3.6 Geometric asymmetry of the longitudinal member

The thin-walled T-joints considered up to this point have all been symmetric, that is $L_1 = L_2$. For $L_1 \neq L_2$, the stresses at corners B and C at the top of the connection (see Figure 15a) are different and consequently, two membrane stress amplification parameters ξ_m^B and ξ_m^C can be defined as:

$$\xi_m^B = \left| \frac{(\sigma_m^x)_{\max}^B}{\sigma_{nom}} \right| \quad \text{and} \quad \xi_m^C = \left| \frac{(\sigma_m^x)_{\max}^C}{\sigma_{nom}} \right| \tag{7}$$

These parameters were determined for $1 \leq L_2 / L_1 \leq 4$, where $L_1 = 0.56\,L$ and are shown in Figures 15b and 15c.

The results presented can be interpreted as follows. In asymmetric T-joints one portion of the connection must carry an additional load (i.e., $M_1 > M/2$). Consequently, as the ratio of L_2 / L_1 increases, the stress amplification parameter for corner B decreases while that of corner C increases. This can be observed in Figure 15b. These results are replotted in Figure 15c in terms of the thin-wallness ratio *a/t*. Note that when the ratio of $L_2 / L_1 = 1$, ξ_m^B and ξ_m^C coincide with each other.

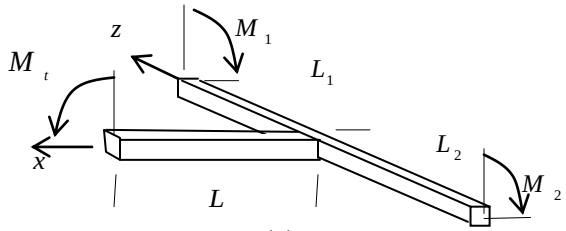

(a)

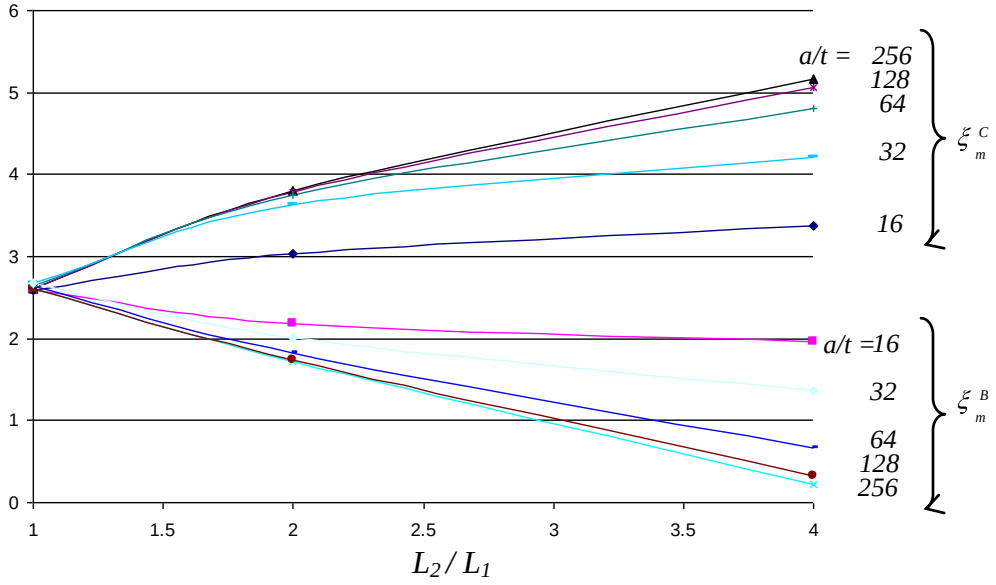

(b)

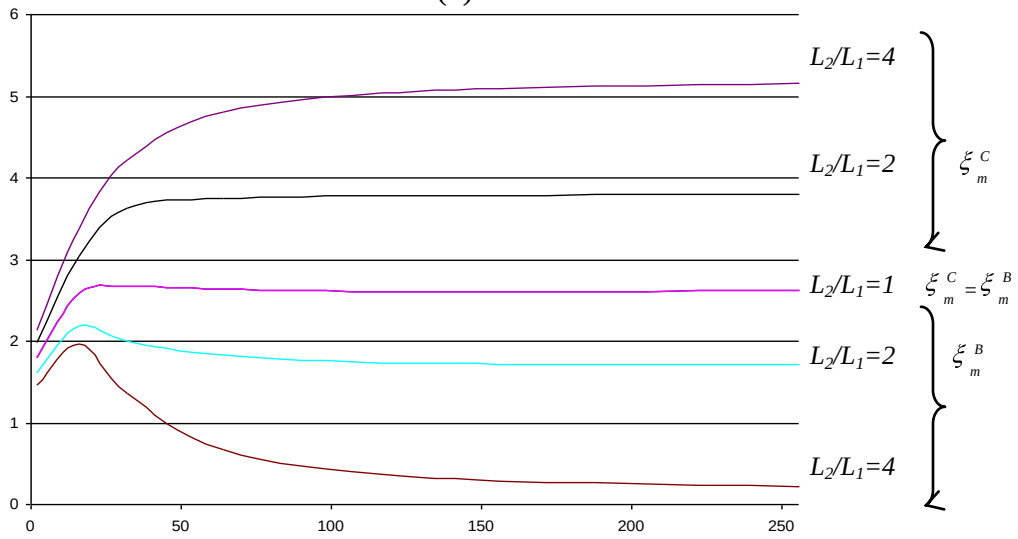

(c)

Figure 15: Effects of asymmetry (the L_2 / L_1 ratio), and the thin-wallness ratio (a/t) on the membrane stress amplification (or reduction) parameters ξ_m^B and ξ_m^C .

4.0 The bending stiffness of the T-joint

As shown in Figure 4, at a sufficient distance (approximately equal to *a*/2) away from the connection, the tubes in T-joints subjected to OPB loads behave like beams. This can be used to identify the joint's rotational (out-of-plane bending) stiffness using the following approach. The total displacement under the moment M can be decomposed into two parts: a portion due to the bending of the tubes as beams, and another portion due to local deformations at the joint, that is:

$$u_M = u_{beam} + \phi L \tag{8}$$

The total displacement u_M for an assumed *a*/*t* ratio can be calculated from the FEM model (using either solid or shell elements). Displacement u_{beam} can be obtained if the tubes are modeled as beams (*beam4* elements were used here) with the bending stiffness EI_z rigidly connected at *T*.

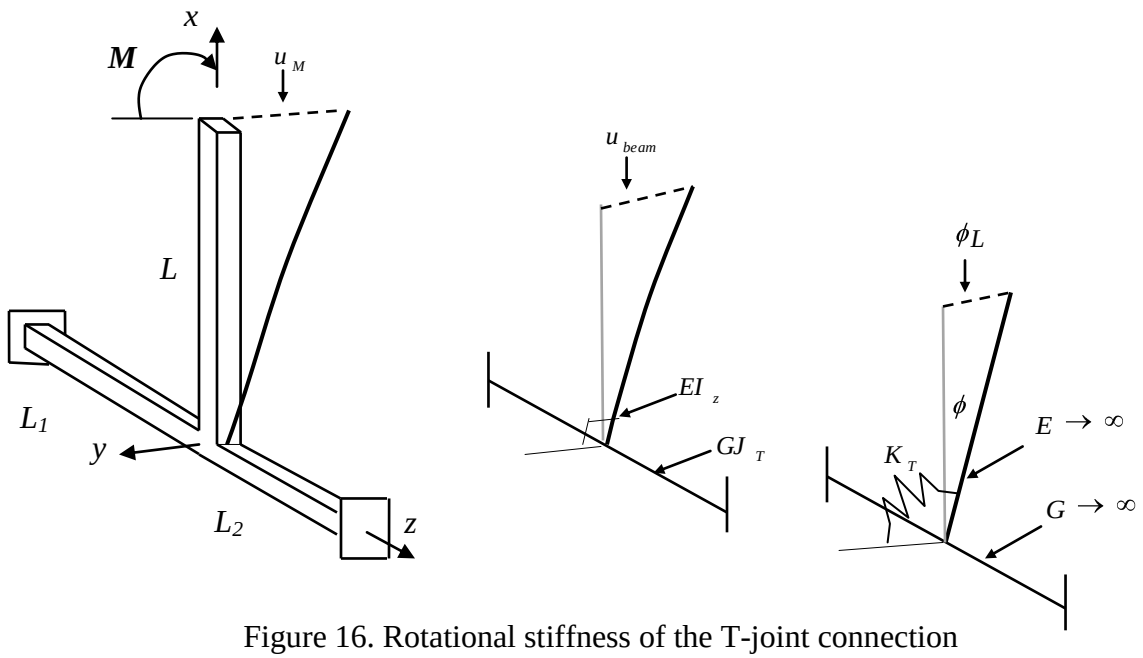

Figure 16. Rotational stiffness of the T-joint connection

Therefore, the rotational stiffness of the joint can be defined as:

$$K_T = \frac{M}{\phi} = \frac{ML}{u_M - u_{beam}} \tag{9}$$

Note that both u_M and u_{beam} vary with the thin-wallness ratio a/t as depicted in Figure 17.

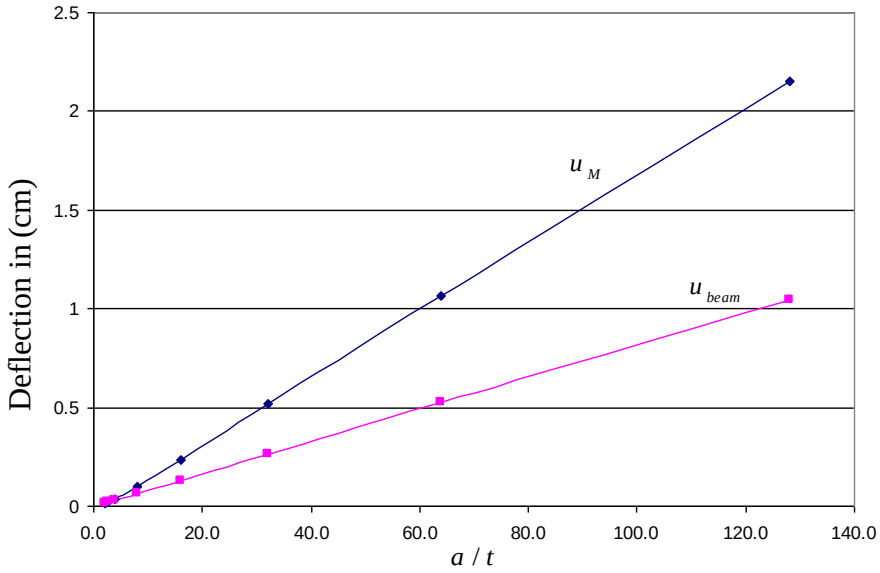

Figure 17: Effects of the thin-wallness ratio a/t on the displacements u_M and u_{beam} for $L_1 = L_2 = 0.56L$

Based on equation 9, the calculated values of the rotational stiffness K_T for $L_1 = L_2 = 0.56L$, and the range of the thin-wallness ratios (a/t = 2.1 to 128) are plotted in Figure 18.

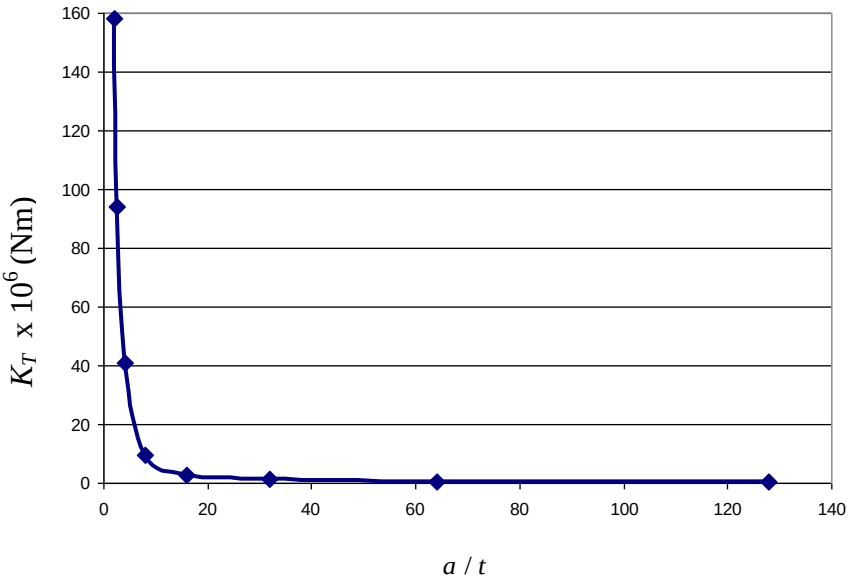

Figure 18: Effects of the thin-walness ratio a/t on the rotational stiffness K_T of the T-joint for OPB loading.

It is convenient to interpret the stiffness K_T in relations to the beam stiffness EI_y using the following reasoning. Assume that the tubes in the vicinity of the T-joint are modeled by the beam elements as depicted in Figure 19.

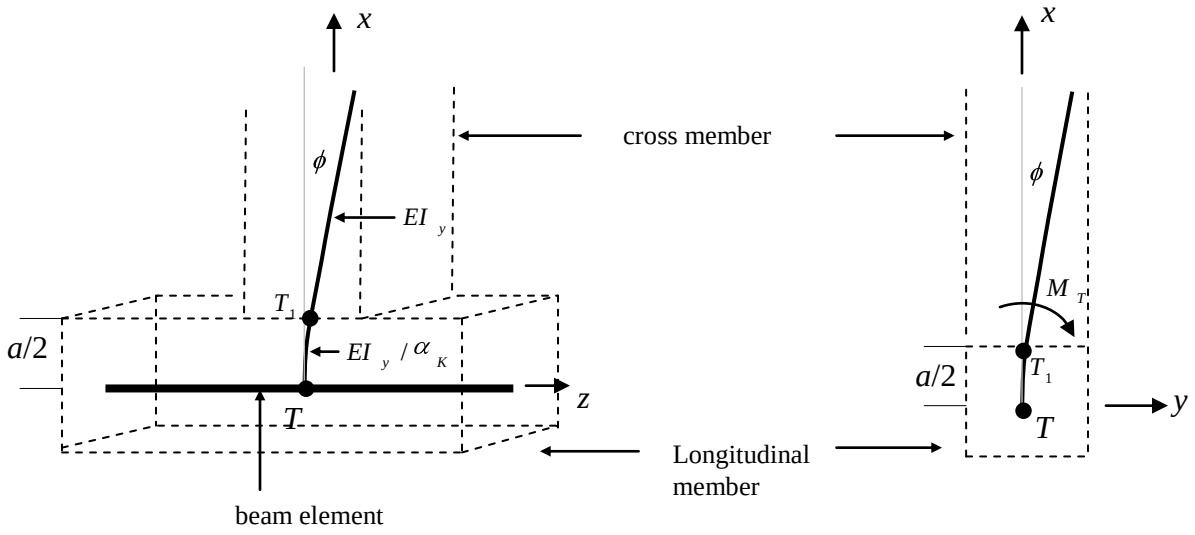

Figure 19. The bending stiffness reduction coefficient

The rotational stiffness of the connection can be embedded in the element TT_1 of length $a/2$ in the form of the *bending stiffness reduction parameter* α_K (i.e., the bending stiffness of this element is EI_y/α_K).

Note that for this element $\phi = \frac{M_T\, a/2}{EI_y}\alpha_K$. Substituting into (9) renders:

$$K_T = \frac{EI_y}{a/2}\frac{1}{\alpha_K} \qquad \text{or} \qquad \alpha_K = \frac{EI_y}{a/2}\frac{1}{K_T} \tag{10}$$

The values of α_K obtained for different a/t ratios are plotted in Figure 20.

Parameter α_K permits inclusion of the local deformation at the T-joint without actually using complex models such as those shown in Figures 3 and 4. Instead, the joint's stiffness characteristics can be recreated by using one modified beam element TT_1 as shown in Figure 19. This should substantially simplify any static (and dynamic) FE

analysis of T-joint connections subjected to OPB loading conditions, which is numerically verified in the next section.

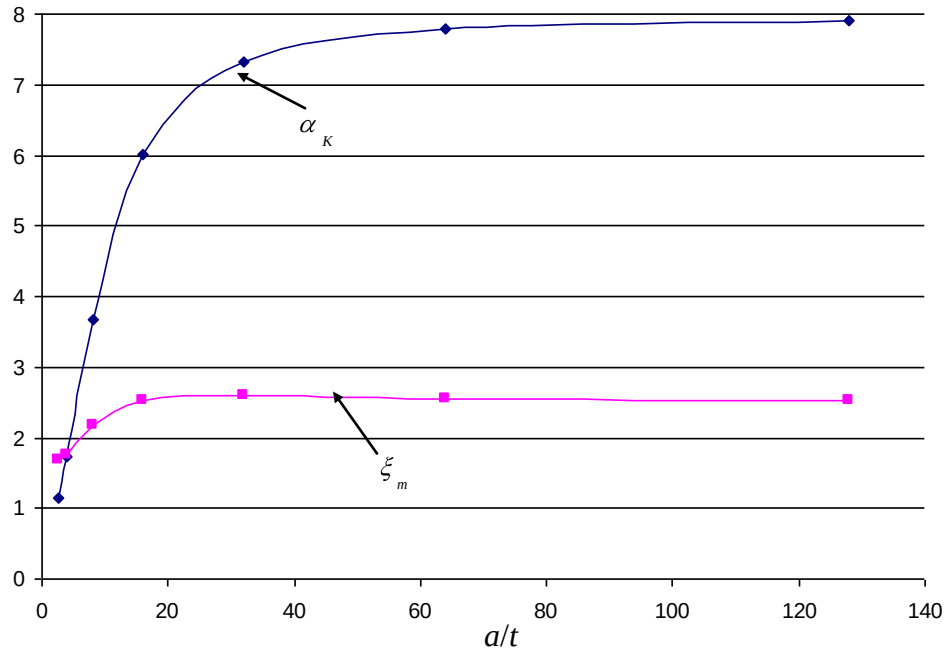

Figure 20: Bending stiffness reduction parameter, α_K, and membrane stress amplification parameter, ξ_m, for $L_1 = L_2 = 0.56L$

5.0 Examples for the application of the stress amplification and stiffness reduction parameters

In this section, two numerical examples employing the stress amplification and stiffness reduction parameters are considered. The first example demonstrates the effectiveness of this approach for a static stress analysis, and the second for dynamics where the out-of-plane free vibrations of the frame are considered. A thin-walled frame with one T-joint is considered for both cases.

5.1 Statics example

For the static stress analysis case, the thin-walled T-joint with the dimensions as shown in Figure 21 is considered. For this frame the thin-wallness ratio a/t=16 and the length of

the longitudinal member is $L_1 + L_2$ where $L_1 = L_2 = 0.56L$. For such dimensions, the stress amplification parameter is $\xi_m = 2.52$ for OPB loading conditions (read from Figure 20). The structure is loaded by a moment M_1 and a force F_1 (both loads subject the connection to out of plane bending loads as shown in Figure 21). For the boundary conditions, the displacements of the center of the frame at the ends D and G are fixed, while the end H is free. The calculated reaction forces at D and G and the maximum stresses at the joint were recorded for two loadings:

Case 1: F_1 =7,793N and $M_1 = 0$

Case 2: F_1 =7,793N and M_1 = 2410 N.m.

The frame was first modeled by 30 beam elements (180 DOF) as shown in Figure 21a. The stiffness of the element between nodes 1 and 22 was reduced by 2.52. Then the frame was modeled by shell elements (this model had over 36000 DOF). The reaction forces/moments and the maximum stress from both models are listed in Table 3. The bending moment in node 22 of the beam model is used to determine the nominal bending stress for this T-joint.

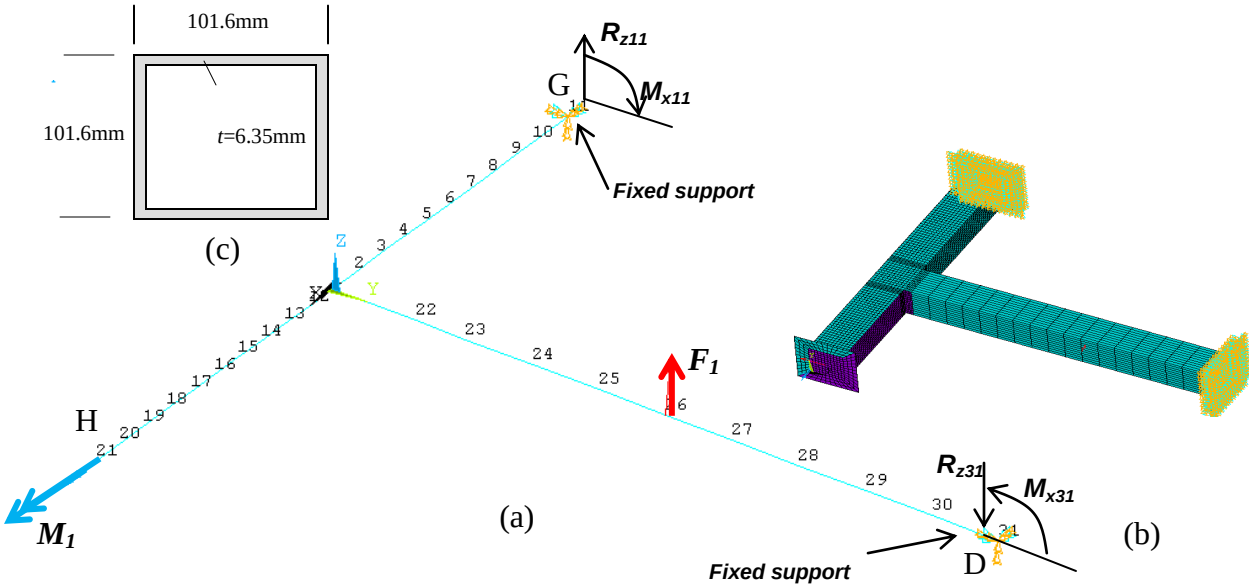

Figure 21: Static example of a thin-walled frame modelled by: a) beam elements, b) shell elements, and c) frame's cross-section.

Table 3: Comparison of modified beam and shell models					
Case 1	R_{z11}**(N)**	M_{x11}**(N.m.)**	R_{z31}**(N)**	M_{x31}**(N.m.)**	**Max membrane Stress (Mpa)**
Beam Model (modified)	3949.5	942.9	3949.5	137.6	42.1
Shell Model	3928.3	944.4	3928.3	131.0	39.1
Percent error (%)	0.5%	- 0.2%	0.5%	5%	7.7%
Case 2					
Beam Model (modified)	1661.9	979.7	9454.7	828.3	410.6
Shell Model	1946.5	952.5	9739.4	916.7	384.4
Percent error (%)	-14.6%	2.8%	-2.9%	-9.6%	6.8%

The results presented in Table 3 show that in general a very good agreement exists between the results obtained from the shell model and those obtained from the modified beam model. Using the stress amplification parameter, the error in the maximum membrane stresses for cases 1 and 2 are 7.7% and 6.8% respectively. As a point of interest, if the element between nodes 1 and 22 is not modified then the error in the maximum membrane stress increases to 56% (σ_{max}=18.6MPa) for case 1, and 53%

(σ_{max} =182MPa) for case 2. Similar observations were also made in the case of reaction forces/moments. For instance, if no stress amplification is used then the reaction error in R_{z31} increases from 0.5% to about 10% (R_{z31} =4,309.6N) for case 1. For case 2, the reaction error in M_{x31} increases from 2.8% to about 15% (M_{x31} = 808N.m.). Similar increases in the percentage errors were obtained for the other reaction forces/moments.

The stiffness reduction parameter can be used to obtain the deflections of the above frame as well. However, for the loading and imposed boundary conditions of the frame (depicted in Figure 21) these deflections are relatively small. To better demonstrate the effectiveness of the stiffness reduction parameter, a third case with different loading and boundary conditions is considered. For this case, the displacements of the center of the frame at the ends H and G are fixed, while the end D is free to move. A force, F_2 =17,793N and a moment M_2 = 2410 N.m. were applied to end D (shown in Figure 22). It should be noted that the dimensions of the frame are kept the same as that of the previous example.

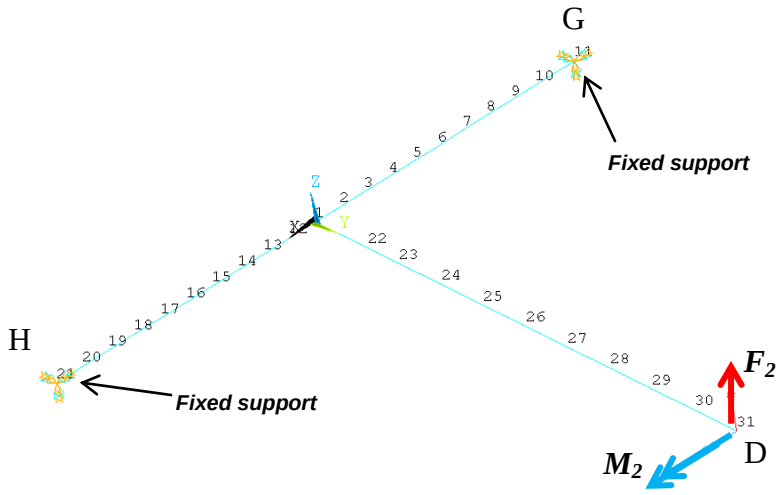

Figure 22: Thin-walled frame subjected to the action of force F_2 and moment M_2

For the above frame with the thin-wallness ratio of *a/t*=16 and the length of the longitudinal member of $L_1 + L_2$ where $L_1 = L_2 = 0.56L$, the stiffness reduction parameter is equal to approximately $\alpha_K = 6.1$ (see Figure 20). The deflection of node 31 calculated using the shell model is 2.9mm and for the modified beam model is 2.6mm (10% error). If the element 1-22 is not modified then the displacement of node 31 is 1.6mm (45% error).

5.2 Dynamic example

In addition to the static stress analysis, the out-of-plane free vibrations of the frame were considered. The same frame with dimensions as that shown in Figure 21 is employed. The boundary conditions are those depicted in Figure 22. The displacements of the center of the frame at the ends H and G are fixed, while the end D is free to move.

The frequencies of the first two out-of-plane vibration modes for the shell model were 288.6Hz and 1396.6Hz, respectively. For the beam model with modified element 1-22 (i.e., stiffness reduction parameter $\alpha_K = 6.1$) the same frequencies were 296.9Hz (2.9% error) and 1460.9 (4.6% error) respectively. If the element 1-22 was not modified, then the first natural frequency would become 376.9Hz (30.6% error), while the second frequency would be 1508.0Hz (8.0% error).

The effectiveness of the presented approach is clear for both the static and dynamic examples. It should be noted that the FE model of the frame made of beam elements is substantially easier to build and operate than any model made of shell or solid elements. The number of DOFs of the beam model in Figure 21a is about 200 times smaller than the corresponding model in Figure 21b (for the static analysis the beam model can further be reduced by using only four elements between the nodes 1-11, 1-21, 1-22, 22-31).

6. Conclusions

This paper proposed an accurate and computationally efficient approach to model out-of-plane loaded frames made of hollow square tubes connected by T-joints. Detailed FE studies were performed using shell and solid elements to analyze the transfer of the out-plane-bending moment from the cross member to the longitudinal member of such joints. The local effects at the connection of the T-joints with geometric symmetry were characterised by the stress amplification parameters (ξ_m, ξ_b) and the stiffness reduction parameter α_K, which were determined in terms of the thin-wallness ratio a/t and the length of the longitudinal member. Effects of geometric asymmetry on the stress amplification and stiffness reduction parameters were also considered. The stiffness reduction parameter allows modelling the T-joint by one beam element with modified bending stiffness. Since away from the joint the tubes behave like beams, the entire frame can be effectively modeled by simple beam elements with the reaction forces/moments, deflections, and the natural frequencies of vibrations calculated accurately. Then, using the forces from the modified beam model, the maximum stress in the frame can be calculated by applying the stress amplification parameters. As demonstrated, such an approach is capable of rendering the results that are similar to the results of the FE models consisting of much more complicated shell or solid elements. These models however, include several thousands more degrees of freedom and are much more difficult to construct and operate.

References

[1] Moazed R, Szyszkowski W, Fotouhi R. The in-plane behaviour and FE modeling of a T-joint connection of thin-walled square tubes. *Journal of Thin-Walled Structures* (2009); 47(7): 816-825.

[2] Hong K, Hyeon S, Dae W, and Young K, New accurate efficient modeling techniques for the vibration analysis of T-joint thin-walled box structures. *International Journal of Solids and Structures* (2002); 39(11): 289302909.

[3] Hong K, and Young K, One-dimensional analysis of thin-walled closed beams having general-sections. *International Journal for Numerical Methods in Engineering* (2000); 49(5): 653-668.

[4] Kim, J.H., and Kim, Y.Y., Analysis of thin-walled closed beams with general quadrilateral cross sections. *Transactions of the ASME. Journal of Applied Mechanics* (1999); 66(4): 904-912.

[5] Shao Y-B, Lie S-T, Chiew S-P, Huang Z-W. Evaluation of geometrical effect on stress distribution for tubular T-joints under axial load. *International Journal of Space Structures* (2006); 21(2): 77-91.

[6] Shao Y-B. Geometrical effect on the stress distribution along weld toe for tubular T- and K-joints under axial loading. *Journal of Constructional Steel Research* (2007); 63(10): 1351-60.

[7] Pang H-J, Lee C-W. Three-dimensional finite element analysis of a tubular T-joint under combined loading. *International Journal of Fatigue* (1995); 17(5): 313-320.

[8] Boge F, Helland T-K, Berge S. Low cycle fatigue of T-tubular joints with out-of-plane bending loading. *Proceedings of the International Conference on Offshore Mechanics and Arctic Engineering* (2007); v(4): 107-115.

[9] Waalen J, Berge S. Low cycle fatigue of T-tubular joints with in-plane bending loading. *Proceedings of the International Conference on Offshore Mechanics and Arctic Engineering* (2005); v(3): 211-219.

[10] Mashiri F-R, Zhao X-L, Grundy P, Tong L. Fatigue design of welded very thin-walled SHS-to-plate joints under in-plane bending. *Journal of Thin-Walled Structures* (2002); 40(2): 125-151.

[11] Mashiri F-R, Zhao X-L. Stress concentration factors and fatigue failure under in-plane bending. *Journal of Thin-Walled Structures* (2006); 44(2): 159-69.

[12] Mashiri F-R, Zhao X-L, Grundy P. Stress concentration factors and fatigue failure of welded T-connections in circular hollow sections under in-plane bending. *International Journal of Structural Stability and Dynamics* (2004); 40(3): 403-422.

[13] Bian L-C, Lim J-K. Fatigue strength and stress concentration factors of CHS-to-RHS T-joints. *Journal of Constructional Steel Research* (2003); 59(5): 627-640.

[14] Van der Vegte G-J, Makino Y. Ultimate strength formulation for axially loaded CHS uniplanar T-joints. *Journal of Offshore and Polar Engineering* (2006); 16(4): 305-312.

[15] Jun L, and Jin X, Response of flexure-torsion coupled composite thin-walled beams with closed cross-sections to random loads. *Mechanics Research Communications* (2005); 32(1): 25-41.

[16] Fung T-C, Soh C-K, Chan T-K. Stress concentration factors of doubler reinforced tubular T joints. Journal of Structural Engineering (2002); 128(11): 1399-1412.

[17] Lee M-K, Llewelyn-Parry A. Offshore tubular T-joints reinforced with internal plain annular ring stiffeners. Journal of Structural Engineering (2004); 130(6): 942-951.

[18] Herion S, Mang F, Puthli R. Parametric study on multiplanar K-joints with gap made of circle hollow sections by means of the finite element method. In: Proceedings of the 6th international offshore and polar engineering conference. IV. 1996, p. 68–73.

Chapter 4. Welded T-joint connections of square thin-walled tubes under a multi-axial state of stress

ABSTRACT

T-joint connections are used extensively in industry as parts of machine components and structures. The T-joint connection is typically constructed through the welding of its tubular members, with significant stress and strain concentrations occurring at the toe of the weld under loadings. In this paper, a welded T-joint connection of square hollow section (SHS) tubes subjected to a multi-axial state of stress is examined both numerically and experimentally. The hot spot strains and stresses in the connection are determined through a detailed finite element (FE) analysis of the joint. The weld geometry is accurately modelled using FE. To model the weld, several full-scale welded T-joints were cut at the connection to obtain the size and depth of penetration of the weld. For the experimental study, a test rig with a hydraulic actuator capable of applying both static and cyclic loadings is designed and used. Strain gauges are installed at several locations on the joint to validate the FE model. The verified FE model is then used to study the through-the-thickness stress distributions of the tubes. It is shown that the membrane stresses which occur at the mid-surface of the tubes remain similar regardless of the weld geometry. The weld geometry only affects the bending stresses. It is also shown that the stress concentrations are highly localized at the vicinity of the weld toe. At a distance of about ½ of the weld thickness from the weld-toe, the effect of the weld geometry on the bending stresses becomes insignificant as well. To reduce the stress concentrations at the T-joint, plate reinforcements are used in a number of different arrangements and dimensions to increase the load carrying capacity of the connection.

Keywords: hollow square tubes, welded connection, finite element analysis, hot spot stresses, strain gauges.

3.0 Introduction

In the design of machine components, tubular T-joints are used extensively in industrial applications as load carrying members. These members are usually characterized by their 'thin-wallness' which is defined as the ratio of the width or diameter of the tube to its thickness. As the 'thin-wallness' ratio increases, the stress distribution at the connection between the two members becomes increasingly uneven with high stress concentrations occurring at some points. These stresses, which occur locally at the connection, can be many times bigger than the nominal stresses in the connecting members. The stress concentration factors (SCFs) are the ratio of the local stresses at the connection to the nominal stresses occurring away from the joint on the connecting members. The hotspot stresses are those which are obtained by the extrapolation of the local stresses to the perceived failure-critical points (such as weld toes). The T-joint connection must be designed and reinforced in such a way to allow for the smooth transfer of the forces and bending moments from one member to another; minimizing the hot spot stresses at the connection.

Many researchers have studied the behaviour of tubular T-joints under different types of loadings. Shao et al. [1-2] examined the geometrical effect on the stress distribution for circular hollow section (CHS) T/K-joints under axial loading. Using finite elements, parametric equations were proposed to relate the SCFs at the connection to certain geometrical parameters of the tubes, such as diameter and tube thickness. The effects of boundary conditions, chord length and chord end conditions on the ultimate strength of axially loaded CHS planar T-joints were considered in [3]. The SCFs and fatigue failure of T-joints for CHS-to-CHS, CHS-to-plate and square hollow section (SHS)-to-plate under in-plane bending (IPB) conditions were examined in [4-6].

Three dimensional finite element (FE) studies to determine the hot spot stresses for CHS-to-CHS T-joints subjected to the action of axial, IPB and out of plane bending (OPB) conditions were performed in [7]. Rectangular hollow section (RHS)-to-CHS T-joints subjected to axial and in-plane bending loads were experimentally studied in [8-10]. In these studies, both static and cyclic loadings were applied to the joints and the hot spot stresses and the corresponding SCFs were determined. An extensive FE study to obtain characteristic parameters (such as length, thickness, etc.) for the stress distribution at the intersection of several tubular joints were presented in [11-12].

Experimental and numerical studies on the increase in the load carrying capacity of CHS T-joints reinforced with the application of doubler or collar plates were performed in [13-15]. The SCFs of doubler plate reinforced T-joints subjected to axial tension/compression, IPB and OPB were considered. The SCFs of the reinforced joints were determined to be lower than those for the unreinforced joints. Offshore tubular T-joints reinforced with internal plain annular ring stiffeners subjected to brace compression were studied in [16]. An experimental study on the reinforcement of plate-to-RHS T-joint connections was performed by [17]. Plates were welded to the faces of the chord members and the RHS braces to stiffen the joint.

In this paper, the behaviour of a SHS T-joint subjected to a multi-axial state of stress with and without reinforcement plates is considered. A detailed FE analysis of the joint using 3D solid elements is performed. The hot spot stresses and strains are determined using FE. One of the contributions of this research work is the experimental verification of the FE model developed for analysis of welded SHS T-joints subjected to a multi-axial state of stress. A test rig with a hydraulic actuator, capable of applying both static and cyclic

loadings, has been designed and used in the experiments. Several strain gauges have been installed around the T-joint connection in order to verify the validity of the FE model. The good agreement between the FE analysis and experimental results and the precise modelling of the welded T-joint will be discussed. It is believed that this research work should contribute to the understanding of the effects of the weld geometry on the bending and membrane stresses. It will be shown that the membrane stresses are nearly unaffected by the presence of the weld. The bending stresses on the other hand are amplified by existence of welds; however these amplifications are highly localized and typically become insignificant within a distance of approximately ½ of the weld thickness away from the weld-toe. To reduce the stress concentrations, internal and external reinforcements for the T-joint are also considered.

4.0 Numerical modelling of a tubular T-joint

The FE modelling of welded tubular joints is a very challenging as well as delicate task due to the complicated 3-D profile of the weld. Previously, many researchers have ignored the modelling of the weld due to the difficulties that exist in the accurate modelling of the weld profile. These researchers mainly adopted shell elements for modelling of the tubes' structure. However, two main problems arise in using shell elements for modelling tubular joints: 1) How to model the 3-D weld profile accurately with shell elements, and 2) shell elements (representing mid-surfaces of the structure) assume a linear stress distribution through the thickness of the tubes and do not take into account the physical thickness of the members. For these reasons, in recent years, researchers have used solid elements to model the tubes as well as the weld geometry. Herion et al [18] found that solid elements can more accurately model the welded

connection than shell elements. That study suggested that the best results are obtained by using solid elements for the modelling of both the tubes and the weld profile.

Due to the inability of the shell elements to accurately model the interaction between the tubular members and the weld, and the proven effectiveness of solid elements for the modelling of welded joints, solid elements have been used for modelling both the tubes and the welds in this study. The numerical modelling of the weld and the tubular members is performed using the commercial finite element package, ANSYS [19]. The developed FE model is based on the assumption of linear elasticity and small strains/displacements. Linear solid elements (8-noded) with three translational degrees-of-freedom at each node were used to model the tubes. Hexahedral element geometries were used for this purpose. The weld was modelled with tetrahedral quadratic solid elements (10-noded). It should be noted that, as a check for the element compatibility between the lower and higher order elements in the FE model, the entire structure was modelled with quadratic solid elements as well. It was observed that with the meshing (i.e., element sizes) employed in this study, the results (stresses/displacements) for quadratic solid elements were very similar to the results for the linear solid elements. In general, 4 solid elements were employed to model the tubes' thickness (shown in Figure 1). It should be noted that when quadratic solid elements are used, shear locking is not a concern. However, for the 8-noded linear solid elements, extra displacement shapes were included for shear locking considerations. The shape functions for this element with the extra displacement shapes are included in Appendix A.

The mesh generation in any finite element analysis (FEA) is crucial as it significantly affects the accuracy of the results. A sub-zone mesh generation technique is used for the

numerical modelling in this study. According to this approach, the meshed structure can be divided into 3 regions based on the stress gradients and the computational time required: 1) refined mesh zones, 2) coarse zones (or the far field zones), and 3) transition zones. The meshing of these zones for the FE modelling of the tubes is shown in Figure 1. The refined mesh zone consists of the regions very close to the connection of the tubes including the weld toe. The mesh in this region must be very fine to capture the true state of stress and the stress concentrations at the connection. Part of this region is enlarged and presented in Figure 1b. Different mesh densities should also be used in this region to verify the convergence of the FE results. Coarse zones are regions far away from the T-joint connection. The mesh density in these regions has no or insignificant effect on the stresses at the connection. Relatively large element sizes can be used in these regions as can be seen in Figure 1. The transition zone connects the refined and coarse mesh zones. Using the sub-zone mesh generation technique is very beneficial in significantly reducing the number of degrees-of-freedom of the FE model.

Measurements of the weld size (i.e., location of the weld toe, height and width of the weld) have also been taken from the actual samples. These measurements were used in the FE models to accurately model the weld. Due to the local notch stress concentrations, the weld toe is predominately the location for the maximum stresses, causing fatigue cracks and plastic deformation to be initiated at these locations. For this reason, the profile of the weld can be somewhat arbitrary as long as the location of the weld toe, the height, width and depth of penetration of the weld are approximately the same as the real welded samples [2]. The modelled weld is presented in Figure 2.

It should be noted that full penetration welds were modelled for the FE analysis. To ensure that the same depth of weld penetration exists in the actual welded samples, several T-joints were cut along the lines A1 and A2 as shown in Figure 3a. Figures 3b and 3c depict the weld profile in the actual samples as seen from the interior of the T-joint. It can be observed that the full penetration welds in the FE model provide a good resemblance of the welds in the actual samples.

The weld toes have sharp corners, as they were not ground. It should be noted that with the existence of sharp corners at the weld toes, the elastic stress is theoretically infinite at these locations and the hot spot stress approach is a technique used to obtain a realistic finite value. Determination of the hot spot stresses requires the extrapolation of the stresses on the surface of the tubes and does not take into account such factors as the through the thickness stress gradients. A more detailed analysis of the T-joint can be based on fracture mechanics (F-M) methodology taking into account the crack growth and the actual stress gradients. The failure criteria then would be based on the values of the critical stress intensity factors and the material fracture toughness. The F-M approach requires much more computational effort and is better suited for the analysis of joints where cracks have already occurred. Another technique that has appeared more recently in the literature is the "Dong's method" [20] which defines a mesh insensitive or "equivalent-structural stress" based on the assumption of linearly elastic material. In this technique the stresses at the weld toe are broken down into the membrane, bending, and a non-linear component due to the local notch effect. This technique requires the additional computational effort of post processing the FE results. It is also worthwhile to mention that in certain locations along the weld toe where the maximum stresses occur, the

material typically does not behave entirely elastic anymore. This non-linear effect is not taken into account if the developed FE model is based on linear elasticity.

Currently, the hot-spot stress concept, when effectively linked to the finite element results, is considered to be an efficient methodology for engineering design in industry [21]. In this paper, once the weld was modelled accurately, the stresses at the weld toe (i.e., hotspot stresses) were calculated by linearly extrapolating the stresses at the elements close to the weld as has also been done in [15-17].

3.0 Experimental test fixture

In order to verify the validity and accuracy of the developed FE model for the prediction of the stresses and strains along the weld toe of the T-joints, an experimental test rig has been designed for the testing. The T-joint specimens are identical to those used in many types of agricultural machinery. These samples are welded using the inert metal gas welding (MIG) process with full penetration welds according to the AWS specifications [22]. For the preparation of the samples, three 6.35mm (1/4 inch) thick end plates are welded to the tubes to facilitate the specimen installation as well as load application. A schematic diagram of the T-joint is given in Figure 4. The T-joints are fabricated from structural steel with a yield and an ultimate tensile strength of 540MPa of 600MPa, respectively.

The test rig that has been designed for the testing of the T-joints is shown in Figure 5. For the application of the load, a hydraulic actuator capable of applying both static and cyclic loadings of up to 94000N (tension-compression) was employed. The hydraulic actuator was connected to the test fixture through the use of a coupler. In order to ensure the accuracy of the applied loads, a pressure transducer was used to measure the actual

applied pressure (i.e., corresponding to a particular force). This measurement was then used for comparison with the desired applied force. A "Simulink" program was developed in "Matlab" to record and store data from the pressure transducer and the strain gauges. For the mounting of the T-joints, the ends of the specimen were fixed to the test fixture using 4 bolts to ensure fixed end boundary conditions at supports 1 and 2 (shown in Figure 6b), and also to ensure that no slipping occurs between the end of the specimen at connection 3 and the test fixture (also shown in Figure 6b). The schematic diagram of the loading and the boundary conditions are depicted in Figure 6. It should be noted that in reality the boundary conditions are somewhere between fixed and simply supported [7].

Two T-joint samples were monitored using strain gauges. On these two specimens, a total of 8 strain gauges were installed around the connection of each T-joint. The locations of these strain gauges are shown in Figure 6 (note that the locations shown in Figure 6d are approximate and are not to scale). In most of the reviewed literature, only the strains perpendicular to the weld toe have been measured as those parallel to the weld are assumed to be relatively small. In this study, for each location, a two-channel 90º tee rosette strain gauge with a gauge length of 1.57mm (0.062in) was used to measure the strains perpendicular and parallel to the weld toe (i.e., X and Z directions for locations 2-8 as shown in Figure 6d). The FE results were read at the centre of the gauge location. For location 1, strains were measured in the X and Y directions. A similar approach as to those used in references [1,2,4] was used for the placement of the strain gauges. The strain gauges shown in Figure 6 are 6.35mm (1/4 inch) away from the weld toe (with the exception of location 4). The strain gauge in location 4 is installed at a distance of

50.8mm (2 inches) from the weld toe, therefore not affected by the stress concentrations at the weld. Using the above strain measurements, the stresses in the X and Z-directions for locations 2-8 can be calculated as follows:

$$\sigma_x = \frac{E}{1-\nu^2}\left(\varepsilon_x + \nu\varepsilon_z\right) \quad (1)$$

$$\sigma_z = \frac{E}{1-\nu^2}\left(\varepsilon_z + \nu\varepsilon_x\right) \quad (2)$$

Where E is the modulus of elasticity and ν is the Poisson's ratio of the T-joint sample. The assumption made in using equations 1 and 2 is that plane stress state exists and the material is linearly elastic.

4.0 Experimental and numerical results

To assess the effectiveness and accuracy of the modelling, the numerical and experimental results were compared to verify the reliability of the FE model. For this purpose, static loads ranging from 4,448*N* (1,000 lbs) to 53,380*N* (12,000 lbs) were applied to the model and to the test specimens. The applied load was not increased past 53,380*N* (12,000 lbs) to ensure that no plastic strains occurred. A linear relationship between the applied load and the measured experimental strains was found and is shown in Figure 7. This plot depicts the strains in the X-dir (i.e., perpendicular to the weld toe). It should be noted that the magnitude of these strains are much larger than the strains that are parallel to the weld. A linear relation was also observed in the case of the strains parallel to the weld toe (not shown here).

In Figure 7, the solid lines represent the measured experimental strains. Due to a strain gauge malfunction at location 3, the corresponding values are not reported. The strains obtained from the simulations and those from the experiments are tabulated in Table 1 for locations 4 and 6. In addition, for ease of comparison, the strain values obtained from the

FE model for location 6 in the X-direction are also shown in Figure 7. The results show that in general a very good agreement exists between the experimental and numerical strains for both locations (4 and 6 in X and Z directions). Strain readings from the other locations also provided similar results. It was observed that with an increase in the applied load, there was a better agreement between the FEA and experimental results. This is expected as the experimental strains are less prone to noise at larger loads. At small strains, any minor noise or disturbance can affect the accuracy of the experimental readings. In table 1, it can be seen that for location 4 (in both the X and Z-directions) there exists some discrepancies between the FE results and the measured strains also at higher loads. However, it should be noted that the magnitude of the strains in location 4 are still relatively small even at these higher loads (i.e., about 7 times smaller than the magnitude of the strains in 6X at 12000lbs) and therefore are more prone to noise.

From Table 1, it can be observed that the experimental strains perpendicular to the weld toe at location 6 are about 4.8 times larger than the strains parallel to the weld. This ratio is about 5.7 times for the FEA results. The dominating role of the strains perpendicular to the weld toe was also observed at the other locations. This is in agreement with the work of [7,8, and 10] which suggest that the strains and stresses normal to the weld toe are mainly responsible for plasticity/crack initiation and propagation.

Table 1: FEA and experimental strain readings at locations 4 and 6 of the T-joint (strain values are in μ-strain)

12000lbs (53380*N*)	4X	4Z	6X	6Z
FEA	330.1	116.6	2626.4	458.1
Experimental	412.9	173.8	2550.0	533.9
8000lbs (35586 *N*)				
FEA	220.1	77.7	1750.9	305.4
Experimental	267.8	124.9	1642.0	295.9
6000lbs (26689 *N*)				
FEA	165.1	58.3	1313.2	229.0
Experimental	177.7	90.6	1190.0	201.4
4000lbs (17793*N*)				
FEA	110.1	38.9	875.5	152.7
Experimental	105.0	54.7	775.8	119.3
2000lbs (8896*N*)				
FEA	55.0	19.4	437.7	76.3
Experimental	44.2	29.5	359.9	39.8

Location 6 is of special interest here, since both the experimental and numerical results show the maximum hot spot stresses are located at the weld toe close to this location. The fatigue tests on the T-joints also showed the first signs of fatigue crack initiation to be at the weld toe at this location, as shown in Figure 8.

The FEA strains and stresses perpendicular to the weld toe along the path starting at location 8 and ending at location 6 (6.35mm from weld toe) for the applied load of 53,380*N* (12000 lbs) are plotted in Figure 9. This path will be referred to as the top of the connection from hereon. These values have to be extrapolated to obtain the stresses and strains at the weld toe. According to [18], the stresses and strains in the critical regions of tubular joints vary linearly. For this purpose, a linear extrapolation technique was used. As the reliability of the FE model was verified through the comparison of the FE and experimental strains at several locations, the FE model was used to obtain the second set

of values required for the linear extrapolation. These strains and stresses were read at a distance of 12.7mm from the weld toe. The results presented from hereon correspond to the applied load of 53,380*N* (12000 lbs).

One of the most attractive features of using the linear extrapolation method to obtain the stresses and strains at the weld toe, is its relative mesh insensitivity. Both finer and coarser mesh sizes were analyzed to demonstrate the mesh insensitivity of this approach. The refined mesh zone shown in Figure 1b was used with element sizes of 1/2t, 3/4t, and 1t for the convergence test, where t is the tubes' thickness of 6.35mm (1/4 inch). Table 2 summarizes the three different FE models. The stress distribution in the X-direction at the weld toe at the top of the T-joint connection is depicted in Figure 10, showing a very good agreement amongst the three element sizes (in particular for mesh sizes of 1/2t and 3/4t). Due to the mesh insensitivity of the stresses and strains with these meshings, the element size equal to 1t in the refined mesh zone was chosen for the analysis, as reported below.

Table 2: Summary of the three different FE models

Mesh	1/2t	3/4t	t
Element size	3.175(mm)	4.765(mm)	6.35(mm)
Number of elements	41780	37274	35038
Number of nodes	53733	48006	45241

From Figure 9, it can be observed that as the weld toe in the proximity of location 6 is approached, the stresses and strains increase very rapidly. All of the 6 components of the stress and strain distributions (i.e., normal and shear) along the weld toe are presented in Figure 11. It is important to examine these strains and stresses in detail to obtain insight into the components of stress that cause the most damage. The dominating role of the normal stresses and strains in the X direction is shown in Figure 11. The normal stresses

in the X-direction are the highest with a maximum value of approximately 630MPa at the weld toe at location 6, followed by the stresses in the Z-direction which have a maximum value of nearly 220MPa (located at 0.06m distance between locations 6 and 7). It can be observed that these components of stress cause the most damage. Therefore, if plastic deformation or fatigue cracking is a concern, the modification of the connection should focus on a design that reduces the X-direction normal stresses to be the most effective.

In structural analysis, the stress distribution over the plate thickness is usually nonlinear in the vicinity of a notch, such as a weld toe. This stress distribution can be broken down into three components. The membrane stresses (σ_m) which are constant through the thickness of the plate and the bending stresses (σ_b) which assume a linear distribution through the thickness of the plate, with the mid-plate thickness serving as the neutral point. The remaining stress ($\sigma_{nonlinear}$) is from the local notch effect and is nonlinear. The decomposition of the local stress in the vicinity of the notch is given as follows:

$$\sigma_{Notch} = \sigma_m + \sigma_b + \sigma_{nonlinear} \quad (3)$$

As a point of interest, to observe the local notch effect, the stresses and strains were also obtained for the model without the weld profile at distances of t (6.35mm) and $2t$ (12.7mm) from the location of the weld toe. Although for the model without welds no weld profile existed, the strains and stresses were linearly extrapolated to the location of the virtual weld toe. The stresses obtained from the model without welds along with those obtained from the model including the welds, for the direction perpendicular to the weld toe are plotted in Figure 12.

From Figure 12, it is observed that the stresses perpendicular to the weld toe for the FE model that includes the weld profile are higher than their counterparts without the weld.

This is particularly more pronounced in the proximity of location 6. The maximum stresses in the X-direction along the weld toe predicted by the FE model with the welds is approximately 630MPa, while those predicted from the model without welds is about 515MPa. A similar type of observation was made in regards to the strains, not reported here. It is also interesting to observe the distance along the X1 axis on the T-joint (shown in Figure 13) at which the effects of the weld profile disappear. The origin of the X1 axis starts at the weld toe and is located at 0.04m from the right end of the connection (i.e., nearly the centre of the top of the connection). The stresses (along the X1 axis) correspond to those on the mid-thickness of the tubes (i.e., membrane stresses) and the top surface which includes both the membrane and the bending stresses. These stresses are plotted for the FE models with and without the weld profile. It should be noted that the stress distributions in the model which includes the weld profile include the nonlinear stress distribution, $\sigma_{nonlinear}$, through the thickness of the tubes due to the local notch effect.

From Figure 13, it can be observed that the weld profile affects the stress distributions on the T-joint connection up to a distance of approximately 0.035m. After this distance, the stresses are identical in the models with and without the weld profiles. In Figure 13a, it can be seen that at a distance of approximately ½ of the weld thickness (0.00635m = 1/4 inch) from the location of the weld toe the stresses in the model with the weld profile are 180MPa, while those without the weld profile are 165MPa (about 8% difference). From this figure it can be seen that the effects of the weld geometry are highly localized in the vicinity of the weld toe. In Figure 13b, which depicts the stresses occurring at the mid-surface of the tubes (membrane stresses), it is observed that the stresses with and without

the weld profiles are nearly identical. These membrane stresses were not extrapolated to the location of the weld toe, and were directly obtained from the FE results file. Overall, the inclusion of the weld resulted in about a 3% increase in the membrane stresses up to a distance of 3.5cm. Therefore, in general the membrane stresses remain unaffected by the weld geometry. Similar observations were made for other locations around the T-joint (not shown here). This indicates that only the bending stresses are affected by the presence of the weld. This effect is highly localized and is only significant for distances of less than ½ of the weld thickness from the weld toe.

5.0 Reinforcement of the connection

The reinforcement of tubular joints in engineering applications poses a challenge. The ideal reinforcement should not only decrease the hotspot stresses and strains at the connection, but also must be practical for employment in new and existing structures. Certain reinforcement configurations which use internal stiffeners can prove to be difficult or impossible to carry out in the field due to accessibility issues once the structure is constructed. The schematic diagram of the T-joint stiffened both internally and externally for this study is shown in Figure 14.

To reinforce the connection internally, two plates made up of shell elements (SHELL63 from the Ansys program library), as shown in Figure 14b, were added to the FE model. The thickness of the reinforcement plates was varied in the range of 3.175mm to 12.7mm. The configuration of the plates in this arrangement provided little improvement to the reduction of the maximum hotspot stresses and strains at the weld toe. In comparison to the T-joint without the reinforcements, the internally stiffened T-joint with 12.7mm reinforcement plates resulted in the maximum stresses to be reduced by 8%

(from 630 MPa to 580 MPa). More importantly, these stresses remained almost unchanged with varying reinforcement plate thickness. The maximum stresses perpendicular to the weld toe were reduced to 595 MPa for a plate thickness of 12.7mm, and to 580 MPa for a plate thickness of 3.75mm (i.e., 2.5% reduction of maximum stresses with 4 times increase in the plate thickness). The effect of the internal plate thickness on the hotspot stresses at the weld toe is presented in Figure 15.

In the case of externally reinforced T-joints, the effect of stiffeners with different geometric parameters such as plate thickness and length were examined (shown in Figure 14d). The thickness of the plate reinforcement varied from 3.175mm to 12.7mm, while the length of the plate varied from 25.4mm to 63.5mm. Figure 14c presents the meshing for the case of t = 6.35mm and L = 63.5mm. The effects of the reinforcement plate (thickness and length) on the maximum stresses at the weld toe are shown in Figures 16 and 17. Figure 16 considers the effect of the thickness of the reinforcement plate for the case of L=63.5mm and Figure 17 considers the effect of the length of the reinforcement plate for the case t=12.7mm.

In Figure 16, it can be observed that for the externally reinforced T-joint, the maximum stresses perpendicular to the weld toe have been reduced from 630 MPa to approximately 540 MPa for a plate thickness of 3.175mm and to 468MPa for a plate thickness of 12.7mm (i.e., 13% and 26% reduction of maximum stresses, respectively). In the FEA, the external reinforcement plates can take any size. However, the thickness of these plates was not increased past 12.7mm (twice the tube thickness of 6.35mm) due to design and welding issues that arise in practice. The proper welding of the reinforcement plates (such as full penetration welds through the thickness of the plates) becomes more

difficult when welding thicker plates onto the tubes. In addition, it was observed that the length of the external plate reinforcements is more effective on the reduction of the hotspot stresses.

From the above results, the effectiveness of the external reinforcement plates is clear. The best results have been obtained for the case where external stiffeners with a length of 63.5mm and thickness of 12.7mm are used. The stress and strain distributions for this case in the direction perpendicular to the weld toe (X-dir) are shown in Figure 18. In the case of the stiffened T-joint, up to a distance of approximately 0.05m from the right end of the connection, a slight increase in the stresses and the strains along the weld toe is observed. However, the maximum hot spot stresses and strains have been drastically decreased (i.e., by 26%) compared to the unstiffened T-joint connection. A similar trend was also observed in the reduction of stresses and strains in the Z-direction (i.e., direction parallel to the weld) not shown here.

It is observed that with an increase in the length of the external reinforcement plates, the maximum stresses at the connection continually decrease as well. Based on this, the question that arises is as follows: if the maximum stresses at the connection continually decrease as the length of the reinforcement plates is increased, what plate length can be considered as adequate? According to [23], SHS-to-SHS tubular T-joint connections behave as beams at sufficient distances away from the connection. However, at smaller distances close to the connection, there exists significant distortion of the cross-sections due to the thin-wallness of the tubular members which causes significant stress and strain concentrations. In [23], this distance was found to be approximately equal to the length of one of the sides of the square cross-section of the tubular members. It should be noted

that the beam element model assumes an ideal rigid connection with no stress/strain concentrations. For this reason, the length of the reinforcement plates that result in similar maximum stresses as to those of the beam model can be considered as "optimal" or "adequate" reinforcement plate length. Any further increase in the length of the plates can result in the over reinforcement of the connection, with little or no beneficial effects, as cracks can develop at locations other than the connection of the T-joint structure.

From the above discussion, a FE model constructed from beam elements with both torsional and bending degrees of freedom as shown in Figure 19 was developed. The BEAM4 element from the Ansys program library, which is a 3D elastic beam, was used for this purpose. The dimensions of the beam element model were taken to be the same as that of its solid element model counterpart. For the beam elements, the following parameters were used: the area moment of inertia $Iz = Iy = 3.67E\text{-}06$ m^4 (8.83 in^4), the beam cross sectional area $A = 2.42E\text{-}03$ m^2 (3.75 in^2), and the torsional constant $J = 6.66E\text{-}06$ m^4 (16 in^4). Using these parameters, the maximum stresses at the connection of the T-joint were found to be 279 MPa. These stresses occurred in the element between nodes 11 and 22. Based on this stress magnitude, a series of numerical experiments were then performed with the length of the reinforcement plate increased in the solid element model to determine the maximum stresses at the connection.

From the numerical experiments it was observed that with a plate reinforcement length of 126mm (and 12.7mm thickness) the maximum stresses of the solid element model at the T-connection were reduced from 630MPa to approximately 310MPa (51% decrease). It should be noted that with these dimensions of the external reinforcement plates, the maximum stresses at the connection have significantly decreased. These stresses are very

close to those obtained using the FE model constructed from beam elements which was 279MPa. For this reason, the length of the reinforcement plates was not increased any further beyond 126mm.

6.0 Conclusions

Through a detailed numerical and experimental study, the stress and strain distributions along the weld toe of a SHS-to-SHS tubular T-joint were determined. Several full-scale welded T-joints were cut at the connection to obtain the size and the depth of penetration of the weld for the accurate FE modelling. The FE results were compared with the experimental strain readings using the strain gauges installed on several full-scale T-joint samples. It was shown that the developed FE model is reliable for the modeling of SHS T-joint connections and that it can be used to accurately predict the hotspot stresses and strains. The location of a crack due to fatigue on an experimentally tested T-joint corresponded very closely to the location of the maximum stresses obtained from the FE model. With the examination of through-the-thickness stresses, it was observed that the weld geometry, which can have a random nature in practice, affects only the bending stresses, while the membrane stresses remain almost unaffected. At the very vicinity of the weld toe there exists large stress concentrations. The effect of the weld geometry on the bending stresses, however, is highly localized at the connection. This effect drops to about 8% at a distance of about ½ of the weld thickness from the weld toe. The verified FE model was also used to study the behaviour of reinforced T-joint connections. It is shown how the reinforcing plates of various dimensions and locations can reduce stresses in the connection. Clearly, the purpose of such reinforcements is to limit the local deformations, and consequently stress concentrations in the joint. The results and

conclusions of this research work can be used as a tool for engineers and researchers working in the manufacturing and construction industries.

Appendix A: shape functions

For the 8-noded linear solid elements, extra displacement shapes were included for shear locking considerations. The shape functions for this element with the extra displacement shapes (i.e., u_1, u_2 and u_3) are as follows [19]:

$$
\begin{aligned}
u = \frac{1}{8}(& u_I(1-s)(1-t)(1-r) + u_J(1+s)(1-t)(1-r) \\
&+ u_K(1+s)(1+t)(1-r) + u_L(1-s)(1+t)(1-r) \\
&+ u_M(1-s)(1-t)(1+r) + u_N(1+s)(1-t)(1+r) \\
&+ u_o(1+s)(1+t)(1+r) + u_P(1-s)(1+t)(1+r)) \\
&+ u_1(1-s^2) + u_2(1-t^2) + u_3(1-r^2), \qquad -1 \le s \le 1, -1 \le t \le 1, -1 \le r \le 1
\end{aligned}
$$

$$v = \frac{1}{8}(v_I(1-s)..... \quad \text{(analogous to } u\text{)},$$

$$w = \frac{1}{8}(w_I(1-s)..... \quad \text{(analogous to } u\text{)},$$

where *s*, *t*, and *r* are the orthogonal axis in a right handed local coordinate system and *u*, *v* and *w* are the translations in the *s*, *t*, and *r* directions, respectively. Subscripted values such as u_I , v_I , w_I refer to the translations *u*, *v* and *w* of node *I* and so on. The indices *I*, *J*, *K*, *L*, *M*, *N*, *O*, and *P* refer to the eight nodes of the solid element.

References

[1] Shao Y-B, Lie S-T, Chiew S-P, Huang Z-W. Evaluation of geometrical effect on stress distribution for tubular T-joints under axial load. International Journal of Space Structures (2006); 21(2): 77-91.

[2] Shao Y-B. Geometrical effect on the stress distribution along weld toe for tubular T- and K-joints under axial loading. Journal of Constructional Steel Research (2007); 63(10): 1351-60.

[3] Van der Vegte G-J, Makino Y. Ultimate strength formulation for axially loaded CHS uniplanar T-joints. Journal of Offshore and Polar Engineering (2006); 16(4): 305-312.

[4] Mashiri F-R, Zhao X-L, Grundy P, Tong L. Fatigue design of welded very thin-walled SHS-to-plate joints under in-plane bending. Journal of Thin-Walled Structures (2002); 40(2): 125-151.

[5] Mashiri F-R, Zhao X-L. Stress concentration factors and fatigue failure under in-plane bending. Journal of Thin-Walled Structures (2006); 44(2): 159-69.

[6] Mashiri F-R, Zhao X-L, Grundy P. Stress concentration factors and fatigue failure of welded T-connections in circular hollow sections under in-plane bending. International Journal of Structural Stability and Dynamics (2004); 40(3): 403-422.

[7] Pang H-J, Lee C-W. Three-dimensional finite element analysis of a tubular T-joint under combined loading. International Journal of Fatigue (1995); 17(5): 313-320.

[8] Bian L-C, Lim J-K. Fatigue strength and stress concentration factors of CHS-to-RHS T-joints. Journal of Constructional Steel Research (2003); 59(5): 627-640.

[9] Boge F, Helland T-K, Berge S. Low cycle fatigue of T-tubular joints with out-of-plane bending loading. Proceedings of the International Conference on Offshore Mechanics and Arctic Engineering (2007); v(4): 107-115.

[10] Waalen J, Berge S. Low cycle fatigue of T-tubular joints with in-plane bending loading. Proceedings of the International Conference on Offshore Mechanics and Arctic Engineering (2005); v(3): 211-219.

[11] Chang E, Dover WD. Characteristic parameters for stress distribution along the intersection of tubular Y, T, X and DT joints. The Journal of Strain Analysis for Engineering Design (2001); v(36): 323-339.

[12] BOWNESS D, LEE MMK. A finite element study of stress fields and stress intensity factors in tubular joints. The Journal of Strain Analysis for Engineering Design (1995); v(30): 135-142.

[13] Choo Y-S, Van Der Vegte G-J, Zettlemoyer N, Li B-H, Liew J-R. Static strength of T-joints reinforced with doubler or collar plates. I: Experimental investigations. Journal of Structural Engineering (2005); 131(1): 119-128.

[14] Van Der Vegte G-J, Choo Y-S, Liang J-X, Zettlemoyer N, Liew J-R. Static strength of T-joints reinforced with doubler or collar plates. II: Numerical simulations. Journal of Structural Engineering (2005); 131(1): 129-138.

[15] Fung T-C, Soh C-K, Chan T-K. Stress concentration factors of doubler reinforced tubular T joints. Journal of Structural Engineering (2002); 128(11): 1399-1412.

[16] Lee M-K, Llewelyn-Parry A. Offshore tubular T-joints reinforced with internal plain annular ring stiffeners. Journal of Structural Engineering (2004); 130(6): 942-951.

[17] Kosteski N, Packer J-A, Cao J-J. Experimental study of through plate, transverse plate, and stiffened plate-to-RHS member connections. Proceedings of the International Offshore and Polar Engineering Conference (1999); v(4): 38-45.

[18] Herion S, Mang F, Puthli R. Parametric study on multiplanar K-joints with gap made of circle hollow sections by means of the finite element method. In: Proceedings of the 6th international offshore and polar engineering conference. IV. 1996, p. 68–73.

[19] Ansys Version 11.0 Standard User's Manual, 2008. (www.ansys.com).

[20] Hiroko K, Pingsha D. Equilibrium-equivalent structural stress approach to fatigue analysis of a rectangular hollow section joint. International Journal of Fatigue (2005); 27(1): 85-94.

[21] Lotsberg I, Sigurdsson G. Hot spot stress S-N curve for fatigue analysis of plated structures. Transactions of the ASME. Journal of Offshore Mechanics and Arctic Engineering (2006); 128(4): 330-336.

[22] AmericanWelding Society. ANSI/AWS D1.1-96 Structural welding code steel. Miami, USA; 1996.

[23] Moazed R, Szyszkowski W, Fotouhi R. The in-plane behaviour and FE modeling of a T-joint connection of thin-walled square tubes. Journal of Thin-Walled Structures (2009); 47(7): 816-825.

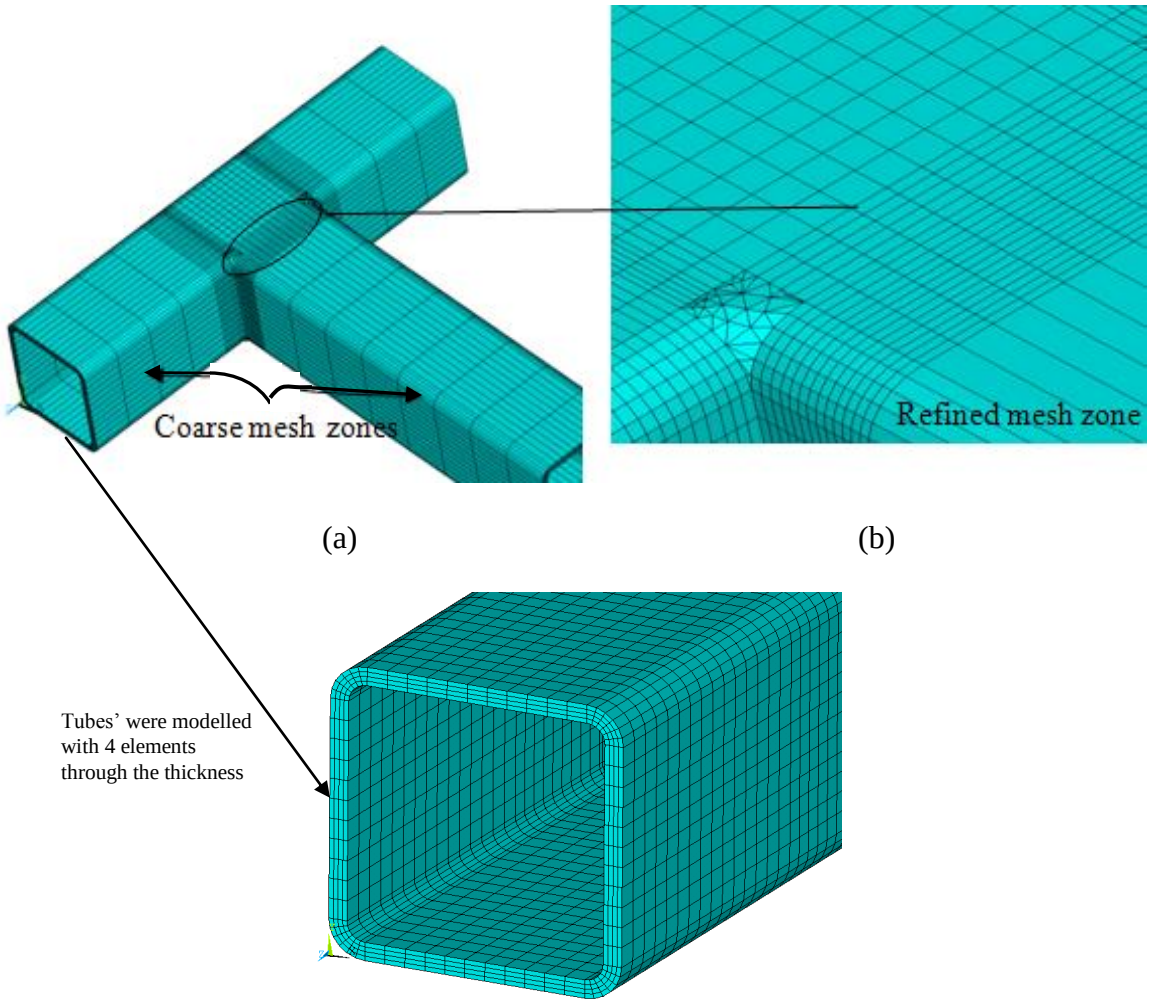

Figure 1: FE solid element model of the T-joint without welds: a) overall view of the meshed T-joint, b) refined mesh zone, and c) meshing of the tubes' thickness

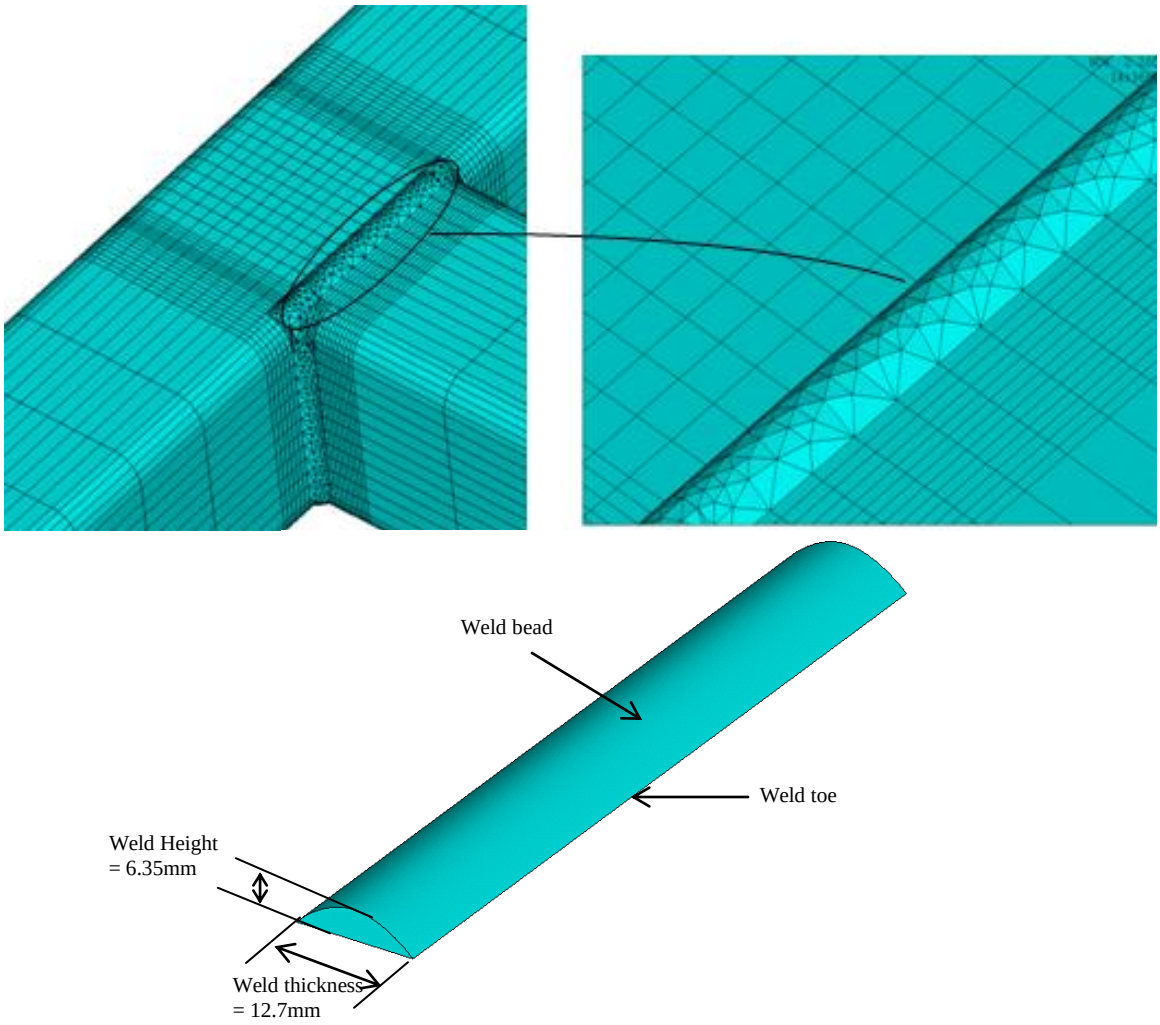

Figure 2: FE model of the welded joint using tetrahedron volume elements

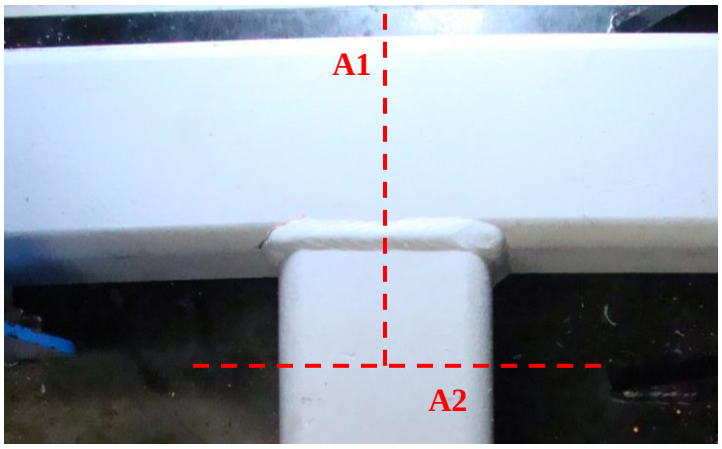

(a)

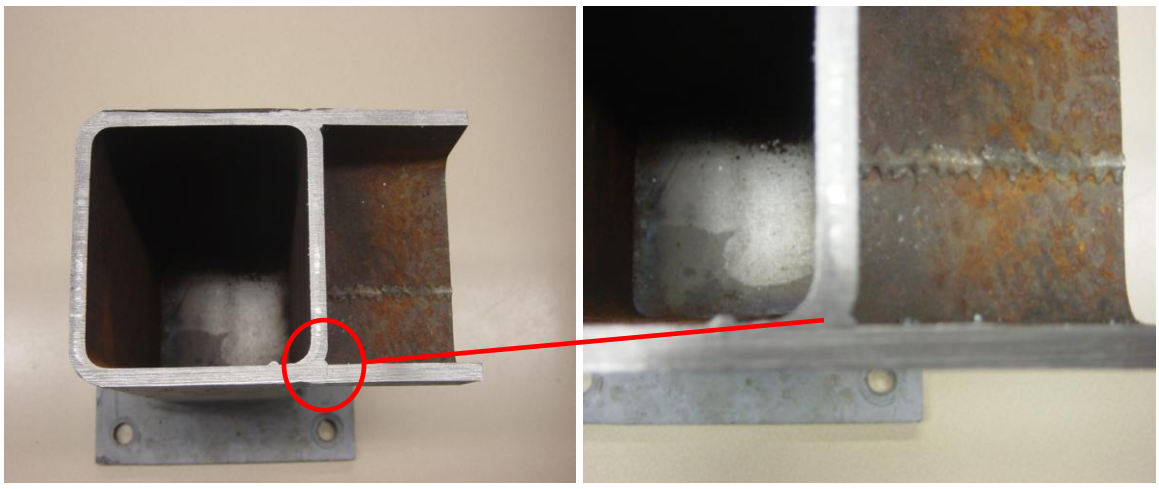

(b) (c)

Figure 3: a) T-joint connection cut along the lines A1 and A2 and b,c) weld profile and depth of penetration as seen from the inside of the connection.

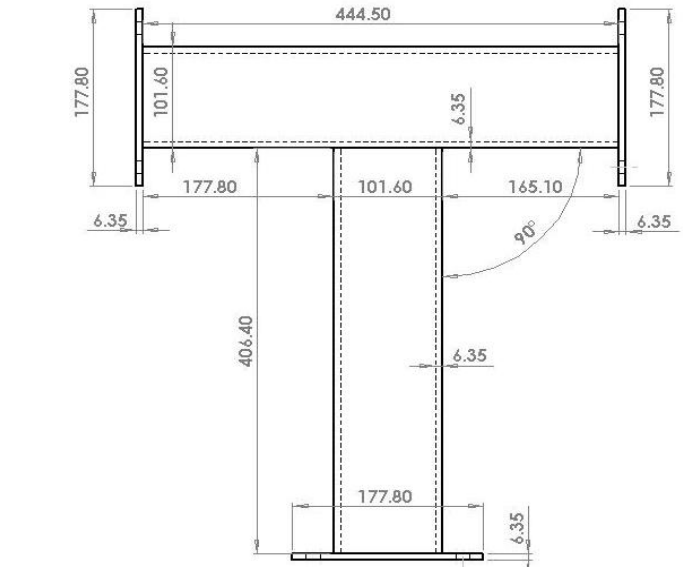

(a)

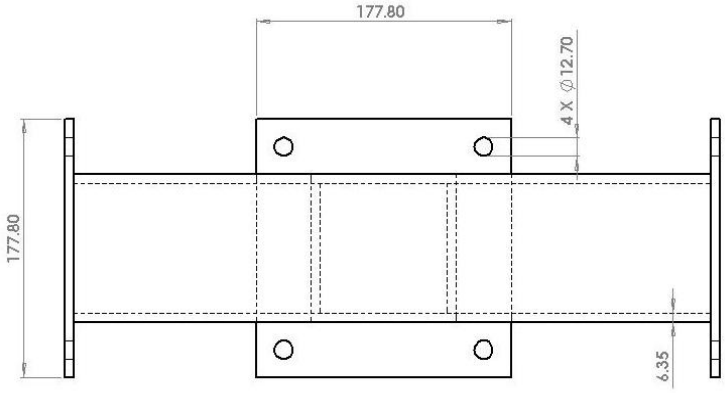

(b)

Figure 4: Configuration and dimensions of the T-joint samples (all dimensions in mm)
a) top view b) front view

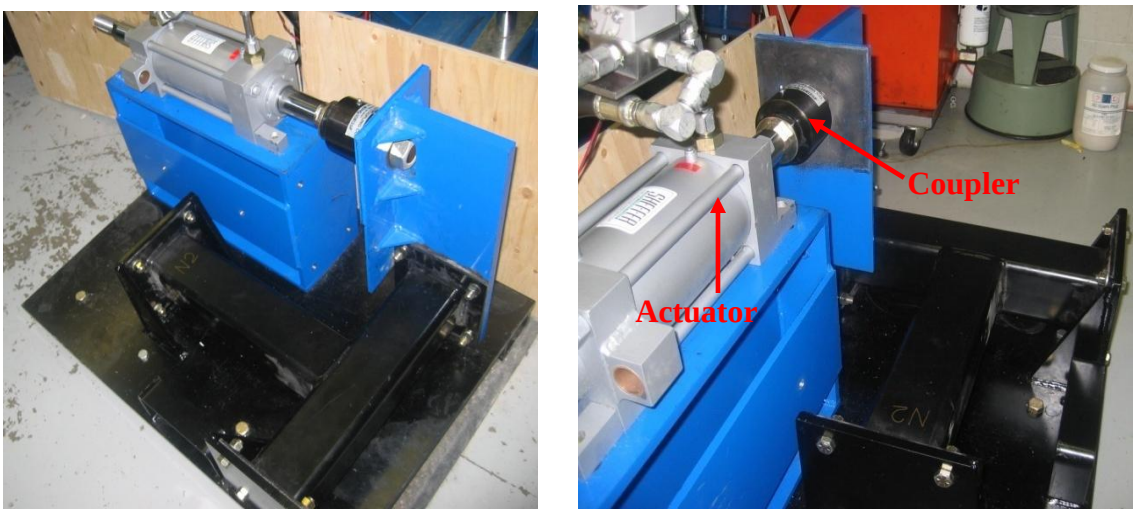

(a) (b)

Figure 5: Test rig and loading mechanism (a) front view (b) rear view

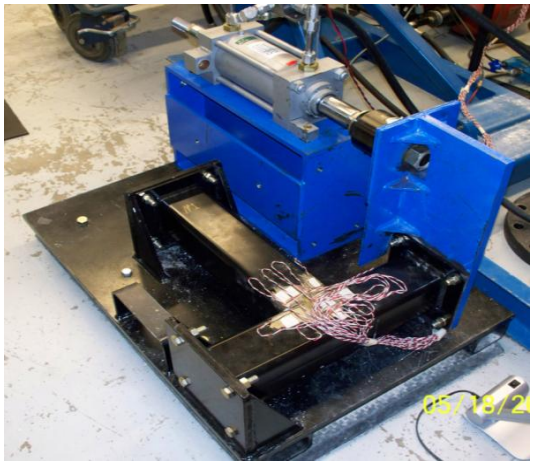

(a)

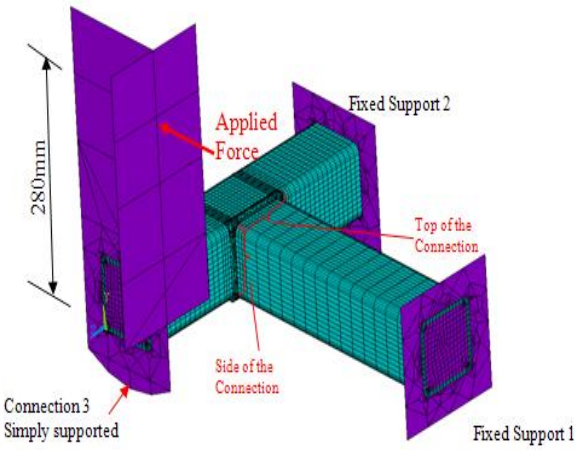

(b)

(c)

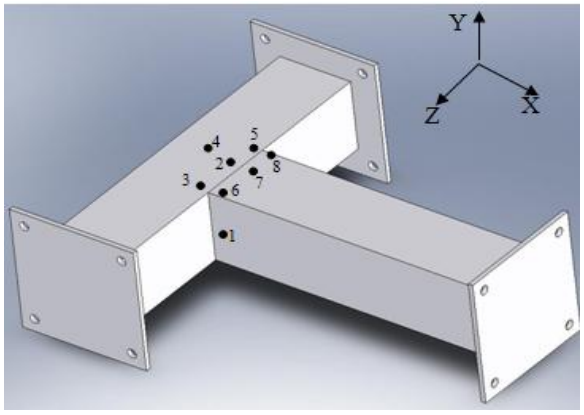

(d)

Figure 6: Locations 1 to 8 of strain gauges installed: a) Overall view of the test fixture, b) Corresponding FE model with loading mechanism and applied boundary conditions, c) Close up view of the strain gauges installed, and d) locations of the strain gauges

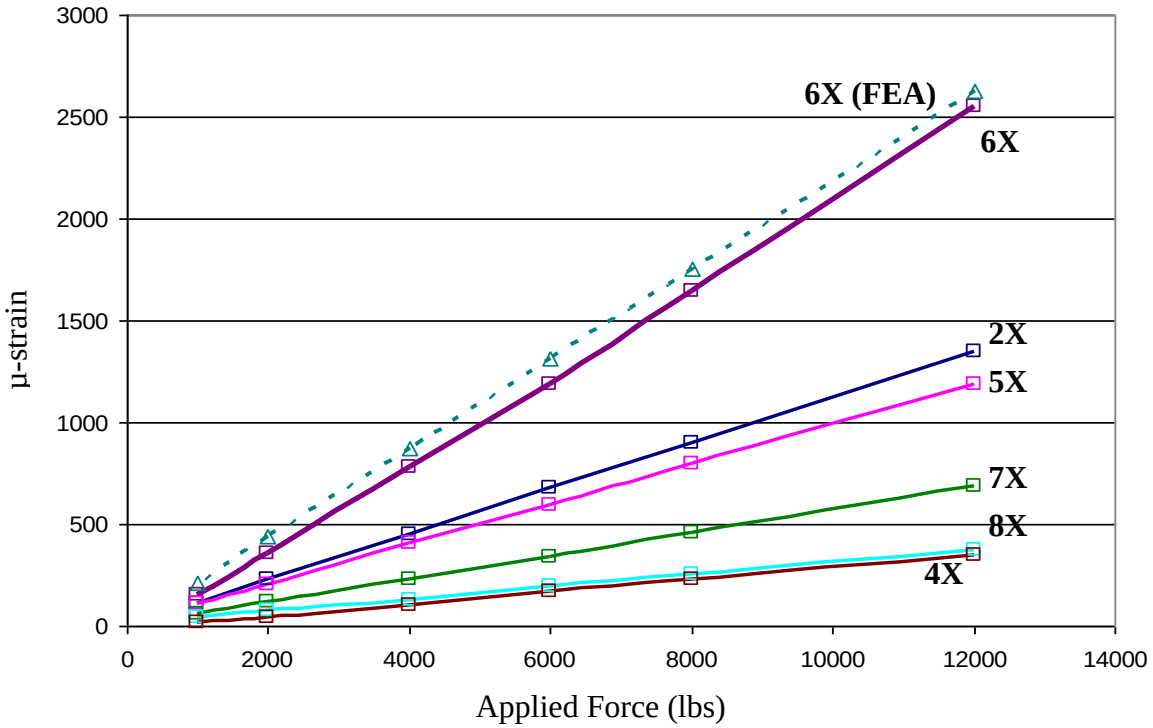

Figure 7: Measured experimental and FEA strains from the application of loads ranging from 1,000 lbs to 12,000 lbs at locations 2 and 4-8 in the X-direction

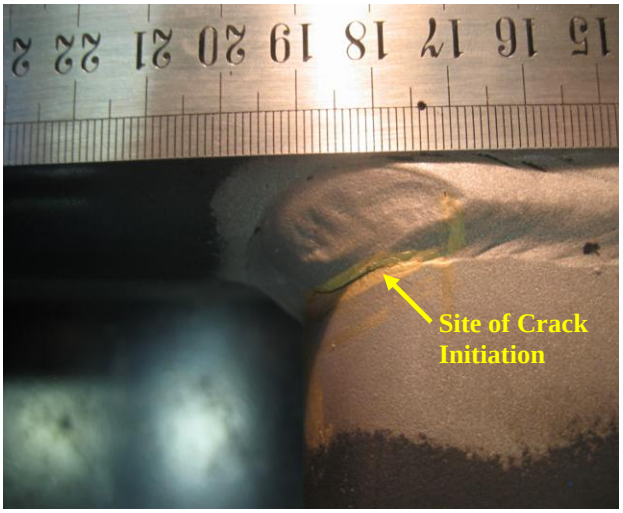

Figure 8: Site of crack initiation at the weld toe which is close to location 6 (site of maximum stress in FEA results).

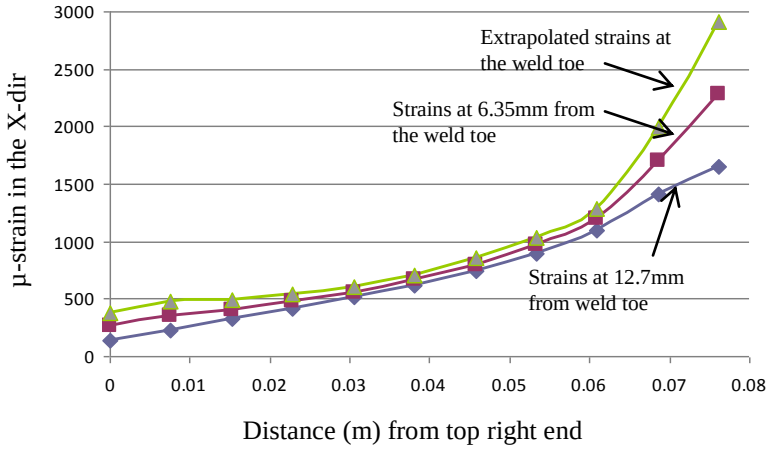

(a)

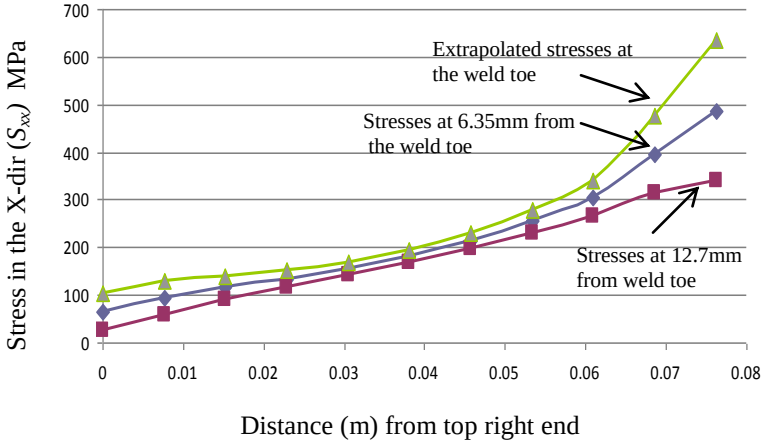

(b)

Figure 9: FEA Strain and stress distributions on top of the T-joint connection in the X-dir for 53,380 *N* (12,000lbs) from top right end (location 8) to top left end (location 6)

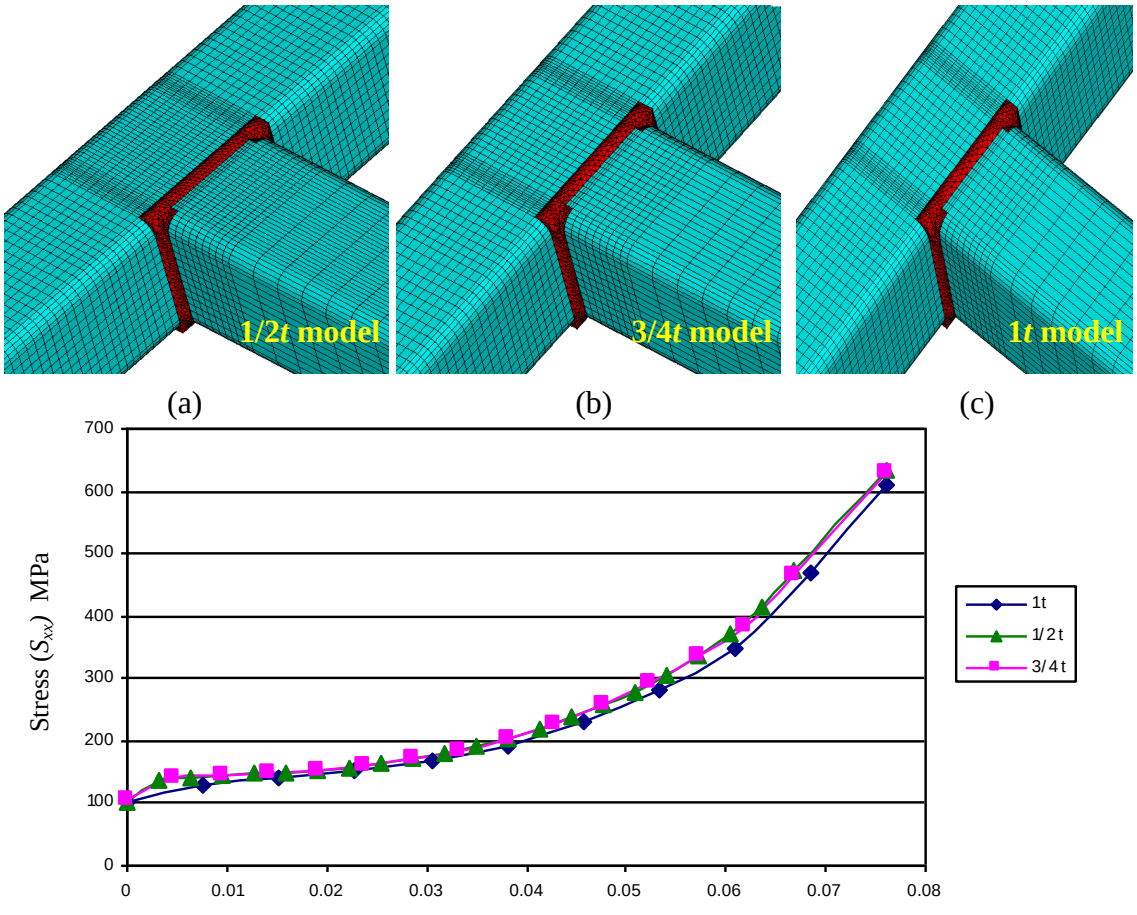

Figure 10: Results of the mesh sensitivity analysis: a)1/2*t* model, b)3/4*t* model, c)1*t* model, and d) Stresses in the X-dir at the weld toe, tube thickness (*t*) = 6.35mm (1/4 inch)

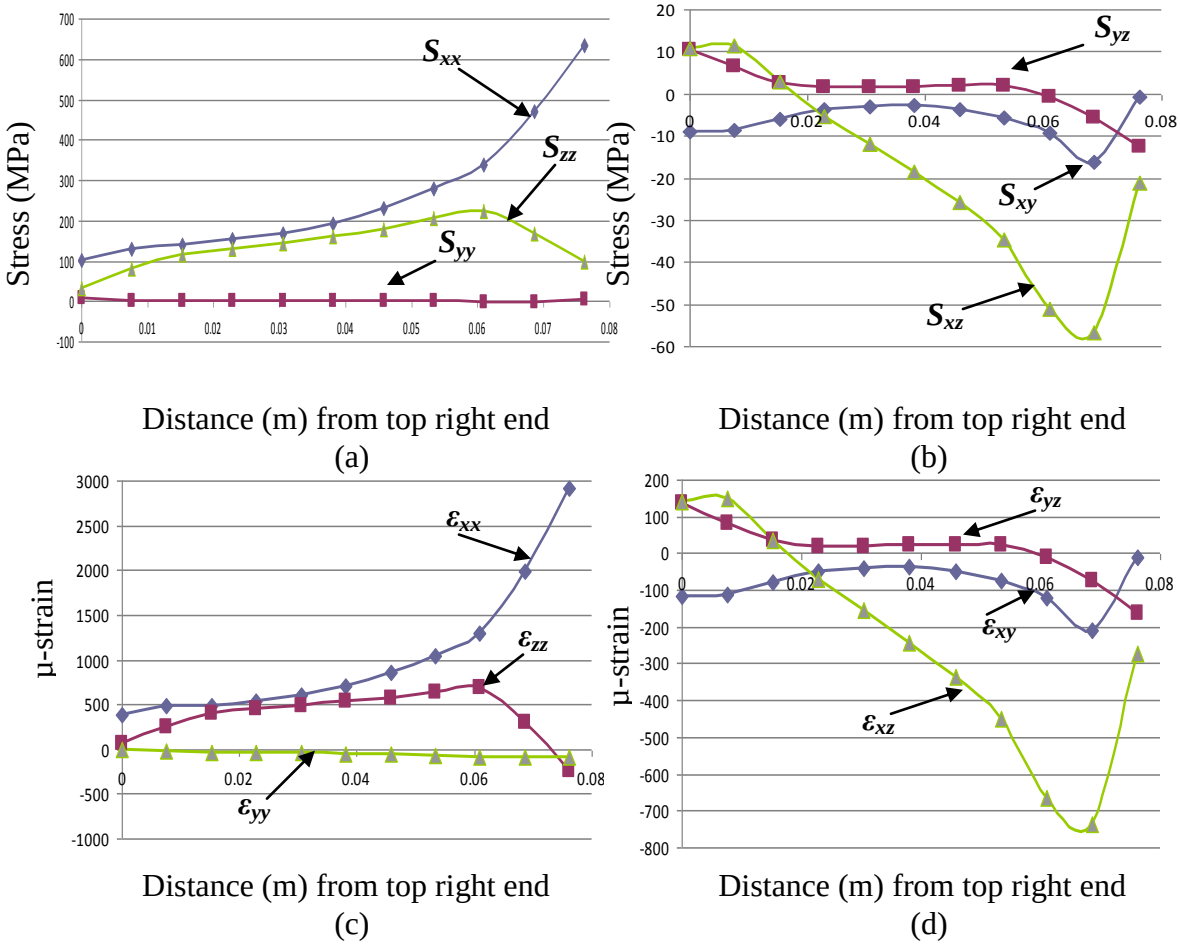

Figure 11: Stress and Strain distribution along the weld toe at the top of the T-joint connection: a) Normal stresses, b) Shear stresses, c) Normal strains, and d) Shear strains.

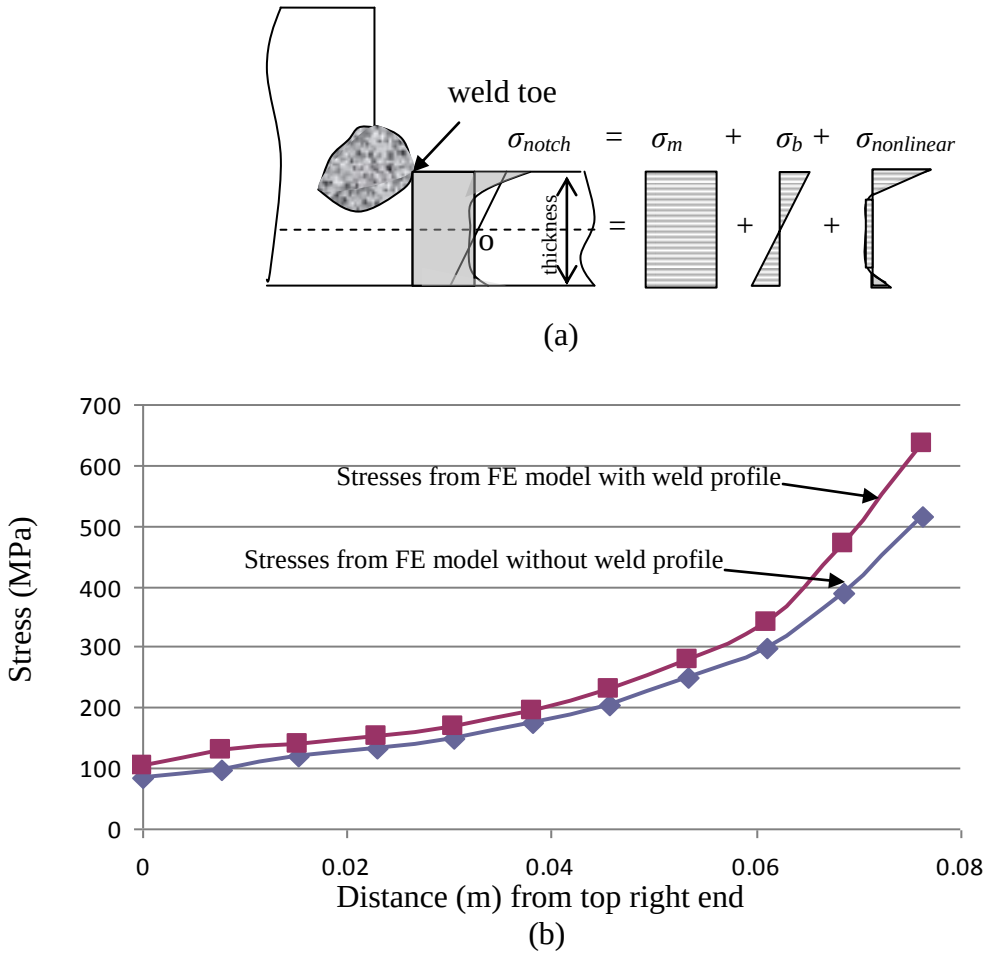

Figure 12: a) Decomposition of the local notch stress and b) Stresses at the weld toe in the X-direction with and without weld profiles.

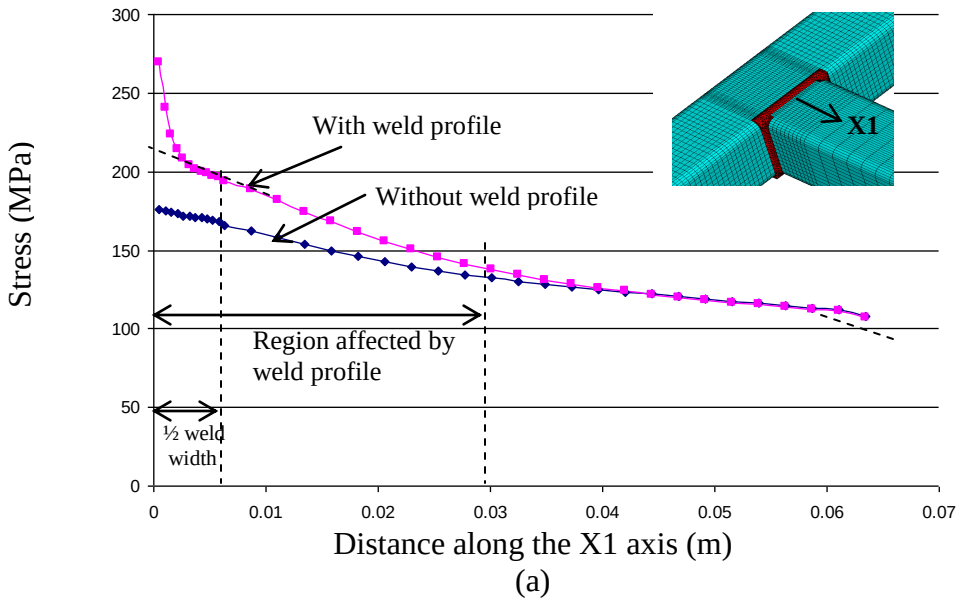

(a)

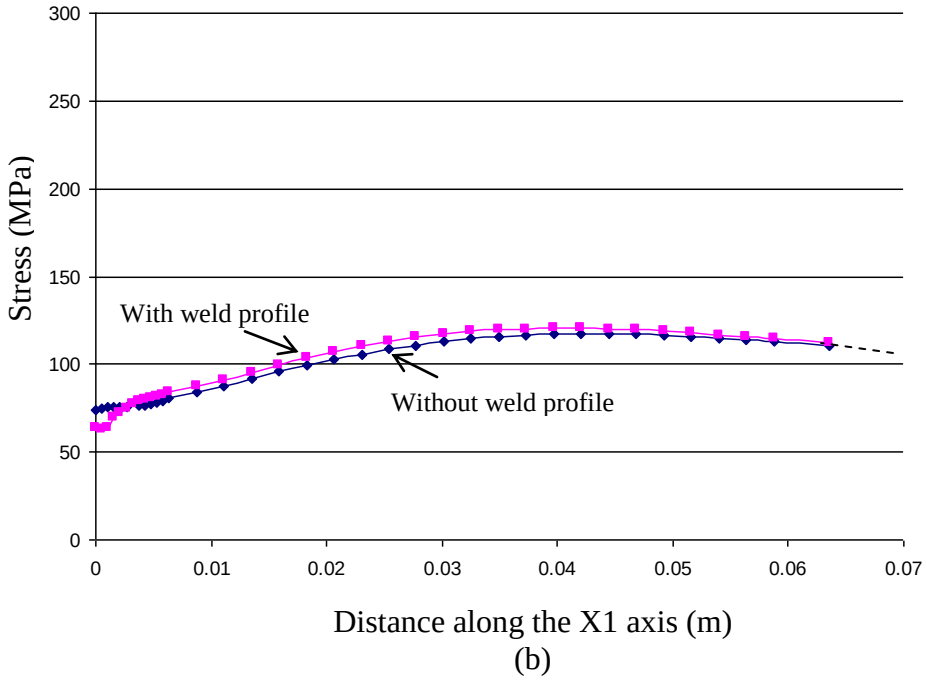

(b)

Figure 13: Stresses (S_{xx}) along the X1 axis: a) Membrane and bending stresses, and b) Membrane stresses

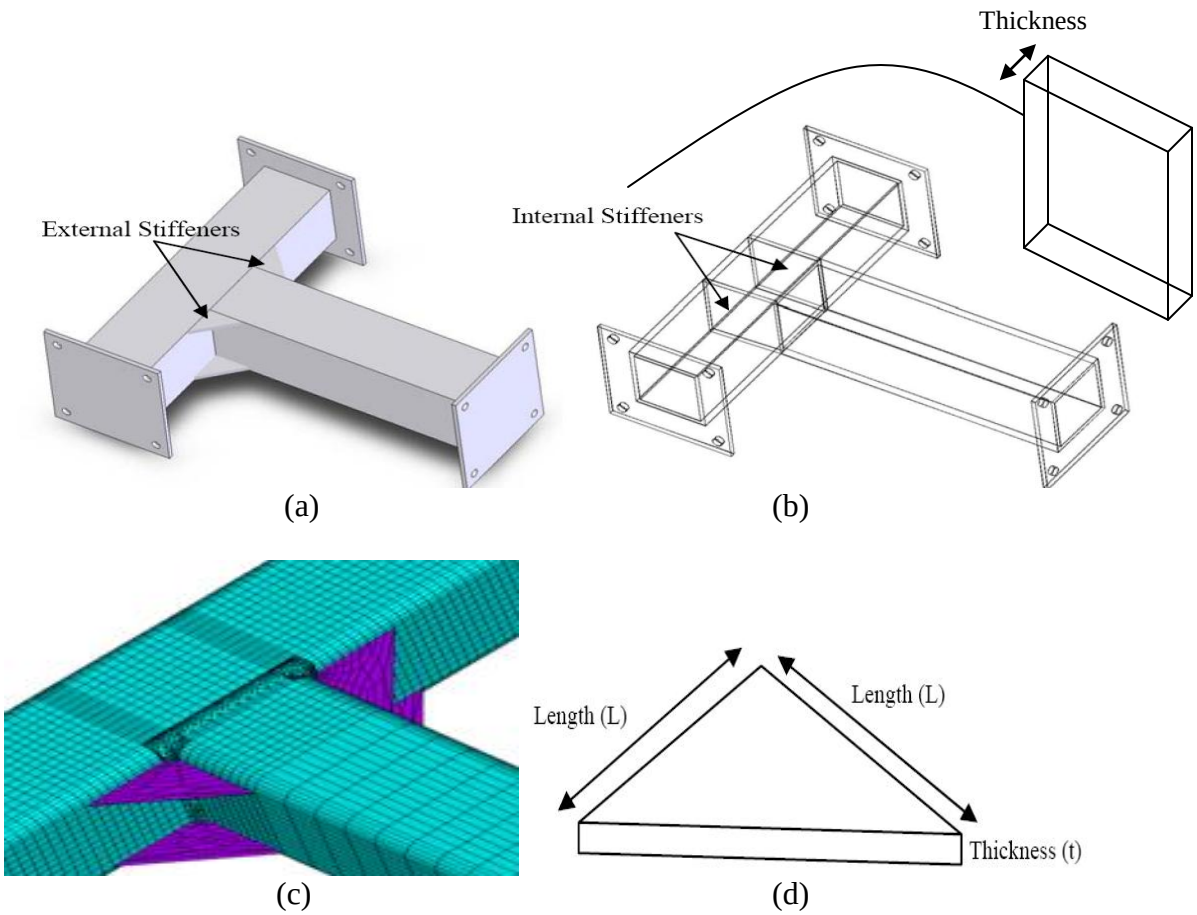

Figure 14: The reinforced T-joint: a) externally stiffened, b) internally stiffened, c) meshing of externally reinforced connection and d) geometric parameters of the external stiffener

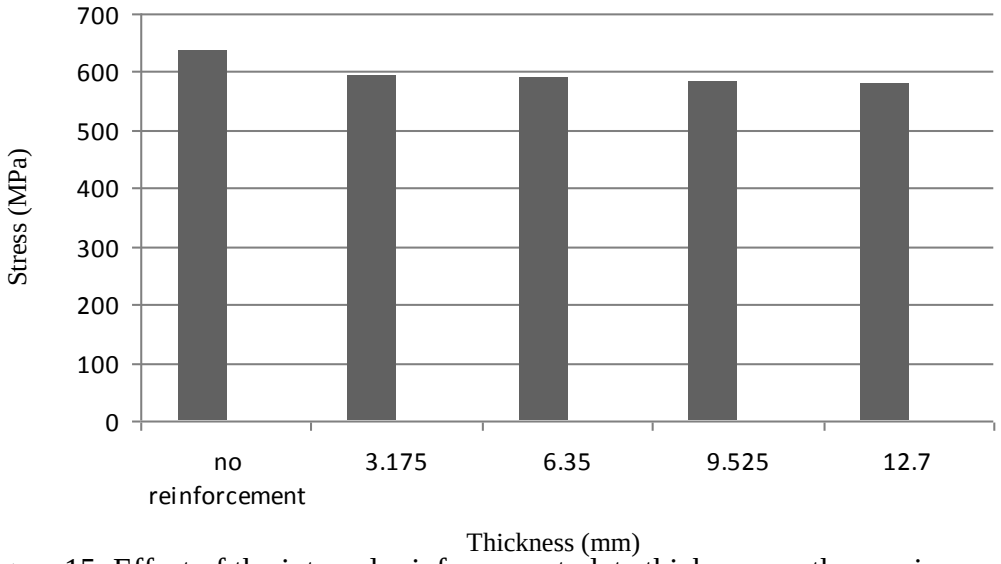

Figure 15: Effect of the internal reinforcement plate thickness on the maximum stresses in the X-direction

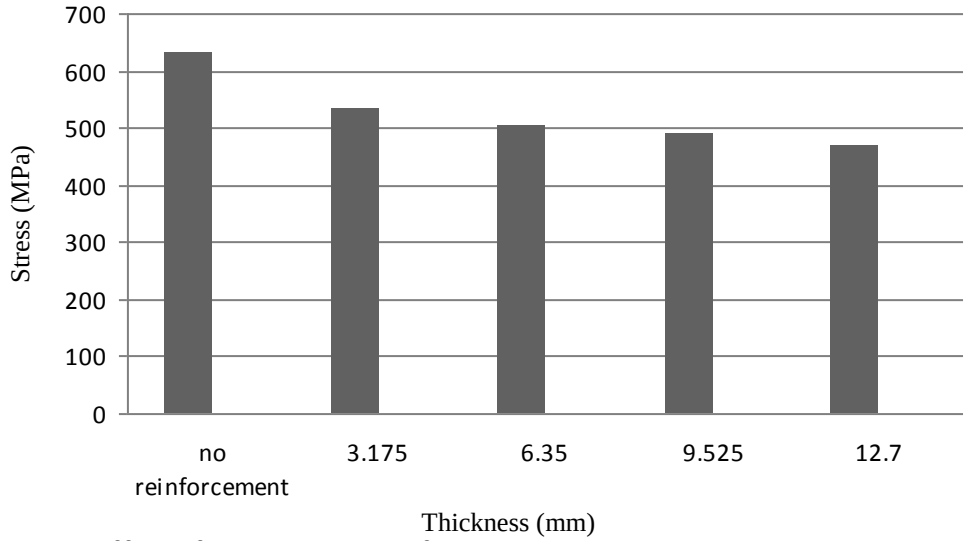

Figure 16: Effect of the external reinforcement plate thickness on the maximum stresses in the X-direction for the case L = 63.5mm

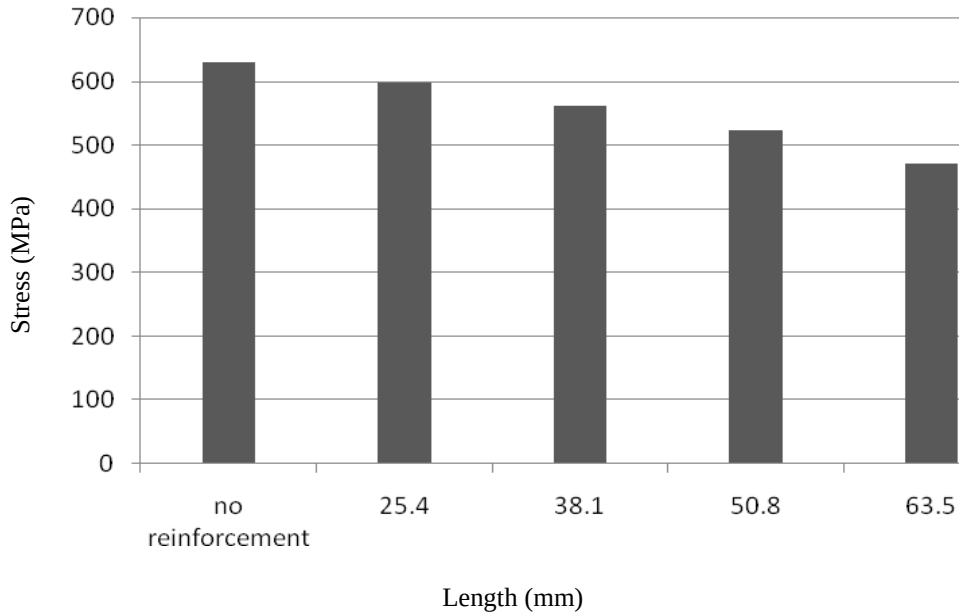

Figure 17: Effect of the external reinforcement plate length on the maximum stresses in the X-dir for the case t =12.7mm

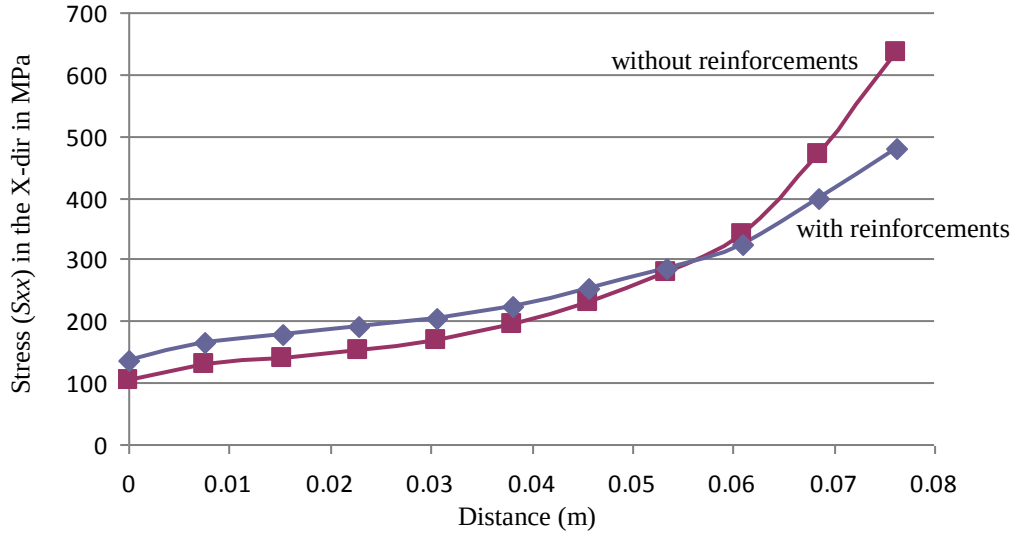

(a)

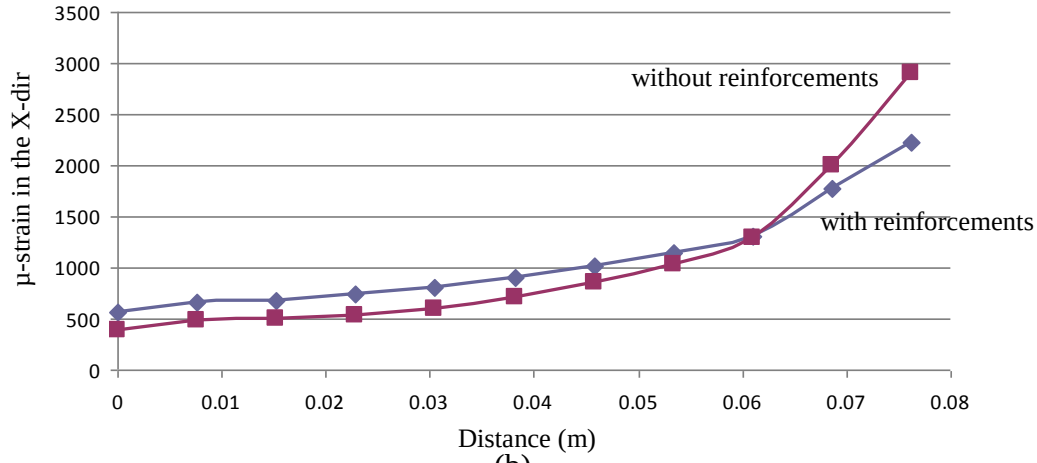

(b)

Figure 18: FEA results along the weld toe at the top of the connection (a) hotspot stresses, and (b) hotspot strains

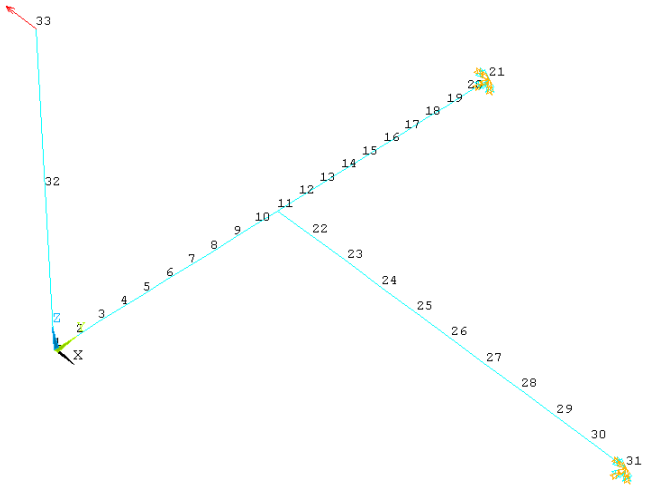

Figure 19: FE model using beam elements to calculate the stresses at the T-joint connection

Chapter 5. The influence of mechanical and laser cutting on the fatigue strengths of square hollow-section welded T-joints

Abstract

T-joint connections are commonly encountered in many machine components and load carrying members. The T-joint connections can be fabricated using traditional mechanical cutting or by laser cutting techniques. The present study investigates the feasibility of using laser cutting to produce welded square hollow-section T-joints with similar or higher fatigue strengths than their conventional mechanical cut counterparts. A total of 21 full-scale T-joint samples, typical of those found in the agricultural industry, were included in this study. Nineteen of these samples were examined with the intention to form a fatigue crack of approximately 3.8cm (1.5 inches) in length, and 2 samples with strain gauges attached for strain measurements. The experimental results of the full-scale T-joints subjected to cyclic loads showed that the fatigue strength of the samples that were manufactured with laser cutting were higher than those fabricated with mechanical cutting. A finite element analysis (FEA) of the T-joints was also performed, and the FEA results of the numerical study were verified with the strain measurements.

Keywords: T-joints; fatigue strength; laser cutting; welds; finite element analysis.

1.0 Introduction

Modern developments in cutting and welding techniques have provided engineers with a range of alternatives for fabricating machine parts. Consider a welded T-joint connection (a hollow 4×4 tube to another 4×4), in which the straight edge of one tube is cut by conventional mechanical cutting tools (i.e., flame cutting) and welded to the body of the other tube to form the T-joint. This connection needs two or three pass of welding to fill in all the gaps. The tubes can be cut using a laser beam to fit the profile of body of the other tube before welding. Then one pass of weld may be enough to obtain the same

strength as conventional cut and several pass of welds. Previous studies on sheet steels have suggested that laser cutting results in higher fatigue strengths than mechanical cutting. However, to the best of the authors' knowledge, there are no such studies performed on more complicated steel structures such as the aforementioned T-joints. To increase the use of laser cutting for such structures, there is a need for more testing and analysis.

Laser cutting may increase the cost of manufacturing initially; however, it will reduce the overall cost and time of welding in the long run. Cutting with laser has many advantages over conventional mechanical cutting; one advantage is the high flexibility in changing from one geometry to another due to numerical control and the absence of mechanical tools [1]. This translates to shorter production series and quicker prototype development. Another advantage, which is more important for us, is the possibility to cut components with very complicated geometries with high precision [2].

The cut edges of steel components by laser cutting differ from mechanically cut edges in properties, which influence the fatigue life of components to different degrees. Only a few researchers have studied the influence of mechanical cutting versus laser cutting. The effects of surface finish from different machining operations were studied in [3-4]. In the last of these publications, the combined effect of surface finish and inclusions were considered. The effect of different cutting processes on the fatigue properties and hence the fatigue life of sheet steels were studied by [4-5]. Meurling et al. [1,6] performed a series of detailed tests to experimentally determine the difference in fatigue properties of mechanical and laser cut specimens of a wide range of steel sheets. Their study included 3 carbon steel sheets and 3 stainless steel sheets of different strength levels. The studies

concluded that both under constant and variable amplitude cyclic loads, laser cutting produced higher fatigue strengths than its mechanical cut counterpart.

This paper presents the results of an experimental investigation on the influence of laser cutting versus mechanical cutting on the fatigue behaviour of square hollow-section (SHS) welded T-joints. The research work presented focuses on the practicability of using this technology to produce welded connections of higher strength than the "conventional" welded T-joints. An experimental test fixture with a hydraulic actuator capable of applying both static and cyclic loadings was designed and used for the experiments. A total of 21 full-scale T-joint samples, typical of those found in the agricultural machineries were included in this study. Nineteen of these samples were subjected to cyclic loads until a fatigue crack of approximately 3.8cm (1.5 inch) in length was formed. On two samples, eight strain gauges were installed around the connection of each T-joint for strain measurements. A finite element analysis (FEA) using solid elements was also performed to gain further insight into the stresses that occur at the welded connection of the two different types of T-joints. The results of the FEA were verified using the experimental strain measurements.

The fatigue properties of the weld (i.e., electrode) and parent material (steel used for the manufacturing of the tubes) were determined using small krouse laboratory samples subjected to rotating bending fatigue tests. The full-scale T-joint samples manufactured through mechanical and laser cutting were tested at a number of different load levels in order to obtain the fatigue strength (load-life curve) of the joints with the two different cutting techniques. As presented in this paper, the experimental study showed that the

fatigue strength of the T-joint samples manufactured with laser cutting was higher than those fabricated with mechanical cutting.

2.0 T-joint connections fabricated with laser and mechanical cutting

In order to obtain an acceptable level of strength in the welding of most machine parts, usually more than one welding pass is required. A typical case of this situation is in a welded connection where two hollow tubes of the same cross section are welded together to form a T-joint. To form this T-joint, traditionally, the straight edge of one tube is cut using the conventional mechanical cutting and welded to the body of the other tube. It is clear that to fill in all the gaps where the two tubes connect, two or three passes of weld are usually required. The tubes can be cut using a laser beam to fit the profile of body of the other tube before welding. Then, one pass of weld may be enough to obtain the same strength as conventional cut and several passes of weld.

The schematics of the edges of the tubes cut using traditional mechanical tools and a laser beam are shown in Figures 1a) and 1b), respectively. The samples constructed using mechanical cutting (i.e., torch) are referred to as “conventional” samples. Specimens constructed using laser cutting technology with the profile shown in Figure 1b are from hereon referred to as “couped” specimens. In Figures 1c and 1d it can be seen that for the couped T-joints the tubes are connected together leaving very little gaps at the connection. In comparison, the conventional samples usually require two or three passes of weld.

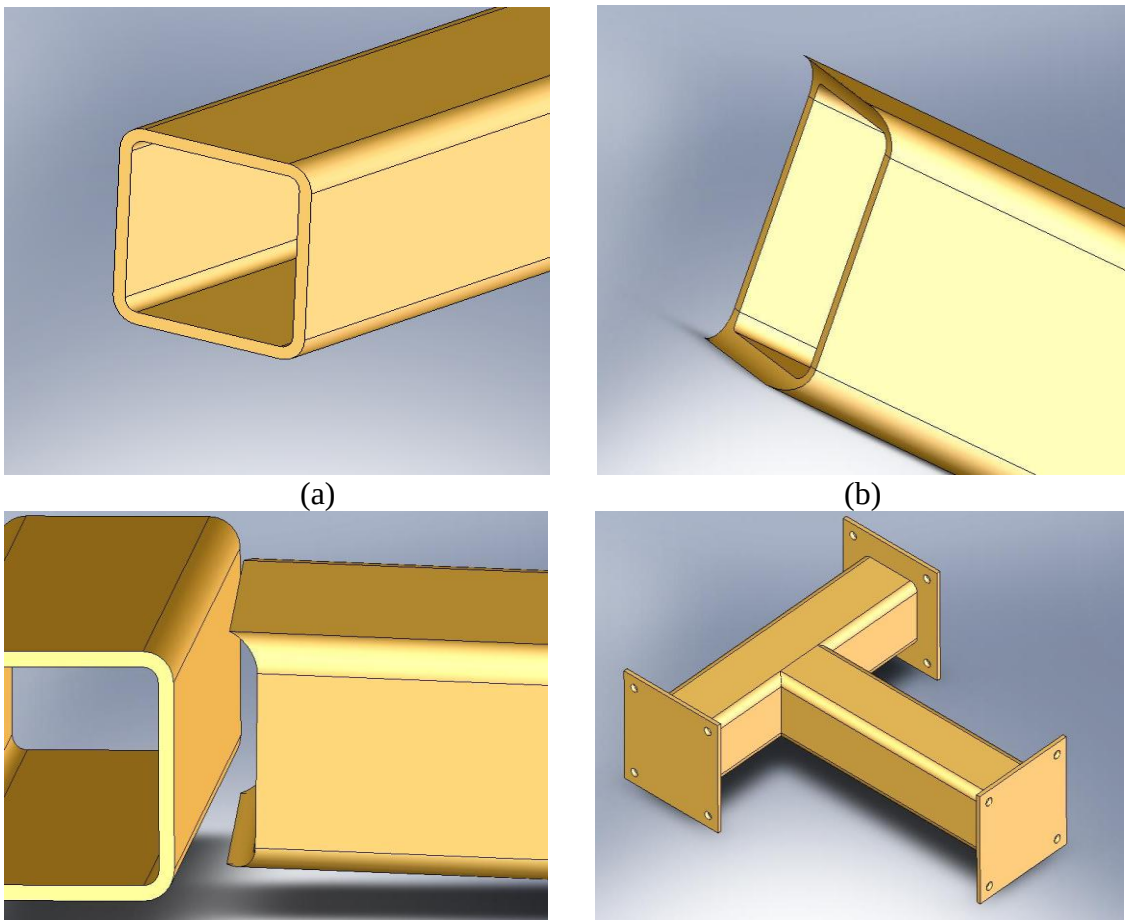

(a) (b)

(c) (d)

Figure 1: Test specimen: (a) Schematics of traditional mechanical cut edge (b-c) Schematics of laser cut edge and (d) the cuped T-joint connection.

3.0 Experimental Test Fixtures

Two test fixtures were developed for this experimental study. The first test fixture was designed so that the T-joints are subjected to the actions of only in-plane loads (as the applied force is in the plane of the T-joints), while the second test fixture subjected the T-joints to a more general loading (i.e., out-of-plane loads were applied). The test rig shown in Figures 2a and 2b will from hereon be referred to as test rig 1. The test rig shown in Figures 2c and 2d will be referred to as test rig 2.

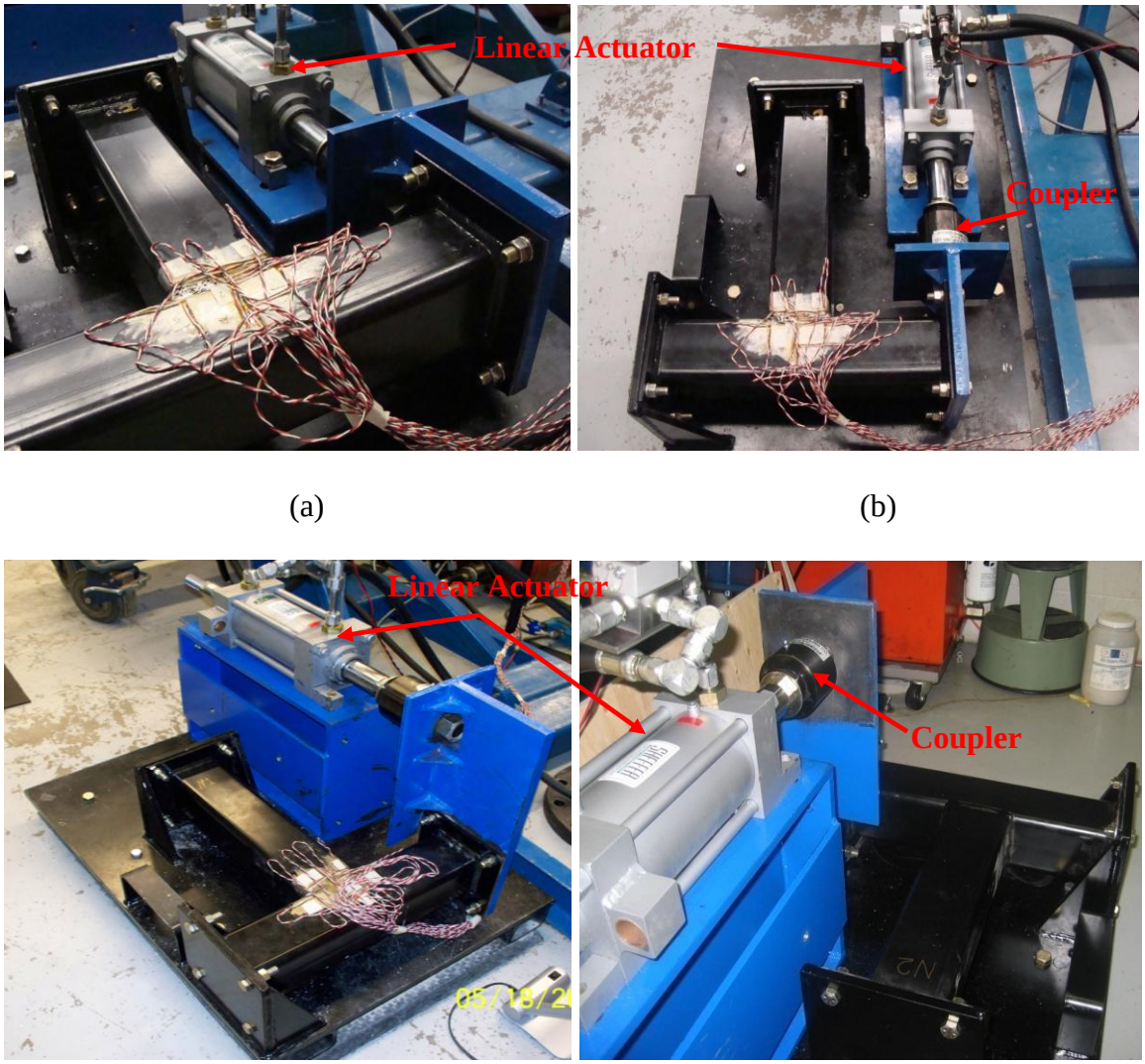

(a) (b)

(c) (d)

Figure 2: Test rig and loading mechanism (a and b) for in-plane loading conditions and (c and d) for general loading conditions (out-of-plane loads)

In both of the test fixtures, for the mounting of the T-joints, the ends of the specimen were fixed to the test rig using 4 bolts to ensure fixed end boundary conditions. For the application of the load, a linear hydraulic actuator capable of applying both static and cyclic loadings of up to 94000*N* (21,132lbs) in tension-compression was employed. The hydraulic actuator was connected to the test fixture through the use of a coupler shown in Figures 2b) and 2d). In order to ensure the accuracy of the applied loads, a pressure transducer was used to measure the actual applied pressure (i.e., corresponding to a

particular force). This measurement was then used for comparison with the desired applied force. The T-joint samples had three 6.35mm (1/4 inch) thick end plates welded to them to facilitate the specimen installation as well as load application. The T-joints are fabricated from structural steel with a yield and an ultimate tensile strength of 540MPa and 600MPa, respectively.

For the control of the hydraulic actuator, a "Simulink" program was developed in "Matlab". The block diagram made in Simulink is presented in Figure 3. The developed program has three main purposes: 1) control of the hydraulic actuator (i.e., signal generation, magnitude and frequency of the applied load) and feedback from the pressure transducer, 2) data collection (i.e., storage of the experimental strain readings from the strain gauges) and 3) safety. Since fatigue tests usually happen over extended periods of time, it is important to design the control setup of the actuator such that it would be safe to run the experiments with minimal supervision. In Figure 3, channels u[1], u[2] and u[3] represent the desired input pressure applied to the actuator, the actual actuator pressure which is obtained from the feedback of the pressure transducer, and the oil level in the hydraulic system, respectively. Channels u[4]-u[7] are used for data collection from the strain gauges. The safety monitor blocks in the diagram, check for the oil level as well as the difference between the desired and the actual applied force. If the oil level in the hydraulic system is lower than a specified value or the difference between the actual and desired input pressures are too large, the system is automatically shut off for safety purposes.

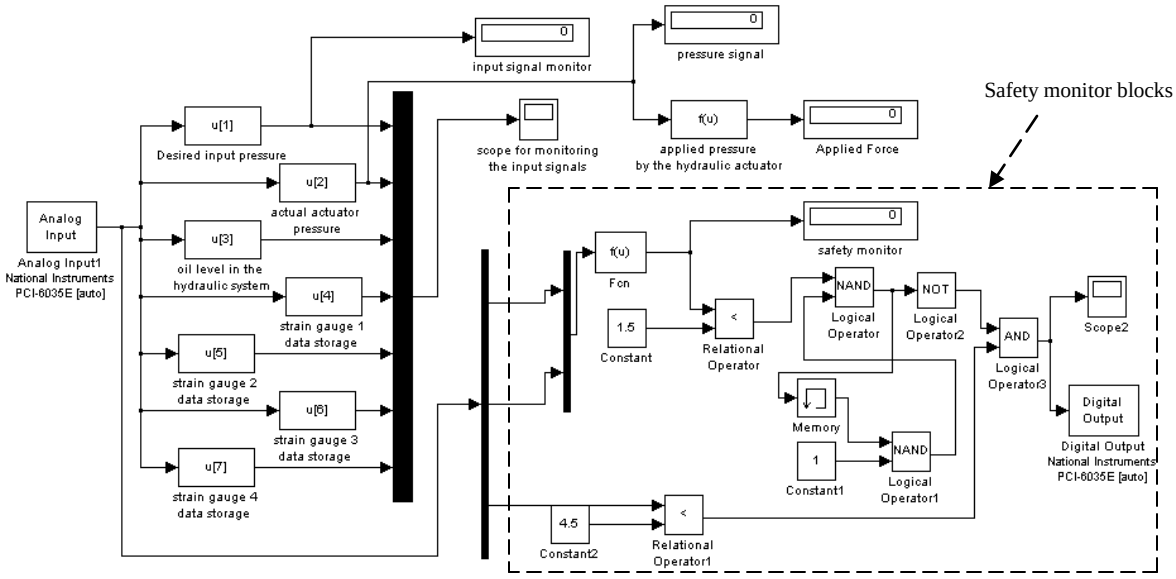

Figure 3: Simulink program developed for the control of the hydraulic actuator

Two T-joint samples (one couped and one conventional) were monitored using rosette strain gauges. For these two specimens, a total of 8 strain gauges were installed around the connection of each T-joint. The locations of these strain gauges are shown in Figure 4 (the shown locations are not to scale). For each location, a two-channel 90º tee rosette strain gauge was employed. These strain gauges are capable of measuring the strains in the perpendicular and parallel directions to the weld toe (i.e., X and Z directions for locations 2-8). For location 1, strains were measured in the X and Y directions. In most of the reviewed literature, only the strains perpendicular to the weld toe have been measured as those parallel to the weld are assumed to be relatively small. The strain gauges shown in Figure 4 are 6.35mm (1/4 inch) away from the weld toe (with the exception of location 4). The strain gauge in location 4 is at a distance of 50.8mm (2 inches) from the weld toe, therefore not affected by the stress concentrations at the weld.

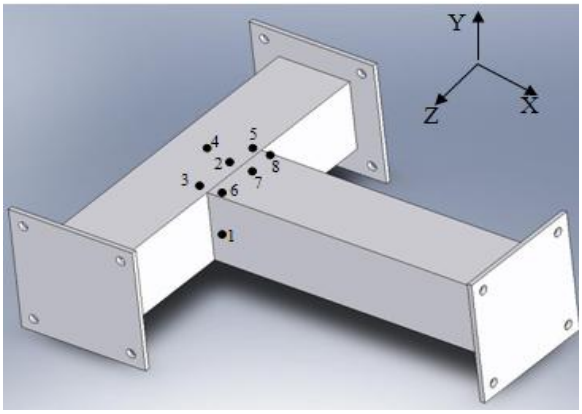

Figure 4: Locations 1 to 8 of the strain gauges installed

The mechanical and laser cut samples are both welded using the inert metal gas welding (MIG) process according to the AWS specifications [7]. In Figures 5 and 6, these two samples are shown. To examine the welding, and to accurately model the welds for the FE study, the samples were cut at different locations of the connection. The cuts were made along the lines A1, A2, A3 (shown in Figure 5a) on two couped samples and along the lines A1 and A2 (shown in Figure 6a) on two conventional samples. Figure 5b depicts the depth of weld penetration on a couped sample along the line A3 (i.e., the centerline of the connection), while Figure 6b depicts the depth of weld penetration along the centerline of the connection for a conventional sample. It is worth noting that in general the height of the weld is smaller in the conventional samples with through-the-thickness weld deposit (full-penetration welds). In the case of the couped samples, the weld penetration extends to approximately half of the thickness of the tubes and the height of the weld deposit is generally larger as well. Similar observations were made regarding the profile and depth of penetration of the weld along the other cuts made at the connection.

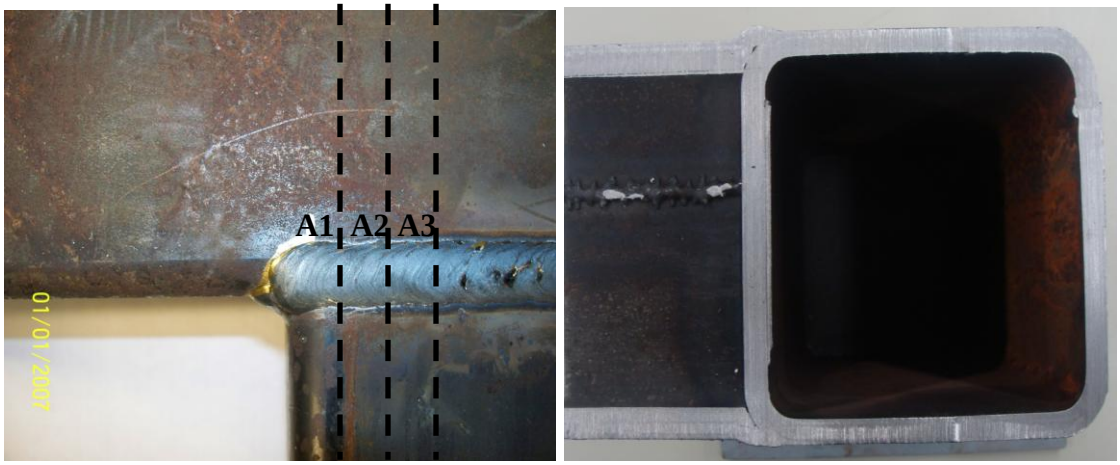

Figure 5: a) Couped sample and b) weld profile
shown for the cut made along line A3

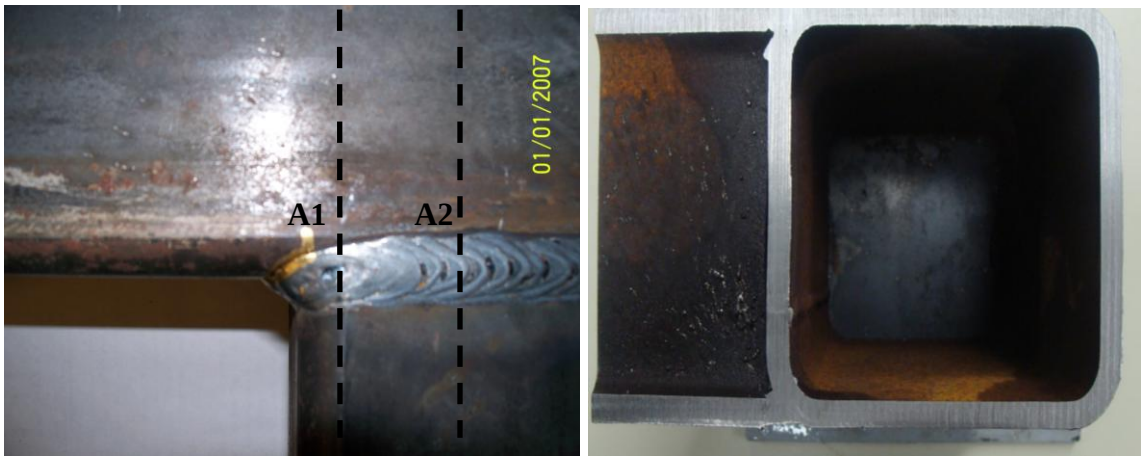

Figure 6: a) Conventional sample and b) weld profile
shown for the cut made along line A2

4.0 Experimental Results

4.1 Fatigue properties of the weld and parent material

The specimen geometry used for the fatigue strength testing of the weld and parent material is shown in Figure 7a. The specimen preparation and fatigue tests were based on the ASTM standards [ASTM E468-90(2004)e1]. All samples were machined from 19mm (3/4 inch) thick plates. In the case of the welded samples, the entire specimen was not manufactured using the weld metal. Plates constructed from the parent material were cut

as shown in Figure 7b and then welded and machined to the geometry shown in Figure 7a.

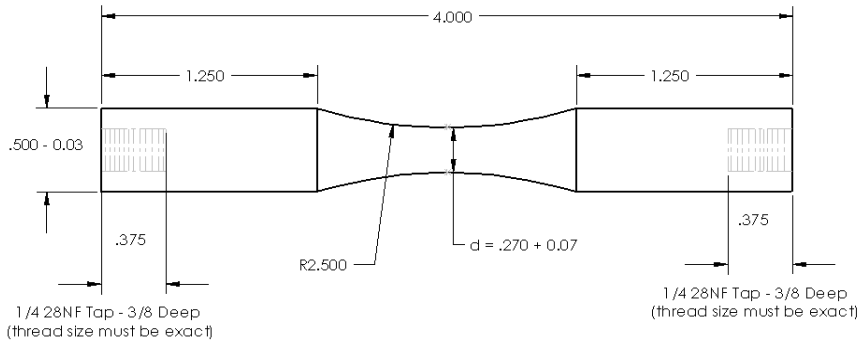

(a)

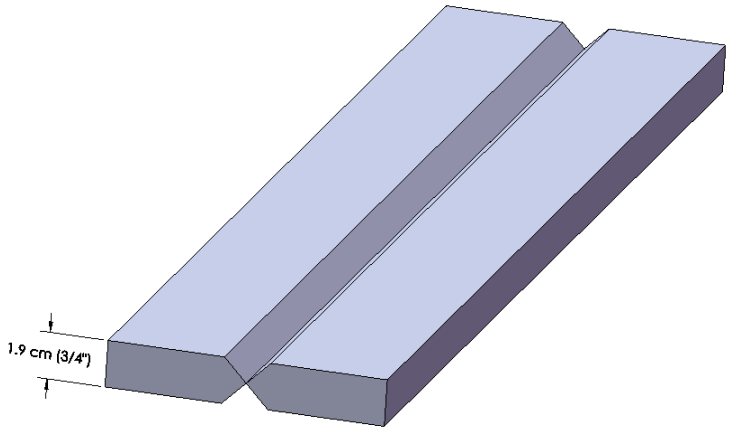

(b)

Figure 7: a) Geometry of krouse specimen for the fatigue testing of the weld and parent materials and b) plates used for the preparation of the welded samples

Constant stress amplitude tests were performed on both materials using a rotating bending fatigue testing machine. The tests were performed at least at 9 different load levels and to a maximum life of ten million cycles or to failure with full separation of the specimens, which ever occurred first. The stress was fully reversed. For the weld material, a minimum of 5 samples were tested at each load level, while for the parent material a minimum of 3 samples were tested. In the welded samples, all fatigue cracks and fractures occured in the welded portion of the specimens, providing the fatigue

strength of the weld material. The results of the fatigue tests obtained from the krouse specimens for both the parent and welded materials are shown in Figure 8. It can be observed that the fatigue strength of the weld material is higher than that of the parent material. The endurance limit of both materials is approximately the same (about 310 MPa).

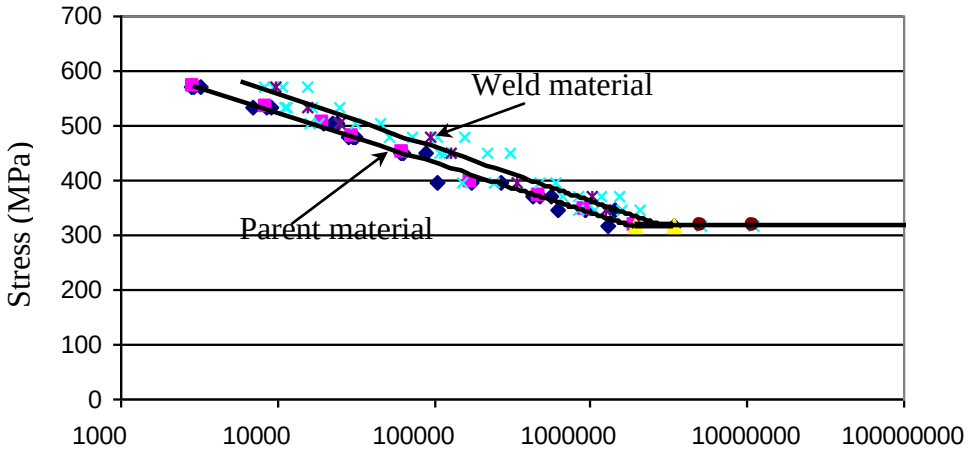

Figure 8: S-N curves of the weld and parent materials.

4.2 Strain gauge measurements

For the measurement of the experimental strains, static loads ranging from F = 4,448N (1,000 lbs) to 53,380N (12,000 lbs) were applied using the hydraulic actuator in both (in-plane and out-of-plane) test fixtures. The schematics of the loadings for both cases are shown in Figure 9. The applied load was not increased past 53,380N (12,000 lbs) to ensure that no plastic strains occurred. It should be noted that for test rig 1 (shown in Figures 2a and b) the force, F, is applied in the plane of the T-joint. On the other hand, for the test rig 2 (shown in Figures 2c and d), the force, F, is applied at a height (i.e., out-of-plane of the T-joint). This subjects the T-joint to the combined action of a 53,380N force and a moment equal to M = 53,380N × 0.33m = 17,615.4Nm (15,600 in-lbs). The

loading corresponding to this case will be referred to as "general loading" conditions from hereon.

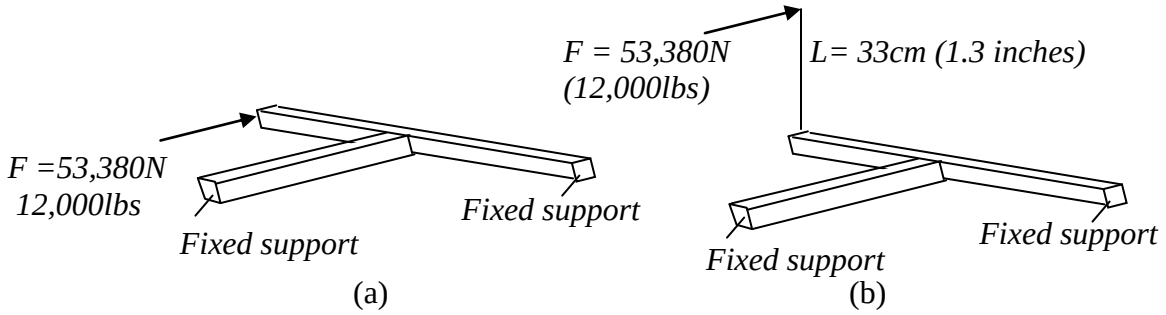

Figure 9: a) in-plane loading, and b) general loading conditions

The linear relationship between the applied load and the measured strains were found and are shown in Figure 10. In the figure, the strains in the X-dir (i.e., perpendicular to the weld toe) are depicted. It should be noted that the magnitude of these strains are much larger than the strains that are parallel to the weld. A linear relation was also observed in the case of the strains parallel to the weld toe (not shown here). It can be observed that the maximum strains occur at location 6 for both loading conditions (in-plane and general). As it will be shown, the weld toe close to location 6, is also the site of crack initiation when the T-joints are subjected to cyclic loadings. Therefore, the stresses which occur in regions in the vicinity of location 6 are of particular interest here. The results plotted in Figure 10 are for a conventional sample. The same experiments were also repeated for the couped samples and it was observed that the strain readings remain similar to those of the conventional sample. For location 6, the measured strains for both conventional and couped samples subjected to in-plane and general loading are shown in Figure 11.

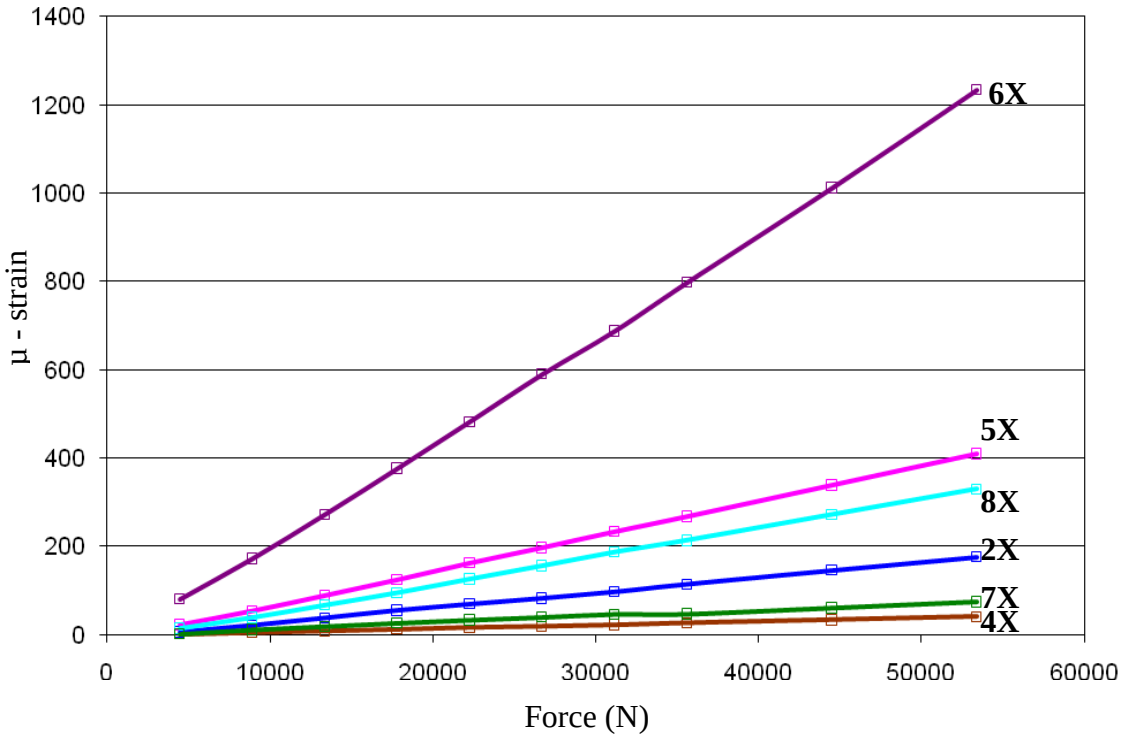

(a)

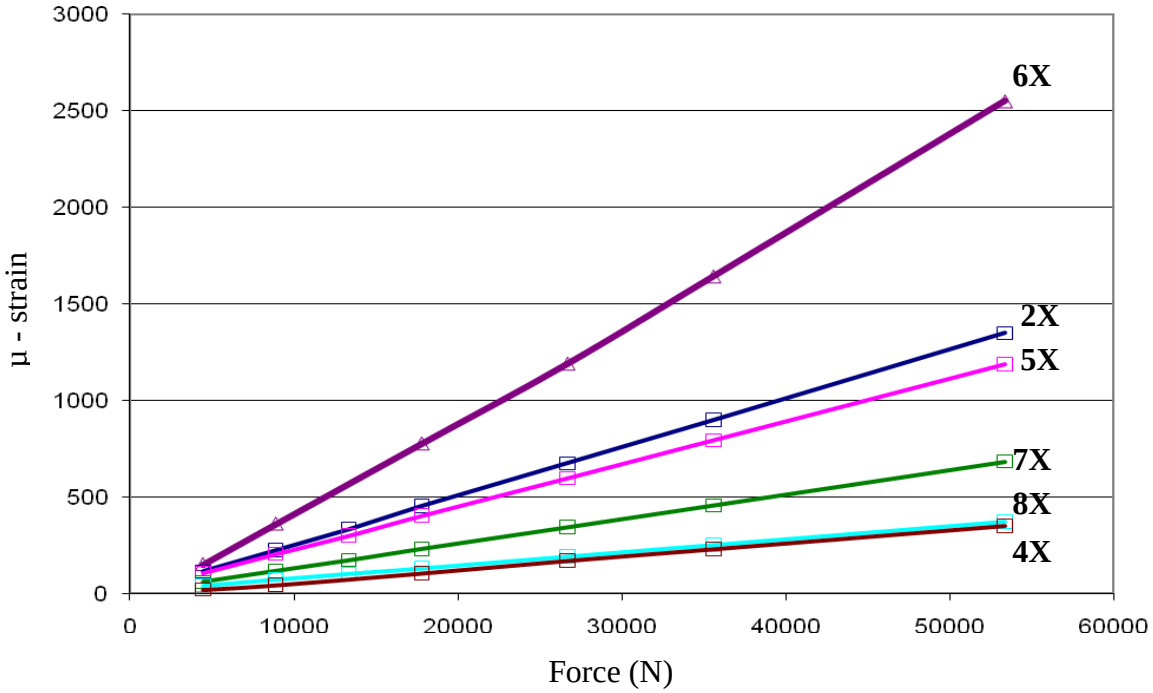

(b)

Figure 10: Measured strains in the X-dir for conventional sample for a) in-plane loading and b) general loading

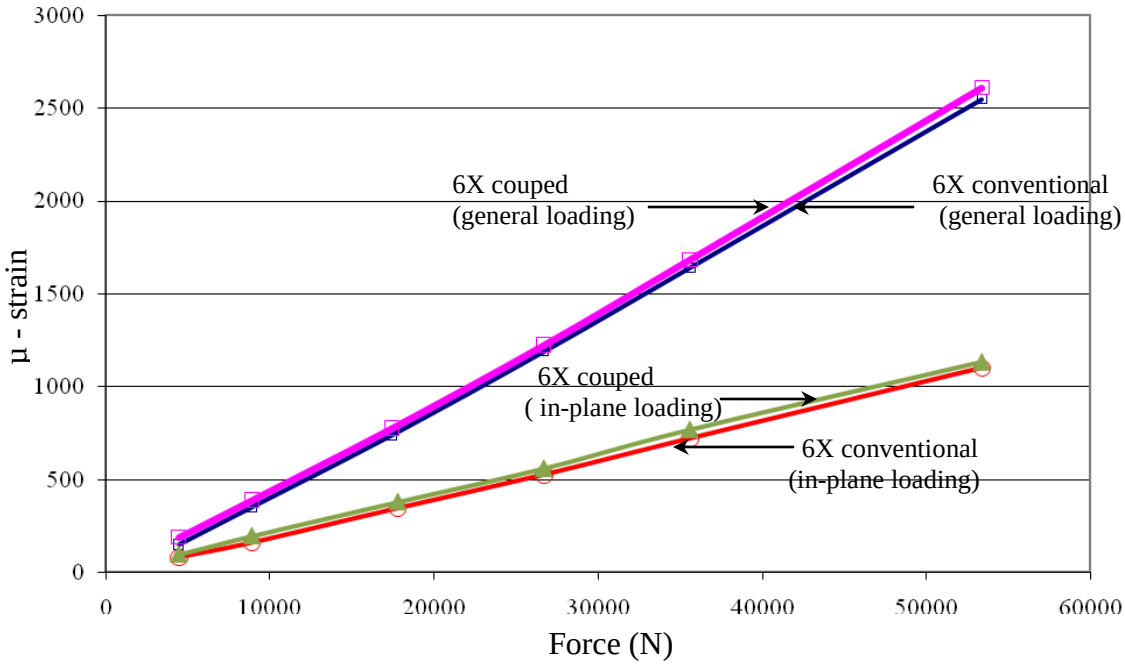

Figure 11: Comparison of the strain readings at location 6 in the X-direction for the conventional and couped samples

5.0 Finite element analysis

5.1 Finite element modeling of full-scale samples

The numerical modeling of the welded T-joint connection is performed using ANSYS [8], the commercial finite element package. The developed FE model is based on the assumption of linear elasticity and small strains/displacements. Due to the inability of the shell elements to accurately model the interaction between the tubular members and the weld, solid elements have been used for modeling both the tubes and the welds in this study. Quadratic solid elements (20-noded) with three translational degrees-of-freedom at each node were used to model the weld and the tubes' structure. In order to accurately capture any non-linear stress gradients through the thickness of the tubes, 10 solid elements were employed to model the tubes' thickness (shown in Figure 12). Previous numerical experiments by the authors [9-11], have shown that the SHS-SHS T-joints

behave similar to beams at a sufficient distance from the connection. This distance is approximately equal to one side length of the cross-section. For this reason and also for numerical efficiency, only regions close to the connection were modeled with solid elements. Away from the connection the tubes were modeled by beam elements as shown in Figure 12 (beam 4 from the FE software library was used). For the beam elements, the following parameters were used which corresponded to the cross-sectional properties of the tubes: the area moment of inertia $Iz = Iy$ = 3.67*E*-06 m^4 (8.83 in^4), cross sectional area A = 2.42*E*-03 m^2 (3.75 in^2), and the torsional constant J = 6.66*E*-06 m^4 (16 in^4).

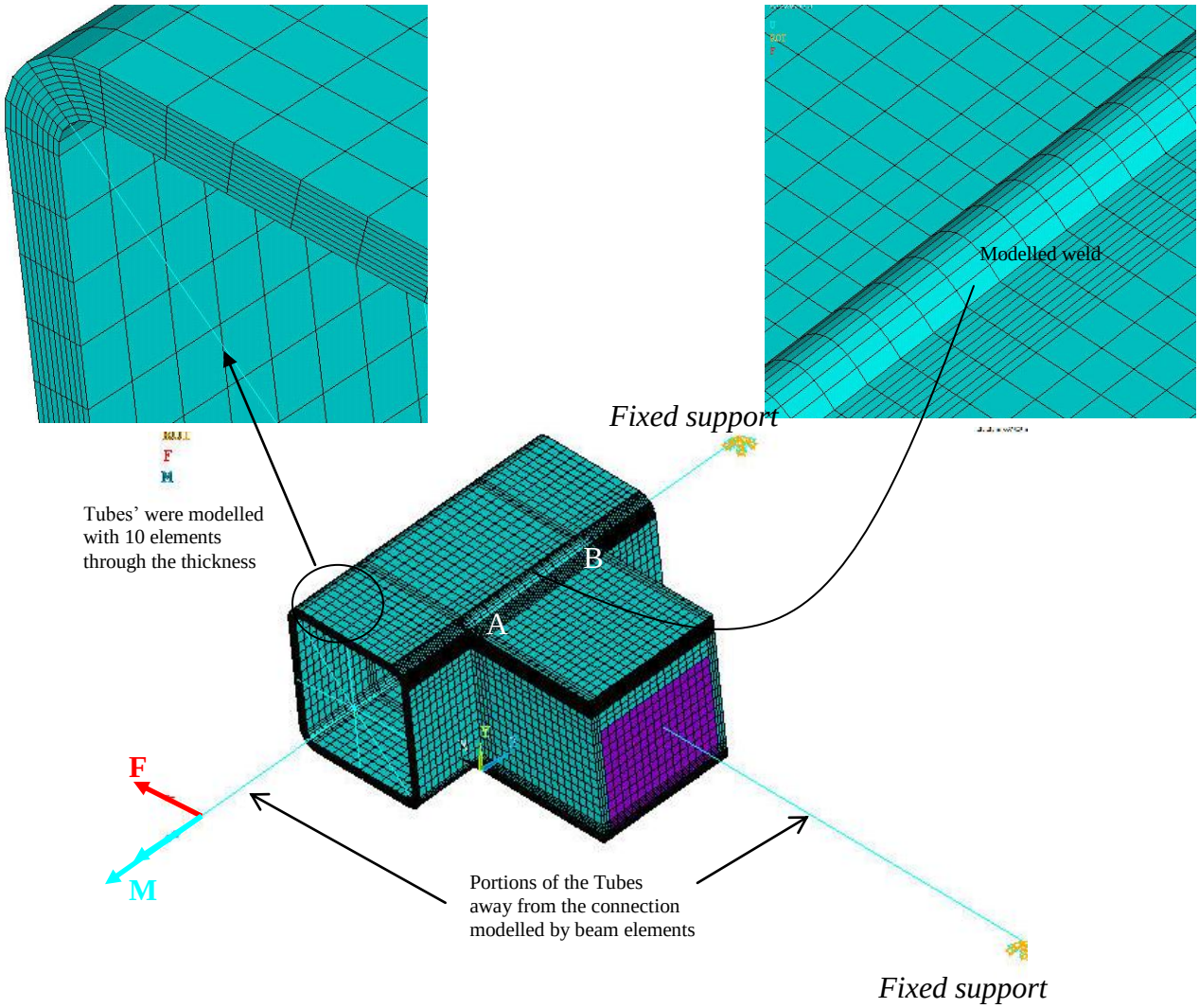

Figure 12: FE solid element model of the welded T-joint

For the accurate FE modeling, measurements of the weld profile (location of the weld toe, approximate height, width of the weld, and depth of penetration) have been taken from the actual samples. Due to the local notch stress concentrations, the weld toe is typically the location for the maximum stresses, causing fatigue cracks and plastic deformation to be initiated at these locations. For this reason, the profile of the weld can be somewhat arbitrary as long as the weld penetration and dimensions are similar to the actual welded samples. It should be noted that full penetration welds (as shown in Figure 6) were modeled for the conventional samples. Figures 13a and 13b depict the FE model of the cross-section corresponding to that of a conventional sample. The figures show the nodes of the modelled cross-section. All nodes along the path between nodes 1 and 3 (shown in Figure 13b) which are common between the tubes and the weld are connected, resembling a full penetration weld. In the case of the couped samples, the weld penetration extends to approximately half of the thickness of the tubes (as shown in Figure 5) and has been modeled as such for the FEA. Figures 13c and 13d represent the modeled cross-section and the corresponding nodes for a couped sample. To model the depth of penetration in the couped T-joint samples, the path shown between nodes 1 and 2 in Figure 13d was modeled with two sets of coincident nodes which are not connected to one another. The length and geometry of this path was chosen so that it resembles that of a typical couped T-joint. The path between nodes 2 and 3 shown in Figure 13d was modeled with one set of nodes which are common between the tubes and the welds. The same meshing (i.e., identical element sizes and shapes) were used for the FE models of the couped and conventional samples.

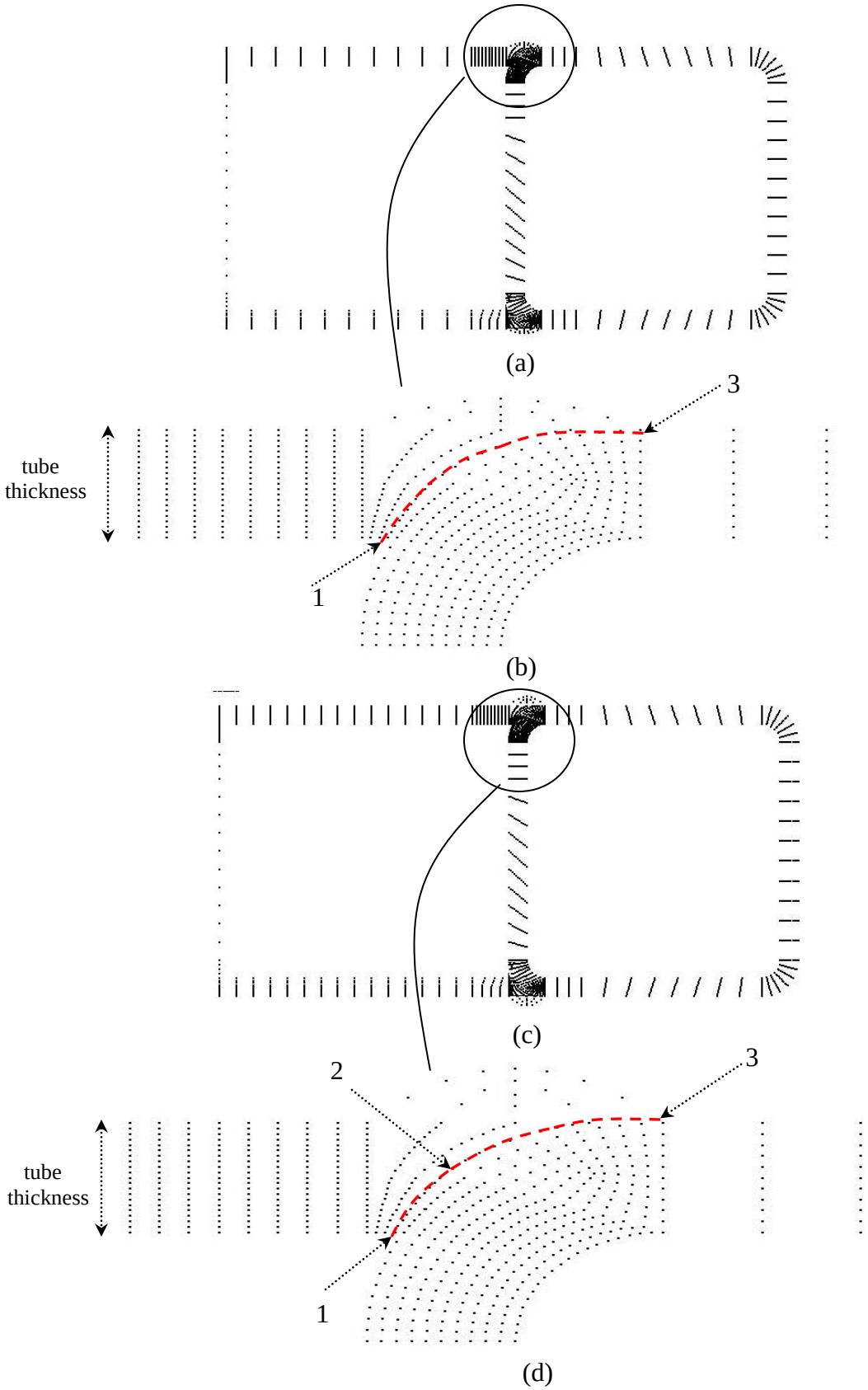

Figure 13: Modeled cross-section and corresponding nodes in FEA for a-b) conventional and c-d) couped T-joint

5.2 FEA results and verification

To assess the effectiveness and accuracy of the modeling, the numerical and experimental results were compared to verify the validity of the developed FE models. As mentioned previously, static loads ranging from 4,448*N* (1,000 lbs) to 53,380*N* (12,000 lbs) were applied in the experiments. The same loads were also applied in the FE models. The experimental and FE strains for both loading conditions (in-plane and general) and for both types of samples (couped and conventional) were compared. The strains obtained from the simulations and those from the experiments are tabulated in Table 1 for location 6 (i.e., gauge location where the maximum strains occurred). The results show that in general a good agreement exists between the experimental and numerical strains. From Table 1, it can be observed that the strain readings for the couped samples are slightly higher than those of the conventional samples. For instance, for the case of F = 53,380N (12,000lbs) and for general loading conditions, the FEA results show about 5% increase (from 2407 to 2525 μ-strain) in the strains of the couped samples relative to those of the conventional samples. This ratio is about 3% for the experimental results (from 2250 to 2610 μ-strain). Similar observations can be made for the in-plane loading conditions.

Table 1: FEA and experimental strain readings at location 6 in the X-direction of the T-joint (strain values are in μ-strain)

12000lbs (53380*N*)	**6X general loading (couped)**	**6X general loading (conventional)**	**6X in-plane loading (couped)**	**6X in-plane loading (conventional)**
FEA	2525	2407	945	895
Experimental	2610	2550	1106	1050
8000lbs (35586 *N*)				
FEA	1683	1604	630	597
Experimental	1685	1642	769	720
6000lbs (26689 *N*)				
FEA	1263	1203	473	448
Experimental	1225	1190	560	510
4000lbs (17793*N*)				
FEA	842	802	315	298
Experimental	776	741	381	345
2000lbs (8896*N*)				
FEA	421	401	158	149
Experimental	390	352	196	160

As the validity of the FE models were verified through the comparison of the FE and experimental strains, the developed models were used to obtain a more thorough understanding of the stress distribution around the connection of the couped and the conventional samples. It should be noted that with the existence of sharp corners at the weld toes, the elastic stress is theoretically infinite at these locations. This means that one can not simply obtain the stresses at the weld toe from the FE results file, as they do not converge and are mesh sensitive. A detailed analysis of the T-joint can be based on the fracture mechanics (F-M) methodology taking into account the crack growth and the local stress gradients. The failure criteria would then be based on the values of the critical stress intensity factors and the material fracture toughness. The F-M approach however requires relatively expensive computational efforts and is well suited for the analysis of

joints where cracks have already occurred. Another technique commonly used for the approximation of the stresses at the weld toe is the hot spot stress approach [11-14]. This approach requires the extrapolation of the local stresses close to the weld, to the location of the weld toe. Currently, the hot spot stress concept, when effectively linked to the FE results, is considered to be an efficient methodology for engineering design in the industry [15]. This approach when applied to the couped and conventional samples employed in this study, results in nearly the same stresses at the weld toe. This is because the stresses in the vicinity of the weld toes in these two types of samples are very similar to one another.

In this study, the main point of interest is the relative increase in the fatigue strength of the couped samples to that of the conventional samples. The fatigue strength of the T-joints is governed by the local stresses that occur at the failure critical points such as the weld toes. Even though the developed FE models can not be used to obtain the exact magnitude of the stresses at the location of the weld toe, however, since the meshing (i.e., element sizes) for the conventional and couped samples are identical, the relative stress amplification/reduction between these two different types of samples can be accurately obtained.

For comparison, along the weld toe at the top of connection (the path starting at point B and ending at point A, shown in Figure 12), the stresses on the mid-thickness of the tubes (i.e., membrane stresses) and the top surface (which includes both the membrane and the bending stresses) are considered. Figures 14 and 15 depict the FEA results for the general loading conditions and a couped sample. All of the 6 components of the stress distributions (i.e., normal and shear) and the Von-Mises equivalent stresses at the

connection are considered. It is important to examine these stresses in detail in order to obtain insight into the components of stress that cause the most damage. The dominating role of the normal stresses in the x-direction on the membrane and bending stresses can be observed in Figures 14 and 15.

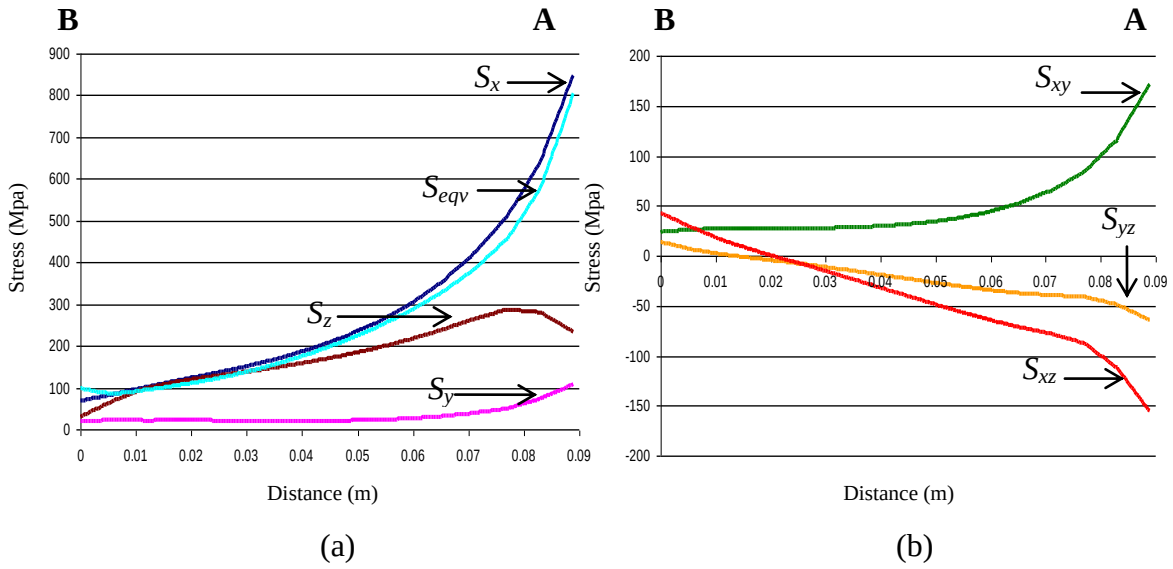

Figure 14: Stresses along the path BA (shown in Figure 12) for the top surface of the tube: a) Normal stress and b) Shear stress components

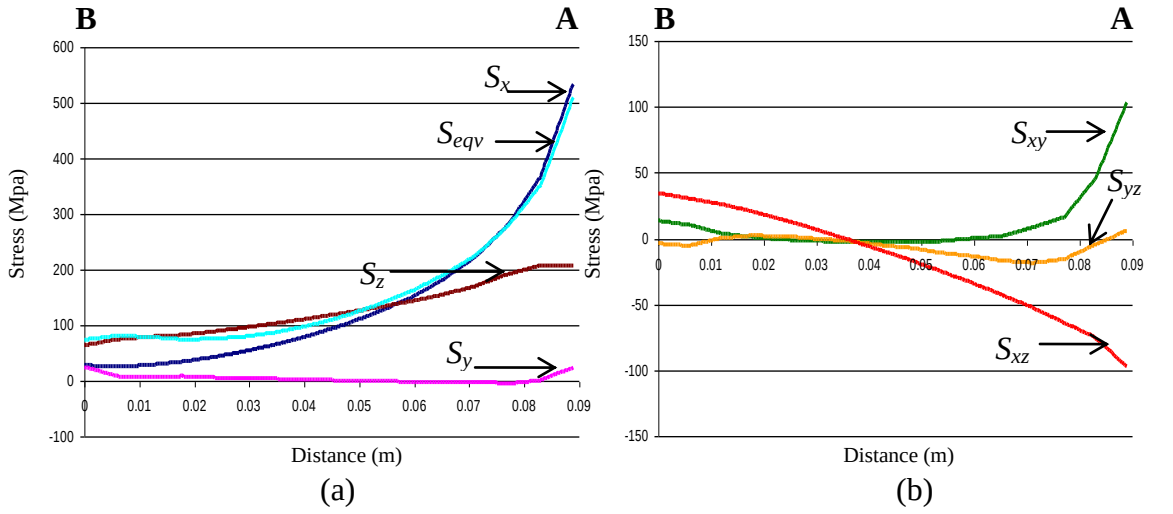

Figure 15: Stresses along the path BA (shown in Figure 12) for the mid-thickness of the tube: a) Normal stress and b) Shear stress components

The normal stresses in the x-direction are the highest with a maximum value of approximately 846MPa at the weld toe at location 6 (near point A) on the top surface, and 520MPa at the mid-thickness of the tubes. It can be observed that the x-direction component of normal stress causes the most damage. The values of the Von-Mises equivalent stresses are very close to the values of the stresses in the x-direction. This is expected as the stresses in the x-direction are much larger than the other components of stress. Similar observations were made from the FEA results for of the conventional samples. Also, for the case of the in-plane loading conditions, it was observed that the x-direction stresses are the most dominant. This is in agreement with the works of [16-19] which suggest that the strains and stresses normal to the weld toe (i.e., x-direction in this study) are mainly responsible for plasticity/crack initiation and propagation.

As the dominating role of the x-direction stresses was observed and discussed from Figures 14 and 15, these stresses were examined in more details for the comparison of the stress distribution around the connection of the couped and conventional samples. Figures 16a) and 16b) depict the FEA results for the general and in-plane loading conditions in the x-direction, respectively. For both loading conditions, only a slight increase in the stresses of the couped sample relative to the conventional sample is observed. For the general loading conditions, the maximum membrane stresses for the conventional sample were 500MPa while for the couped sample were 520MPa (about 4% increase). At the top surface (i.e. at the weld toe) of the connection, the maximum stresses were 828MPa and 846MPa for the conventional and couped samples, respectively (about 2% increase). Similar observations were also made in the case of the in-plane loading conditions, where

the stress distribution in the vicinity of the couped and conventional samples was observed to be very similar.

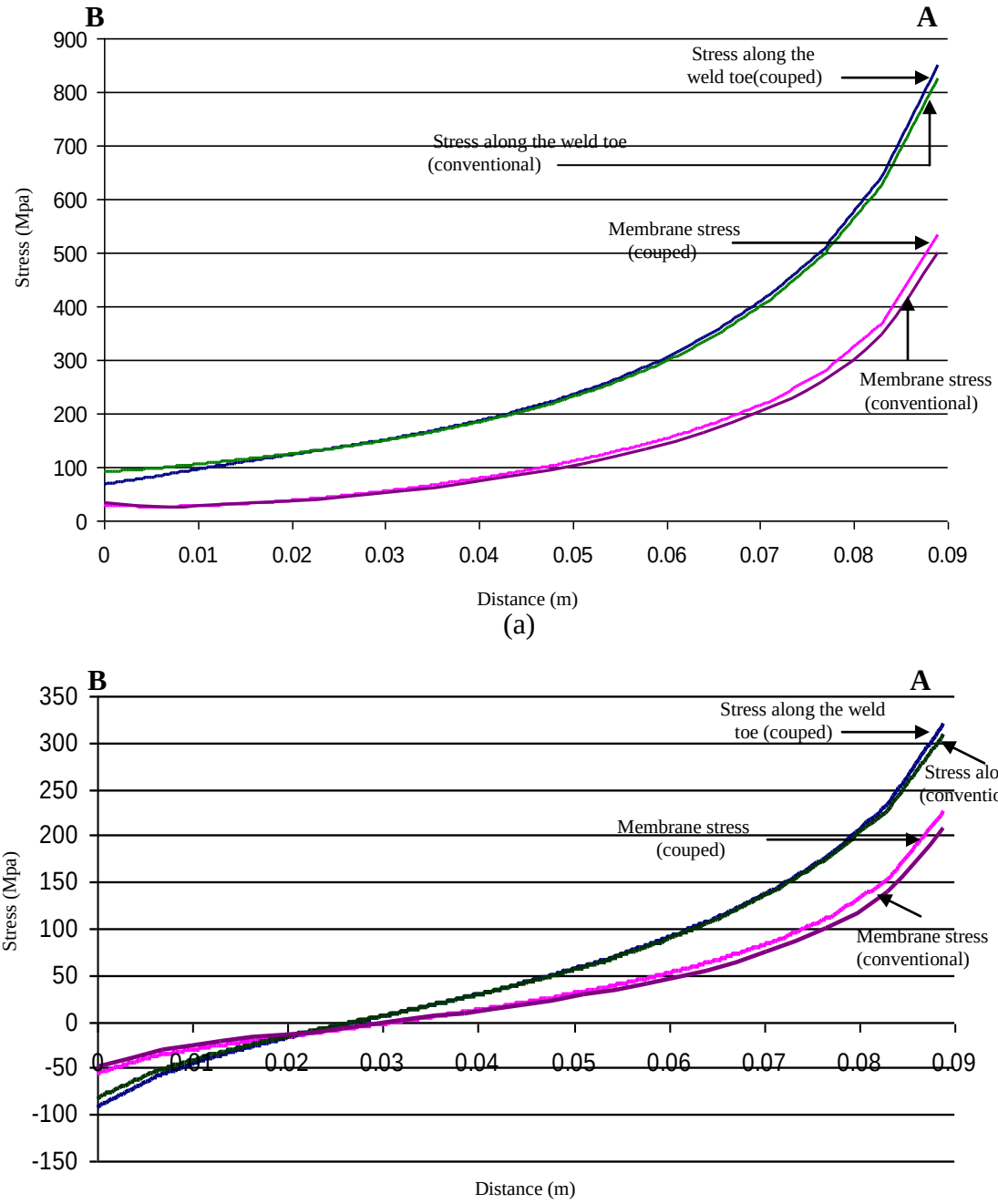

Figure 16: Membrane and bending stresses in the X-direction for the couped and conventional samples for a) general and b) in-plane loading conditions

6.0 Fatigue tests performed on full-scale T-joint samples

The fatigue tests of the full-scale T-joints were performed using test rig 2 (general loading conditions). It was observed that with cyclic loads of less than ±17793N (4000lbs) there were no signs of cracks on the conventional or couped samples at over 1 million cycles. Experimental and simulations results suggested that the resulting stresses from applied loads of less than 4000lbs were below the endurance limit of the material, therefore the specimens did not fail. For the fatigue tests, when a crack of approximately 3.8cm (1.5 inches) in length was formed, the specimen was considered to have failed and the cyclic load was removed. This crack length was chosen to ensure that the fatigue crack on all of the T-joint samples has reached a size which is visible without difficulty by the naked eye. It is well known that the frequency of the applied load has no significant effect on the fatigue life of the component. In this study, the frequency of the applied load was kept in the range of 0.1Hz to 0.5Hz. The reason for operating at these low frequencies was due to the induced vibrations on the test fixture at higher frequencies. This was one of the challenges of working with full-scale samples.

The fatigue cracks on all, but two of the T-joint samples were initiated at the weld toe close to location 6 (point A), which corresponds well with the location of the maximum stresses from the FEA. The cracks were initiated and propagated at the weld toe. Figure 17a shows a typical cracked T-joint. It should be noted that the cracks on the two T-joints that did not occur at the weld toe, were still in the vicinity of location 6. On these two samples the cracks initiated and propagated at the weld itself, not the weld toe. This can be the result of some imperfections and irregularities in the microstructure of the weld. The crack on one of these samples is shown in Figure 17b. The initiation of the crack at

the weld toe of the T-joints is expected. The fatigue tests on the small krouse specimens showed that the weld material has a higher fatigue strength than the parent metal. In addition, the weld toe is influenced by the relatively weaker material properties of the heat affected zone and the maximum stresses (large stress concentrations) typically occur there.

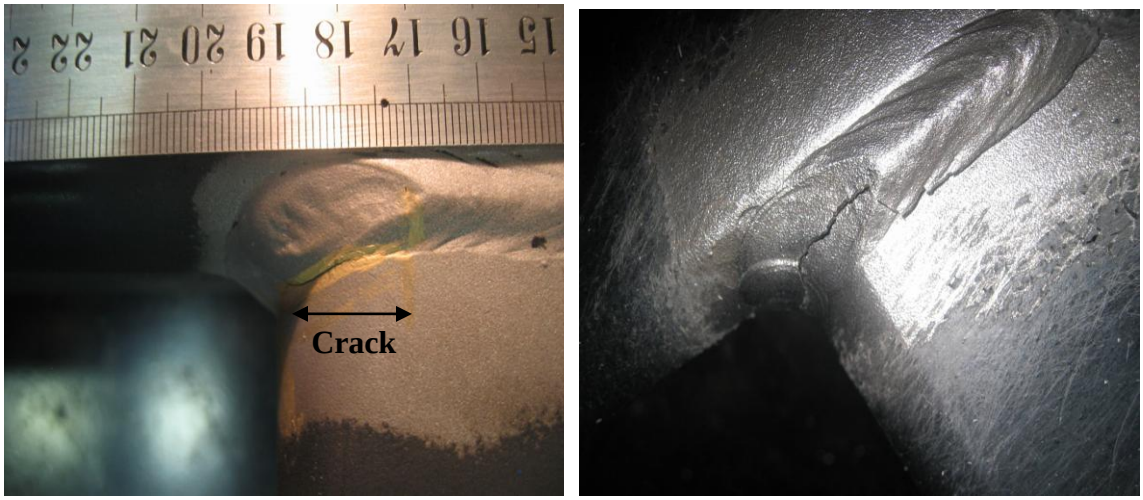

(a) (b)

Figure 17: T-joint sample with fatigue crack initiated a) at the weld toe close to location 6. and b) at the weld itself close to location 6.

Figure 18 presents the load-life diagram of the couped and conventional samples. It can be seen that the couped samples typically have a higher fatigue strength than their conventional counterparts. This increase in fatigue strength is more pronounced with high cycle fatigue (i.e., smaller loads). For instance, for the conventional and couped samples tested at 12,000lbs, the fatigue life was found to be 201 and 234 cycles, respectively. In comparison, at 4,500lbs, the fatigue life of the conventional sample was 75,000 cycles while that of the couped sample was 120,000 cycles.

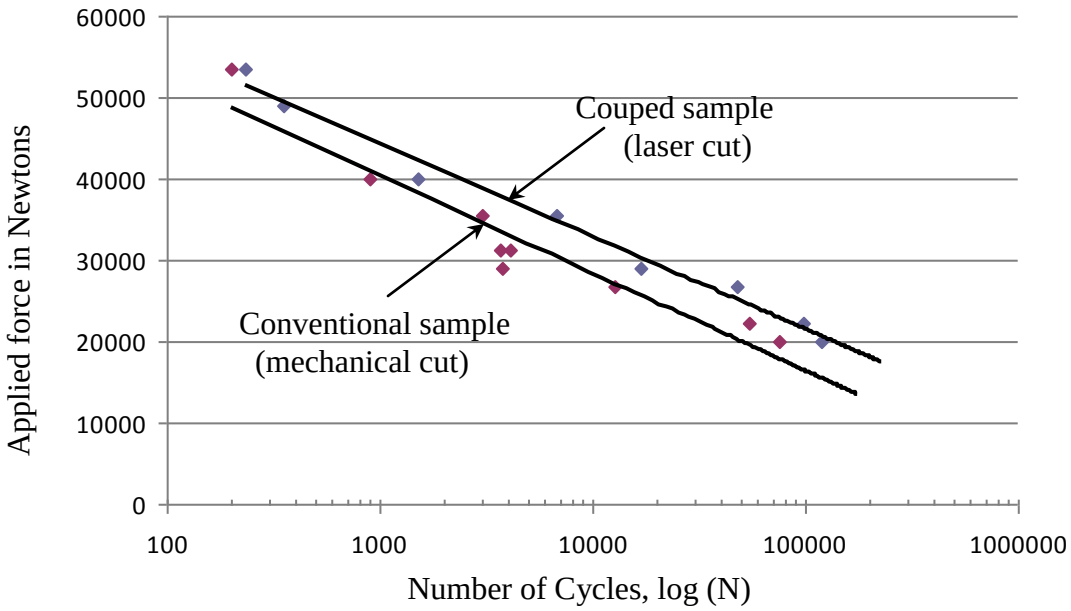

Figure 18: Load-life diagram to failure for 3.8 cm (1.5 inch) fatigue crack for loads ranging from 4,500-12,000 lbs (20,017 to 53,379 N).

The static FEA of the couped and conventional T-joints showed that the stresses at and in the vicinity of the weld toe of the couped samples are only marginally higher (generally less than 5%) than the conventional samples. Similar observations were made from the experimental study and strain measurements subjecting the T-joints to static loads. The fatigue tests on the T-joints however show that the couped samples have a higher fatigue strength than their conventional counterparts. The main reason for this increase in the fatigue life of the couped samples can be attributed to the improvement in the mechanical properties as a result of laser cutting versus mechanical cutting. This is in agreement with experimental studies by Meurling et al [1,2, and 4] on sheet steels that suggested laser cutting produces higher fatigue strengths than mechanical cutting. This increase in strength could be up to 30% [1]. In those studies, the main explanation for the lower fatigue lives after mechanical cutting was the presence of larger surface defects on the cut edges relative to laser cut edges.

7.0 Conclusions

The use of laser cutting technology to produce SHS-to-SHS T-joint connections of higher fatigue strength in comparison with those produced using traditional mechanical cutting tools was investigated. On two T-joint samples, 8 strain gauges were installed around the connection of each sample for strain measurements and to verify the FE models. The FEA results were compared with the experimental strain readings and it was shown that the developed FE models are valid for the modeling of both the conventional and couped SHS T-joint connections. The fatigue properties of the weld (i.e., electrode) and parent material (steel used for the manufacturing of the tubes) were determined using laboratory krouse samples subjected to rotating bending fatigue tests. For the fatigue tests of the T-joints, 19 full-scale welded samples (both couped and conventional) with dimensions typical to those found in the agricultural industry were used. The T-joint samples were subjected to cyclic loads. It was observed that the fatigue strength of the couped samples in general is higher than the conventional samples. The results of the experimental and FEA investigations suggest that the tubes can be effectively cut using laser beam to fit the profile of body of the other tube before welding. Then one pass of weld is enough to obtain a higher fatigue strength than conventional cut and several pass of welds. This will result in shorter production series and quicker prototype developments. The results of this research work can be used as a tool for engineers and researchers working in the manufacturing and construction industries.

References

[1] Meurling F, Melander A, Linder J, and Larsson M. The influence of mechanical and laser cutting on the fatigue strengths of carbon and stainless sheet steels. *Scandinavian Journal of Metallurgy* (2001); 30(5): 309-319.

[2] Meurling F, Melander A, Linder J, Larsson M, and Trogen H. The influence of laser cutting on the fatigue properties of thin sheet steels. *Swedish Institute for Metals Research Report* (1998); IM-3691.

[3] Sperle J.O. Influence of parent metal strength on the fatigue strength of parent material with machines and thermally cut edges. *Welding in the World Journal* (2008); 52(7-8): 79-92.

[4] Maronne E, Galtier A, Robert J.L., and Ishikawa T. Cutting process influence on fatigue properties of steel sheets. *Advances in Damage Mechanics* (2003); 13-22.

[5] Rashed F, and Nassef A. Effect of low cycle fatigue on surface finish. *American Society of Mechanical Engineers (ASME): Contact Problems and Surface Interactions in Manufacturing and Tribological Systems* (1993); v(67): 327-332.

[6] Meurling F, Melander A, and Linder J. Comparison of the fatigue characteristics of punched and laser cut stainless steel sheets. *Scandinavian Journal of Metallurgy* (1998); 3v(30): 351-372.

[7] AmericanWelding Society. ANSI/AWS D1.1-96 Structural welding code steel. Miami, USA; 1996.

[8] Ansys Version 11.0 Standard User's Manual, 2008.

[9] Moazed R, Szyszkowski W, Fotouhi R. The in-plane behaviour and FE modeling of a T-joint connection of thin-walled square tubes. *Journal of Thin-Walled Structures* (2009); 47(7): 816-825.

[10] Moazed R, Fotouhi R, Szyszkowski W, and Bitner, D. Welded T-joint connections of square thin-walled tubes under a multi-axial state of stress. *Journal of Strain Analysis for Engineering Design* (In Press).

[11] Moazed R, Fotouhi R, Szyszkowski W. Out-of-plane behaviour and FE modeling of a T-joint connection of thin-walled square tubes. *Submitted to the Journal of Thin-Walled Structures* (unpublished).

[12] Fung T-C, Soh C-K, Chan T-K. Stress concentration factors of doubler reinforced tubular T joints. Journal of Structural Engineering (2002); 128(11): 1399-1412.

[13] Lee M-K, Llewelyn-Parry A. Offshore tubular T-joints reinforced with internal plain annular ring stiffeners. Journal of Structural Engineering (2004); 130(6): 942-951.

[14] Kosteski N, Packer J-A, Cao J-J. Experimental study of through plate, transverse plate, and stiffened plate-to-RHS member connections. Proceedings of the International Offshore and Polar Engineering Conference (1999); v(4): 38-45.

[15] Lotsberg I, Sigurdsson G. Hot spot stress S-N curve for fatigue analysis of plated structures. Transactions of the ASME. Journal of Offshore Mechanics and Arctic Engineering (2006); 128(4): 330-336.

[16] Pang H-J, Lee C-W. Three-dimensional finite element analysis of a tubular T-joint under combined loading. International Journal of Fatigue (1995); 17(5): 313-320.

[17] Bian L-C, Lim J-K. Fatigue strength and stress concentration factors of CHS-to-RHS T-joints. Journal of Constructional Steel Research (2003); 59(5): 627-640.

[18] Hiroko K, Pingsha D. Equilibrium-equivalent structural stress approach to fatigue analysis of a rectangular hollow section joint. International Journal of Fatigue (2005); 27(1): 85-94.

[19] Nazari A, Daniel W.J.T., Guan Z, Gurgenci H. Parametric equations using generic representation of joint stiffness. Transactions of the ASME. Journal of Offshore Mechanics and Arctic Engineering (2007); 129(2): 131-137.

Chapter 6: Conclusions, Contributions and Future Works

In this dissertation, the behaviour of SHS-to-SHS T-joint connections subjected to static and cyclic loads was studied. The results and conclusions of this research work have practical applications and can be used by engineers and researchers working in the manufacturing and construction industries. In section 6.1, the summary and conclusions of this thesis are presented. Also, the contributions of the candidate's work are highlighted in section 6.2. The potential future works which can be done in the continuation of this work are presented in section 6.3.

6.1 Summary and conclusions

The deformation patterns and stress distribution around the connection of SHS-to-SHS T-joint connections subjected to different loading conditions were examined in detail in chapters 2 and 3. In chapter 2, the behaviour of SHS T-joint connections subjected to in-plane bending (IPB) loading conditions was analyzed. The reasons for the stress concentrations and the stiffness reduction of the connection, when the T-joints are subjected to such loading conditions were provided. The parameters characterizing the connection's stiffness and the stress concentrations were found to be only dependent on the tube's thin-wallness ratio. A simplified approach for the analysis of the SHS-to-SHS T-joint connections under IPB loading conditions was proposed and the effectiveness of the approach was demonstrated by numerical examples. The approach introduced in chapter 2 successfully showed that the computational complexity involved in preparing detailed models of the T-joint connection when using shell and solid elements can be substantially reduced.

In chapter 3, the approach presented for the analysis of the T-joint connections under IPB loads was extended to situations where the T-joint connections are subjected to out-of-

plane bending (OPB) conditions. The parameters characterizing the stress concentrations and the connection's stiffness were found to be dependent on both the tube's thin-wallness ratio and the length of the longitudinal member for such loading conditions. Using these parameters, a relatively simple and accurate approach was proposed to allow modelling the tubular T-joints with the aid of one dimensional beam elements with certain properties modified. The approach's efficiency was evaluated using a few numerical examples. Chapters 2 and 3 addressed objectives 3 and 4 of this thesis.

In chapter 4 (objective 2), a welded T-joint connection of square hollow section tubes subjected to a multi-axial state of stress was examined both experimentally and numerically. In the experimental study, a test fixture with a hydraulic cylinder capable of applying both cyclic and static loads was designed and employed. Several strain gauges (a total of 16 on 2 samples) were installed around the connection of the T-joints to validate the results of the FEA. For the FE modelling, several full-scale welded T-joints were cut at the connection to obtain the size and depth of penetration of the weld. Upon the verification of the developed FE models using the experimental strain measurements, the models were used to study the through-the-thickness stress distributions of the tubes. Also, in order to limit the local deformations and to reduce the stress concentrations at the connection, plate reinforcements were used in a number of different arrangements and dimensions (objective 5). This resulted in a significant increase in the load carrying capacity of the T-joint. Chapter 4 accomplished objectives 2 and 5 of this thesis.

In chapter 5, the feasibility of using laser cutting to produce welded SHS-to-SHS T-joint connections with similar or higher fatigue strengths than conventional mechanical cut T-joints was investigated. In the study, a total of 21 full-scale T-joints were included.

Nineteen of these T-joint samples were subjected to cyclic loads with the intention to form a fatigue crack of approximately 3.8cm (1.5 inches) in length. On two of the T-joint samples strain gauges were attached. FE models of both types of T-joints manufactured with the different cutting techniques were also developed. The FE models were used for the comparison of the stress distribution around the connection of the two different T-joints. The FEA results of the numerical study were verified with the strain measurements.

6.2. Contributions of the research:

The contributions of the candidate's research cover the objectives stated in section 1.2. The contributions of this research work can be summarized as follows:

6.2.1. Contribution 1 - The use of laser cutting technology to produce SHS-to-SHS T-joint connections of higher fatigue strength in comparison with those produced using traditional mechanical cutting tools.

Previous investigations on sheet steels have concluded that under constant and variable amplitude cyclic loads, laser cutting produces higher fatigue strengths than its mechanical cut counterpart. However, there are no such studies performed on full-scale and more complicated steel structures such as the T-joint samples employed in this study. The results of the experimental investigations on 21 samples from this study showed that the T-joint connections constructed using laser cutting provide higher fatigue strengths than the T-joint connections fabricated using mechanical cutting. Laser cutting is also beneficial as it will result in shorter production series and quicker prototype

developments. The results of this research work can be used as a tool for engineers and researchers working in the manufacturing and construction industries. This contribution is discussed in chapter 5.

6.2.2. Contribution 2- The accurate FE modelling of the welded SHS-to-SHS T-joint, and the effects of the weld geometry on the stresses at the connection.

A detailed FE model of the tubes and the weld using solid elements was constructed. Upon the verification of the FE model with experimental strain measurements, the effects of the weld geometry on the stresses in the vicinity of the connection were considered. It was observed that the membrane stresses remain unaffected by the weld geometry. The weld geometry only affects the bending stresses. The effect of the weld geometry on the bending stresses however, is highly localized and typically disappears within a distance of half of the weld width from the location of the weld toe. This finding is important as it shows that a particular geometry of the weld does not affect the maximum membrane stresses predicted by the simplified approach presented in chapters 2 and 3. This contribution was detailed in chapter 4 of this thesis.

6.2.3. Contribution 3- The thorough understanding of the behaviour of SHS-to-SHS T-joint connections subjected to in-plane and out-of-plane bending (IPB and OPB) loads.

Through a detailed FEA using shell and solid elements, the reasons for the local stress concentrations and deformations in the vicinity of the connection of the T-joints were provided. The parameters identifying the joints' stress concentrations and stiffness

reduction for different loading conditions were obtained. This understanding was crucial for the development of a simplified approach for the analysis of SHS-to-SHS T-joint connections (contribution 2) and also for the proper reinforcement of the T-joint connection (contribution 4). Contribution 1 of this research work was discussed in detail in chapters 2 and 3.

6.2.4. Contribution 4 - The development of a simplified and accurate approach for the prediction of the stiffness and maximum stresses at the connection of SHS-to-SHS T-joints.

For the accurate prediction of the state of stress at the connection of the tubular members, relatively complex FE models constructed from shell or solid elements are required. The approaches presented in chapters 2 and 3 allow for the accurate modelling of the tubes using simple beam elements with certain properties modified. The development of such beam models is much easier and computationally efficient. It is observed that the proposed approach can accurately predict all the important information of structural analysis such as the reaction forces, maximum stresses, deflections and natural frequencies. This contribution and several examples showing the correctness of the approach were provided in chapters 2 and 3.

6.2.5. Contribution 5 - The proper reinforcement of the T-joint connection in order to improved its load carrying capacity.

The large stress concentrations and local deformations which occur in the vicinity of the connection of the tubular T-joints due to applied loads, significantly reduce the load

carrying capacity of the structure as a whole. To minimize these local deformations, the effects of both internal and external reinforcement plates were considered. It was observed that external reinforcement plates can significantly reduce the maximum stresses at the connection of the T-joint. This contribution which is discussed in chapter 4 has practical applications for both new and existing T-joints used in structural components.

6.3. Potential future works

The extension of the research work presented in the previous chapters of this thesis can be from both experimental and numerical view points. The results of this study provide an in depth understanding and foundation for future research on tubular T-joint connections. The possible future research directions are as follows:

1- In the FE models presented in chapters 4 and 5, the effects of residual stresses and thermally induced distortions at the welded connection were ignored. The MIG welding process employed for the construction of the T-joints consist of melting and solidification of the weld and base metals. As a result of the intense heat concentration in a localized zone and the subsequent cooling, the temperatures which occur in the vicinity of the weld are not uniform. Plastic strains may occur due these localized temperature gradients which lead to residual stresses. The investigation of the effects of the residual stresses caused by welding, on the behaviour of the welded structure is an interesting research project. Such a study can have both experimental and numerical components. The

residual stresses should first be measured using experimental techniques and then be integrated into the FE model.

2 – The extension of the simplified approaches proposed for the analysis of SHS-to-SHS T-joint connections to tubular T-joints of different cross-sections (i.e., circular, rectangular, etc). For this purpose, a comprehensive understanding of the behaviour of the tubular T-joint under different types of loadings should first be developed. This would be similar to the understanding of the deformation patterns and stress distribution at the connection of SHS T-joints presented in chapters 2 and 3. The possibility of using FE models consisting of simple modified beam elements for the analysis of T-joints of different cross-sections can be an interesting research study.

3- Extending the numerical study on the simplified approaches to tubular joints of different geometric configurations of the connecting members (i.e., Y, K, L-joints, etc.). In such cases, in addition to the tubes' thickness and cross-sectional dimensions, geometric parameters such as the angle at which the tubular members are connected to one another can affect the stiffness and stress distribution at the connection.

4- Examination of the behaviour of the T-joint connections subjected to low cycle fatigue. Due to the extent of plastic deformation in low-cycle fatigue, usually a strain-life approach is used in studies involving fatigue failures at cycles lower than a 1000 (some experts use 10,000 cycles). This study can be extended to obtain the strain-life curves for the materials (both welded and parent) using krouse samples. Once the strain-life curves are obtained, they can be used in conjunction with the fracture mechanics approach to numerically obtain the total life of the T-joints. Fracture mechanics approaches are often

used to predict the rate of crack propagation (e.g. Paris law) and hence to estimate the total life of the component. The failure criteria in this case is be based on the values of the critical stress intensity factors and the material fracture toughness. The stress intensity factors can be determined from a detailed FEA. The estimated lives of the T-joints using FEA can then be compared and verified with those obtained from an experimental study.

Appendix A: Design and detailed drawings of the test beds used for the experimental study

This section presents the test beds developed for the purposes of the experimental study of the T-joint connections. The experimental test fixtures were designed at the University of Saskatchewan and manufactured at the R & D Department of CNH Canada, Saskatoon plant. Figure 1A, shows the different parts of the experimental apparatus.

The experimental test bed consists of 5 main parts. These different parts are as follows:

1. Base: Three quarter inch thick structural steel plate
2. T-joint samples: The test specimens are bolted to the apparatus for the experiments. These specimens are fixed on two ends (bolted to the base) as can be seen in figure 1A and attached (bolted) to part 3 on one end.
3. A T shape part for the transfer of the applied loads to the test specimens. The linear actuator exerts a force onto this part through the use of a coupler.
4. Stand for the placement of the hydraulic actuator: A linear actuator is bolted down to this part and this part is bolted down to the base (part 1) itself.
5. Hydraulic actuator for the application of the static and cyclic loads.

It should be noted than only the T-shaped part 3, and the stand (part 4) have been redesigned for the experimental test rig 2. The remainder of the parts are common between the two test fixtures.

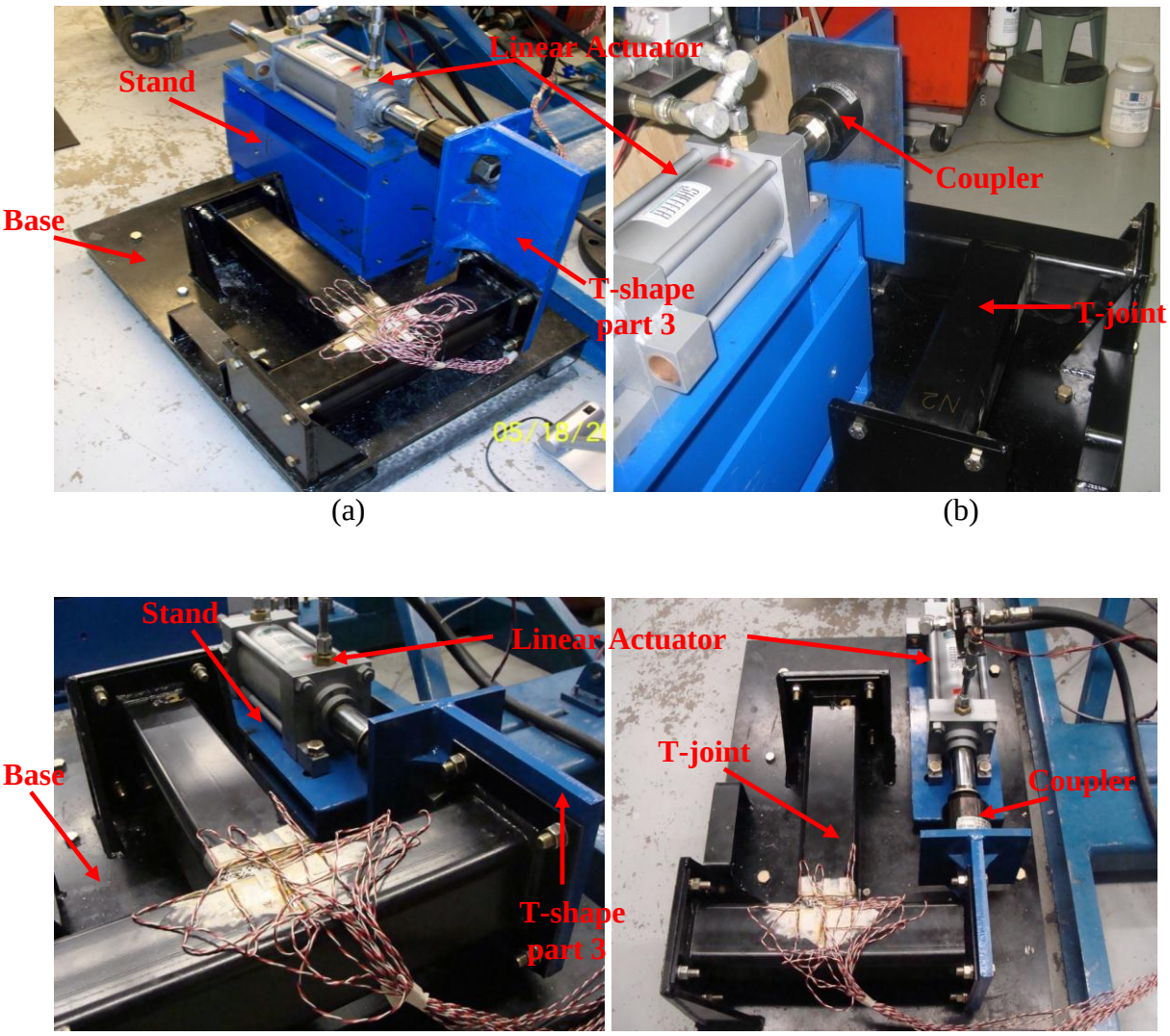

(a) (b)

(c) (d)

Figure 1A: Test rig and loading mechanism (a and b) for test rig 2 (out of plane load is applied) and (c and d) for test rig 1 (in-plane load is applied)

A1 - Detailed drawings of Part 1 (base where the T-joint connection, the stand and the hydraulic actuator are bolted to)

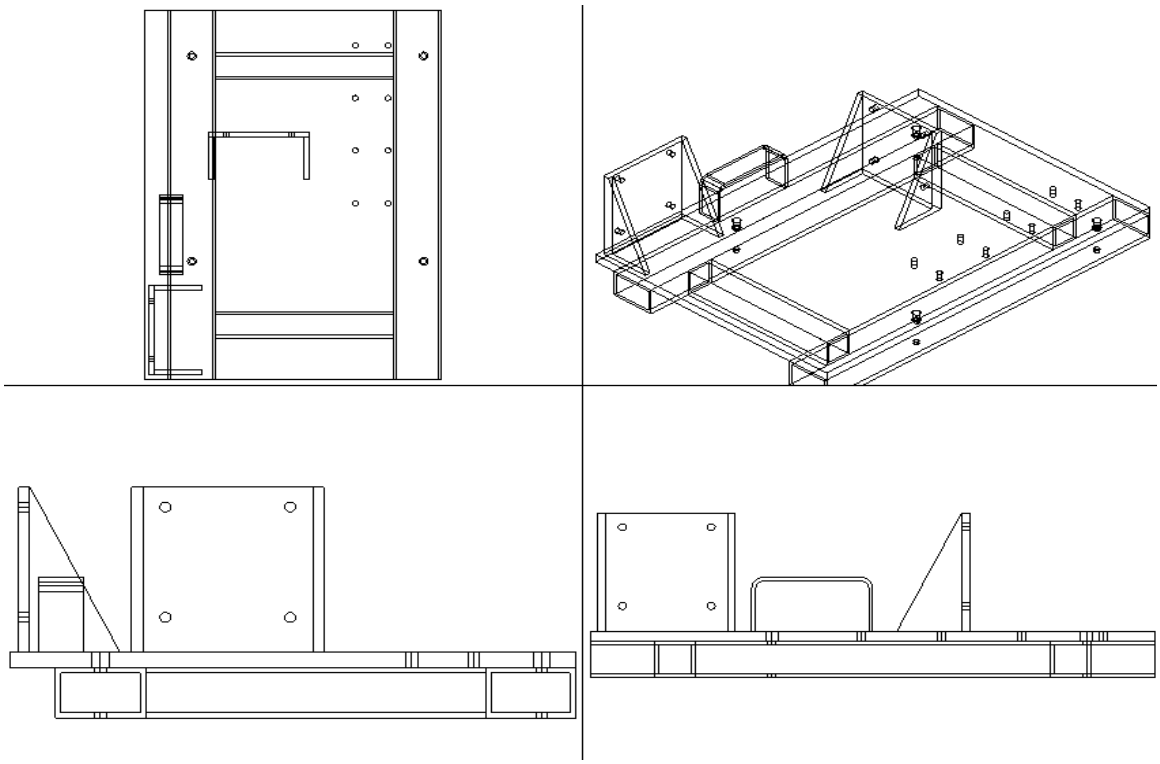

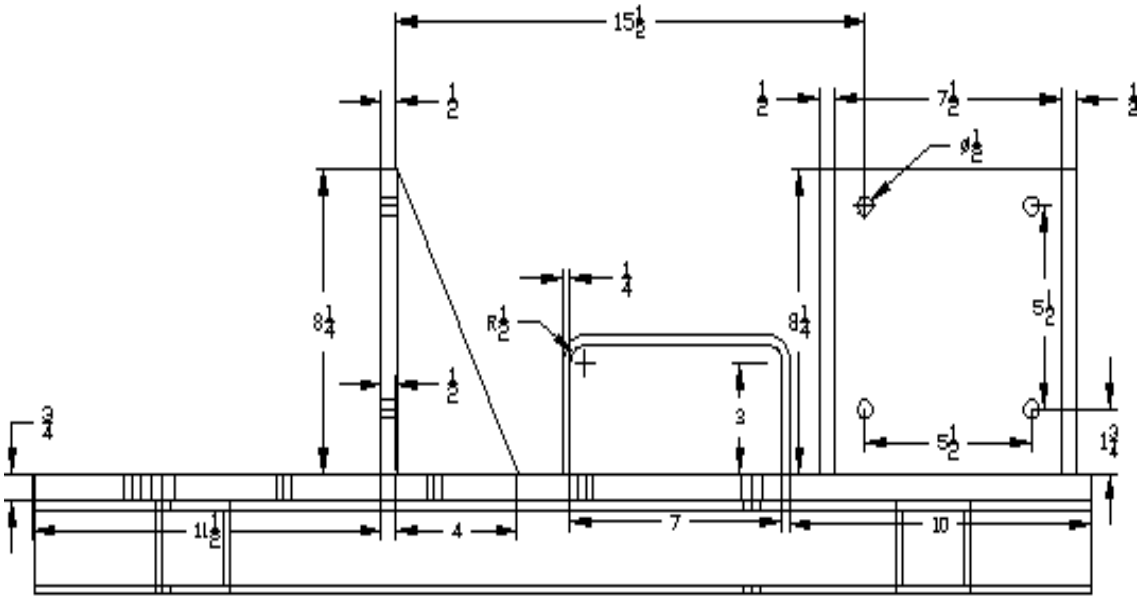

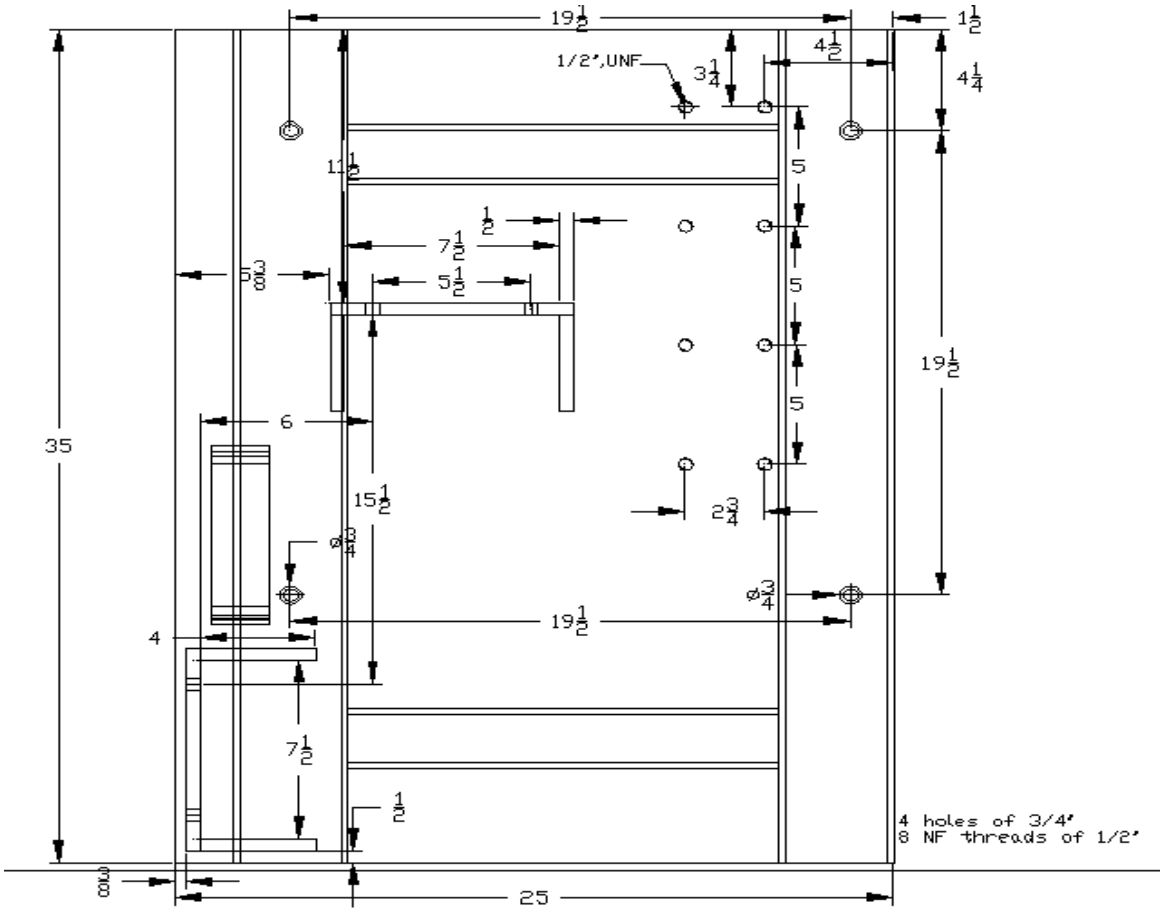
19½
1½
1/2",UNF
3¼
4½
4¼
1½
5
7½
½
5⅜
5½
5
19½
5
35
6
15½
2¾
ø¾
ø¾
19½
4
7½
½
4 holes of 3/4"
8 NF threads of 1/2"
⅜
25

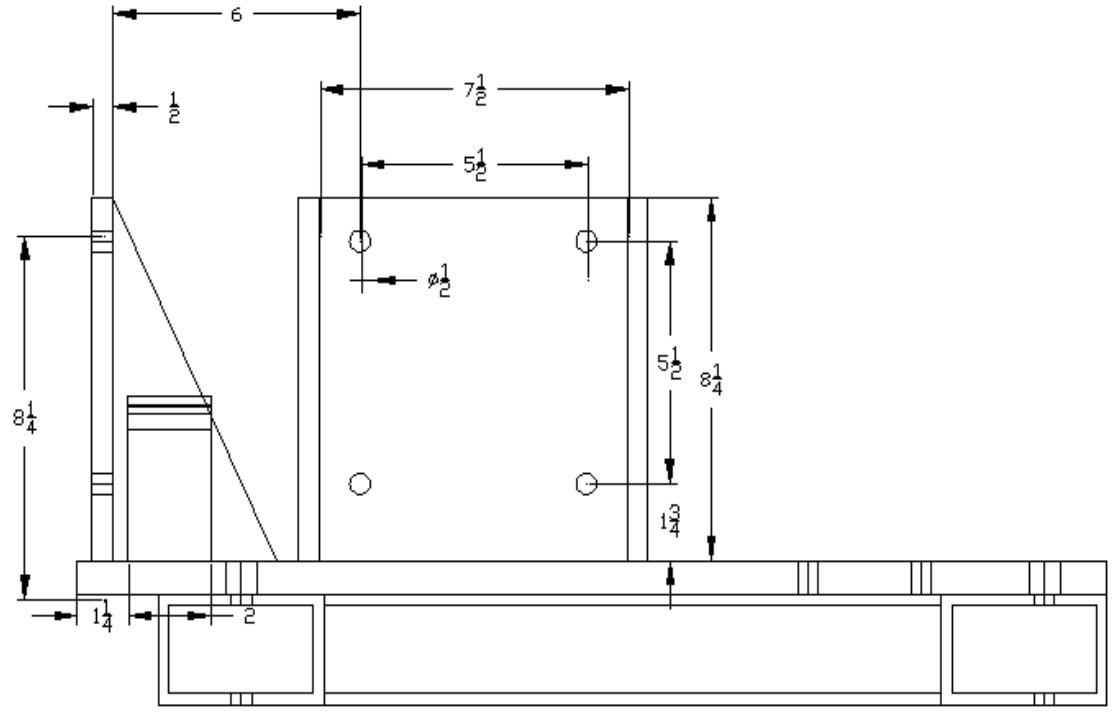
6
½
7½
5½
ø½
8¼
5½
8¼
1¾
1¼
2

A2 - Detailed Drawings of the T-joint samples (part 2)

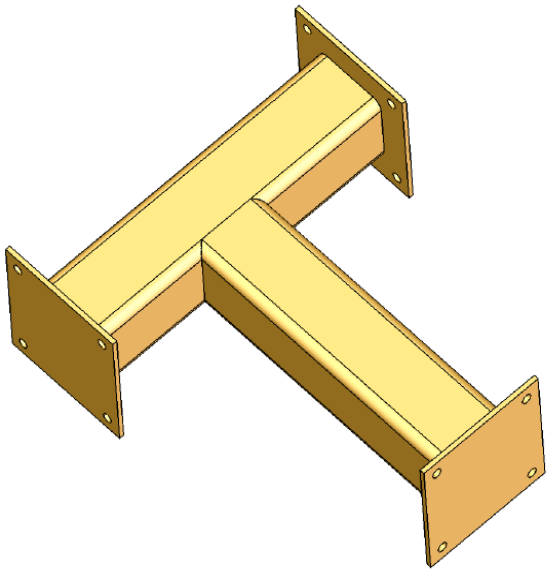

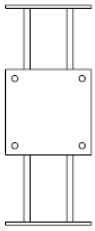

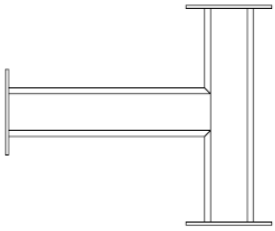

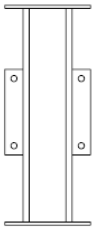

		UNLESS OTHERWISE SPECIFIED:		NAME	DATE
		DIMENSIONS ARE IN INCHES TOLERANCES: FRACTIONAL ± ANGULAR: MACH ± BEND ± TWO PLACE DECIMAL ± THREE PLACE DECIMAL ±	DRAWN		
			CHECKED		
			ENG APPR.		
			MFG APPR.		
		INTERPRET GEOMETRIC TOLERANCING PER:	Q.A.		
		MATERIAL	COMMENTS:		
NEXT ASSY	USED ON	FINISH			
APPLICATION		DO NOT SCALE DRAWING			

PROPRIETARY AND CONFIDENTIAL

THE INFORMATION CONTAINED IN THIS DRAWING IS THE SOLE PROPERTY OF <INSERT COMPANY NAME HERE>. ANY REPRODUCTION IN PART OR AS A WHOLE WITHOUT THE WRITTEN PERMISSION OF <INSERT COMPANY NAME HERE> IS PROHIBITED.

TITLE:
Couped T-joint connection
4"X4"X0.25" square tube

SIZE	DWG. NO.	REV
A		
SCALE: 1:10	WEIGHT:	SHEET 2 OF 6

5 4 3 2 1

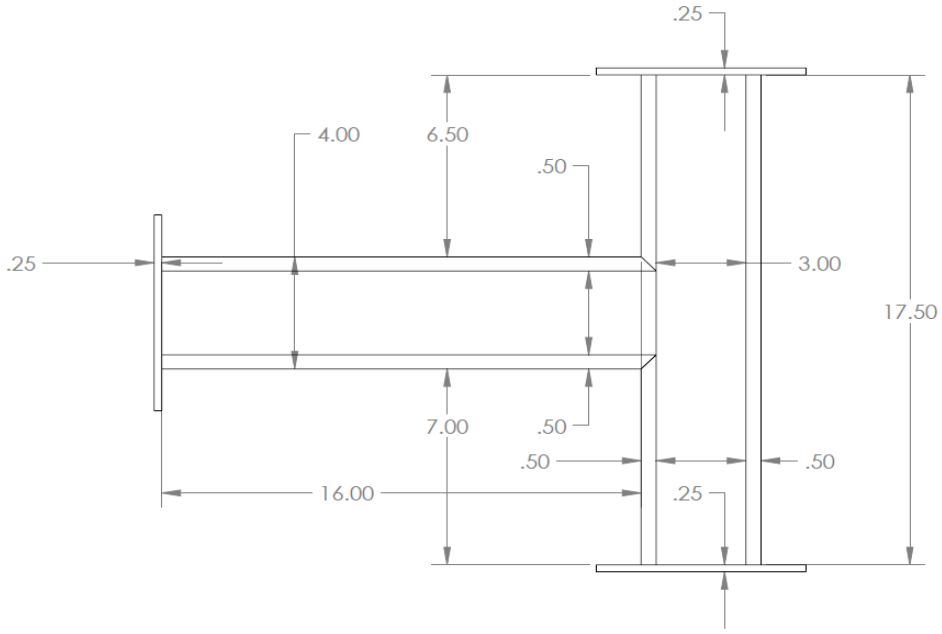

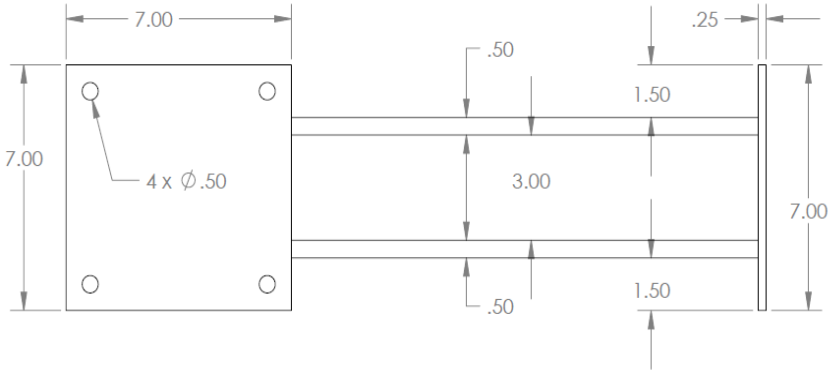

		UNLESS OTHERWISE SPECIFIED:		NAME	DATE
		DIMENSIONS ARE IN INCHES TOLERANCES: FRACTIONAL ± ANGULAR: MACH ± BEND ± TWO PLACE DECIMAL ± THREE PLACE DECIMAL ±	DRAWN		
			CHECKED		
			ENG APPR.		
			MFG APPR.		
		INTERPRET GEOMETRIC TOLERANCING PER:	Q.A.		
		MATERIAL	COMMENTS:		
NEXT ASSY	USED ON	FINISH			
APPLICATION		DO NOT SCALE DRAWING			

TITLE:
Couped T-joint connection
4"X4"X0.25" square tube

SIZE	DWG. NO.	REV
A		
SCALE: 1:10 WEIGHT:		SHEET 5 OF 6

5 4 3 2 1

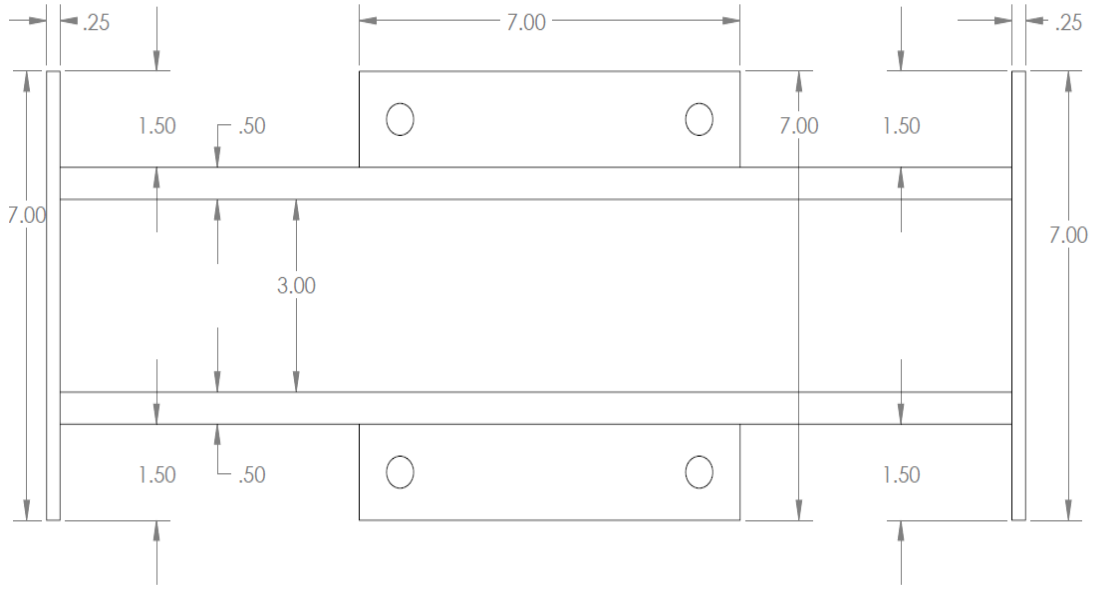

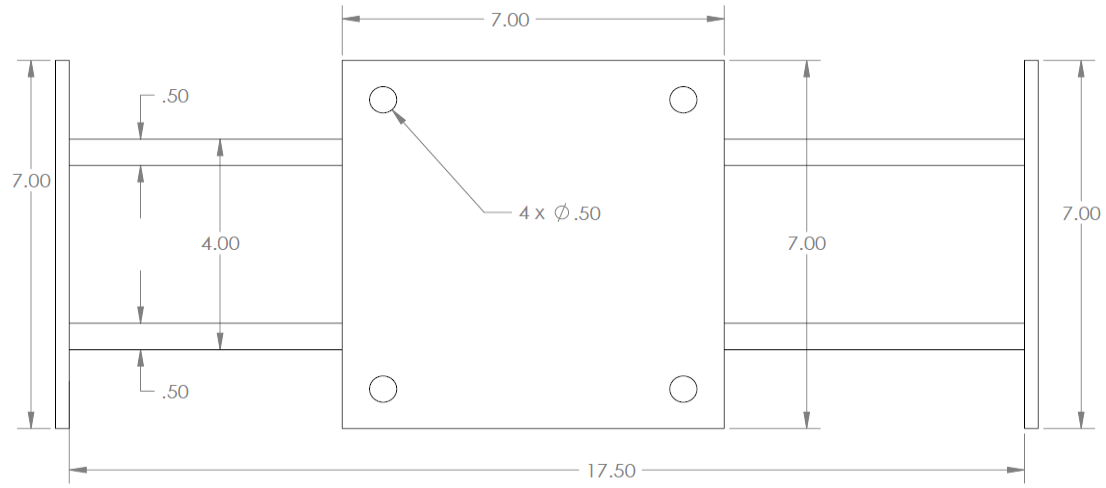

		UNLESS OTHERWISE SPECIFIED:		NAME	DATE
		DIMENSIONS ARE IN INCHES TOLERANCES: FRACTIONAL ± ANGULAR: MACH ± BEND ± TWO PLACE DECIMAL ± THREE PLACE DECIMAL ±	DRAWN		
			CHECKED		
			ENG APPR.		
			MFG APPR.		
		INTERPRET GEOMETRIC TOLERANCING PER:	Q.A.		
		MATERIAL	COMMENTS:		
NEXT ASSY	USED ON	FINISH			
APPLICATION		DO NOT SCALE DRAWING			

TITLE:
Couped T-joint connection
4"X4"X0.25" square tube

SIZE	DWG. NO.	REV
A		
SCALE: 1:10	WEIGHT:	SHEET 4 OF 6

5 4 3 2 1

A3 - Detailed Drawings of part 3 (corresponding to test rig 2)

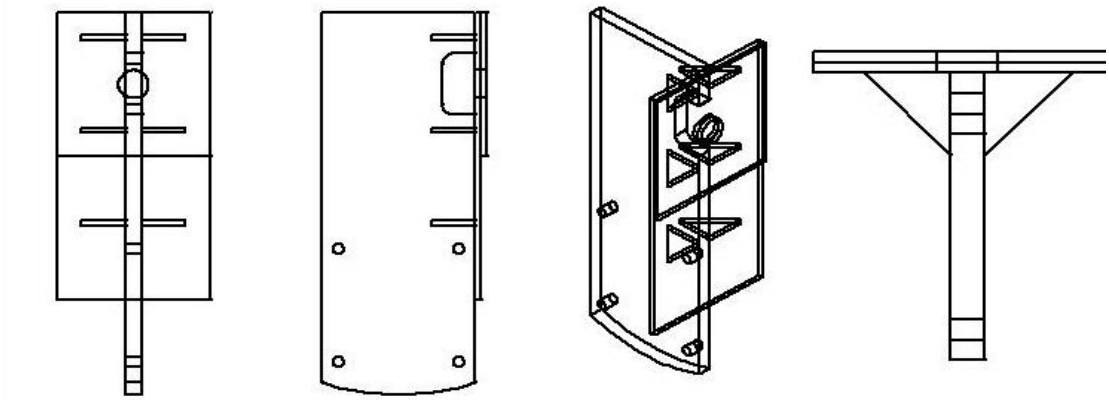

UNLESS OTHERWISE SPECIFIED:

	NAME	DATE
DRAWN	R.M.	Feb 21,07
CHECKED	R.F.	Feb 21,07
ENG APPR		
MFG APPR		
Q.A		
COMMENTS: All plate are welded 1/4"		

TITLE: Part 3 - redesigned part for th application of higher loads

SIZE A | DWG. NO. Assem2s | REV

SCALE: 1:10 WEIGHT: | SHEET 1 OF

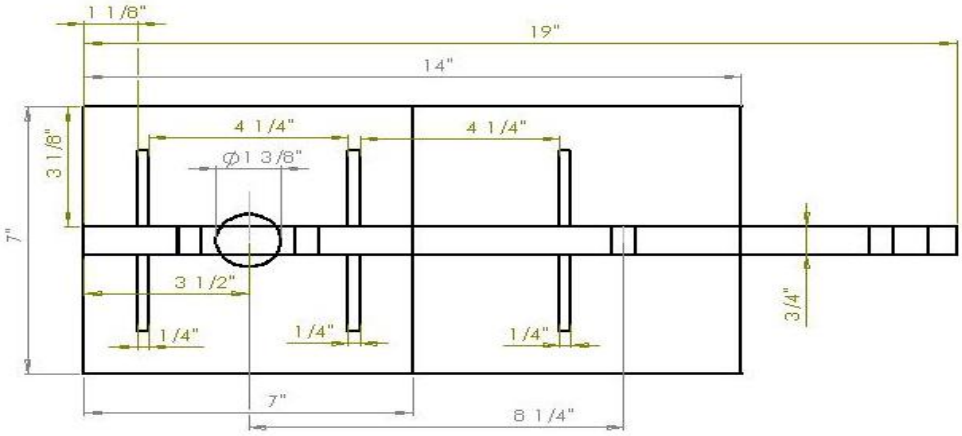

UNLESS OTHERWISE SPECIFIED:

	NAME	DATE
DRAWN	R.M.	Feb 21,07
CHECKED	R.F.	Feb 21,07
ENG APPR		
MFG APPR		
Q.A		
COMMENTS: All plate are welded 1/4"		

TITLE: Back view of part 3

SIZE A | DWG. NO. Assem2s | REV

SCALE: 1:10 WEIGHT: | SHEET 2 OF

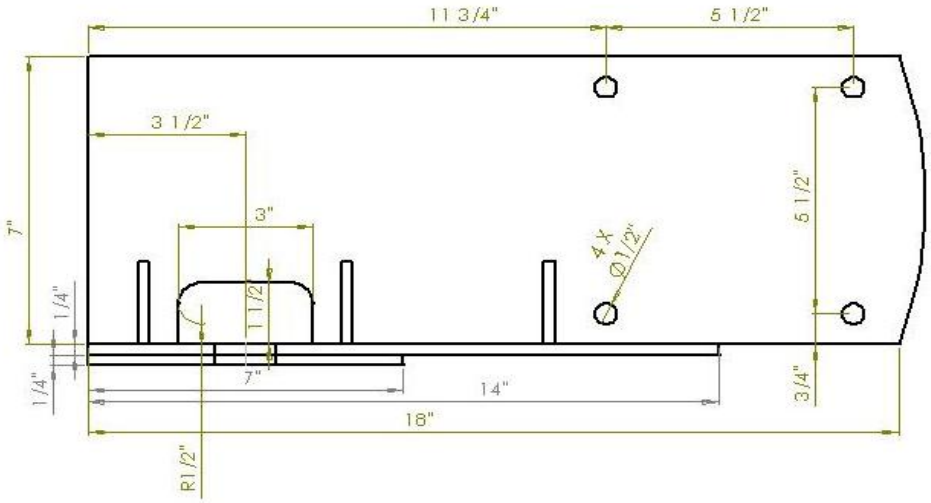

UNLESS OTHERWISE SPECIFIED:		NAME	DATE		
DIMENSIONS ARE IN INCHES TOLERANCES: FRACTIONAL ± ANGULAR: MACH ± BEND ± TWO PLACE DECIMAL ± THREE PLACE DECIMAL ±	DRAWN	R.M.	Feb 21,07		
	CHECKED	R.F.	Feb 21,07	TITLE: Side view of part 3	
	ENG APPR				
	MFG APPR				
INTERPRET GEOMETRIC TOLERANCING PER:	Q A				
MATERIAL	COMMENTS: All plate are welded 1/4"			SIZE A	DWG. NO. Assem2s
FINISH				SCALE: 1:10	WEIGHT: SHEET 3 OF
NEXT ASSY / USED ON					
APPLICATION	DO NOT SCALE DRAWING				

PROPRIETARY AND CONFIDENTIAL
THE INFORMATION CONTAINED IN THIS DRAWING IS THE SOLE PROPERTY OF <INSERT COMPANY NAME HERE>. ANY REPRODUCTION IN PART OR AS A WHOLE WITHOUT THE WRITTEN PERMISSION OF <INSERT COMPANY NAME HERE> IS PROHIBITED

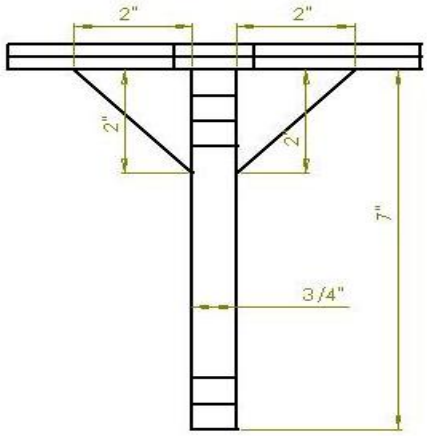

UNLESS OTHERWISE SPECIFIED:		NAME	DATE		
DIMENSIONS ARE IN INCHES TOLERANCES: FRACTIONAL ± ANGULAR: MACH ± BEND ± TWO PLACE DECIMAL ± THREE PLACE DECIMAL ±	DRAWN	R.M.	Feb 21,07		
	CHECKED	R.F.	Feb 21,07	TITLE: Top view of part 3	
	ENG APPR				
	MFG APPR				
INTERPRET GEOMETRIC TOLERANCING PER:	Q A				
MATERIAL	COMMENTS: All plate are welded 1/4"			SIZE A	DWG. NO. Assem2s
FINISH				SCALE: 1:10	WEIGHT: SHEET 4 OF
NEXT ASSY / USED ON					
APPLICATION	DO NOT SCALE DRAWING				

PROPRIETARY AND CONFIDENTIAL
THE INFORMATION CONTAINED IN THIS DRAWING IS THE SOLE PROPERTY OF <INSERT COMPANY NAME HERE>. ANY REPRODUCTION IN PART OR AS A WHOLE WITHOUT THE WRITTEN PERMISSION OF <INSERT COMPANY NAME HERE> IS PROHIBITED

A4 - Detailed Drawings the Stand (part 4) for test rig 2

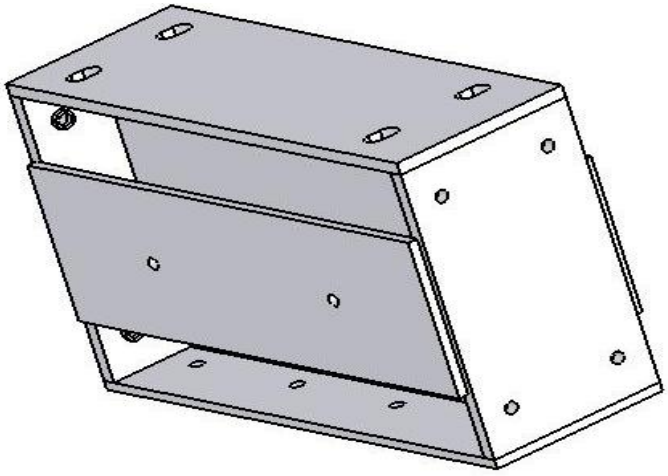

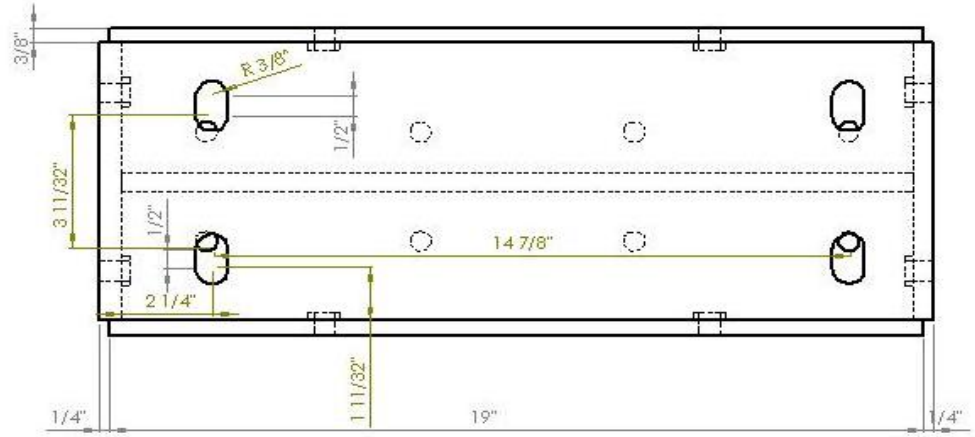

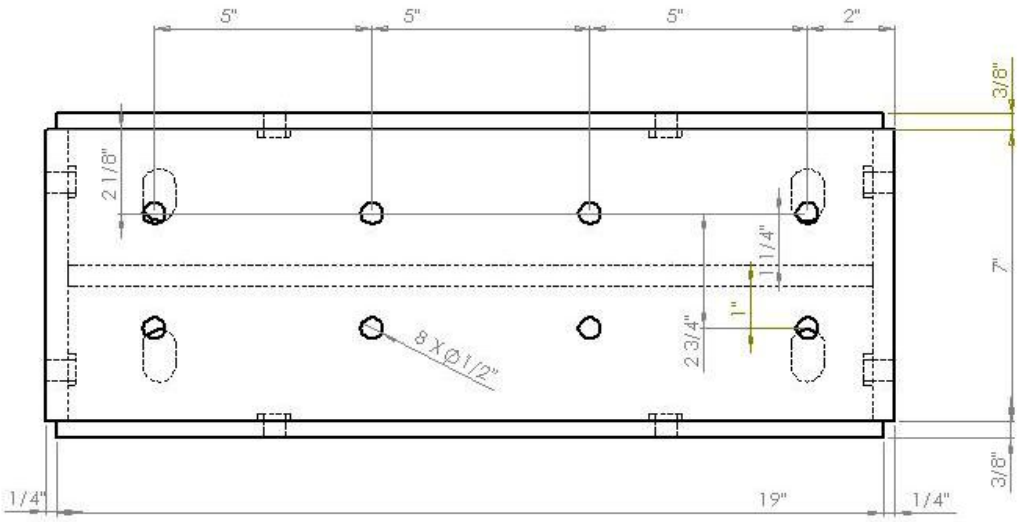

UNLESS OTHERWISE SPECIFIED:
DIMENSIONS ARE IN INCHES
TOLERANCES:
FRACTIONAL ±
ANGULAR: MACH ± BEND ±
TWO PLACE DECIMAL ±
THREE PLACE DECIMAL ±
INTERPRET GEOMETRIC TOLERANCING PER:
MATERIAL
FINISH
NEXT ASSY | USED ON
APPLICATION
DO NOT SCALE DRAWING

	NAME	DATE
DRAWN	R.M.	Feb 21 0
CHECKED	R.F.	Feb 21 0
ENG APPR		
MFG APPR		
Q.A		

COMMENTS:
All plate are welded
1/4"

TITLE: Bottom View of the star

SIZE | DWG. NO. | REV
Astandplates1
SCALE: 1:10 WEIGHT: | SHEET 2 OF

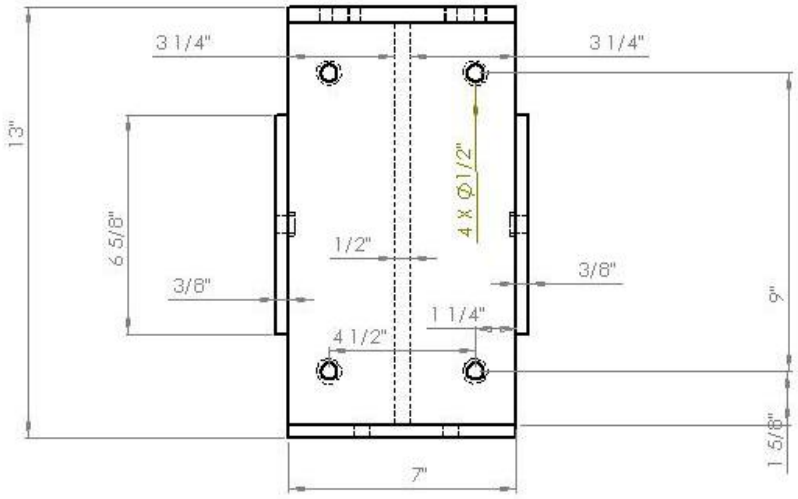

UNLESS OTHERWISE SPECIFIED:
DIMENSIONS ARE IN INCHES
TOLERANCES:
FRACTIONAL ±
ANGULAR: MACH ± BEND ±
TWO PLACE DECIMAL ±
THREE PLACE DECIMAL ±
INTERPRET GEOMETRIC TOLERANCING PER:
MATERIAL
FINISH
NEXT ASSY | USED ON
APPLICATION
DO NOT SCALE DRAWING

	NAME	DATE
DRAWN	R.M.	Feb 21 0
CHECKED	R.F.	Feb 21 0
ENG APPR		
MFG APPR		
Q.A		

COMMENTS:
All plate are welded
1/4"

TITLE: Front view of the stand

SIZE | DWG. NO. | REV
Astandplates1
SCALE: 1:10 WEIGHT: | SHEET 2 OF

all threads are 1/2"-20UNF

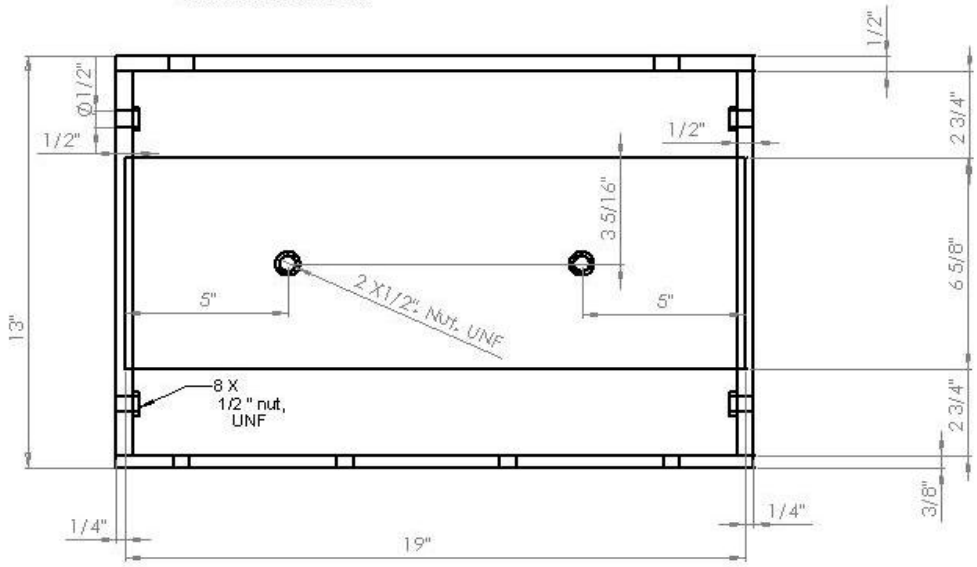

		UNLESS OTHERWISE SPECIFIED:		NAME	DATE
		DIMENSIONS ARE IN INCHES TOLERANCES: FRACTIONAL ± ANGULAR: MACH ± BEND ± TWO PLACE DECIMAL ± THREE PLACE DECIMAL ±	DRAWN	R.M.	Feb 21 0
			CHECKED	R.F.	Feb 21 0
			ENG APPR		
			MFG APPR		
		INTERPRET GEOMETRIC TOLERANCING PER:	Q A		
		MATERIAL	COMMENTS:		
		FINISH	All plate are welded 1/4"		
NEXT ASSY	USED ON				
APPLICATION		DO NOT SCALE DRAWING			

PROPRIETARY AND CONFIDENTIAL
THE INFORMATION CONTAINED IN THIS DRAWING IS THE SOLE PROPERTY OF <ENTER COMPANY NAME HERE>. ANY REPRODUCTION IN PART OR AS A WHOLE WITHOUT THE WRITTEN PERMISSION OF <ENTER COMPANY NAME HERE> IS PROHIBITED

TITLE: Side View of the stand

SIZE DWG. NO. REV
Astandplates1

SCALE: 1:10 WEIGHT: SHEET 1 O

A5 - Detailed Drawings of part 3 (for test rig 1)

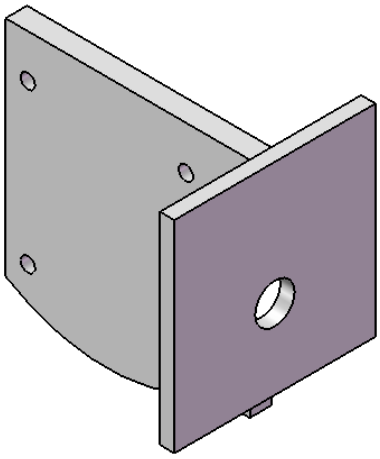

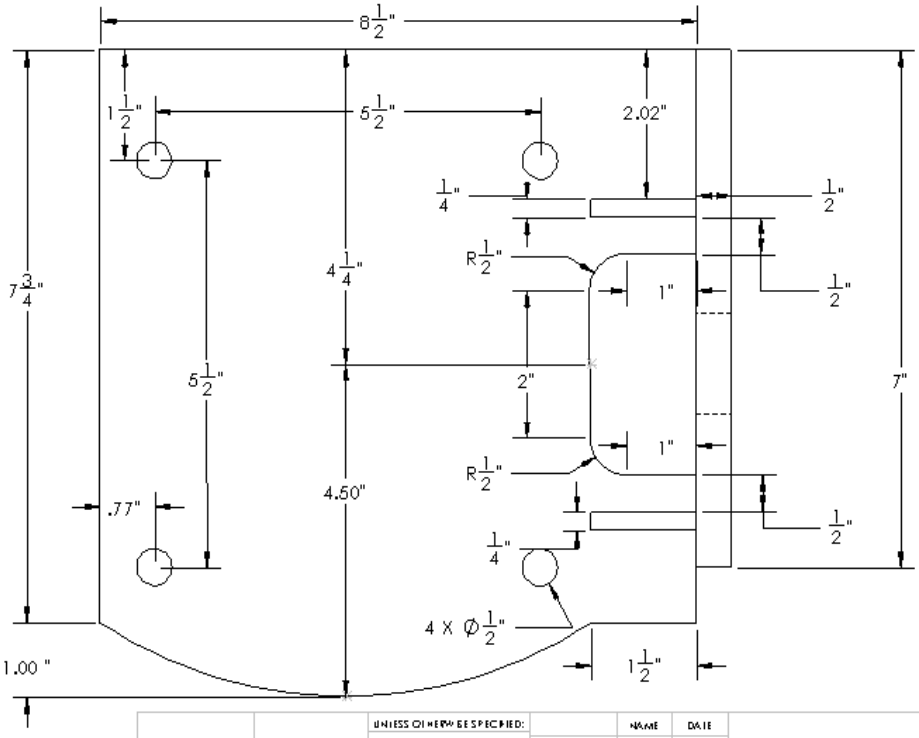

		UNLESS OTHERWISE SPECIFIED:		NAME	DATE	
		DIMENSIONS ARE IN INCHES TOLERANCES: FRACTIONAL ± ANGULAR: MACH ± BEND ± TWO PLACE DECIMAL ± THREE PLACE DECIMAL ±	DRAWN	R.M.	17/6/09	TITLE: Side View
			CHECKED	R.F.	17/6/09	
			ENG APPR.			
			MFG APPR.			
		INTERPRET GEOMETRIC TOLERANCING PER:	Q.A.			
PROPRIETARY AND CONFIDENTIAL THE INFORMATION CONTAINED IN THIS DRAWING IS THE SOLE PROPERTY OF <INSERT COMPANY NAME HERE>. ANY REPRODUCTION IN PART OR AS A WHOLE WITHOUT THE WRITTEN PERMISSION OF <INSERT COMPANY NAME HERE> IS PROHIBITED		MATERIAL	COMMENTS: all plates are welded 1/4"			SIZE A DWG. NO. Assem1 REV
		FINISH				
NEXT ASSY	USED ON					SCALE: 1:5 WEIGHT: SHEET 2 OF 4
APPLICATION		DO NOT SCALE DRAWING				

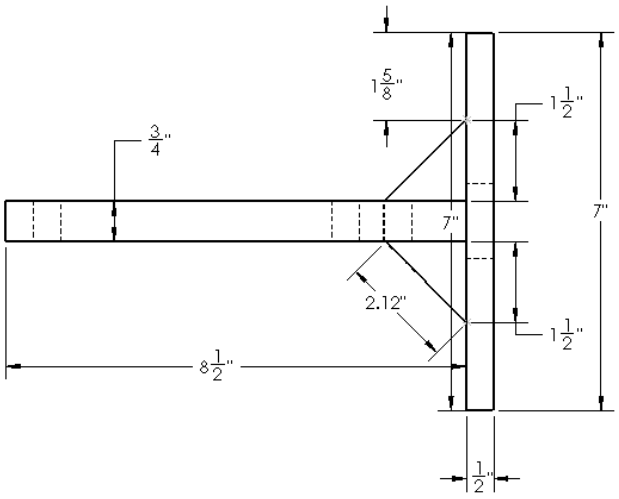

		UNLESS OTHERWISE SPECIFIED:		NAME	DATE
		DIMENSIONS ARE IN INCHES TOLERANCES: FRACTIONAL ± ANGULAR: MACH ± BEND ± TWO PLACE DECIMAL ± THREE PLACE DECIMAL ±	DRAWN	R.M.	17/6/09
			CHECKED	R.F.	17/6/09
			ENG APPR.		
			MFG APPR.		
		NEXT PRELIGEOMETRIC TOLERANCING PER:	Q.A.		
		MATERIAL	COMMENTS: all plates are welded 1/4"		
NEXT ASSY	USED ON	FINISH			
APPLICATION		DO NOT SCALE DRAWING			

PROPRIETARY AND CONFIDENTIAL

THE INFORMATION CONTAINED IN THIS DRAWING IS THE SOLE PROPERTY OF <INSERT COMPANY NAME HERE>. ANY REPRODUCTION IN PART OR AS A WHOLE WITHOUT THE WRITTEN PERMISSION OF <INSERT COMPANY NAME HERE> IS PROHIBITED.

TITLE: **Top View**

SIZE	DWG. NO.	REV
A	Assem1	
SCALE: 1:4	WEIGHT:	SHEET 3 OF

5 4 3 2 1

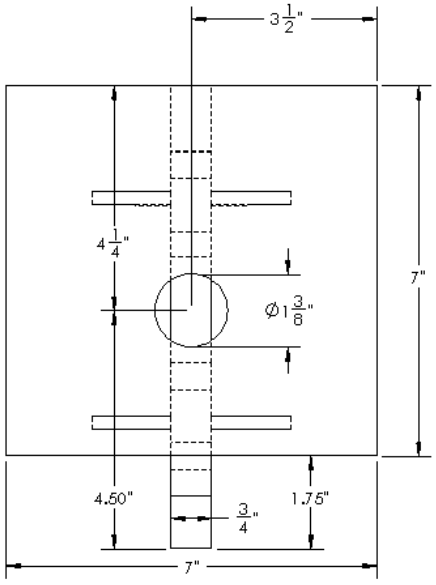

		UNLESS OTHERWISE SPECIFIED:		NAME	DATE
		DIMENSIONS ARE IN INCHES TOLERANCES: FRACTIONAL ± ANGULAR: MACH ± BEND ± TWO PLACE DECIMAL ± THREE PLACE DECIMAL ±	DRAWN	R.M.	17/6/09
			CHECKED	R.F.	17/6/09
			ENG APPR.		
			MFG APPR.		
		INTERPRET GEOMETRIC TOLERANCING PER:	Q.A.		
		MATERIAL	COMMENTS: all plates are welded 1/4"		
NEXT ASSY	USED ON	FINISH			
APPLICATION		DO NOT SCALE DRAWING			

PROPRIETARY AND CONFIDENTIAL

THE INFORMATION CONTAINED IN THIS DRAWING IS THE SOLE PROPERTY OF <INSERT COMPANY NAME HERE>. ANY REPRODUCTION IN PART OR AS A WHOLE WITHOUT THE WRITTEN PERMISSION OF <INSERT COMPANY NAME HERE> IS PROHIBITED.

TITLE: **Front View**

SIZE	DWG. NO.	REV
A	Assem1	
SCALE: 1:4	WEIGHT:	SHEET 4 OF 4

5 4 3 2 1

A6 - Detailed Drawings the Stand (part 4) for test rig 1

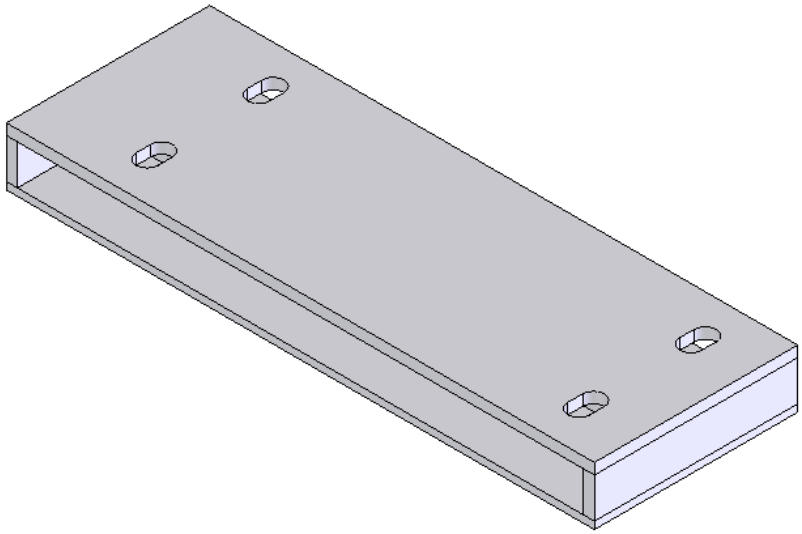

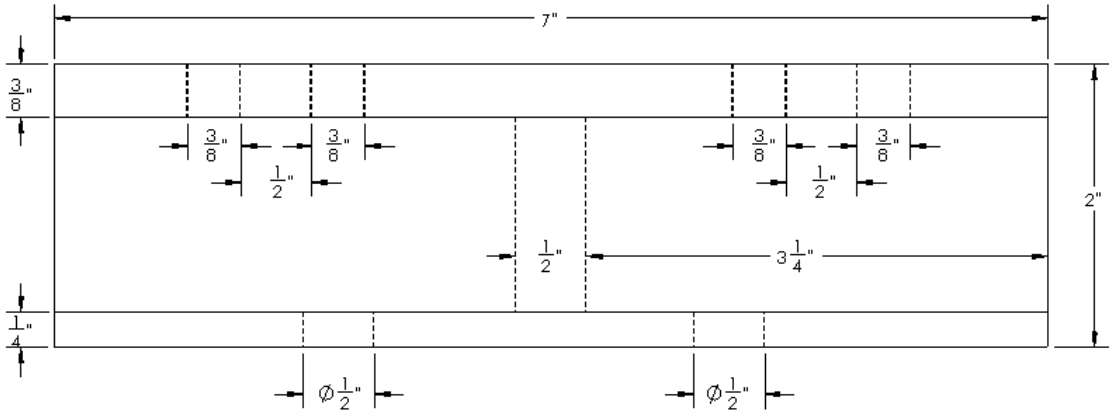

		UNLESS OTHERWISE SPECIFIED:		NAME	DATE
		DIMENSIONS ARE IN INCHES TOLERANCES: FRACTIONAL ± ANGULAR: MACH ± BEND ± TWO PLACE DECIMAL ± THREE PLACE DECIMAL ±	DRAWN	R.M.	17/6/09
			CHECKED	R.F.	17/6/09
			ENG APPR.		
			MFG APPR.		
		INTERPRET GEOMETRIC TOLERANCING PER:	Q.A.		
		MATERIAL	COMMENTS: all plates are welded 1/4"		
NEXT ASSY	USED ON	FINISH			
APPLICATION		DO NOT SCALE DRAWING			

PROPRIETARY AND CONFIDENTIAL
THE INFORMATION CONTAINED IN THIS DRAWING IS THE SOLE PROPERTY OF <INSERT COMPANY NAME HERE>. ANY REPRODUCTION IN PART OR AS A WHOLE WITHOUT THE WRITTEN PERMISSION OF <INSERT COMPANY NAME HERE> IS PROHIBITED.

TITLE: Front View of the stand

SIZE: A | DWG. NO.: standplates | REV

SCALE: 1:5 | WEIGHT: | SHEET 2 OF 4

5 4 3 2 1

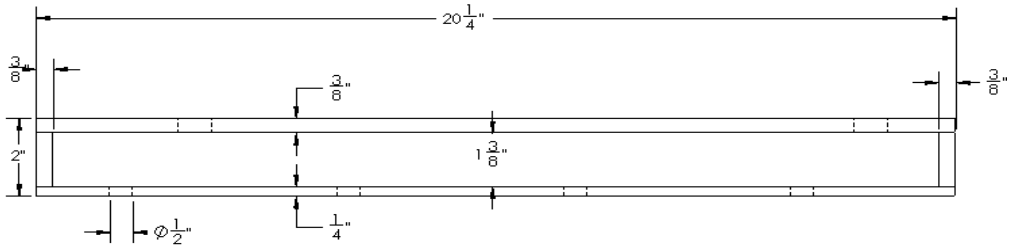

UNLESS OTHERWISE SPECIFIED:		NAME	DATE		
DIMENSIONS ARE IN INCHES TOLERANCES: FRACTIONAL ± ANGULAR: MACH ± BEND ± TWO PLACE DECIMAL ± THREE PLACE DECIMAL ±	DRAWN	R.M.	17/6/09	TITLE: Side View of the stand	
	CHECKED	R.F.	17/6/09		
	ENG APPR.				
	MFG APPR.				
INTERPRET GEOMETRIC TOLERANCING PER:	Q.A.				
MATERIAL	COMMENTS: all plates are welded 1/4"			SIZE: A	DWG. NO.: standplates
FINISH				SCALE: 1:8	WEIGHT:
NEXT ASSY / USED ON					SHEET 3 OF
APPLICATION / DO NOT SCALE DRAWING					

PROPRIETARY AND CONFIDENTIAL
THE INFORMATION CONTAINED IN THIS DRAWING IS THE SOLE PROPERTY OF <INSERT COMPANY NAME HERE>. ANY REPRODUCTION IN PART OR AS A WHOLE WITHOUT THE WRITTEN PERMISSION OF <INSERT COMPANY NAME HERE> IS PROHIBITED.

5 4 3 2 1

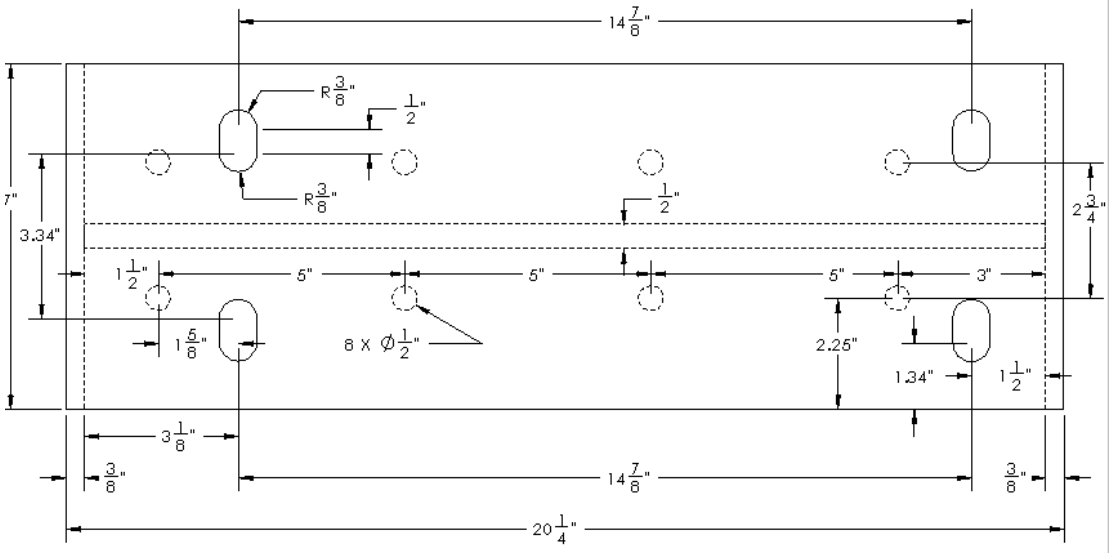

UNLESS OTHERWISE SPECIFIED:		NAME	DATE		
DIMENSIONS ARE IN INCHES TOLERANCES: FRACTIONAL ± ANGULAR: MACH ± BEND ± TWO PLACE DECIMAL ± THREE PLACE DECIMAL ±	DRAWN	R.M.	17/6/09	TITLE: Top View of the stand	
	CHECKED	R.F.	17/6/09		
	ENG APPR.				
	MFG APPR.				
INTERPRET GEOMETRIC TOLERANCING PER:	Q.A.				
MATERIAL	COMMENTS: all plates are welded 1/4"			SIZE: A	DWG. NO.: standplates
FINISH				SCALE: 1:8	WEIGHT:
NEXT ASSY / USED ON					SHEET 4 OF 4
APPLICATION / DO NOT SCALE DRAWING					

PROPRIETARY AND CONFIDENTIAL
THE INFORMATION CONTAINED IN THIS DRAWING IS THE SOLE PROPERTY OF <INSERT COMPANY NAME HERE>. ANY REPRODUCTION IN PART OR AS A WHOLE WITHOUT THE WRITTEN PERMISSION OF <INSERT COMPANY NAME HERE> IS PROHIBITED.

5 4 3 2 1